Computational models for the extrusion-based additive manufacturing

Original Citation:
Computational models for the extrusion-based additive manufacturing / Pricci, Alessio. - ELETTRONICO. - (2024). [10.60576/poliba/iris/pricci-alessio_phd2024]

Published version
Politecnico di Bari
DOI:10.60576/poliba/iris/pricci-alessio_phd2024

Politecnico
di Bari

Department of Electrical and Information Engineering

INDUSTRY 4.0

Ph.D. Program

SSD: ING-IND/16–TECHNOLOGIES AND MANUFACTURING SYSTEMS

SSD: ING-IND/06–FLUID DYNAMICS

Final Dissertation

Computational models for the extrusion-based additive manufacturing

---

by

Pricci Alessio

Supervisors:
Prof. Gianluca Percoco
Prof. Marco D. De Tullio
Prof. Luigi Tricarico

Coordinator of Ph.D. Program:
Prof. Ciminelli Caterina

Course n°36, 01/11/2020-31/10/2023

Politecnico
di Bari

Department of Electrical and Information Engineering

INDUSTRY 4.0
Ph.D. Program

SSD: ING-IND/16–TECHNOLOGIES AND MANUFACTURING SYSTEMS
SSD: ING-IND/06–FLUID DYNAMICS

Final Dissertation

Computational models for the extrusion-based additive manufacturing

by

Pricci Alessio

Pricci Alessio

Referees:
Prof. Hassan Alaa
Prof. Smith Douglas

Supervisors:
Prof. Gianluca Percoco
Prof. Marco D. De Tullio
Prof. Luigi Tricarico

Coordinator of Ph.D. Program:
Prof. Ciminelli Caterina

Preface

The work described in the present Ph.D. thesis has been performed at the "Interdisciplinary Additive Manufacturing (IAM) Lab", Taranto (Polytechnic of Bari).
The present PhD thesis refers to the following 5 papers, in which the candidate is first author, published in international journals and national conferences.

- "Analytical and numerical models of thermoplastics: A review aimed to pellet extrusion-based additive manufacturing" **A. Pricci**, M.D. de Tullio, G. Percoco – Polymers, 2021

- "Semi-analytical models for non-Newtonian fluids in tapered and cylindrical ducts, applied to the extrusion-based additive manufacturing" **A. Pricci**, M.D. de Tullio, G. Percoco – Materials & Design, 2022

- "Modeling of extrusion-based additive manufacturing for pelletized thermoplastics: Analytical relationships between process parameters and extrusion outcomes" **A. Pricci**, M.D. de Tullio, G. Percoco – CIRP Journal of Manufacturing Science and Technology, 2023

- "Semi-analytical and numerical models to predict the extrusion force for silicone additive manufacturing, as a function of the process parameters" **A. Pricci**, S M A. I. Ovy, G. Stano, G. Percoco Y. Tadesse – Additive Manufacturing Letters, 2023

- "Non-Newtonian, non-isothermal three-dimensional modeling of strand deposition in screw-based material extrusion" **A. Pricci**, G. Percoco – Materials Research Proceedings: Materials Research Forum LLC (MRF), Proceeding of the XVI AITEM Conference, 2023

Other studies which are currently under review in international journals and conferences, whose content is not part of the present dissertation are listed below.

- "A generalized method aiming at predicting the polymer melts flow field in the metering zone of large-scale single-screw extruders" **A. Pricci**, G. Percoco

- "Electromagnetic-assisted silicone additive manufacturing: reducing printing force for bio-inspired soft robots" G. Stano, **A. Pricci**, A. Pavone, G. Percoco

- "Enhancing extrusion of silicone for additive manufacturing of biomimetic soft structures" **A. Pricci**, G. Stano, A. Pavone, O. Fiume, G. Percoco

To my beloved parents

Table of contents

List of figures

List of tables

List of abbreviations

4IR	Fourth industrial revolution
AM	Additive manufacturing
BAAM	Big area additive manufacturing
BVP	Boundary value problem
CAD	Computer-aided design
CFD	Computational fluid dynamics
DIW	Direct ink writing
DT	Digital twin
FDM	Finite difference method
FEM	Finite element method
FFF	Fused filament fabrication
FVM	Finite volume method
GNF	Generalized non-Newtonian fluid
IM	Injection moulding
J-H	Jeffery-Hamel
LFAM	Large format additive manufacturing
MEX	Material extrusion
MiE	Micro-extrusion
ODE	Ordinary differential equation
PAM	Pellet additive manufacturing
SSE	Single-screw extruder
VOF	Volume-of-fluid
WRMS	Weissenberg-Rabionowitsch-Mooney-Schofield

Abstract

The Fourth Industrial Revolution (4IR) has introduced new business models focused on consumers and product customization. As a natural consequence, both the quantity of the service provided and the added value have increased.

Additive Manufacturing (AM) is one of the nine pillars of 4IR; it enables the production of small batches of customized and lightweight components on demand. In addition, it plays a key role in sustainability, as it offers opportunities to minimize waste, energy consumption and use eco-friendly materials. In the framework of sustainability, the transportation emissions are lowered by this decentralized and flexible production.

Furthermore, a second key pillar of 4IR is Digital Twin (DT), which indicates a virtual simulation of a real-world machine, product or complex system; in general, DT is based on data collected through a complex network of sensors, to better analyze the behavior of real systems.

However, computer simulations are gaining increasing attention, because of the possibility to analyze quantities that cannot be measured directly and gain a deep insight of physical processes occurring in AM. On the one hand, analytical methods allow for a closed form solution of a given problem with many assumptions. On the other hand, fully numerical methods describe more complex scenarios, but they can be computationally expensive. An intermediate solution is given by semi-analytical models.

In the present work, different Material Extrusion (MEX) processes have been studied by means of both semi-analytical and fully numerical methods.

In the first part of the dissertation the screw-based MEX, based on the processing of pelletized thermoplastics has been reviewed and studied mathematically; for the first time, a complete model aiming at coupling the screw-barrel and deposited layer dynamics has been formulated. The influence of process parameters on important flow characteristics (i.e., mass flow rate, pressure and melting profile) has been explored.

In the second part, generalized methods to solve the flow in i) straight cylindrical ducts and ii) tapered cone geometries, usually found as internal geometrical features in the nozzles used in all MEX processes, have been formulated. The first method has been validated with respect to literature data, while the latter has been compared with real force measurement by means of a silicone MEX custom-made setup.

Then, a model for the counterpressure arising under the extrusion head has been developed and validated using the same MEX setup; the composite model (made up of nozzle flow and deposited bead models) showed an accuracy up to 99.7[%] in predicting overall printing force; this paves the way for the application of the proposed methods in other MEX processes modeling, control and optimization.

KEYWORDS: Additive Manufacturing, Material Extrusion, Extrusion Force, Counterpressure Force, Jeffery-Hamel flow, Semi-analytical Methods, Numerical Modeling

1. General outline of the dissertation

1.1. Introduction

4IR can be defined as the combination of the main advances in robotics, internet of things, 3D printing and other technologies which are revolutionizing the way we live.

The main points of 4IR are automation, interoperability, and transparency of information [1], combined with an underlying ethics conscious of the need for processes with low environmental impact.

AM is one of the key pillars in the upcoming 4IR, leading to the manufacturing of a physical three-dimensional object starting from a computer-aided design (CAD) model.

Moreover, AM allows substantial savings in terms of logistic costs, giving the opportunity to perform 3D printing once the printing file has been acquired, wherever the 3D printer is located.

AM satisfies the growing need for product customization, leading to the development of functional, flexible, and efficient parts and assemblies.

In accordance with ISO ASTM 52900:2015 there are seven AM process groups, based on different physical and working principles: MEX, sheet lamination, binder jetting, directed energy deposition, powder bed fusion and vat photopolymerization.

This thesis focuses on the mathematical modeling of different MEX techniques; a material is pushed through an extruding nozzle to build the workpiece layer-by-layer. A first classification can be made with respect to the material being extruded (i.e., thermoplastics and silicones), the original state of the material (i.e., pelletized, filament and paste-like material) and the pushing mechanism (i.e., screw-, gear- and piston-assisted extrusion). At the state of the art, there are three different MEX processes:

- **Fused Filament Fabrication** (FFF): thermoplastic material is initially given in the form of filament wound in coils and a pair of counter rotating gears pushes the filament downwards; then, the solid filament enters a zone heated above the polymer melting point; then, the molten material is extruded through a nozzle and deposited layer-by-layer.

- **Direct Ink Writing** (DIW): silicone material is initially given as a reservoir inside a syringe. A piston moves axially to extrude the material through a tapered needle, to be dispensed layer-by-layer.

- **Pellet-based additive manufacturing** (PAM): thermoplastic material is initially given in the form of pellet. This is conveyed in a screw-barrel system, analogue to the one used in Single-Screw Extrusion (SSE). At a given axial position a gradual melting process takes place and the molten material moves towards the extruding nozzle under the influence of pressure. Then, deposition happens layer-by-layer, similarly to the other MEX techniques.

It should be mentioned that hybrid solutions where a thermoplastic (stiff) substrate is extruded in combination with silicone (soft) elements are emerging.

In the present thesis, special attention has been given to DIW and PAM, because of their application in middle- and large-scale AM.

1.2. Aim and scope

The main purpose of the dissertation is the advancement of the mathematical modeling of middle- and large-scale MEX technologies. To achieve this goal, both semi-analytical and numerical models have been formulated, with the following main findings:

- **Thermoplastics PAM**: this thesis presents the first mathematical model aiming at describing the dependence of the pellet-extrusion outcomes (i.e., mass flow rate, melting and pressure profiles) on printing parameters.

- **Silicone DIW**: the effect of counterpressure on the extruded mass flow rate of a moisture-cured silicone has been investigated; the model is valid for all generalized non-Newtonian fluids (GNFs) such as thermoplastics and silicones.

1.3. Structure of the thesis

The thesis is made up of six additional chapters, where each chapter is written as a self-standing study that includes its own introduction, literature review, result discussion and conclusions.

The work starts by finding the most comprehensive mathematical model to describe single-screw extrusion of thermoplastics; then, the model has been coupled with an enhanced model of layer extrusion, to study the effect of printing speed and layer height on the delivered mass flow rate. The same behavior has been observed experimentally and numerically, by testing several printing scenarios with a pellet extruder available at the "Interdisciplinary Additive Manufacturing (IAM) Lab", Taranto (Polytechnic of Bari).

The extrusion theory applies to power-law rheologies. At first, an attempt to extend the model for the nozzle (both tapered and cylindrical sections) has been made; simple iterative schemes for the extrusion of GNFs have been proposed and validated against literature data.

Then, also the theory for layer extrusion has been extended to deal with all GNFs and it has been applied to moisture-cured silicone extrusion; the theory has been tested with respect to a custom-made MEX setup.

A comprehensive scheme has been reported below:

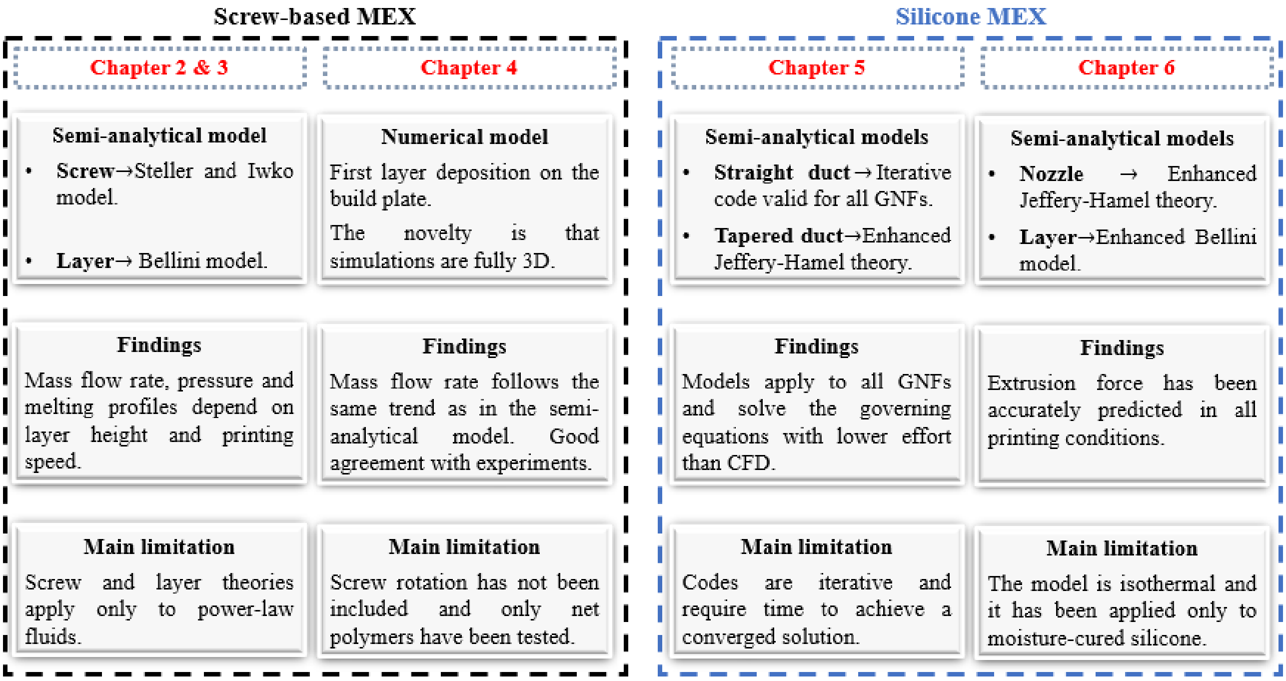

Screw-based MEX		Silicone MEX	
Chapter 2 & 3	**Chapter 4**	**Chapter 5**	**Chapter 6**
Semi-analytical model • **Screw**→Steller and Iwko model. • **Layer**→ Bellini model.	**Numerical model** First layer deposition on the build plate. The novelty is that simulations are fully 3D.	**Semi-analytical models** • **Straight duct**→Iterative code valid for all GNFs. • **Tapered duct**→Enhanced Jeffery-Hamel theory.	**Semi-analytical models** • **Nozzle** → Enhanced Jeffery-Hamel theory. • **Layer**→Enhanced Bellini model.
Findings Mass flow rate, pressure and melting profiles depend on layer height and printing speed.	**Findings** Mass flow rate follows the same trend as in the semi-analytical model. Good agreement with experiments.	**Findings** Models apply to all GNFs and solve the governing equations with lower effort than CFD.	**Findings** Extrusion force has been accurately predicted in all printing conditions.
Main limitation Screw and layer theories apply only to power-law fluids.	**Main limitation** Screw rotation has not been included and only net polymers have been tested.	**Main limitation** Codes are iterative and require time to achieve a converged solution.	**Main limitation** The model is isothermal and it has been applied only to moisture-cured silicone.

Figure 1.1. Global scheme of the dissertation.

Therefore, the dissertation is organized as follows:

- Chapter 2 – **A literature review of the analytical and numerical models used in single-screw extrusion**: a review of the existing literature on SSE modeling has been outlined; the purpose is twofold: i) to establish the state-of-the art in SSE modeling, and ii) to investigate the main assumptions underlying these models.

- Chapter 3 – **Modeling of the extrusion-based additive manufacturing: how printing parameters affect extrusion outcomes**: a composite model has been presented to describe a generic SSE extruder, together with its validation. In addition, the model has been applied to PAM, to find the influence of the main extrusion parameters on counterpressure arising in practical printing conditions.

- Chapter 4 – **A non-Newtonian, non-isothermal and three-dimensional CFD model of strand deposition in PAM**: Computational Fluid Dynamics (CFD) studies have been formulated to study the influence of printing parameters on the strand cross-sectional shape in PAM. CFD results have been also validated experimentally and the influence of counterpressure on mass flow rate has been shown.

- Chapter 5 – **Semi-analytical models aiming at describing the flow of non-Newtonian fluids in tapered and cylindrical ducts, applied to thermoplastics and silicone MEX**: a semi-analytical method based on the Jeffery-Hamel (J-H) flow formulation has been proposed to generalize the study of the flow in straight and cylindrical ducts that can be found in all MEX processes, no matter of the material being extruded. The novelty is that the semi-analytical formulation applies practically to every material rheology. This model is an original extension of the widely adopted Bellini extrusion model.

- Chapter 6 – **Application of the generalized MEX model to the silicone based additive manufacturing**: the new semi-analytical method aiming at describing the extrusion force in nozzles for MEX has been applied to silicone-based MEX. In addition, a semi-analytical model of the counterpressure arising in isothermal MEX has been developed and experimentally validated. This work was carried out in collaboration with Humanoid Biorobotics, and Smart Systems (HBS Lab) of the University of Texas at Dallas.

- Chapter 7 – **Conclusions and further works**: results are discussed, and conclusions are summarized.

2. A literature review of the analytical and numerical models used in single-screw extrusion

2.1. Chapter organization

PAM extrusion systems consist of a screw-barrel system where the pelletized feedstock is conveyed, melted and transported towards an extruding nozzle. To date, there is no specific mathematical and/or computational model which allows to predict the characteristics of this very complex extrusion system (i.e., mass flow rate, pressure and melting profiles) as a function of the different processing parameters (i.e., screw speed, printing speed, layer height and temperature of the heated zones).

Because of the similarity of the working principle and internal structure of PAM extruders with SSE, the idea was that to review the main models for SSE with a very specific purpose: to select the most advanced models to build a composite mathematical model for PAM extrusion (which has been done in Chapter 3).

The chapter is organized as follows: in Section 2.2, a general introduction to the advantages and disadvantages of PAM extrusion with respect to FFF is given. Then, the internal structure and polymer melting dynamics for a SSE is outlined in Section 2.3. Next, in Section 2.3.1, solid-conveying zone is discussed both analytically (Section 2.3.1.1) and numerically (Section 2.3.1.2). The distinction is justified by the purpose to give a better understanding in the framework of the different zones. The same distinction is made for compression and metering zones, respectively in Sections 2.3.2 and 2.3.3.

2.2. Introduction

Among AM processes, FFF is the most widespread (see: Figure 2.1 – a); it consists in manufacturing products starting by extruding a polymeric material given in the form of a filament, which is then gradually molten through an extrusion system. Initially, raw filament is pushed down by a pair of wheels. Then, the filament reaches the heated part of the extrusion system. A gradual melting process begins because of the heat generated by a series of resistors. Finally, the fused filament is extruded through a nozzle, and it is deposited layer-by-layer until the final object has been built.

In PAM (see: Figure 2.1 – b), the material is initially given in the form of pellet, and it is conveyed through a hopper in a screw-barrel system, similarly to what happens in SSE.

Because of the load exerted both by the rotating screw and gravity, the pellet drops downstream in PAM extruders screw vanes, following a helical path. The pellet is gradually heated until it reaches the melting point (although there is a softening zone instead of a sharp melting point for amorphous polymers).

External heat is provided by several heated sections, namely the barrel. The barrel is the external envelope which contains the extrusion screw. Finally, the molten polymer reaches the extrusion nozzle and is deposited as a filament whose continuity is primarily related to the pellets' dimensions and hygroscopic content [2]. The first can lead to clogging and stall of the screw or to a non-uniform deposition [3]. The latter can be minimized by subjecting the pellet to controlled thermal cycles.

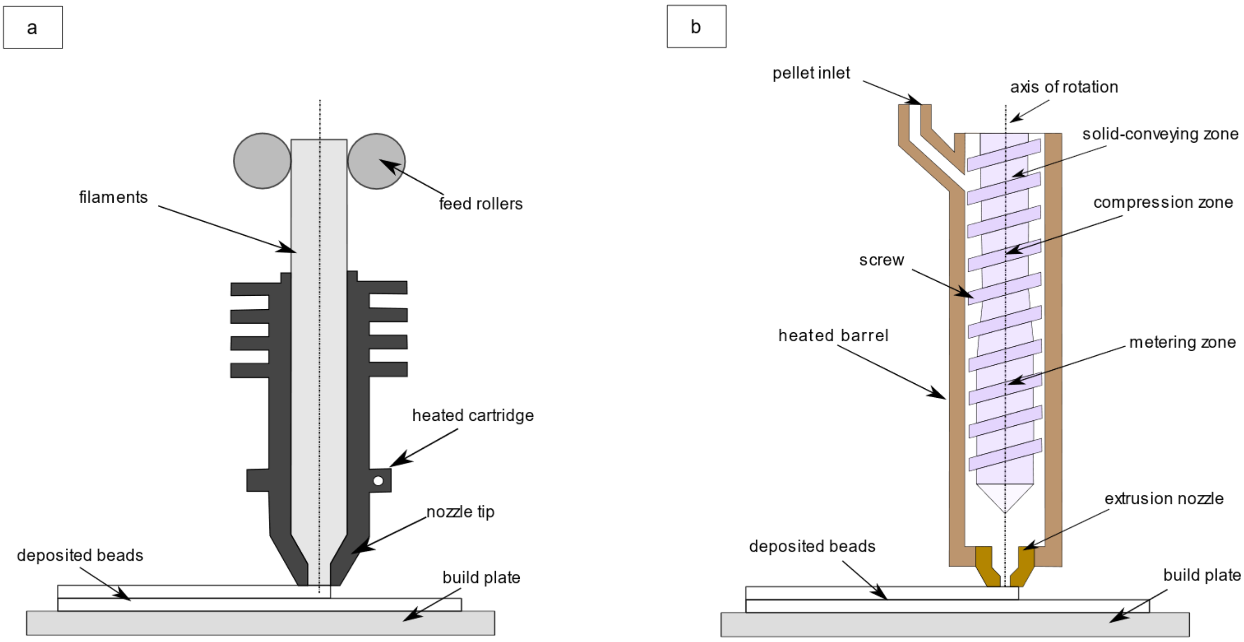

Figure 2.1. a.) Perspective view of FFF process; b.) front view of the complete extrusion system in PAM.

In reference to PAM, a distinction must be made with respect to the printable volumes. For low printable volumes, the expression Micro-Extrusion (MiE) is used, while for larger ones the process is called Big Area Additive Manufacturing (BAAM) or Large-Format Additive Manufacturing (LFAM).
FFF provides an effective benchmark for MiE, because of the similarity in terms of printable volumes.
The low environmental impact, lower costs, and the possibility to combine pellets of different material in MiE are the main advantages over the well-established FFF process.
On the other hand, the rate of deposition in BAAM is much higher than in FFF and MiE; in fact, in FFF, there is a limitation in diameter for the filaments that can be printed. In addition, the extrusion nozzle dimensions for both FFF and MiE are much smaller than that in BAAM.

The FFF process suffers from several limitations, such as:

- filament is expensive, if compared to the same material given in the form of pellet,
- limited range of materials for filament deposition,
- buckling of the filament if its feeding speed is too high,
- high energy consumption of conventional filament extrusion systems,
- high environmental impact of the filament,
- low printing volumes, and
- low productivity.

The weaknesses of the FFF process become strengths for PAM systems. Indeed, cost related to the use of pellet as raw material can be reduced by a factor 20× if compared to the same material given in the form of filament [4].

The range of printable materials is wider by far, because not every polymeric material can be supplied in the form of filament, while it can be purchased in granular or pellet form.

By using a pelletized feedstock there is no buckling, which is a problem strictly related to the push of the solid filament inside FFF heating chamber.

It has been demonstrated (Figure 2.2) that about 95[%] of the energy consumption of a conventional manufacturing 3D printing process is related to the heating of the temperature-controlled environment where the deposition process takes place [5]. In the case of both advanced FFF and PAM processes, it is possible to overcome this problem by adding carbon fibers as reinforce material. This solution increases thermal conductivity and reduces thermal expansion coefficient, allowing for a very good bond of the filaments deposited without the need for an oven [5].

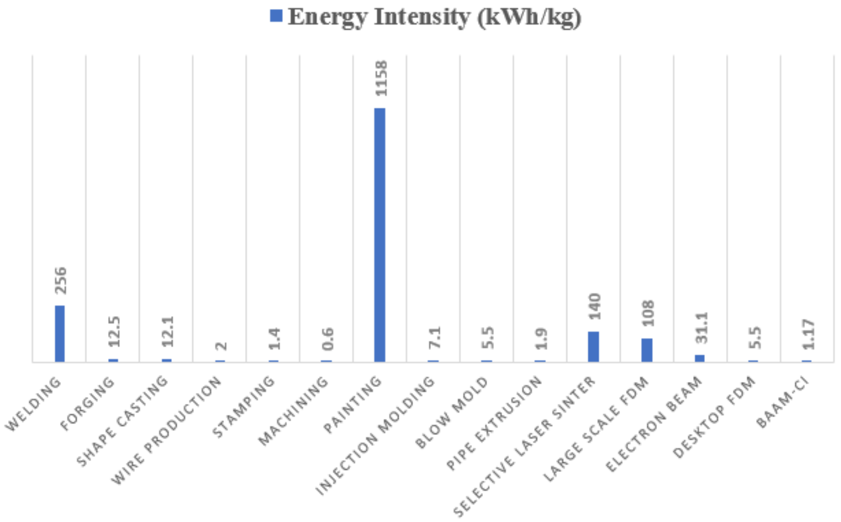

Figure 2.2. Energy requested for different manufacturing processes — reprinted from [5].

It has been stated that 4IR principles look for low environmental impact manufacturing processes. The impact related to pellet disposal is lower than for filament. In addition, while in FFF there are two melting steps, namely melting of pellet material to create filament and then the melting process of that filament in the FFF machine, in PAM there is only the pellet melting process, without the need to produce filaments as intermediate products.

These advantages are shared by BAAM and MiE because they are not related to extruder dimensions.

In fact, the main difference between BAAM and MiE lies in the larger size of the former.

Because of the higher extruder diameter, the printing volume in BAAM grows significantly; in general, the printing volume in FFF and MiE lies in the range 0.03–0.3 [m^3] [4]. The printing dimensions stated by the same authors for a BAAM apparatus allows to manufacture products up to 6 [m] long, 2.4 [m] deep, and 1.8 [m] high, namely about 10 times more than in FFF and MiE.

Productivity increases, turning to BAAM, because of a growth up to 200× of the mass flow rate [4]. This large increase in mass flow rate is possible also because of nozzle dimension; while in FFF and MiE, nozzle diameter is typically of 0.03 [cm] [3], in BAAM it is 0.8 [cm], which is around 30 times larger [6].

All these advantages call for models, analytical and/or numerical, that can be used to perform accurate analysis of PAM processes and that can account for different dimensions involved in BAAM and MiE.

Clearly, PAM is not free of disadvantages, especially when it comes to BAAM, because of the bigger dimensions of the final products and the higher deposition rate. In fact, it can be stated that:

- BAAM is a single material process; it could be difficult to remove support structures without proper post-processing; part orientation becomes more critical than in the case of FFF,

- The larger bead size reduces the printable resolution of the features that can be made by BAAM; the nozzle dimension which gives the best compromise between resolution and printing speed must be chosen,

- BAAM exhibits poor surface finish caused by the larger bead dimensions, if compared to FFF,

- The higher temperatures, larger size, and both bead width and height develop higher internal stress and warping, and

- It is more difficult to cool down the layer deposited by BAAM because the deposition rate is higher than in FFF.

To date, no specific model describing the complete extrusion dynamics inside PAM extruders, both at large (BAAM) and low (MiE) scales, has been formulated.

However, it must be recognized that SSE, which is a widely studied manufacturing process, shares several aspects with PAM. It is worth noting, however, that some of the main assumptions applied in modeling the SSE process cannot be used in the transition to a mathematical theory for MiE, mainly because of the smaller size of the extrusion system used (i.e., the 28 [mm] initial screw diameter in [7], in contrast with the 63.5 [mm] of the SSE studied in [8–10]).

It is also expected that smaller dimensions have an influence on melting performances, an aspect that will be addressed in Section 2.3.2.

2.3. Models for the Material Extrusion

A SSE includes three important areas for material extrusion; these are the solid-conveying zone, compression zone, and metering zone. This internal architecture is common to the Injection Moulding (IM), BAAM, and MiE processes.

Before moving to outline the analytical and numerical models which have been proposed in literature for SSE process modeling, it is important to pause on the internal structure of a single-screw extruder (see: Figure 2.3).

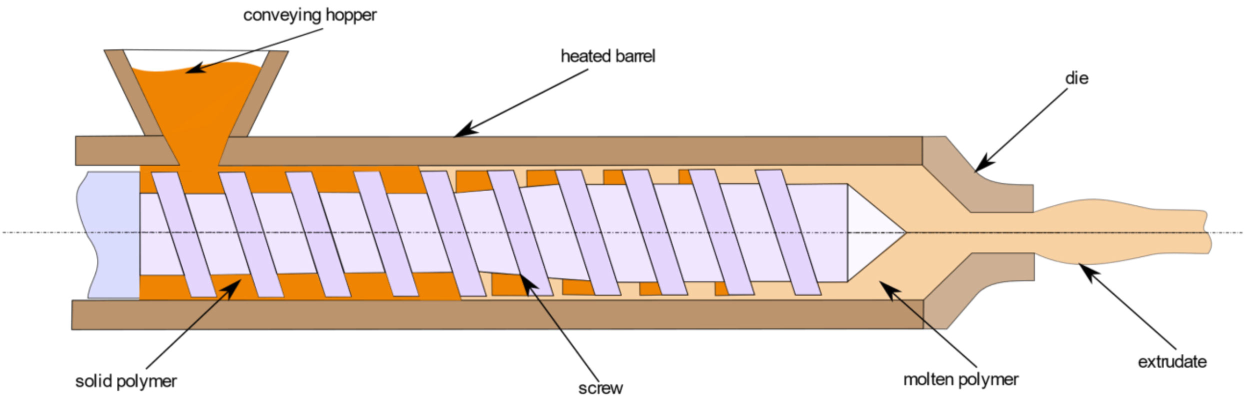

Figure 2.3. Scheme of the extrusion process in SSE.

The extrusion system consists of a screw housed in a barrel; the assembly made of both screws and barrel (named as screw-barrel system, in the rest of the dissertation) is joined on the one hand to the hopper for the supply of raw material and on the other hand to a closed die (IM), to an open die (SSE) or to the extruding nozzle (BAAM /MiE).

Barrel and screw are separated by a radial clearance where both leakage flow and high viscous thermal dissipation occur.

Material is initially conveyed in the solid-conveying zone in the form of pellet or granules through a hopper. Moving downstream from the hopper there is the screw, enclosed by the barrel.

Then, mass flow rate passes through geometrical vanes between screw and barrel, usually characterized by a constant cross-section in the solid-conveying zone.

From an experimental, analytical, and numerical point of view, pressure increases as the flow rate moves downstream. Because of this pressure, there is at first compaction of polymeric material, which reduces the air gaps between pellets.

The surrounding barrel is usually heated in different sections at different temperatures. Through thermal conduction, heat reaches the polymeric pellet material and, when solid temperature exceeds melting point, a gradual melting process begins. Melting is due to both conduction and heat generated by viscous dissipation; this process takes place in the compression zone. It is characterized by a screw channel cross-section usually tapered; the initial to final channel depth ratio is referred to as compression ratio.

Polymer melts according to a certain melting mechanism (Maddock, Lindt, or Klenk), which can change under different operating conditions. Further details on these mechanisms will be given in Section 2.3.2.

Finally, the material, which now is only at molten state, is transferred towards the die, in the case of an IM machine, in the so-called metering zone. Generally, it is characterized by a constant cross-section, as in the case of the solid-conveying zone. The operative point of a single-screw extrusion process is identified by the intersection of the operating characteristics of both die and screw, which are the pressure-flow rate relationships for the two elements.

In the following, the main works presented in the literature for SSE/IM process modeling are reviewed, underlining what assumptions cannot be applied in the extension of those models to BAAM and MiE.

2.3.1. Solid-Conveying Zone

2.3.1.1. Analytical Modeling

The first pioneering work aiming at analytically describing the solid-conveying zone is due to Darnell and Mol [11], who described the polymeric material as a whole and rigid body during the entire conveying process (Figure 2.4). In their model, as in many works derived from it, it is assumed that there are no air gaps; therefore, the mutual sliding of pellet particles is nullified.

In this model, the rigid motion of the whole body takes place under the influence of the friction forces which are generated at the contact interface between the polymer and metal surfaces of screw and barrel. This is also known as the solid friction model.

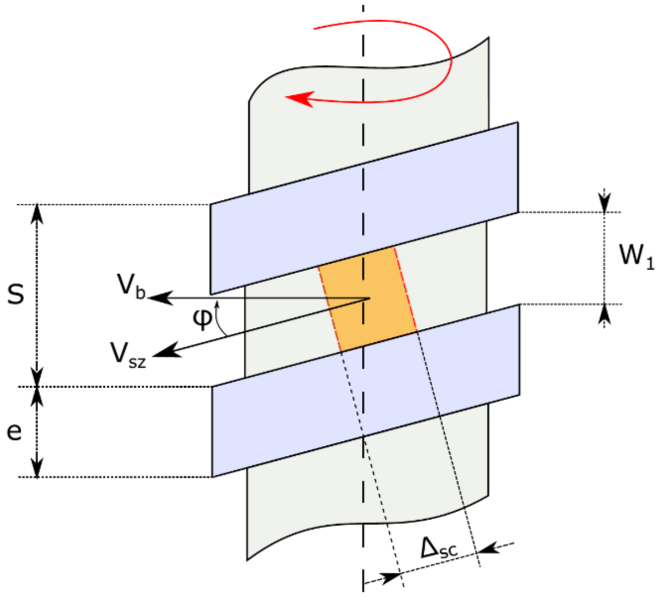

Figure 2.4. Solid conveying kinematics and geometry; W_1 - channel width at mean diameter, S - screw lead, e - flight width, φ - helix angle, Δ_{sc} - computational step in downstream direction, V_b - barrel velocity, V_{sz} - solid body velocity.

Another study [12] states that polymer melts rapidly and adheres to walls when the temperature exceeds melting point. This theory is based on experimental observation. The same author suggests in [13] a model where the motion of the solid material happens because of thin molten layers located on both barrel and screw surfaces. This model is known as the viscous drag model.

Early models, e.g., that proposed in [11], include the assumption of an isotropic pressure, which is not the case even in the solid-conveying zone.

A way to consider the anisotropic pressure distribution, which is expected to characterize the solid body during its motion, is to replace the usual isotropic pressure with a compressive stress system with screw root, flights, and barrel surface pressures which are proportional to that along downstream direction [14].

Moreover, the assumption of isothermal conditions is frequently used, which is in contrast with the experimental evidence; indeed, on the contact surface between polymer and metal, there is a large heat exchange, which results in anisotropic distribution of temperature in the solid polymer.

However the assumption of isothermal process is locally justifiable in the models where the calculation of solid properties in solid-conveying zone is performed by dividing the channel in the downstream direction in a series of little increments; for each step, it is possible to evaluate a mean temperature and the friction coefficients at screw and barrel surfaces at that given temperature, obtaining more accurate results if compared to the use of mean values for the whole conveying process. A similar study has been proposed in [15]; by performing a force balance for each segment of solid material, the pressure along the screw axis as a function of geometric screw parameters can be obtained. Pressure in this model is anisotropic and the channel cross-section can be also variable.

In [16], there is a similar computation of the temperature distribution in the solid body, which allows for an accurate calculation on the one hand of the friction coefficient and on the other hand of the axial position where the melting process begins.

In [17], it is assumed that the solid body is pushed upwards, orthogonally to the screw, by the flights. This vertical thrust is assumed to be proportional to the frictional force exerted by the pellets as they move in relative motion with respect to the barrel.

Analytical models described so far do not consider either gravity or centrifugal forces, which can also play a significant role in solid-conveying zone of IM, BAAM, and MiE screw-extruders.

In particular, Darnell and Mol find an exponential relationship between the locally isotropic pressure and axial position along the machine, finding a pressure profile which is independent of the real arrangement of the extrusion system. Lovegrove in [18] modified Darnell and Mol's theory by adding a pressure term related to the two volume forces mentioned earlier, material being conveyed and the real system arrangement, namely horizontal or vertical. Another advantage of Lovegrove's theory is that it considers local pressure as anisotropic through the same approach suggested by Schneider in [14]. Considering local pressure as anisotropic and accounting for the effect of a vertical arrangement are key points for an analytical modeling of solid-conveying zone, both in the case of BAAM and MiE.

Nevertheless, all these studies start from the assumption of considering the material as a whole body in rigid motion, which is not the case in real extrusion systems. The only way to consider the complex dynamics of pellets, determined by their interaction, is to turn to numerical models.

2.3.1.2. Computational Modeling

There are different ways to deal with the motion of solids in screw vanes of the feeding zone. A first approximation is generally given by considering the solid body as a fluid with a very high viscosity and treating it through CFD techniques.

In [19], the problem of the motion of the solid polymer was handled by assuming an incompressible fluid of high viscosity, performing a finite difference study in non-isothermal conditions and with a wall-sliding motion proportional to the shear stress.

The assumption of dealing with the solid as a fluid with very high viscosity was also applied for modeling the other zones of extrusion process, namely the compression and metering zones, in CFD. For the last turns of solid-conveying zone, this approach was followed in [8–10,20].

A limit which is shared by the described analytical models and this first class of computational ones is that they do not consider the internal friction which arises because of the mutual sliding of the involved pellets. Internal friction is disregarded because of the assumption of a whole, compact body in the solid-conveying zone, subject to a rigid motion in the downstream direction.

To overcome this limit, the discrete element method (DEM) is one of the best choices, but the drawback is that its accuracy is strictly related to an accurate experimental characterization of the material being extruded. Fundamental properties which must be set up, regardless of the DEM software used, are the coefficient of restitution, both internal and external friction coefficients, and the most appropriate contact model [21].

In all the DEM models, the interaction between single particles is considered (Figure 2.5) by determining for each of them both normal and tangential actions exchanged with the neighbor particles, as well as the gravity effect. Then, dynamics equations are solved, and acceleration is determined for each particle. Finally, velocity and position of all pellets are determined by integration and this information is used for the next time step.

Figure 2.5. Overview of a DEM simulation of spherical particles.

In contrast to the finite element method (FEM), finite volume method (FVM), and finite difference method usually implemented for the numerical solution of governing equations in fluid dynamics problems, in DEM, the particles are no longer linked by a rigid mesh [22].

Another drawback of DEM lies in the high time required to perform computations, mainly because of the low time step needed for obtaining an accurate simulation of momentum exchanged between pellets.

Various DEM three-dimensional models have been developed to simulate both the hopper and conveying zones of a single-screw extruder used for IM [22–26].

The experimental investigations lead by Celik in [22] show how flow rate and pressure field depend in a great extent on the shape of particles used in DEM simulations.

Moreover, material and pellet shape also affect temperature field and the force exchanged by the particles [21].

In [27] DEM is applied to predict velocity profile in both downstream and cross direction, as well as coordination number, finding numerical results which show a good agreement with the experimental ones.

It is also possible to use DEM to show the dependence of flow rate on geometric and operating conditions in the solid-conveying zone [23]; authors address the problem of the influence of a series of characteristic parameters of the solid-conveying zone on the flow rate. The software used to perform DEM simulations is EDEM. At first, the excellent correspondence for LPDE between experimental and numerical flow rate values at different screw rotational speeds is observed. This is achieved through a proper testing of the material under extrusion, which allows to determine the exact value for both internal and external friction coefficients. Subsequently, authors perform a dimensional analysis to assess the influence of the main parameters, which are flow rate, screw diameter, screw speed, channel height, and the extension of the zone below the hopper. Finally, they determine the functional dependence of non-dimensional flow rate on the other non-dimensional parameters through a polynomial regression of numerical data (Figure 2.6).

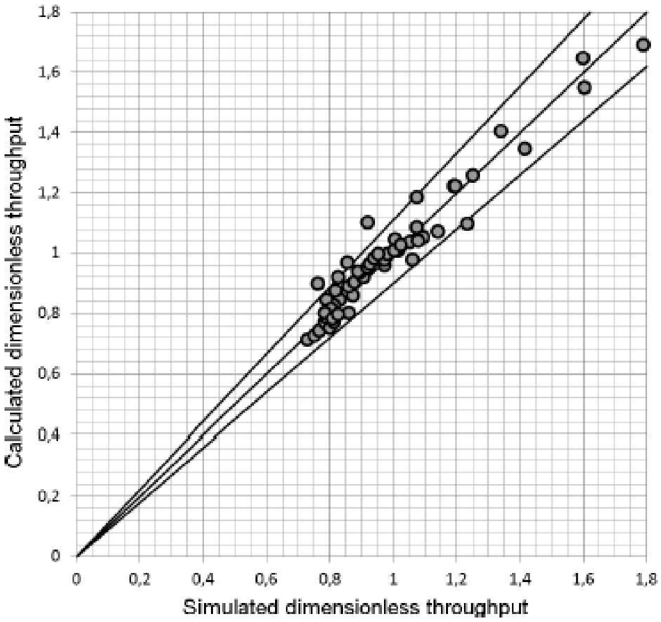

Figure 2.6. Example of polynomial regression of data.

The predictive capabilities of DEM are remarkable, and it is natural to think of an integration of this method with the numerical methods related to the compression and metering zones, usually studied through CFD techniques.

Through this combined approach, a more accurate quantitative description of the extrusion process along the entire feed-zone length for PAM processes is expected.

2.3.2. Compression Zone

2.3.2.1. Analytical Modeling

The first analytical work for the prediction of melting length in single-screw extrusion was proposed by Tadmor in [28], developed according to the experimental data of Maddock and Street [29].

In [29], a series of studies on the dynamics of the melting process were carried out by means of the screw pulling-out technique. It consists of stopping the extrusion system, cooling it quickly, and, lastly, removing the external barrel. The state of the polymer in the screw vanes is thus clearly visible.

By cutting the polymer along the axial direction, it is possible to measure, vane by vane, both the solid and melt content, finding the local melting rate. Usually, the same material with a different pigment is added in the extrusion process, to separate the solid zone from the molten one [8–10].

On the base of their first pioneering studies, Maddock and Street found that the material melts only near the barrel surface because the polymer temperature is locally higher than its melting point. This thin molten layer shifts slowly towards the active flight, while the solid material is in contact with the passive flight. In this way, there is the formation of a melt pool where the molten polymer accumulates.

This melting mechanism, namely the formation of a recirculating melt pool on the active flight while the solid bed is near the passive flight, is called the Maddock melting mechanism, and it has been noted for a large class of polymers used in the single-screw extrusion. A schematic representation of this process is also given in Figure 2.7.

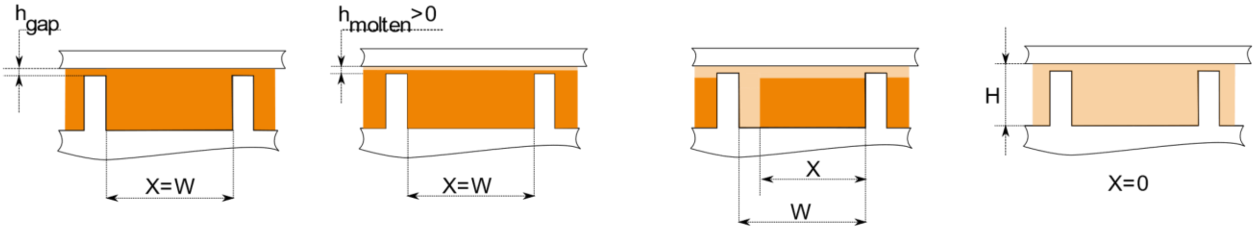

Figure 2.7. Maddock melting mechanism: W—channel width, H—channel height, h_{gap}—radial clearance between screw flights and barrel, h_{molten}—local molten layer thickness, X—local solid bed width.

In the analytical study performed in [28], the channel is assumed to be unwound from the screw. Because of this assumption, the influence of screw curvature on flow and temperature fields is neglected. It must be pointed out that this assumption is justifiable only for extruders with a diameter sufficiently large, as in the case of BAAM, SSE and IM, but not in the case of MiE.

Tadmor assumes that the solid bed remains of rectangular cross-section while moving downstream is in a homogeneous state, that the local solid–melt interface is not varying in time, and that all thermodynamics properties are constants. Moreover, molten polymer is assumed to be a Newtonian incompressible fluid.

The analytical solution proposed by Tadmor in [28] is based on some assumptions which are too strict for real applications in the field of IM and PAM processes. First, the constitutive relation chosen for polymer modeling is not representative of most real polymers' rheological behavior; in fact, polymers generally exhibit a power-law and temperature-dependent behavior. For a given temperature, there is an exponential relationship between shear stress and shear rate. This dependence no longer exists in Newtonian fluids. In several further works [30,31], polymers have been modeled as a power-law fluid with an Arrhenius correction, to consider the relationship between rheological parameters and temperature.

It is important to underline that Tadmor included both non-Newtonian behavior and a molten layer thickness which is variable along screw axis in its model [32], still under the common assumption of a constant downstream velocity for solid bed. Two additional problems of Tadmor's theory are the assumptions of a linear temperature profile in the molten layer which forms between solid and barrel surfaces and that of zero pressure gradient.

In [30], the energy equation for a power-law fluid was solved analytically. Through a thermal balance on the interface between solid and melt polymer, the author then evaluates the melting rate. It is further demonstrated how this quantity decreases by increasing the gap between flights and screw, and how it is related to barrel temperature.

In general, the energy requested for polymer melting is given by two main contributions: the first is heat conducted from the heated barrel towards the polymer and the second is viscous heating. The latter consists of heat generated by viscous dissipation, and it is due to shear dependent behavior of the polymer in the molten layer. It is estimated that ca. 80[%] of the total heat required for polymer melting is given by viscous heating [7] for a standard single-screw extruder.

The relative importance of viscous heating and conduction heat transfer is defined by the Brinkman number (Br).

A very impressive study regarding the influence of both extruder dimensions and operating conditions on Br and melting rate was presented in [7]. In fact, the main purpose in [7] was to give a deep insight into pellet extrusion-based systems' melting dynamics. It was demonstrated that in the case of MiE and applying the modified Tadmor model proposed in [32], lower values of Br characterize most of the screw length because the local value of shear rate is lower than in the case of a standard SSE extruder. The opposite tendency was shown in the last few turns of compression zone. It is interesting that, for fixed operating conditions, rheological and thermo-fluid dynamics parameters for both solid and melt phases are the same as in [10], so the influence on Br is due only to screw dimensions. All previous conclusions are represented in Figure 2.8.

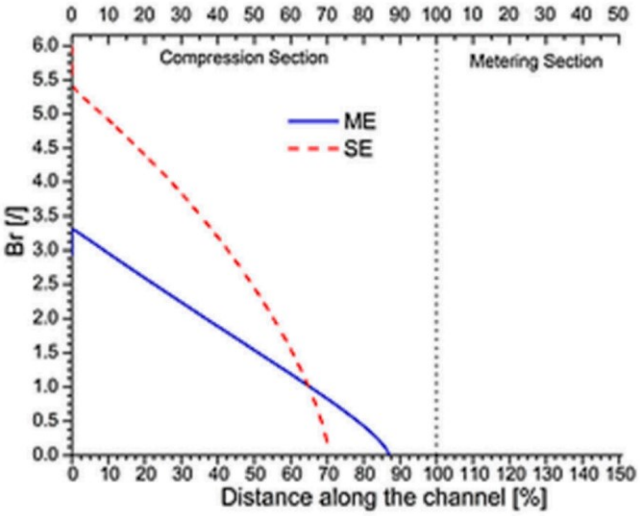

Figure 2.8. Brinkman number (Br) along screw channel direction for both the standard extruder used in the SSE process (SE) and the mini-extruder (ME) used in the pellet extrusion-based process — reprinted from [7].

The main problem is that in [7], the modified Tadmor model [32] was implemented, which is valid for polymer flow in flat rectangular channels. Turning to PAM, this assumption is no longer valid for MiE because curvature cannot be neglected, but it can still be applied in BAAM process modeling because of the higher diameter/channel width ratio.

As mentioned earlier, the Maddock melting mechanism is the most observed, but it cannot be valid for all polymers and operating conditions.

In fact, melt pool can also form close to the passive flight; this is referred to as the Klenk melting mechanism [33] and it has been observed for Polyvinyl Chloride (PVC).

It is even possible that there is a melt pool both close to the active and passive flight, with thin melt layers near both the screw and barrel surfaces; in this case, the solid material is encapsulated in molten polymer. In literature, this behavior is commonly known as the Lindt melting mechanism [31]. This melting mechanism was initially observed for Polypropylene (PP).

As well as implementing this model for the first time, Lindt shows in [31] how the melting mechanism is strictly dependent on the transversal force acting on the solid polymer, where this force depends on the pressure gradient, already for the simple Newtonian case.

Both melting mechanisms are represented in Figure 2.9.

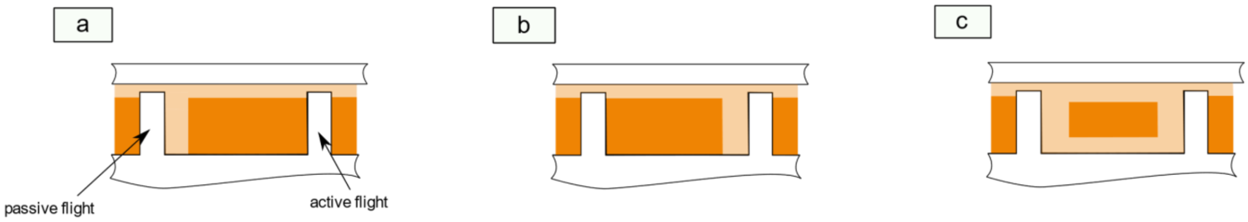

Figure 2.9. a.) Klenk; b.) Maddock; c.) Lindt melting mechanism.

Other works [34–37] determined the power consumption in the extrusion process in the compression zone. The power required to melt a polymer can be calculated analytically if the wall shear stress is also known. Wall shear stress is derived by the knowledge of the flow field. Furthermore, wall shear stress is a function of sliding velocity and metal surface temperature [34].

Moreover, the gap between top of the flights and barrel is a region of flow field where there is significant viscous dissipation which must be quantified to evaluate the total power needed for extrusion, i.e., as in the mathematical model proposed in [35].

2.3.2.2. Computational Modeling

There are different limitations related to the analytical investigation of the compression zone; the most important is related to the fact that a specific melting mechanism must be assumed. In fact, it can vary with operating conditions, as shown in the previous section. Other problems are related to the highly non-linear nature of the coupled partial differential equations which must be solved.

Additionally, one of the most widespread assumptions in the analytical modeling of the compression zone is that of the no slip condition at the walls. As highlighted in [38,39], many materials of industrial interest exhibit wall slip. Some of these materials are PVC, High Density Polyethylene (HPDE), ceramic materials, foodstuffs such as meat and dough, filled polymers such as Wood–Plastic Composites (WPC), and elastomers [38].

The problem of the wall slippage is handled by an analytical point of view in [37], where the equations for a one-directional Newtonian fluid in a straight channel were solved. Now, it is well known that flow behavior in all extrusion zones is at least two-directional, and that fluid must be modeled properly as a non-Newtonian fluid whose rheological parameters are a function of temperature. In [38–40], the problem of modeling wall slipping materials during extrusion process in single-screw extruders was addressed through CFD.

CFD simulations overcomes the analytical difficulties related to the highly non-linear and coupled nature of the equations; by solving conservation principles, namely mass, momentum, and energy equations together with an appropriate constitutive relation for the material being extruded, there is no longer the necessity to know a priori the melting mechanism. Moreover, the influence of the slippage parameters can be investigated for the materials listed above.

In addition, CFD simulations allow to study control volumes of complex shapes, such as the curved geometries involved in the modeling of real extruding vanes of MiE; this can be used to relax the widely adopted assumption of a straight rectangular channel and to develop predictive computational models.

Authors in [8] lead both numerical analysis with PELDOM software and experimental investigations through the screw pulling-out technique for an IM single-screw extruder. Their purpose was to analyze the melting mechanism and pressure development during the melting of Acrylonitrile Butadiene Styrene (ABS) in a straight channel.

In performing the experiments, black pigmented ABS was added with the purpose of identifying where the material was in the molten state. It was found that the melting process follows, both analytically and numerically, the Maddock melting mechanism, but the numerical results show a larger melting rate.

The same authors in [10] used PELDOM software to analyze the melting process dynamics and evolution of the pressure profile along the screw axis for ABS extrusion. It was demonstrated through a parametric study that increasing screw temperature leads, for a given axial position, to a decrease in the content of solid material and to an increase of predicted pressure.

These profiles are also largely dependent on the viscosity of the polymer. Increasing viscosity leads to a net increase of the axial pressure and to a decrease in the solid content. A similar behavior was found decreasing the flow rate. It is remarkable that in their last work [10], the authors implemented a direct comparison of experimental, numerical, and analytical results (Figure 2.10); the latter are extracted through Tadmor's model.

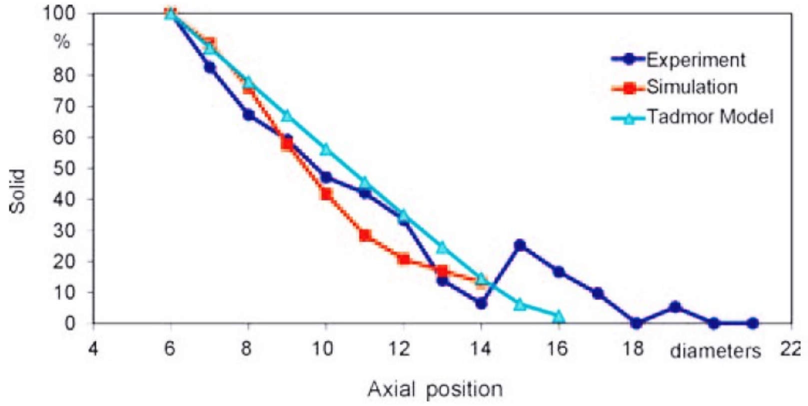

Figure 2.10. Experimental, CFD, and analytical predictions of the solid content in screw vanes of an IM extruder—reprinted with permission from [10].

Figure 2.10 shows how the modified Tadmor model, which also accounts for the non-Newtonian behavior of molten polymer, over-predicts the melting rate. The same conclusion can be stated for simulations, in the axial positions from 9 to 13 diameters from the hopper.

In [20], the screw extrusion in a straight channel made of both compression and metering zones is simulated with CFD software Fluent by comparing numerical results with experimental and numerical results given in [10], finding a good agreement in terms of melting rate. However, there is still a different behavior of pressure in the metering zone. The numerically predicted pressure gradient is positive along the entire metering zone, while in experiments (and in other studies performed solely for the metering zone, i.e., the analytical results proposed in [36]), it is negative. The reason for this different behavior is not clear.

2.3.3. Metering Zone

2.3.3.1. Analytical Modeling

Once the polymer is completely molten, it must be moved towards the closed/open die in the case of an IM/SSE extrusion system, or towards the extruding nozzle in the case of PAM extrusion processes.

The first analytical work modeling molten polymer transport is [41]; the isothermal flow of a Newtonian fluid in screw vanes was studied, finding a solution for the two-dimensional pure drag flow.

In [42], the problem was solved for a Newtonian fluid, by determining both the flow rate and pressure distribution under the assumption of a channel of infinite width. The ratio between width and height of the channel is usually referred to as the channel aspect ratio.

These two assumptions, namely Newtonian fluid and an infinite aspect ratio of an unwound screw extruder channel, ensure that, in the case of a one-dimensional flow, the partial differential equation reduces to an ordinary one [42]. This equation, together with the boundary condition of a moving top plate (namely the barrel in IM and PAM processes) with a stationary bottom surface, gives the well-known Couette flow equations. By further assuming that the flow rate in the die is proportional to the associated pressure drop, it has been found that the pumping characteristics in single-screw extrusion are linear both for screw and die. The operating point is given by the intersection of these two characteristics. In [43], these findings are integrated by considering the solution for the two-dimensional problem, always in the case of Newtonian fluid. The author gives some correction coefficients for both pressure and drag flow, to find the right flow rate for the extrusion through channels of semi-elliptical or rectangular cross-section.

Now, let us deal with the power demand in the metering zone. This is made up of both the power requested for extrusion process and power dissipated in the radial gap between flights and barrel. In [44], an analytical solution for the isothermal flow of Newtonian fluids in unwound screw channels which also considers the power consumption related to leakage flow in the gap between flight tips and barrel is proposed.

In [45], the functional dependence of power consumption in the radial clearance between flight and barrel on both flight width and screw length is widely described, showing that in the case of Newtonian fluids, there is an optimal value for radial clearance which allows the designer to minimize this contribution to the total power consumption requested for extrusion.

The problem of the previous studies lies naturally in the Newtonian fluid assumption.

To solve this problem, a first way is to consider a mean value for viscosity when this parameter cannot be considered as constant along the entire screw length [44], but this approach cannot be exhaustive of the real behavior of the polymer, which is widely non-Newtonian with rheological parameters which are also temperature dependent. In fact, in polymer extrusion, it is mandatory to consider the constitutive relation between shear stress, shear rate, and temperature. One study attempted to also estimate leakage flow in the case of an isothermal flow of a power-law fluid [46].

On the other hand, the power required for the extrusion process is strictly related to an accurate calculation of flow field, upon which relies the calculus of wall shear stress and pressure development.

In [47,48], the equations describing the behavior of an isotropic, incompressible, and inelastic fluid are derived through a phenomenological theory for macro-rheology. These works assume that stress tensor is a function of kinematic matrix and some material constants.

In [49], the stationary, laminar, isothermal Couette flow of a non-Newtonian fluid was solved analytically. The relationship between shear stress and shear rate was expanded through a polynomial series and the solution was found considering a shear rate contributing up to third order. The solution can be obtained for an arbitrary number of terms, but the coefficients which appear in the polynomial expansion must be determined experimentally. Similarly, a two-coefficient-based problem for the pseudoplastic material model can be solved. Solutions are proposed both for Rabinowitsch and the general pseudoplastic constitutive relations.

A similar model for the study of a fluid modeled through a Rabinowitsch constitutive relation, but this time in non-isothermal flow conditions, was proposed in [50].

The issue of the evaluation of flow field for non-Newtonian fluids has been also addressed analytically in [51] with the possibility of employing non-Newtonian fluids in thrust bearings, and in [52] for generalized Couette flows. An analytical solution for the isothermal and one-directional flow of a power-law fluid in a channel with varying height in downstream direction was derived in [51].

The assumption of an isothermal flow was removed in [53], where the analytical solution to the thermo-fluid dynamics problem of the transport of molten material was given for a power-law fluid in presence of viscous dissipation.

In [49,51,53], it is also assumed that the channel is flat and characterized by an infinite aspect ratio.

Moving on to PAM processes, a single-screw extruder for MiE is generally smaller than that used for SSE, IM and BAAM; for this reason, both curvature effect and real geometry of the channel must be considered, as seen in the previous section.

In contrast to [43], in [54], the problem for non-Newtonian fluids in finite aspect ratio channels was solved and the effect of lateral screw flights on flow field was addressed. There it was underlined as already in the simplified case of an incompressible, isothermal flow of a non-Newtonian fluid in a finite aspect-ratio rectangular channel and with motion imposed to the barrel, that the problem is modeled by highly non-linear partial differential equations for which an analytical solution no longer exists.

Similarly, an analytical model for the flow of Newtonian fluids in finite aspect ratio channels was proposed in [55], and both the pressure-flow rate relation and flow field along the channel height for corn syrup, which can be assumed as a Newtonian fluid, were well predicted.

In [36,56–59], the authors refer to correction factors for pressure and drag flow, as suggested in the case of Newtonian fluids in [43]; this is a simple solution for considering the limited aspect ratio, and so the influence of both trailing and pushing flights on the flow field. Moreover, it has been shown that at least for the drag flow correction factor, there are no significant differences between the values measured for various polymers and the theoretical values calculated for Newtonian fluids [60,61]. However, there is a lack of information on helix angle influence on the flow field. This effect was addressed in [62], where a complex theory involving channel curvature was developed. Other works where the problem of defining governing equations in frame references different from the Cartesian one was addressed will be shown later in this Chapter.

Few studies face the solution of the problem of modeling non-Newtonian flow behavior by an analytical point of view, and they are based on restrictive assumptions such as isothermal flow through flat rectangular ducts of infinite aspect ratio.

In [63], the analytical solution for the isothermal, incompressible flow of power-law fluid is proposed, where the main task is to optimize geometrical features of the extrusion screw, by trying to link optimal values to rheological parameters, under the assumption of considering a flat channel with infinite aspect ratio. One of the most distinctive results lies in the fact that the optimum helix angle is only a function of power-law index. Validation has been done with the experimental results proposed in [64], finding good agreement only if the power-law index is greater than $1/\sqrt{2}$. Moreover, it is assumed that both channel curvature and flights have no effect on the results and that rheological parameters are independent of temperature. Despite this work being of great importance for giving design optimum indications for a limited range of pseudoplastic fluids, these two latter assumptions are too restrictive for the description of the transport of molten polymer in the metering zone of a MiE, where curvature cannot be neglected.

Other works try to consider channel curvature in metering section through correction factors [62] (Figure 2.11) or achieving the solution in a coordinate system different from the Cartesian one [57,65].

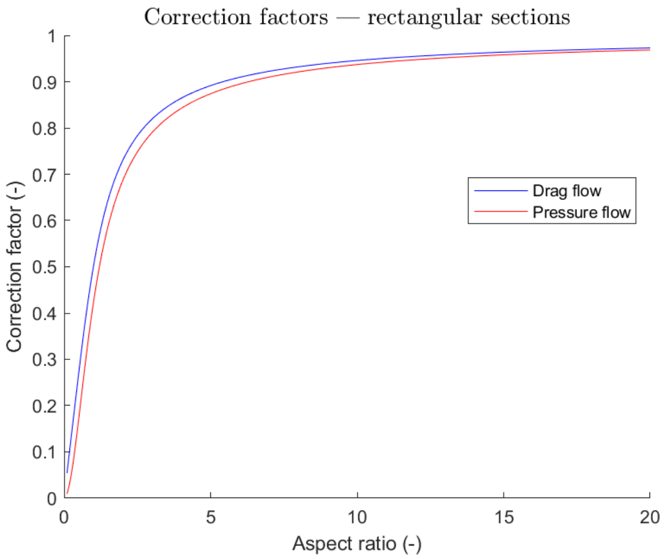

Figure 2.11. Correction factors for rectangular channels for a given aspect ratio (width to height ratio).

The first work which analyses the influence of helix angle and curvature on both flow and pressure fields is [62]. In fact, helix angle changes with radial distance, and this aspect has been neglected in previous studies. The limit of this research is that only Newtonian fluids were discussed.

Different works look for analytical and numerical solutions to consider channel curvature, in the general case of non-Newtonian fluids [32,35,65].

In [57], an analytical solution is proposed in the case of an Ellis fluid, which is a generalization of the power-law constitutive relation. Another way to consider effects related to channel curvature on flow, pressure, and temperature fields is to study the problem in helical coordinates, as in [66–70]. This approach would allow to consider both curvature and helicity of the channel for a single-screw extruder, despite their application being in the field of IM or PAM.

Different helical coordinate systems have been suggested in literature: a physical basis of unit vectors in radial, helical, and axial direction could be used, starting from a cylindrical frame of reference [68], or the coordinate system can be set up starting from a Cartesian one [71].

Finally, as in the case of compression zone, the widely used assumption of no-slip condition at boundary/polymer interfaces must be discussed.

Wall slippage depends on the polymer, single-screw extruder geometry, surface properties, intensity and direction along which pressure gradient acts, shear stress, and shear rate [72].

Physically, by gradually increasing shear stress, there is a transition from no-slip condition to an intermediate situation between no-slip and slippage. By increasing the shear stress above a threshold there is wall slip condition.

Some interesting analytical solutions for Newtonian fluids have been proposed in [72,73], by distinguishing what happens in the case of non-dimensional shear stress where slippage begins is more or less than unity. This analysis leads to the conclusion that slippage can be unilateral, which means that slippage can occur only on a single surface, namely barrel or screw surface, or bilateral. The analytical expressions given in this work link non-dimensional flow rate to non-dimensional pressure gradient in all the possible operating conditions of a single-screw extruder in the metering zone. Results are validated in [72] by means of FEM simulations, with a good overall agreement.

The non-Newtonian behavior under wall slippage is analyzed by the same authors in [74] under the assumption of one-dimensional isothermal flow. It is shown as pumping characteristics of single-screw extrusion deviate from linearity because of both pseudoplastic nature of processed material and wall slip; in fact, linear behavior was predicted for Newtonian fluids under no-slip condition [42].

It can be concluded that analytical modeling of melt flow in screw vanes is a complex task, for which a variety of assumptions have been used in the past decades.

All the assumptions related to the flat plate theory, where curvature is neglected, cannot be used in modeling the MiE, but, if channel height to diameter ratio is low enough, it can be still used to estimate BAAM process performances.

Wall slipping, non-Newtonian fluid behavior, and non-isothermal conditions lead to a system of non-linear partial differential equations, for which it is more appropriate in general to use computational methods.

2.3.3.2. Computational Modeling

Several numerical schemes have been proposed to solve the fluid dynamics problem of molten polymer transport toward the die in IM literature.

Among the main advantages related to numerical modeling of the extrusion process, there is the possibility to consider geometrical features which are too complex to model by an analytical point of view, especially curvature and real cross section shape (with finite aspect ratios).

As an example, a finite difference scheme for the solution of the flow in a channel with finite aspect ratio was proposed in [75]. Results are in good agreement with the analytical solution proposed in [55], already for a coarse mesh. The importance of the study presented in [75] is related to the possibility to perform analysis for non-rectangular cross-sections, such as that normally found in a single-screw extruder. This deviation from the ideal rectangular section is due to the fillets at the bottom of screw flights. By performing numerical simulations there is no longer the need to consider the correction factors for pressure and drag flows represented in Figure 2.11 or the shape factors introduced in [42]. The main drawback of [75] is to consider the isothermal flow of a Newtonian fluid.

There is a wide range of numeric schemes used in literature for melt flow modeling. In [76], the Lattice gas automata method was used, while in [77], flow field in the metering zone under isothermal conditions was investigated via the Lattice–Boltzmann method, finding in the latter a good agreement with the analytical solution proposed in [61].

The main difference between numerical results of simulations conducted in [76,77] lies in the fact that while in the former some unrealistic eddies near the corners of the flight are predicted, in the latter these eddies are absent. These eddies may occur in the metering zone and both their dimensions and their influence on the flow field have been widely studied in [78] by means of OpenFOAM; particles which are involved in these eddies, also referred to as Moffatt eddies, are characterized by a residence time two times larger than that of the mean flow in screw vanes, already in the Newtonian case. In addition, polymer melts in metering zones are subject to a temperature well above melting point and they may run in local thermal degradation, from which defects in the final product can arise. Polymer degradation is enhanced if residence time is too high.

The residence time of the particles involved in Moffatt eddies grows up to three times higher than mean polymer residence time if non-Newtonian fluid behavior in the duct is considered. In any case, Moffatt eddies can be totally avoided in screws where fillets near flights' roots are large enough; in general, the SPI recommendation is to manufacture screws which have fillets' radii greater than half of channel height [79]. This empirical rule is reasonable because it allows to completely avoid Moffatt eddies in the flow field in the metering zone also in non-Newtonian cases [78].

In the previous section it was shown that the power requirement in metering zone has been studied analytically under the assumption of Newtonian fluid, which is not the case in polymer extrusion regardless of the specific manufacturing process.

In [80], experimental results are given for corn syrup and the analytical model proposed in [55] gives good correspondences, but it is still limited to considering Newtonian fluids.

Griffith, in [64], also elaborates a numerical method for the solution of the flow problem in non-Newtonian cases; screw is assumed in motion, while barrel is stationary, that is the real kinematic condition.

Even in the assumption of an infinite aspect ratio, a numerical model where Arrhenius correction is used, to consider the dependence of both consistency index and power-law index on temperature, is developed in [64]. The conservation equations of mass, momentum, and energy are then solved numerically. Results in terms of non-dimensional pumping characteristics for the non-Newtonian case show a clear deviation from the linear behavior predicted in [42], for Newtonian fluids, already discussed in the previous section.

In [66], the effect of curvature of the channel on the flow rate and on the viscous dissipation was shown by considering a two-dimensional, isothermal flow of a power-law fluid. Despite the effect of curvature having been considered, the effects related to the screw flights were neglected. The Radial pressure gradient was neglected because of the very low Reynolds number. There was an overall agreement between the non-dimensional flow rate-pressure relationship found numerically in [64] with the results suggested in [79], where channel was considered flat both for Newtonian and non-Newtonian cases. In other words, results given for a theoretically infinite screw radius match that of flat plate theory. A remarkable influence of aspect ratio on viscous dissipation was also observed.

It can be stated that the effect of both pushing and trailing flights can also be modeled using a different frame of reference. The same approach is possible if the same equations are formulated in the new system.

In [66], a FEM solution was given with the purpose of analyzing a fully developed, isothermal flow of a Newtonian fluid, using a helical frame of reference. This model was then validated with particle tracking technique in [80].

A similar formulation in helical coordinates, but with a functional which takes in account both velocity and temperature was proposed in [68].

An assumption which is very common in many analytical and numerical models is that of a motion given to the barrel. These are also referred to as reverse kinematics conditions.

Investigation of the accuracy given by this kinematics assumption is addressed in different works [81–83].

It has been shown both analytically and experimentally that the assumption of giving the motion to the barrel is justifiable [81]; in particular, the model for the unwound channel with motion given to the barrel and with stationary screw is reasonable if the screw diameter is larger than 10× channel height. In [82], an analytical model, validated through FEM simulations, was given considering the general case of a non-isothermal flow. Results are identical for the two cases.

Temperature field is also the same in the two kinematic conditions, and this has been demonstrated by means of the FVM method [83].

In all studies discussed up to now, the no-slip condition was postulated for the modeling of the metering zone. As in the compression zone, the effect of wall slippage must be quantified to deal with different classes of materials.

The assumption of isothermal flow was neglected in [84], where a FEM 3D model was developed for the prediction of the temperature field development in screw channels under wall slippage.

In [40], CFD analysis was carried out with the software Polyflow for a non-Newtonian fluid. Authors determined flow and pressure fields, and, consequently, pumping characteristics and their dependence on the parameters which rule wall slippage. Finally, they led a similar analysis for the die of an IM single-screw extruder, determining the operating point. Thereby, it was shown how the operating point is influenced by the parameters involved in wall-slip phenomena.

2.4. Conclusions

The most important works related to single-screw extrusion process modeling have been reviewed with the purpose of verifying what assumptions still hold in the study of PAM processes, namely BAAM and MiE.

Some of them must be removed if one wants to extend these models to PAM, especially in the case of MiE because of the lower screw dimensions.

By studying the thermo-fluid dynamic problem of the flow through a rectangular duct, errors are expected to be greater than for BAAM, when it comes to MiE applications; it has been shown in literature that this error increases as long as the ratio between channel width and screw diameter increases.

Dimensions can also affect melting rate; melting length is higher than in a standard single-screw extruder because of the lower Br number, thus operating conditions must be chosen carefully if one desires to avoid defects related to incomplete and/or not homogenous melting in the final product. These conclusions must be proven by means of a model for the compression zone capable of performing analyses which consider the influence of curvature on melting profile.

In addition, the assumption of a stationary screw with moving barrel becomes questionable if the diameter is not larger than 10× channel height, so this aspect must be considered in performing CFD simulations and elaborating analytical models.

Moreover, the no slip condition at both barrel and screw walls must be relaxed for a large range of materials of industrial interest. Because it is analytically difficult to consider the complex polymer rheology, CFD is mandatory. An accurate characterization of the polymers involved in extrusion process is requested, especially when momentum exchange between pellets through DEM must be modeled.

From this perspective, the numerical solution which has the major potential to give the best results in PAM modeling involves a mixed DEM–CFD approach.

However, semi-analytical methods allow for faster computations, and they can be used for process optimization; in the next chapter, a composite mathematical model for SSE and PAM will be described.

3. Modeling of the extrusion-based additive manufacturing: how printing parameters affect extrusion outcomes

3.1. Chapter organization

The aim of this Chapter is to develop a novel, semi-analytical, and iterative code to predict the complete PAM extrusion process of net polymers, dealing with the effect of the most important processing parameters (i.e., layer height and printing speed).

First, a system consisting only of an extrusion screw, a coupling element, and a nozzle (the complete system is named as SSE, in the following) was considered; the purpose was to predict:

- mass flow rate,
- pressure profile, and
- melting profile.

For that purpose, a composite mathematical model was developed in Sections 3.3.1-3.3.5, based on the following sub-models:

- Solid-conveying zone: Darnel and Mol model [11],
- Delay, compression and metering zones: Steller and Iwko model [35], and
- Nozzle zone: Bellini model [3].

Then, both experimental and numerical validations were conducted: experimental for the mass flow rate and numerical for the pressure profile. In the SSE code, the peripheral screw speed is prescribed, and mass flow rate is the primary outcome.

After verifying the adequacy of the SSE model for the proposed screw design, it was extended to PAM extrusion (Section 3.3.6). In the latter case, it is of interest to set the layer properties and to seek for the peripheral screw speed that allows to extrude the given mass flow rate; in this case, the outcomes are:

- peripheral screw speed,
- pressure profile, and
- melting profile.

The fluid dynamics of layer deposition was described accordingly to the model outlined in [85].

The influence of both the layer height and printing speed on the abovementioned process outcomes was investigated, as described in Section 3.5. Further extensions of the proposed formulation are highlighted in the Section 3.6.

3.2. Chapter nomenclature

a	Sensitivity to the temperature coefficient
b	Auxiliary variable for melting profile calculation
A_s	Portion of cross-sectional area filled with the solid phase
A_m	Portion of cross-sectional area filled with the molten phase
A_{total}	Cross-sectional area
$A - B - K$	Geometric parameters used in the solid-conveying theory
c_m	Heat capacity of the molten thermoplastic
c_s	Heat capacity of the solid thermoplastic
$D_{s,inlet}$	Inlet screw diameter
$D_{s,outlet}$	Outlet screw diameter
D	Tip screw diameter
D_1	Local screw mean diameter
D_2	Local diameter near the screw root
D_b	Barrel diameter
$D_{ext}^{(n)}$	External nozzle wall diameter
D_{int}	Inlet diameter of a convergent duct
D_{ext}	Exit diameter of a convergent duct
$D_{s,inlet}$	Screw diameter under the hopper
$D_{s,outlet}$	Screw diameter at the tip
e	Flight width
F_p	Pressure flow shape factor
F_d	Drag flow shape factor
f_b	Friction coefficient at the polymer–barrel contact surface
f_s	Friction coefficient at the polymer–screw contact surface
G	Mass flow rate
g	Gravitational acceleration
H	Generic channel height
H_f	Channel height at the beginning of the feeding zone
$H_{f,end}$	Channel height at the end of the solid-conveying zone
H_m	Channel height at the end of the compression zone
T_{room}	Room temperature
T_b	Barrel temperature
T_m	Melting temperature
T_0	Reference temperature
U_1	First auxiliary variable used to compute the melting profile
U_2	Second auxiliary variable used to compute the melting profile
U_{mean}	Mean velocity near the printing nozzle outlet
U_x	Modified barrel velocity component along the orthogonal direction
U_z	Modified barrel velocity component along the down-channel direction
u_θ	Azimuthal direction (nozzle)
u_z	Down-channel direction (nozzle)
V_b	Barrel velocity
V_{bx}	Barrel velocity component along the orthogonal direction
V_{bz}	Barrel velocity component along the down-channel direction
V_f	Mean velocity at the inlet of a convergent section
V_j	Relative velocity between the barrel and solid bed
V_p	Printing speed
V_{sz}	Solid plug velocity
v_0	Non-dimensional function of the pressure gradient
W_b	Channel width near the barrel surface
W_{bead}	Layer width
W_1	Channel width at the mean screw diameter
W_2	Channel width near the screw surface
X	Solid bed width
X_1	Solid bed width at the end of the solid-conveying zone
x	Transverse direction (Cartesian coordinates)
y	Orthogonal direction (Cartesian coordinates)
z	Down-channel direction (Cartesian coordinates)
α_s	Thermal diffusivity of the solid thermoplastic
β	Half opening angle of a convergent duct

L	Axial length of a generic straight circular zone
L_c	Axial length of a generic convergent section
l_c	Length of the solid-conveying zone
l_t	Transient zone length
k_m	Thermal conductivity of the molten thermoplastic
k_s	Thermal conductivity of the solid thermoplastic
m_{sample}	Mass of an experimental sample
$\dot{m}_{sample}$	Sample mass flow rate
m_0	Consistency index
n	Power-law index
N	Peripheral screw speed
N_f	Number of turns (solid-conveying zone)
N_c	Number of turns (compression zone)
p	Generic symbol for pressure
p_{atm}	Atmospheric pressure value
p_{inlet}	Pressure under the hopper
$p_{final,i}$	Final pressure at the i-th iterative calculation step
Δp	Pressure difference
Q_m	Molten volumetric flow rate
Q_s	Solid volumetric flow rate
$\dot{q}_z$	Weighted volumetric flow rate
R	Diameter of a generic straight circular duct
r	Radial direction (polar coordinates)
r_{int}	Inlet radius of a convergent section of the nozzle
r_{ext}	Exit radius of a convergent section of the nozzle
S	Screw lead
t	Layer height
T	Generic symbol for temperature
$T_{s,mean}$	Solid bed mean temperature
Δ_{dc}	Calculation step in the delay and compression zones
Δp	Generic symbol for pressure difference
ε	Generic symbol for relative error
Δ_{sc}	Calculation step in the solid-conveying zone
$\Delta \mathrm{t}_{sample}$	Time interval
Δz	Calculation step in the down-channel direction
$\partial p/\partial z$	Pressure gradient along the down-channel direction
δ_R	Radial gap between the flight tip and barrel
δ_w	Molten layer at the end of the delay zone
$\dot{\gamma}$	Shear rate
η	Non-dimensional vertical coordinate
η_x	First integration constant
η_z	Second integration constant
λ	Heat of fusion
μ	Dynamic viscosity
ρ_0	Bulk density
ρ_m	Molten phase density
ρ_s	Solid phase density
σ	Slope of the tapered section
τ	Stress tensor
φ_0	Angle between the barrel and solid plug velocities near the barrel surface
φ_1	Angle between the barrel and solid plug velocities at the middle channel height
φ_2	Angle between the barrel and solid plug velocities near the screw surface
χ	Orthogonal to down-channel pressure gradient ratio
Φ_s	Melting rate
θ	Angle between the barrel and relative velocities
ϑ	Circumferential direction (polar coordinates)
ψ	Function used in melting profile evaluation
Ψ	Function used for calculating the pressure profile

3.3. Mathematical formulation

The mathematical model is first developed to fully describe the SSE process. The analysis is based on some assumptions, which are introduced in accordance with each modeling zone for the sake of clarity. Nevertheless, some of them characterize the entire extrusion process, as follows:

- Screw extrusion is modeled as a steady-state process.
- Motion is given to the barrel (reverse kinematic conditions).

SSE is divided into a sequence of zones, which can be modeled separately; the output from each zone is the input to the next one.

The mathematical formulation for SSE describes the behavior of a two-stage single-screw extruder composed of the following zones (Figure 3.1):

- solid-conveying zone,
- delay zone, and
- compression zone.

Moving downstream from the last turn of the SSE, the polymer passes through a coupling element and an extrusion nozzle, where the pressure drops up to atmospheric value. Their internal structures consist of tapered and cylindrical sections through which the molten polymer passes.

In the case of PAM, the molten phase is deposited layer-by-layer.

Before describing the mathematical model, an overview of the input data is presented. The variables used in the model are defined in Section 3.2.

3.3.1. Input data

Three main classes of input parameters can be distinguished:

- rheological data,
- geometrical data, and
- operating data.

Regarding the first class, it is well known (e.g., [32,35]) that most polymers exhibit a non-Newtonian shear-thinning behavior: viscosity changes with respect to both temperature and shear rate. Such dependence no longer exists when a Newtonian fluid is considered.

The proposed model assumes that the molten polymer follows a power-law behavior:

$$\mu = m_0 \dot{\gamma}^{n-1} e^{-a(T-T_0)} \tag{3.1}$$

Here m_0 is the consistency index; n is the power-law index; T is the temperature at which the dynamic viscosity μ is evaluated (in this study, T is the barrel temperature); T_0 is the reference temperature, which is taken as the melting point; and $\dot{\gamma}$ is the shear rate.

The main geometrical features of a two-stage screw are shown schematically in Figure 3.1.

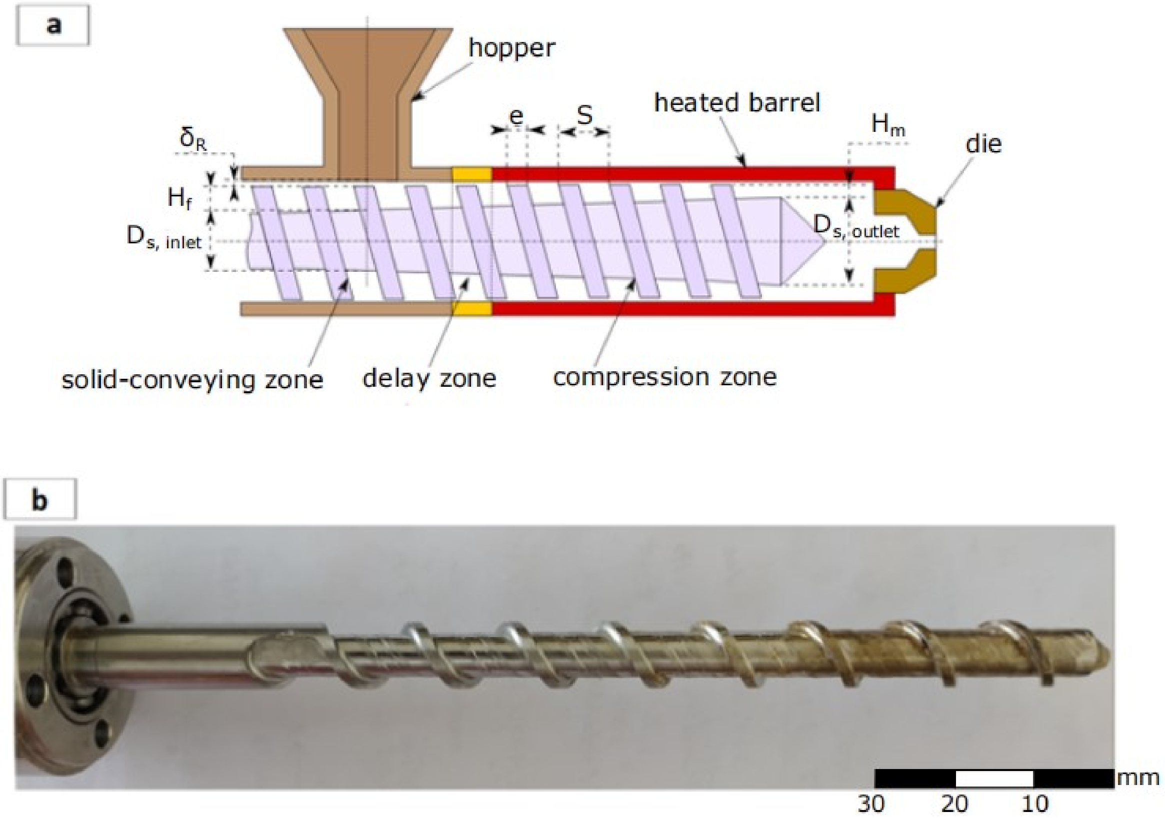

Figure 3.1. a.) Geometrical features of a general purpose two-stage screw. $D_{s,inlet}$: root screw diameter under the hopper; $D_{s,outlet}$: tip screw diameter; H_f: channel height at the beginning of the feeding zone, evaluated under the hopper; H_m: channel height at the end of the compression zone; e: flight width; S: screw lead; δ_R: radial gap between the barrel and screw; b.) Real two-stage screw used in Noztek Pro extruder.

The relevant dimensions are the screw diameter (D), flight width (e), and screw lead (S). The channel height varies along the screw length, ranging from H_f in the solid-conveying zone to H_m at the end of the compression zone.

Experimental validation was performed on the two-stage screw shown in Figure 3.1 – b. This screw model was also used to extend the presented theory to PAM extrusion. In the first part, up to the numerical and experimental validation of the SSE model, the operating data are the barrel temperature T_b and screw-speed N; in SSE, the mass flow rate is an outcome.

In Section 3.3.6, the strand deposition is modelled and the operating parameters are the strand width (W_{bead}), layer height (t) and printing speed (V_p); in PAM case, the screw-speed is an outcome.

3.3.2. Solid-conveying zone

The description of polymer solid-conveying follows the approach given in [11], which is valid under the following assumptions:

- constant material properties,
- locally isotropic pressure distribution, and

- negligible inertia and gravity forces.

The helix channel through which the solid-conveying process occurs is divided into a series of small incremental steps. Here, Δ_{sc} is the down-channel calculation step (Figure 3.2).

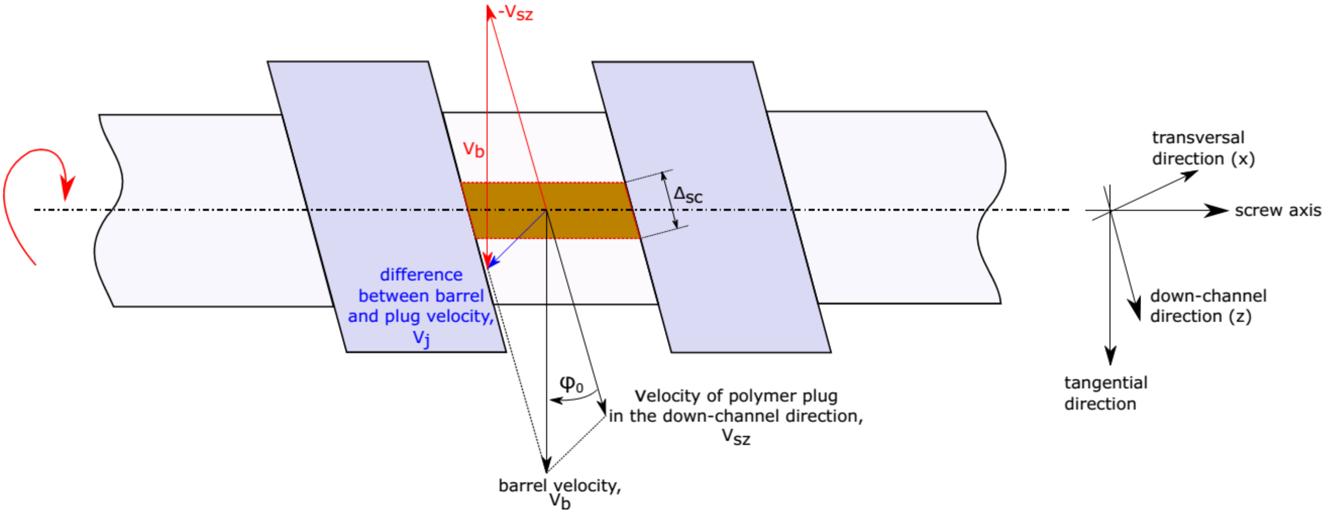

Figure 3.2. Solid-conveying kinematics and geometry.

The pressure profile is calculated from the force and torque balances on finite solid elements, as depicted in Figure 3.2. From the previous calculation step, given the pressure at the center, that is, p_{n-1}, its value at the center of the next one can be computed as:

$$p_n = p_{n-1} e^{\left(\frac{B_1 - A_1 K}{B_2 + A_2 K}\Delta_{sc}\right)} \tag{3.2}$$

The parameters $(B_1, A_1, K, B_2, \text{and } A_2)$ are geometrical functions, whose expressions can be found in [15,35]:

$$A_1 = W_b f_b \sin\theta + 2 f_s H_f \sin\varphi_0 + f_s W_2 \sin\varphi_0 \tag{3.3}$$

$$A_2 = H_f \, W_1 \, \sin\varphi_1 \tag{3.4}$$

$$K = \frac{D_1 \sin\varphi_1 + f_s \cos\varphi_1}{D_b \cos\varphi_1 - f_s \sin\varphi_1} \tag{3.5}$$

$$B_1 = W_b f_b \cos\theta - 2 H_f f_s \sin\varphi_0 \frac{D_1}{D_b} \operatorname{cotg}\varphi_1 - W_2 f_s \sin\varphi_0 \operatorname{ctg}\varphi_2 \frac{D_2}{D_b} \tag{3.6}$$

$$B_2 = W_1 H_f \cos\varphi_1 \frac{D_1}{D_b} \tag{3.7}$$

where W_b, W_1, and W_2 are the channel widths near the barrel, mean screw radius, and screw root, respectively; φ_0, φ_1, and φ_2 are the angles between the barrel and solid plug velocities at the previously indicated radial positions, respectively; D_b, D_1, and D_2 are the barrel, middle screw, and screw root diameters, respectively; f_b

and f_s are the friction coefficients at the polymer–barrel and polymer–screw interfaces, respectively; H_f the channel height at the beginning of the feeding zone; and θ is the angle between the barrel and relative velocities. As outlined in Chapter 2, there are more complex models of solid-conveying that consider pressure anisotropy, that is, the different behaviors near the screw root, flights, and barrel [14]. That models were further extended in [18], where a complex theory involving the effects of both inertial and gravitational forces was derived. Other recent models employ DEM to describe the entire pellet dynamics. Unfortunately, the abovementioned methods require much more computational resources (e.g., [21,23,24]).

The analytical model proposed in [11] was chosen as a reference for modeling the pellet feed process because of the ease of implementation and very low computational cost.

The inlet pressure can be easily calculated as [35]:

$$p_{inlet} = p_{atm} + \rho_0 g D \tag{3.8}$$

where p_{atm} is the atmospheric pressure, ρ_0 is the polymer bulk density, g is the gravitational acceleration, and D is the tip screw diameter. The physical meaning of latter contribution is that of a hydrostatic contribution; the weight of the material under the hopper in the horizontal configuration is considered. The hydrostatic term has been disregarded in computations because it is an order of magnitude lower than the atmospheric pressure.

3.3.3. Delay and compression zones

In delay zone the polymer starts to melt, but this process takes place only at the interface with the heated barrel. When the molten layer thickness exceeds a critical value δ_w, the delay zone ends and the formation of a molten recirculating region, also known as the melt pool, starts [32].

The polymer behavior in the delay zone can be described by the same equations used for modeling the compression zone, with slight modifications. Therefore, the basic mathematical formulation is the same.

First, the barrel velocity components along the transverse (x) and down-channel (z) directions are calculated accordingly to Figure 3.2:

$$V_{bx} = V_b sin(\varphi_0) \tag{3.9}$$

$$V_{bz} = V_b cos(\varphi_0) \tag{3.10}$$

where V_b is the peripheral speed:

$$V_b = \frac{\pi N D_b}{60} \tag{3.11}$$

and φ_0 can be expressed as:

$$\varphi_0 = arctg\left(\frac{S}{\pi D_b}\right) \tag{3.12}$$

The last velocity to be used for the description of these three zones is the relative velocity between the solid plug and barrel (Figure 3.2), whose value is given by:

$$V_j = \sqrt{V_b^2 + V_{sz}^2 - 2V_b V_{sz} cos\ \varphi_0} \tag{3.13}$$

Based on the melting theory presented, the following auxiliary variable can be introduced:

$$b = \frac{a}{n}(T_b - T_m) \tag{3.14}$$

In former expression T_b and T_m are the barrel and melting temperatures, respectively. Variable a is the temperature sensitivity of the parameters of the power-law constitutive relation to the temperature and the exponent of the Arrhenius power-law relation in (3.1).

According to the theory introduced in [35], the following system can be solved to evaluate U_1 and δ_w, where δ_w is the height of the molten layer adjacent to the barrel at the end of the delay zone:

$$\begin{cases} 2m_0\left(V_j^{n+1}\right)\left(\dfrac{e^{-b}+b-1}{b^2}\right)\left(\dfrac{b}{1-e^{-b}}\right)^{n+1}(\delta_w)^{1-n} = U_1 \\ \sqrt{\dfrac{[2k_m(T_b - T_m) + U_1]W_1}{V_{bx}U_2\rho_m[\lambda + c_m\Theta_m(T_b - T_m) + c_s(T_m - T_{s,mean})]}} = \delta_w \end{cases} \tag{3.15}$$

Here ρ_m, λ, c_m, and c_s are the molten density, latent heat, and heat capacities of the polymer in the molten and solid states, respectively.

The parameters U_2 and Θ_m are auxiliary parameters which depends on different properties of the non-isothermal power-law model; they depend on power-law index at reference temperature (n), sensitivity to temperature coefficient (a), barrel temperature (T_b) and melting temperature (T_m), as highlighted in [35].

Equation (3.15) is used to calculate the height of the molten layer at the barrel wall (δ_w). Here, the parameter $T_{s,mean}$ is the solid bed mean temperature:

$$T_{s,mean} = T_m + (T_{room} - T_m)\left(\frac{8}{\pi^2}\right)e^{-\frac{12\alpha_s l_c}{V_{sz}H_f^2}} \tag{3.16}$$

In the above expression, l_c is the axial position for the start of the delay zone, which is the end of the solid-conveying zone. The start of the melting process, which involves a transition from dry friction to viscous drag at the polymer–barrel interface, corresponds to the beginning of the heated barrel; this marks the end of the feeding zone. In addition, α_s is the thermal diffusivity of the solid phase and T_{room} is the room temperature (20 [°C] in all calculations). It is also assumed that the molten layer height varies linearly in the delay zone; its value is zero at the end of the solid-conveying zone and terminates with the calculated δ_w.

The solid bed width is the channel width W_1, as shown in (3.15), because melting occurs only at the polymer–barrel contact surface. With these two datasets, it is possible to calculate the melting rate in the delay zone [35]:

$$\Phi_s = \sqrt{\frac{V_{bx}U_2\rho_m[2k_m(T_b - T_m) + U_1]}{4W_1\left[\lambda + c_m\Theta_m(T_b - T_m) + c_s\left(T_m - T_{s,mean}\right)\right]}} \tag{3.17}$$

Finally, there is no known rigorous calculation procedure for the pressure profile in the delay zone. Because of its small extension in the down-channel direction, it is assumed that pressure is the same as that at the end of the solid-conveying zone.

After the molten layer thickness reaches δ_w, the melt pool begins to expand (Figure 3.3). The melting mechanism must be determined at this point. In this study, it is assumed that the Maddock melting mechanism [86] occurs (Figure 3.3), that is, a molten layer forms at the polymer–barrel interface in the delay zone. Then, it is dragged away to form a molten pool near the active flight, while the passive flight is still in contact with the solid polymer. As the polymer melting continues, the molten pool expands until the polymer is completely molten.

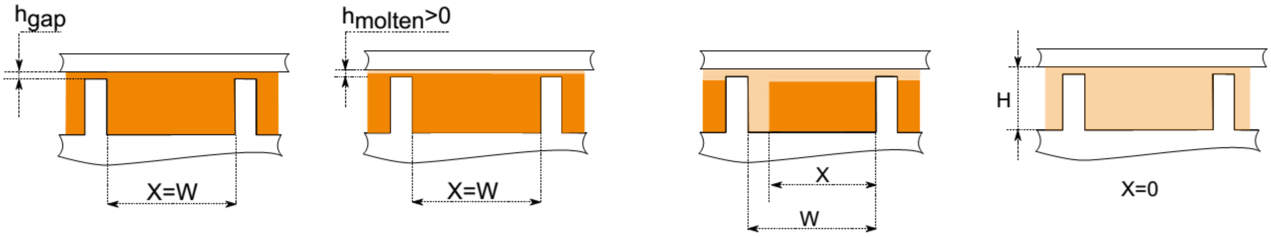

Figure 3.3. Maddock mechanism. W: channel width; h_{gap}: radial clearance between screw flights and barrel; h_{molten}: local melt thickness.

As stated earlier, the equations that describe the melting in the compression zone are very similar to those introduced for the delay zone. The difference is that because of the formation of a melt pool, the channel width W_1 in (3.15) and (3.17) must be replaced by $X(j)$, which is the solid bed width in the j-th calculation step (Figure 3.3).

Given the melting rate, Φ_s, calculated in the previous calculation step, the following nonlinear ODE [32], which represents the variation of the solid bed area in the down-channel direction, can be solved:

$$\begin{cases} \dfrac{dA_s}{dz} = -\dfrac{\Phi_s\sqrt{X}}{\rho_s V_{sz}} \\ X(0) = X_{j-1} \end{cases} \tag{3.18}$$

Here X is the unknown value of the solid bed width, z is the abovementioned down-channel coordinate, and $A_s = HX$ is the local solid bed cross-sectional area under the assumption that the melting layer thickness variation is negligible.

The solution to the previous Cauchy problem can be written in the following form [10,32]:

$$\frac{X}{W_1} = \frac{X_1}{W_1}\left[\frac{\psi}{\sigma} - \left(\frac{\psi}{\sigma} - 1\right)\sqrt{\frac{H_{f,end}}{H}}\right]^2 \tag{3.19}$$

Here W_1 is the geometrical channel width at the local mean channel radial position, H is the local channel height, and X_1 and $H_{f,end}$ are the width of the solid bed and height of the cross-section at the end of the solid-conveying zone, respectively.

The function ψ is defined as:

$$\psi = \frac{\Phi_s}{\rho_s V_{sz}\sqrt{X_1}} \tag{3.20}$$

In (3.19), σ is the slope of the tapered section, which is calculated as follows:

$$\sigma = \frac{H(j) - H(j-1)}{\Delta_{dcm}} \tag{3.21}$$

By discretizing the compression zone in a series of small computational steps, the melting profile, namely, the function $X = X(z)$, where z is the down-channel position, can be evaluated. Subsequently, it is used as an input for the calculation of the pressure profile. Following the procedure given in [35], the mass conservation in the down-channel (z) and transverse direction (x), together with the boundary conditions written in an integral form, can be formulated as:

$$\chi\int_0^1(\eta-\eta_x)\Psi(\eta)d\eta = U_x \qquad (3.22)$$

$$\int_0^1(\eta-\eta_z)\Psi(\eta)d\eta = U_z \qquad (3.23)$$

$$\chi\int_0^1\eta(\eta-\eta_x)\Psi(\eta)d\eta = U_x \qquad (3.24)$$

$$\int_0^1\eta(\eta-\eta_z)\Psi(\eta)d\eta = U_z-\frac{\dot{q_z}}{W_1Hv_0} \qquad (3.25)$$

Where:

$$\Psi(\eta)=[(\eta-\eta_z)^2+\chi^2(\eta-\eta_x)^2]^{\frac{1-n}{2n}} \qquad (3.26)$$

Assuming that the flow of the molten thermoplastic material is at barrel temperature T_b:

$$v_0 = H\left|\frac{\partial p}{\partial z}F_p\frac{H}{m_0}\right|^{\frac{1}{n}} sgn\left(\frac{\partial p}{\partial z}\right) \qquad (3.27)$$

In the previous equations, η is the nondimensional channel height:

$$\eta=\frac{y}{H} \qquad (3.28)$$

The variables η_x and η_z are integration constants, while χ is the ratio of the pressure gradients along the z and x directions, namely:

$$\chi=\frac{\partial p/\partial x}{\partial p/\partial z} \qquad (3.29)$$

The nondimensional variables U_x and U_z are defined as:

$$U_x=\frac{V_{bx}}{v_0} \quad ; \quad U_z=\frac{V_{bz}}{v_0}F_d \qquad (3.30)$$

The quantities F_d and F_p are the shape factors used to account for the effect of the screw flights on the drag and pressure flow, respectively. These two shape factors depend only on geometrical dimensions, as indicated in the following expressions [58]:

$$F_d=\frac{16W_1}{\pi^3H}\sum_{i=0}^{\infty}\frac{1}{(2i+1)^3}tanh\left[\frac{\pi H(2i+1)}{2W_1}\right] \qquad (3.31)$$

$$F_p=1-\frac{192H}{\pi^5W_1}\sum_{i=0}^{\infty}\frac{1}{(2i+1)^5}tanh\left[\frac{\pi W_1(2i+1)}{2H}\right] \qquad (3.32)$$

In the current study, the volumetric flow rate $\dot{q}_z$ is locally calculated as an area mean weighted quantity. Given the area contents of the solid and molten polymers, which are calculated during the melting profile evaluation, the flow rate is:

$$\dot{q}_z = \frac{A_s Q_s + A_m Q_m}{A_{total}} \tag{3.33}$$

Where the volumetric flow rates are:

$$Q_s = \frac{G}{\rho_s} \quad ; \quad Q_m = \frac{G}{\rho_m} \tag{3.34}$$

The latter quantities are the volumetric flow rates if the channel is filled with a solid (Q_s) or molten (Q_m) polymer, respectively.

The nonlinear system aimed at calculating the pressure profile is composed of four equations, that is, (3.22), (3.23), (3.24), and (3.25), in four unknowns (η_x, η_z, χ, and v_0). The solution is performed numerically by evaluating the integrals using the Gauss–Legendre quadrature method (10 nodes show a good compromise between the required computational accuracy and time).

By calculating v_0, the pressure gradient along the down-channel direction for a given axial step $\partial p/dz$ in (3.27) can be determined, and the pressure difference along the entire helix can be solved as:

$$\Delta p = \frac{\partial p}{dz} \Delta_{dc} \tag{3.35}$$

In (3.35), Δ_{dc} is the computational step used to discretize the delay and compression zones.

To date, the semi-analytical formulation has been used for calculating all pressure differences, from the solid pellet inlet up to the last transverse section of the extruder, before coupling the element and nozzle. Nevertheless, the reconstruction of the absolute pressure profile is mandatory. To do so, it is important to know the absolute pressure at the delay zone inlet, which is the pressure at the end of the solid-conveying zone. This is calculated according to the theory presented in Section 3.3.2. Consequently, the pressure profiles of the solid-conveying, delay, and compression zones, in the case of a two-stage screw, can be reconstructed.

Analogously, the final pressure is the input for evaluating the absolute pressure profile in the next extrusion elements, namely, the coupling element and nozzle (and along the strand being deposited on the build plate, in the case of PAM).

3.3.4. Fluid flow in a cylindrical duct

After the polymer is completely molten, it passes through the coupling element and, finally, through the nozzle. The internal shape of the nozzle consists of cylindrical and tapered zones. An example of the internal geometry of a nozzle is schematically shown in Figure 3.4.

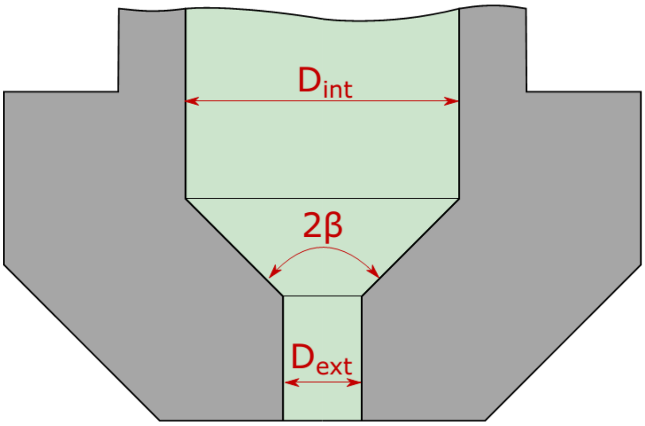

Figure 3.4. Nozzle internal dimensions. D$_{int}$: diameter before the convergent section; 2β: convergent opening angle; D$_{ext}$: diameter after the convergent section.

The mathematical derivation of the axial flow of a power-law fluid through a cylindrical duct has been reported in [87] under the following assumptions:

- laminar flow,
- stationary flow,
- fully developed flow,
- incompressible fluid,
- isothermal flow,
- purely viscous flow (elongational effects are neglected),
- no-slip condition at walls,
- negligible gravitational effects, and
- negligible influence of the screw rotation on the flow field ($u_\vartheta = 0$).

The velocity profile obeys the following equation:

$$u_z(r) = \left(\frac{\Delta p}{2m_0 L}\right)^{1/n} \frac{n}{n+1} R^{\frac{n+1}{n}} \left[1 - \left(\frac{r}{R}\right)^{\frac{n+1}{n}}\right] \tag{3.36}$$

The flow rate in polar coordinates is found by integration:

$$Q_m = \int_0^{2\pi} \int_0^R u_z \, r \, dr d\vartheta = \pi R^{\frac{3n+1}{n}} \frac{n}{3n+1} \left(\frac{\Delta p}{2m_0 L}\right)^{1/n} \tag{3.37}$$

By rearranging the last equation, the pressure drop can be evaluated:

$$\Delta p = \left(\frac{Q_m}{\pi}\frac{3n+1}{n}\right)^n \frac{2m_0 L}{R^{3n+1}} \tag{3.38}$$

The first approach for verifying the latter expression is to check its validity in the Newtonian case, which can be performed by setting $n = 1$. After substitution, Equation (3.38) becomes:

$$\Delta p = 8m_0 L \frac{Q_m}{\pi R^4} \tag{3.39}$$

which can be rearranged to give the flow rate:

$$Q_m = \frac{\pi R^4}{8m_0}\frac{\Delta p}{L} \tag{3.40}$$

The latter is exactly the expression for the Poiseuille flow.

3.3.5. Fluid flow in a tapered duct

Referring to Figure 3.4, the flow inside the converging section of the extrusion nozzle can be calculated using the following expression [85]:

$$\Delta p = \frac{m_0}{3\,n\,tg(\beta)}\left[\frac{1}{(D_{ext})^{3n}} - \frac{1}{(D_{int})^{3n}}\right]\left[V_f\left(\frac{3n+1}{n}\right)\left(\frac{D_{int}}{2}\right)^2 2^{\frac{3n+1}{n}}\right]^n \tag{3.41}$$

where D_{int} is the convergent inlet diameter, while D_{ext} is the exit diameter. Moreover, V_f is defined as the mean inlet flow velocity:

$$V_f = \frac{4Q_m}{\pi D_{int}^2} \tag{3.42}$$

Parameter β is half of the opening angle of the nozzle, which is calculated as:

$$\beta = tg^{-1}\left(\frac{D_{int} - D_{ext}}{2L_c}\right) \tag{3.43}$$

where L_c is the axial length of the converging nozzle. Both theories proposed in Sections 3.3.4 and 3.3.5 are appliable to other straight and tapered channels. In this study, this is the case of the coupling element usually placed between the screw tip and nozzle.

Clearly, another approach would be discretizing the convergent section into a series of small axial steps. The main drawback of this approach is the longer computational time and the fact that the flow field in each of the segments is forced to be purely axial, while the converging wall of the nozzle induces the real streamlines to follow the same pattern; further details on fluid dynamics of complex fluids in nozzles for AM will be discussed in Chapter 5.

3.3.6. Modeling the counterpressure

When dealing with PAM, a factor that can potentially affect the screw-barrel system behavior is the counterpressure that arises because of the layer deposition. In PAM the extruder is placed vertically, and the deposition occurs layer-by-layer until the final part is built.

A major interest is in depositing molten layers with a distance between the nozzle tip and build plate (defined as parameter t, hereinafter), which is smaller than the nozzle exit diameter (D_{ext}), to improve the accuracy and roughness of the printed part and increase its strength already for low-volume applications, such as in FFF [88]. This means that the relative pressure at the nozzle outlet is no longer zero. The atmospheric value is restored only when the molten polymer being deposited on the build plate flows over the nozzle tip external diameter, denoted as $D_{ext}^{(n)}$ in subsequent Figure 3.5.

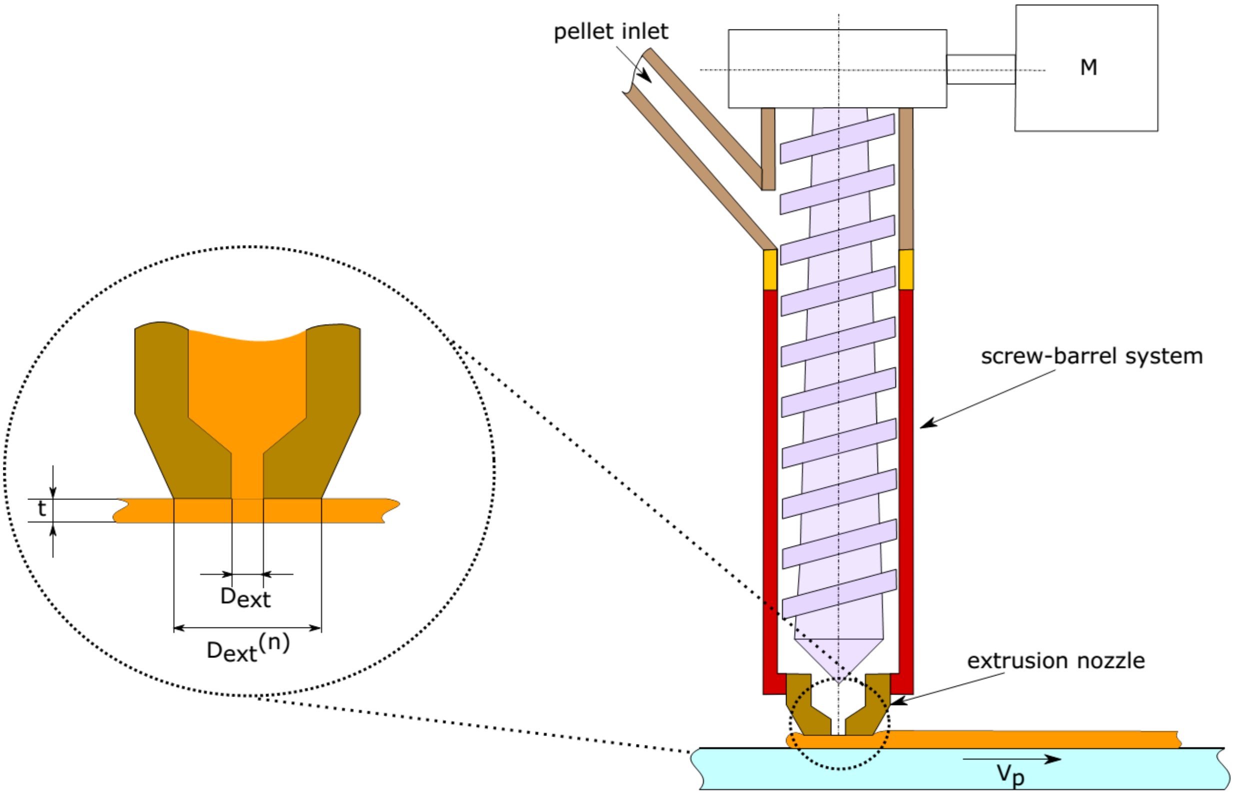

Figure 3.5. Representation of the PAM extrusion process. t: gap between the nozzle external wall and build plate; V_p: printing velocity assigned to the build plate; D_{ext}: exit nozzle diameter; $D_{ext}^{(n)}$: external nozzle wall diameter.

About the study of the PAM process, there are two possible ways to couple the layer with the screw-barrel system:

- To fix the screw peripheral speed N and some printing parameters (i.e., t and V_p) to find the right flow rate $\dot{m}$; in this case, the layer width W_{bead} is calculated by mass conservation when convergence is reached, or

- To fix printing parameters (i.e,: t, V_p and W_{bead}) and to find the right peripheral speed; in this case, the mass flow rate $\dot{m}$ is determined directly at the beginning of the iterative solution process, by means of the printing parameters.

In the former case the controlled input variable is the peripheral screw speed, while in the latter it is the mass flow rate. The two approaches will be called as N-control and m-control, for the sake of brevity.

In the N-control, it is possible to calculate, for a given printing speed (assigned to the build plate under the assumption of reverse kinematic conditions, as also depicted in Figure 3.5) and layer height, the layer width, which can be estimated according to the mass conservation law as follows [89]:

$$W_{bead} = \frac{\pi}{4} \frac{U_{mean}}{V_p} \frac{D_{ext}^2}{t} \tag{3.44}$$

Here U_{mean} denotes the mean velocity near the printing nozzle outlet, V_p the printing speed, and W_{bead} the predicted strand width.

In (3.44) it has been posed that the strand follows the cuboid shape [89].

In this study, the axial portion of the bead where the counterpressure occurs is fixed. Actually, the equations through which a layer of the assigned geometry is studied are the same as those used for the prediction of the pressure profile in the screw extruder, namely (3.22)–(3.25), with one major difference: there is only a nonzero velocity component, which is that along the direction of the printing head (Figure 3.5).

In other words, these equations describe the Couette flow of a power-law fluid in a rectangular duct, whose dimensions follow the imposed PAM operating parameters, together with mass flow conservation (3.44), if one follows the N-control logic.

Hereinafter the focus is on the deposited bead; its geometry is fully constrained and the goal is to determine the screw peripheral speed, to extrude the prescribed mass flow rate (m-control); more details will be given in next Section.

The influences of the two key parameters of the PAM process, namely,

- the velocity of the printing head (V_p), and
- layer height (t)

are investigated, for a fixed layer width, with respect to the main output variables, which are the screw peripheral speed, pressure profile, and melting profile, as presented in Section 3.5.

3.3.7. Convergence criterion

3.3.7.1. N-control iterative code

The pressure profile is evaluated for a given screw speed flow rate (N-control) from the extruder inlet to the nozzle outlet in the case of SSE, where the initial pressure consists of the atmospheric pressure and hydrostatic contribution (3.8). The pressure rises as soon as the material moves toward the last turns of the extruder. Finally, there is a pressure drop in both the coupling element and nozzle. Clearly, for a trial flow rate, the pressure at the nozzle outlet is different from the atmospheric value, which is physically impossible, at least for SSE (no counterpressure).

The mass flow rate must be calculated according to this convergence criterion: recovery of the atmospheric pressure at the end of the nozzle (SSE). To do so, the trial mass flow rate is modified according to the following empirical expression:

$$\begin{cases} G_{i+1} = G_i + 2 * 10^{-8} \dfrac{p_{final,i}}{p_{atm}} & if \quad \dfrac{p_{final,i}}{p_{atm}} \geq 100 \\ G_{i+1} = G_i + 10^{-10} \left(\dfrac{p_{final,i}}{p_{atm}}\right)^2 + \dfrac{1}{100}\left(\dfrac{p_{final,i}}{p_{atm}}\right) & if \quad 1 \leq \dfrac{p_{final,i}}{p_{atm}} < 100 \\ G_{i+1} = G_i - 10^{-10} \left(\dfrac{p_{final,i}}{p_{atm}}\right)^2 - \dfrac{1}{100}\left(\dfrac{p_{final,i}}{p_{atm}}\right) & if \quad -100 < \dfrac{p_{final,i}}{p_{atm}} < 1 \\ G_{i+1} = G_i + 2 * 10^{-8} \dfrac{p_{final,i}}{p_{atm}} & if \quad \dfrac{p_{final,i}}{p_{atm}} \leq -100 \end{cases} \tag{3.45}$$

Here, G_i is the mass flow rate at the previous iteration, G_{i+1} is its value at the next iteration, and $p_{final,i}$ is the pressure value at the nozzle exit (for SSE).
Let's define ΔG_i as the difference between the mass flow rate at next iteration $(i + 1)$ and at previous one (i); it is the entity of the correction between subsequent iterations. The stepwise function has been chosen to perform a lower correction when the ratio between final pressure and atmospheric one is closer to 1. This trend is well described in the following graphical representation of the piecewise function (Figure 3.6):

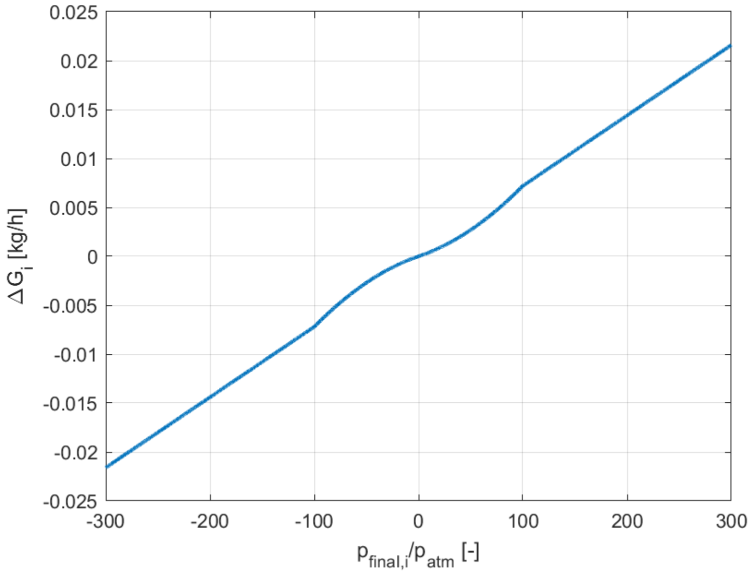

Figure 3.6. Empirical piecewise function. p_{final}: final pressure; p_{atm}: atmospheric pressure; ΔG_i: correction on mass flow rate.

Moreover, the same equations can be applied in the case of PAM extrusion, where the only difference is that the atmospheric pressure must be recovered when the layer passes the nozzle external diameter, namely, the radial portion between D_{ext} and $D_{ext}^{(n)}$, according to Figure 3.5. For this reason, the value of $p_{final,i}$ in (3.45) is that at the nozzle external diameter exit.
The complete flow chart for the N-control iterative code has been reported in the following Figure 3.7:

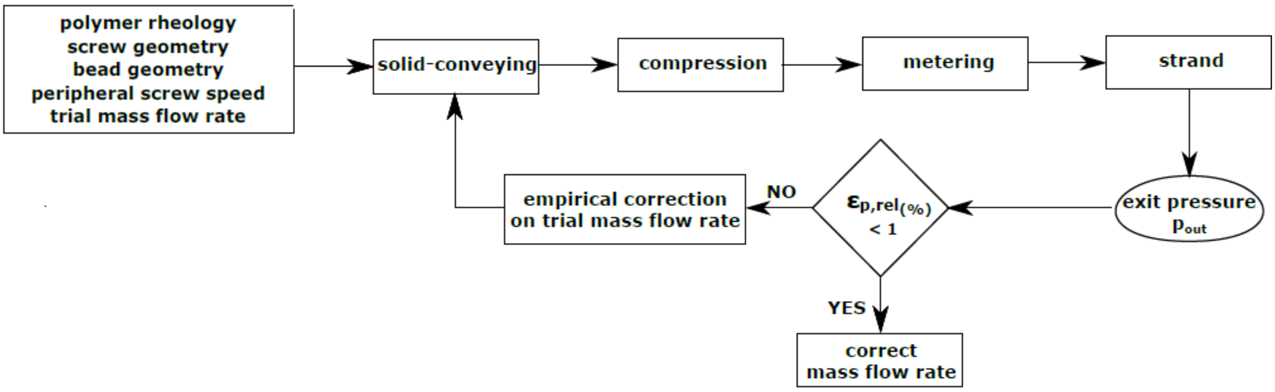

Figure 3.7. Flow chart for the N-control iterative code.

3.3.7.2. m-control iterative code

In real PAM applications, it is preferred to adapt the operating point of the screw-barrel system to the properties of the deposited strand (m-control).

This approach is very similar to what happens in FFF, where there is a direct control on the characteristics of the extruded layer and on the volumetric flow rate, consequently [85].

In practical applications, the focus is on the layer being deposited and on the control of its geometrical features; it is of interest to deposit a layer with prescribed width (fixed in all simulations: 1.2 $D_{ext}^{(n)}$, accordingly to [85]). Because of the fact the layer width has been constrained, if one sets the printing parameters (i.e., printing sped and layer height), the mass flow rate can be calculated by mass conservation:

$$\dot{m} = \rho_s V_p W_{bead} t \tag{3.46}$$

Now, the mass flow rate is prescribed for given printing conditions and the real difference with the flow chart of Figure 3.7 is that W_{bead} is now fixed.

For that reason, the iterative scheme must change; the goal is to calculate the value of peripheral screw speed which allows to extrude the prescribed mass flow rate and to generate a strand with requested characteristics. To do so, the flow chart must be modified:

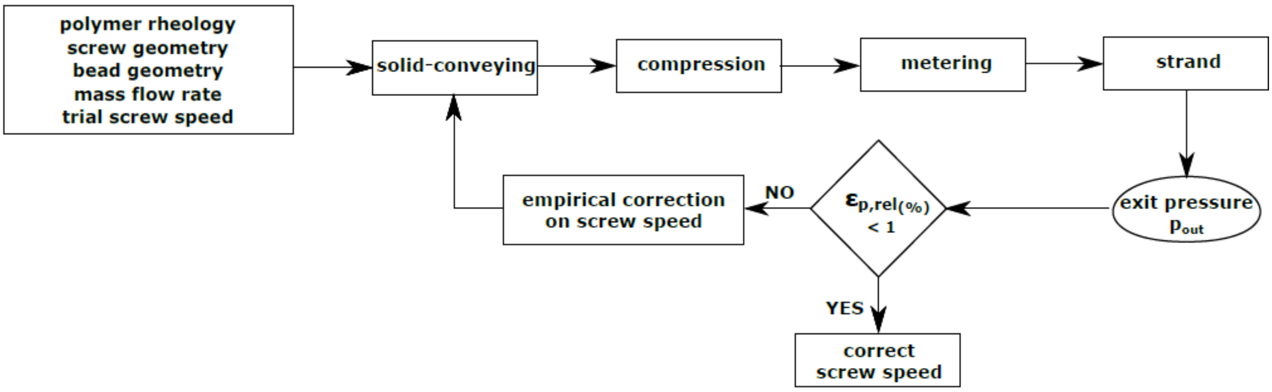

Figure 3.8. Flow chart for the m-control iterative code.

The empirical convergence criterion is modified accordingly to the following equations:

$$\begin{cases} N_{i+1} = N_i - \frac{1}{5}\left(1 + \frac{1}{100}\frac{p_{final,i}}{p_{atm}}\right) & if \quad \frac{p_{final,i}}{p_{atm}} \geq 100 \\ N_{i+1} = N_i - \frac{1}{5}\left[\left(\frac{1}{100}\frac{p_{final,i}}{p_{atm}}\right)^2 + \frac{1}{100}\left(\frac{p_{final,i}}{p_{atm}}\right)\right] & if \quad 1 \leq \frac{p_{final,i}}{p_{atm}} < 100 \\ N_{i+1} = N_i + \frac{1}{5}\left[\left(\frac{1}{100}\frac{p_{final,i}}{p_{atm}}\right)^2 - \frac{1}{100}\left(\frac{p_{final,i}}{p_{atm}}\right)\right] & if \quad -100 < \frac{\mathrm{p_{final,i}}}{\mathrm{p_{atm}}} < 1 \\ \mathrm{N_{i+1}} = \mathrm{N_i} + \frac{1}{5}\left(1 + \frac{1}{100}\frac{\mathrm{p_{final,i}}}{\mathrm{p_{atm}}}\right) & \mathrm{if} \quad \frac{\mathrm{p_{final,i}}}{\mathrm{p_{atm}}} \leq -100 \end{cases} \tag{3.47}$$

Let's define $\Delta \mathrm{N_i}$ as the difference between the screw speed at next iteration $(\mathrm{i}+1)$ and at previous one (i); it is the entity of the correction between subsequent iterations.
The graphical representation has been reported in Figure 3.9:

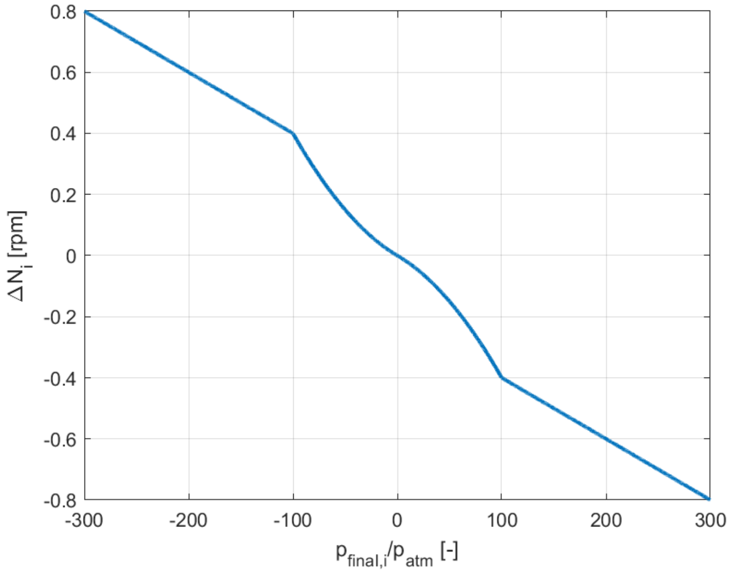

Figure 3.9. Empirical piecewise function. $\mathrm{p_{final}}$: final pressure; $\mathrm{p_{atm}}$: atmospheric pressure; $\Delta \mathrm{N_i}$: correction on screw peripheral speed.

In the following, the original SSE control logic, based on finding the mass flow rate (N-control), is used only for validation purposes (Section 3.4).
When dealing with the PAM process, the control logic focused on finding the correct peripheral screw speed (m-control) is always adopted in computations (Section 3.5.6).

3.4. Numerical and experimental validation

3.4.1. Extrusion system

The N-control mathematical model was experimentally validated by testing a Noztek Pro extruder (SSE), which is commonly used to create filaments from pellets (Figure 3.10).

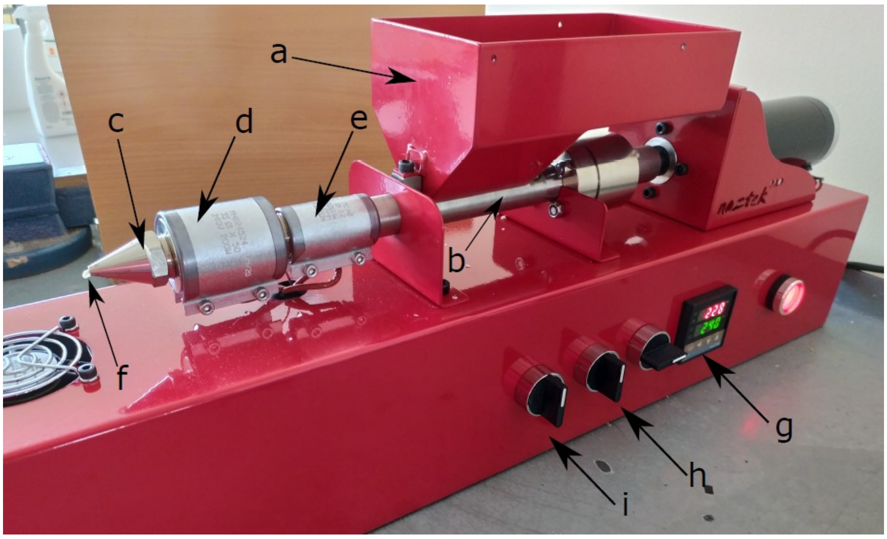

Figure 3.10. Noztek Pro single-screw extruder. a: hopper; b: barrel; c: nozzle; d: heater band; e: preheater band; f: extrudate; g: temperature controller; h: handle for screw rotation; i: handle for the ventilation system.

The extruder is composed of a hopper (a), through which the pelletized material is introduced. Then, there is a two-stage screw whose diameter gradually increases from 9 [mm] (screw rear) to 10.5 [mm] (screw tip). The rotating screw is enclosed within a barrel (b). Then, there is a nozzle (c) through which the molten material is forced to pass. Heat is transmitted to the screw and barrel through a preheater (e) and heater band (d).

First, the temperature is set through a screen (g), depending on the material being extruded. The manufacturer suggests heating the system without activating the screw motion for up to 15 min to fully heat the extruder barrel and prevent screw stall. After this period, the screw motor can be activated through a handle (h), and the screw starts to rotate. Finally, a second handle (i) can be activated to start the ventilation system located near the extrudate exit. This system is employed to increase the solidification rate of the material being extruded and achieve a higher dimensional accuracy for the extruded filament.

It is also important to consider that the extrudate has a slightly larger diameter than that of the extrusion nozzle. This phenomenon is referred to as the Barus effect in the literature [90–93].

Experimentally, a relationship between the nozzle temperature and extrudate diameter has been observed: as the heating temperature increases, the Barus effect decreases. This behavior has been widely documented for FFF [91].

The main features of the Noztek Pro single-screw extruder are listed in Table 3.1.

Table 3.1. Geometrical features of the Noztek Pro single-screw extruder.

Parameter name	**Symbol**	**Value**
Internal barrel diameter	D_b	15 [mm]
Initial screw diameter	$D_{s,inlet}$	9 [mm]
Final screw diameter	$D_{s,outlet}$	10.5 [mm]
Flight width	e	2.5 [mm]
Screw lead	S	20.5 [mm]
Number of turns in feeding zone	N_f	1

Number of turns in compression zone	N_c	2
Channel height in feeding zone	H_f	2.6 [mm]
Final channel height	H_m	2.2 [mm]
Radial gap	δ_R	1 [mm]

A general representation of the dimensions indicated in Table 3.1 is displayed in Figure 3.1.

In the case of Noztek Pro, the pressure starts to drop initially inside the coupling element and then through the nozzle. These two elements are fully illustrated in Figure 3.11 - a, whereas in Figure 3.11 - b, the internal geometrical dimensions of these two elements are given.

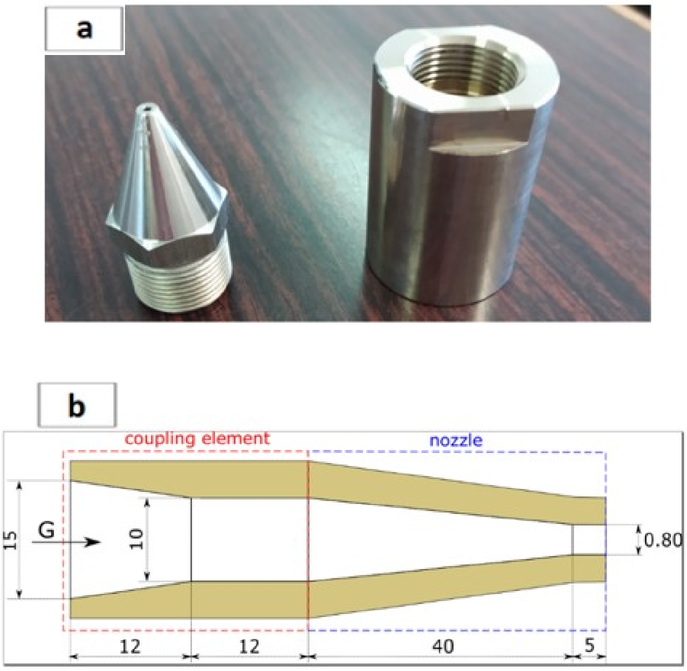

Figure 3.11. a.) Extrusion nozzle (left) and coupling element (right); b.) geometrical features of the coupling element and nozzle (1.75 [mm]).

3.4.2. Mass flow rate evaluation and test condition

The main purpose of the validation process is to calculate the mass flow rate being extruded using Noztek Pro. The following steps were followed:

- The material is extruded freely through the heated nozzle,
- The video recording of the entire extrusion process is started,
- A marker is made on the extrudate by means of an indelible pen,
- The process is repeated to obtain additional samples,
- The screw is stopped and the entire extrudate is cut off,

- The extrudate is further cut in the marked points to obtain samples,
- The samples are weighed using a Kern Emb 200-3 balance (resolution of 0.001 g; full scale of 200 [g]),
- The recorded video is post-processed using a Kinovea video annotation tool, and the time interval between two successive marker positions is evaluated, and
- The mass flow rate of a given sample is estimated as the ratio between its measured mass and the time interval.

Subsequently, both the population mean value and standard uncertainty are computed. The latter is then extended to 99[%] confidence level by means of Student's t tables.
Another approach would be to evaluate the volumetric flow rate and use the information given by both the supplier (solid phase density) and the video recorded (extrusion time) to determine the mass flow rate. Because of the Barus effect and the higher number of uncertainties to be combined, this procedure was disregarded.
The material being tested was ABS MFI-22, which was supplied by Noztek together with the previously described extrusion system. The different input parameters used to perform both the analytical and numerical studies are described in Table 3.2.

Table 3.2. Material data.

Material: ABS MFI-22					
Property	**Description**	**Value**	**Property**	**Description**	**Value**
ρ_s	Solid density [kg/m^3]	1040	λ	Heat of fusion [J/kg]	0
ρ_m	Melt density [kg/m^3]	930	m_0	Consistency index [Pa $*$ s^n]	11000
ρ_0	Bulk density [kg/m^3]	580	n	Power-law index	0.5
c_s	Specific heat of solid phase [J/KgK]	1600	a	Temperature coefficient [1/K]	0.025
c_m	Specific heat of molten phase [J/KgK]	2400	f_b	Friction coefficient at barrel-polymer interface	0.4
k_s	Thermal conductivity of solid phase [W/mK]	0.13	f_s	Friction coefficient at screw-polymer interface	0.4
k_m	Thermal conductivity of molten phase [W/mK]	0.16	T_m	Melting temperature [°C]	210

The rheological constants were estimated as the best fit of the viscosity curves found in the technical datasheet [94]. Both the real and estimated viscosity–shear rate curves at different printing temperatures are depicted in Figure 3.12.

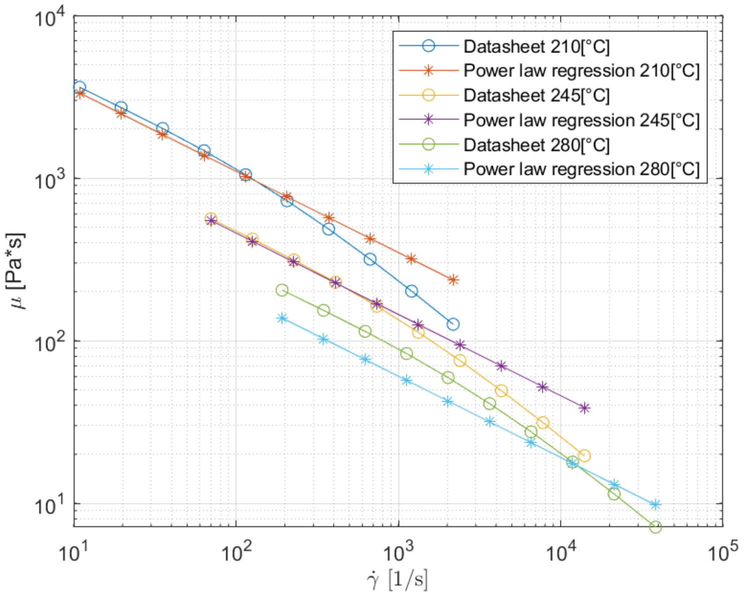

Figure 3.12. Viscosity curves at different temperatures.

The dynamic viscosity estimated based on the rheological parameters in Table 3.2 is in good agreement with the value in the technical datasheet, at least for the extrusion temperature being set ($T_b = 240$ [°C]).
The previously described experimental test was then performed and the mass flow rate was evaluated according to a sample population to obtain both the mean and standard deviation, extended up to 99[%] confidence level by means of Student's t tables (Table 3.3).

Table 3.3. Mass flow rate evaluation based on the video data processing.

Mass Flow Rate Evaluation					
Sample index	**Measured mass [g]**	**Start marking time [s]**	**End marking time [s]**	**Time interval [s]**	**Sample mass flow rate [kg/h]**
1	0.624	59.91	68.30	8.39	0.2677
2	0.488	68.30	74.67	6.37	0.2758
3	0.415	74.67	81.94	7.27	0.2055
4	0.409	81.94	87.85	5.91	0.2491
5	0.500	87.85	94.80	6.95	0.2590
6	0.353	94.80	99.50	4.70	0.2704
7	0.501	99.50	107.49	7.99	0.2257
Standard deviation: 0.024 [kg/h]					
Mass flow rate (99[%] of confidence): 0.250 ± 0.028 [kg/h]					

In Table 3.3, the start and end marking times are referred to the videos recorded experimentally. The difference is the time interval used to estimate the sample mass flow rate:

$$\dot{\mathrm{m}}_{\mathrm{sample}} = \frac{\mathrm{m}_{\mathrm{sample}}}{\Delta \mathrm{t}_{\mathrm{sample}}} \tag{3.48}$$

The next step is to investigate whether the analytically and numerically predicted mass flow rates agree with the experimental values listed in Table 3.3.

3.5. Results and discussion

After determining the experimental mass flow rate, together with its uncertainty interval, the discrepancy between the pressure difference calculated by the analytical code and that predicted by CFD was investigated in the case of SSE. In particular, the Ansys Fluent commercial software based on the finite volume method was implemented to perform the numerical studies.

3.5.1. Modeling of the molten material transport dynamics in the last screw vanes

The validation was run in accordance with the following steps:

- A convergence test with respect to the analytical prediction of both the pressure profile and mass flow rate is performed; the latter is also compared with the experimental prediction, as presented in Table 3.3,
- The melting length, namely, the compression zone length, which is required for the completion of the melting process, is evaluated,
- The portion of the compression zone where the material can be considered completely molten is analyzed numerically, and
- The analytically and numerically predicted pressure profiles are compared to evaluate the relative error.

The first step is the convergence analysis of the analytical code. As stated earlier, the MATAB code can be used to estimate both the mass flow rate and pressure profile iteratively. The compression zone of the two-stage Noztek Pro single-screw extruder must be discretized in a given number of axial steps. The goal is to determine the minimum number of discretized elements that can reach a relative error of less than 1[%]. The reference value for computing the relative error is the value of the target variable at the maximum number of discretized elements (275 in this study). The results of this preliminary study are exhibited in Figure 3.13.

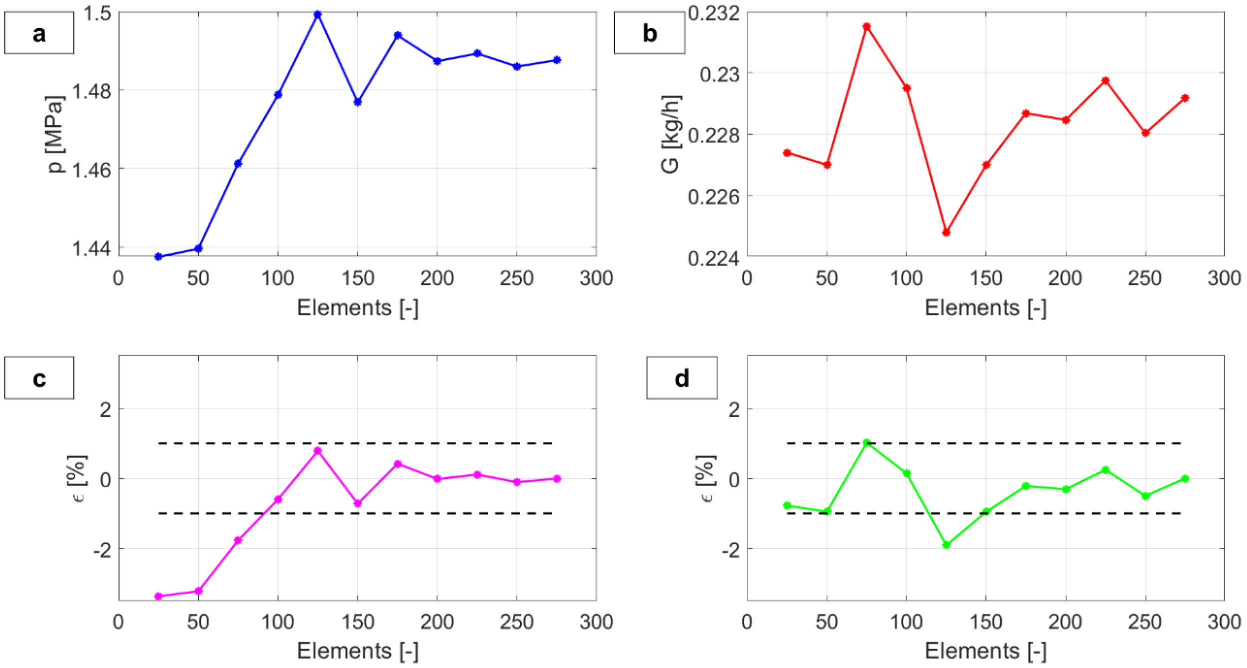

Figure 3.13. a.) Analytically predicted pressure increase as a function of the number of discretized elements; b.) behavior of the mass flow rate; c.) relative error on pressure increase prediction; d) relative error on mass flow rate increase.

The minimum number of discretized elements required to obtain a relative error below 1[%] is 150 (Figure 3.13). The pressure increase refers only to the portion of the compression zone where the thermoplastic material is completely molten, and this zone is also studied numerically to validate the results in terms of pressure. The convergence value of the mass flow rate is 0.227 [kg/h], and the corresponding relative pressure increment is 1.4768 [MPa]. Both results refer to the optimal discretization (150 elements). The predicted mass flow rate is in good agreement with the experimental mean value indicated in Table 3.3. The relative error is 9.34[%], and the analytically predicted mass flow rate value falls within the uncertainty interval being reported.

Moreover, the analytical code allows the prediction of the solid bed profile along the compression zone (Figure 3.14).

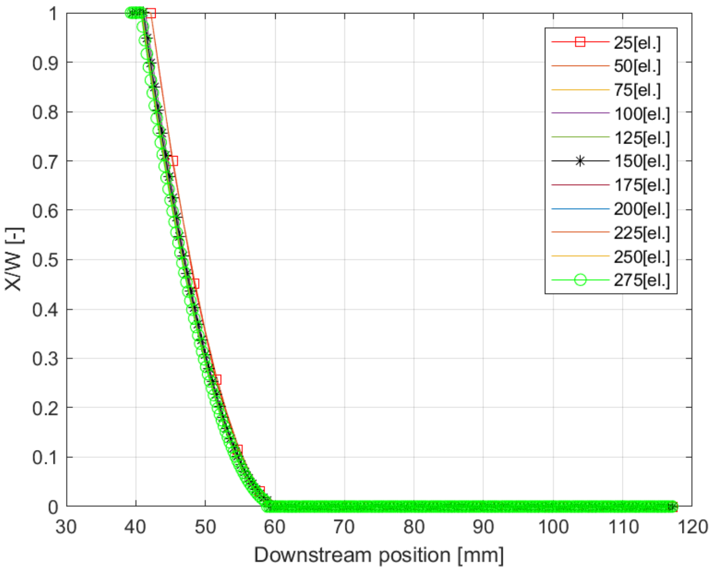

Figure 3.14. Solid bed profile along the compression zone for different numbers of discretized elements. Circular marked red lines, star marked black lines, and square marked green lines refer to the smallest, optimal, and largest number of elements simulated. X: solid bed width; W: channel width..

By processing the results, the portion of the compression zone filled with molten material can be computed. It was found that 57.77 [mm] is occupied by the molten material, while the length of the entire compression zone is 78 [mm]. Only the portion where the material was completely molten was modeled. The assumptions used in the CFD study are the following:

- The fully molten flow is incompressible, stationary, and laminar,
- No-slip condition exists at both barrel– and screw–polymer interfaces, and
- Motion is given to the barrel (reverse kinematics conditions).

The analytically predicted mass flow rate was then implemented as the inlet boundary condition for the CFD study, and a mesh independence test was conducted first. The calculations were performed using a structured computational grid.

Figure 3.15 shows the channel geometry and a sample mesh, together with a full description of the boundary conditions.

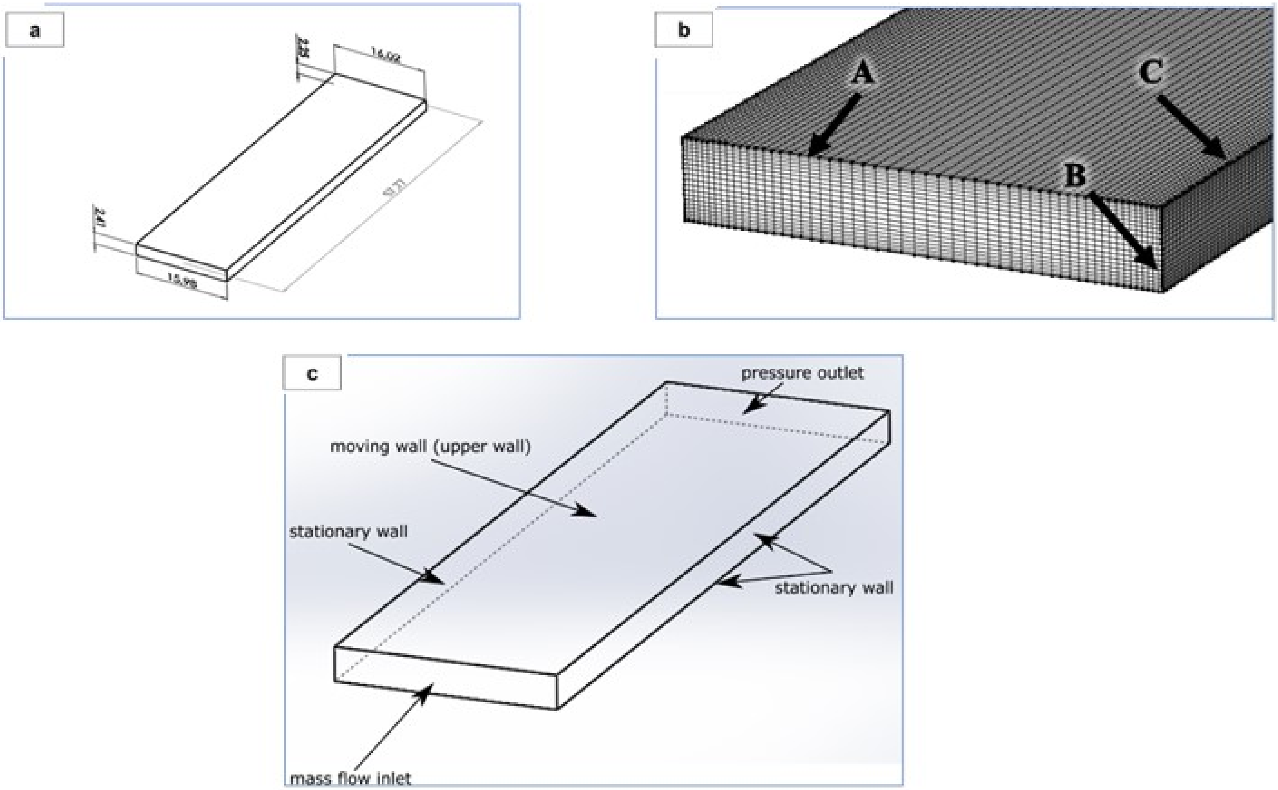

Figure 3.15. a.) Control volume for CFD simulations. b.) A sample mesh with the edges along which the number of nodes has been gradually increased; A: width direction; B: height direction; C: down-channel direction. c.) Boundary conditions for CFD simulations.

The mesh was refined near all the physical walls (Figure 3.15 - b) to obtain a suitable number of grid nodes in the boundary layer regions where higher gradients are expected. The details of the mesh independence tests results are given in Figure 3.16.

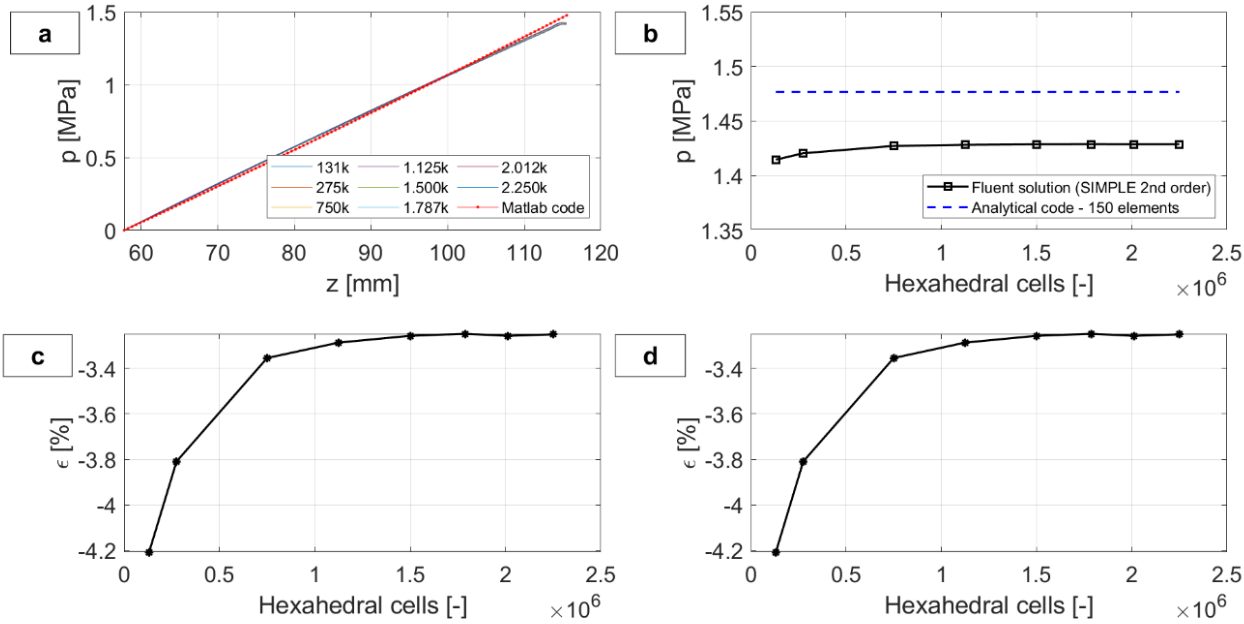

Figure 3.16. a.) Relative pressure profile along the down-channel direction predicted analytically and numerically at different mesh resolutions and only for the completely molten region; b.) comparison with the Fluent solution; c.) relative error of the analytical solution with respect to CFD; d.) relative error of the CFD results with respect to the finest mesh results (mesh indepence test).

The results of this test and a comparison with analytically predicted axial pressure profiles are presented in Table 3.4.

Table 3.4. Parameters and results of the numerical mesh independence test for last screw vanes.

Mesh index	Nodes along A	Nodes along B	Nodes along C	Total hexahedra	Numerically predicted pressure [MPa]	Analytically predicted pressure [MPa]	Relative error [%]
1	35	15	250	131.000	1.4136	1.4768	4.28
2	25	20	250	250.000	1.4196		3.89
3	40	75	250	750.000	1.4258		3.45
4	50	90	250	1.125.000	1.4268		3.38
5	60	100	250	1.500.000	1.4272		3.35
6	65	110	250	1.787.000	1.4274		3.34
7	70	115	250	2.012.000	1.4272		3.35
8	75	120	250	2.250.000	1.4274		3.34

The numerical prediction of the pressure increase shows a good agreement with the analytical one. This is true not only for the overall pressure increase, but also for the intermediate pressure values. In fact, Figure 3.16 - a shows that the pressure increases linearly along the down-channel direction, as documented in other works (e.g., [95,96]).

The physical reason for this little discrepancy between the analytical and numerical overall pressure difference (Table 3.4) relies in a different inlet boundary condition; while in the analytical code the flow is assumed as fully developed in the streamwise direction, which is also representative of the real fluid flow, a constant velocity has been imposed in the CFD simulations. Therefore, the flow profile in CFD needs to develop, leading to partially incorrect (and lower) pressure differences, no matter of the mesh resolution.

3.5.2. Modeling of the flow through the coupling element and nozzle

Having determined both analytically and numerically the pressure profile throughout that portion of the compression zone where the material is completely molten, the last point is to validate the pressure drop that occurs through the remaining two sections of the extrusion system, namely, the coupling element and nozzle. The goal is to evaluate the overall pressure drop along these two elements and determine its relative error with respect to the analytical solution. The approach is very similar to that previously described for the compression zone: a given value of the mass flow rate is imposed as the inlet boundary condition for the CFD simulations, and the pressure drop is validated against the analytically predicted value. Moreover, a mesh independence test is mandatory, as in the analysis of the compression zone. The assumptions made in the CFD simulations are the following:

- The fluid flow is incompressible and stationary,
- 2D axial symmetry is implemented,
- Temperature in the nozzle is held constant; its value is T_b,
- Swirl motions induced by the screw tip are disregarded, and
- No-slip condition exists at both the barrel– and screw–polymer interfaces.

The mass flow rate used as the inlet boundary condition was the value predicted by the analytical code after the convergence study, namely, 0.227 [kg/h]. A set of unstructured meshes was implemented to perform the mesh independence test. Additional details on the number of elements and the discrepancies with respect to the analytical results are listed in Table 3.5.

Table 3.5. Parameters and results of the numerical mesh independence test for the coupling element and nozzle.

Mesh index	Mesh name (COMSOL)	Number of cells	Numerically predicted pressure [MPa]	Analytically predicted pressure [MPa]	Relative error [%]
1	Coarse	3098	1.832	1.881	-2.665
2	Normal	4863	1.839		-2.297
3	Fine	8836	1.849		-1.760
4	Finer	20659	1.863		-1.000
5	Extra fine	48251	1.872		-0.481
6	Extremely fine	93755	1.883		0.091

The results of the test are also displayed in Figure 3.17.

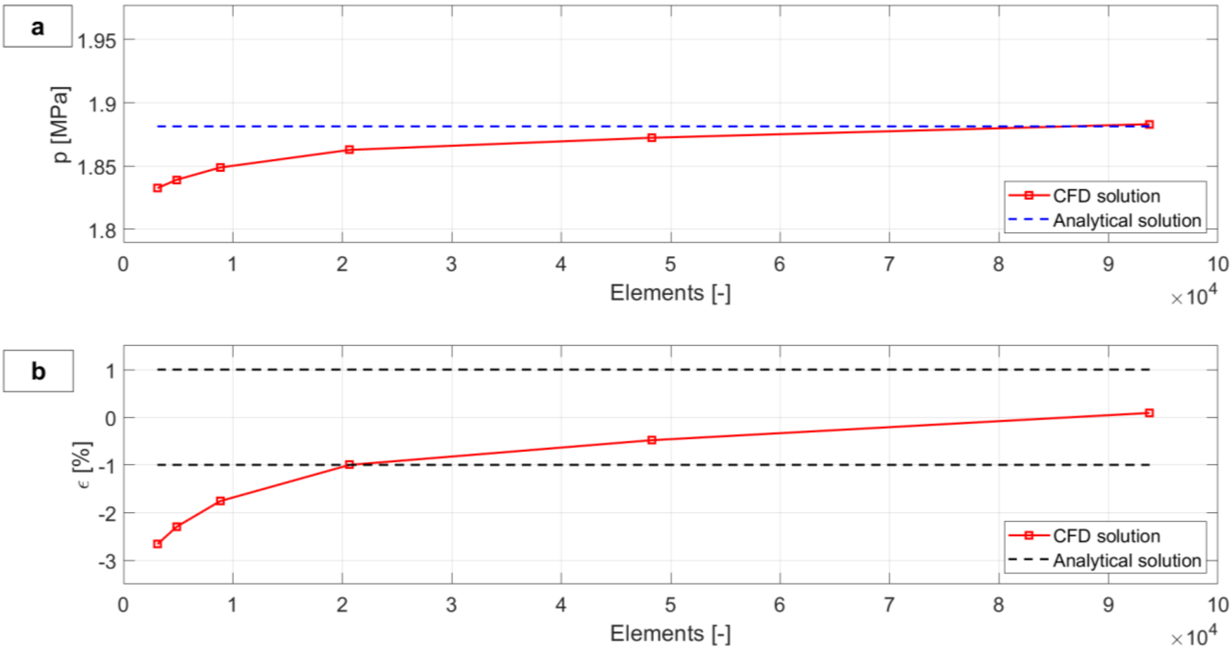

Figure 3.17. a.) Total pressure drop as a function of the number of finite elements; b.) relative error in pressure drop prediction.

3.5.6. Application to PAM process modeling; study of the m-control

The previous validations indicate the correctness of the mathematical modeling of the N-control, when dealing with SSE process.

When dealing with PAM, the main difference with classical SSE models lies in the deposited strand; when the molten material passes through the nozzle, then it encounters the surrounding air and begins to expand (Barus effect). Then the strand is deposited on the built-plate because of both gravity and pressure built-up being generated along the screw-barrel system. The strand begins to exchange heat by conduction at contact surfaces with nozzle, built-plate and other strands (if one looks to the next deposited slices), and by both convection and radiation with air [97]. The cross-sectional strand shape changes from a circular to an oblong one, when layer height is lowered. Lower layer heights are of interest, because the contact area between adjacent stands increases, leading to a better bonding and lower void content. In theory, the ideal situation would be that of a rectangular cross-section, and it was used in all calculations.

For prescribed printing conditions (m-control), the mass flow rate is calculated directly by means of (3.46). The goal is to find the right value of the peripheral screw speed to deposit a layer with prescribed printing parameters, that are strand width (W_{bead}) and height (t) at a given printing speed (V_p).

The influence of the deposited strand on the screw peripheral speed, pressure, and melting profiles was investigated with respect to both the layer height and printing speed. In all calculations, the extrusion temperature was assumed to be equal to that of the nozzle and barrel. In real extrusion conditions, there is a temperature gradient from the nozzle outlet to the build plate through the extruded layer; however, the previous assumption is justified by two main considerations:

- The molten polymer has a low thermal conductivity, and

- The solidification process is not immediately observed under the extrusion nozzle during the deposition process.

The latter process proceeds only when the layer is subjected to both the build plate temperature and room temperature. The abovementioned considerations justify the use of the nozzle temperature in further computations.
Both the layer height and printing speed are varied on three levels, according to Table 3.6.

Table 3.6. Operating parameters being varied in PAM deposition.

Parameter name	**Symbol**	**Value**
Printing speed	V_p	1 [mm/s]
		5 [mm/s]
		10 [mm/s]
Layer height	t	0.4 [mm]
		0.8 [mm]
		1.2 [mm]

The corresponding mass flow rate values are reported in the following Table 3.7:

Table 3.7. Mass flow rate in operating PAM extrusion conditions ($W_{bead} = 1.2\ D_{ext}^{(n)}$).

Simulation index	$\mathbf{V_p\ [mm/s]}$	$\mathbf{t[mm]}$	$\dot{\mathbf{m}}\ \mathbf{[g/h]}$
1	1	0.4	2.87
2	5	0.4	14.38
3	10	0.4	28.75
4	1	0.8	5.75
5	5	0.8	28.75
6	10	0.8	57.51
7	1	1.2	8.63
8	5	1.2	43.13
9	10	1.2	86.26

As can easily be seen from previous table, mass flow rate increases with both layer height and printing speed, because of mass flow rate conservation (3.46).
The corresponding peripheral screw speed are depicted in Figure 3.18.

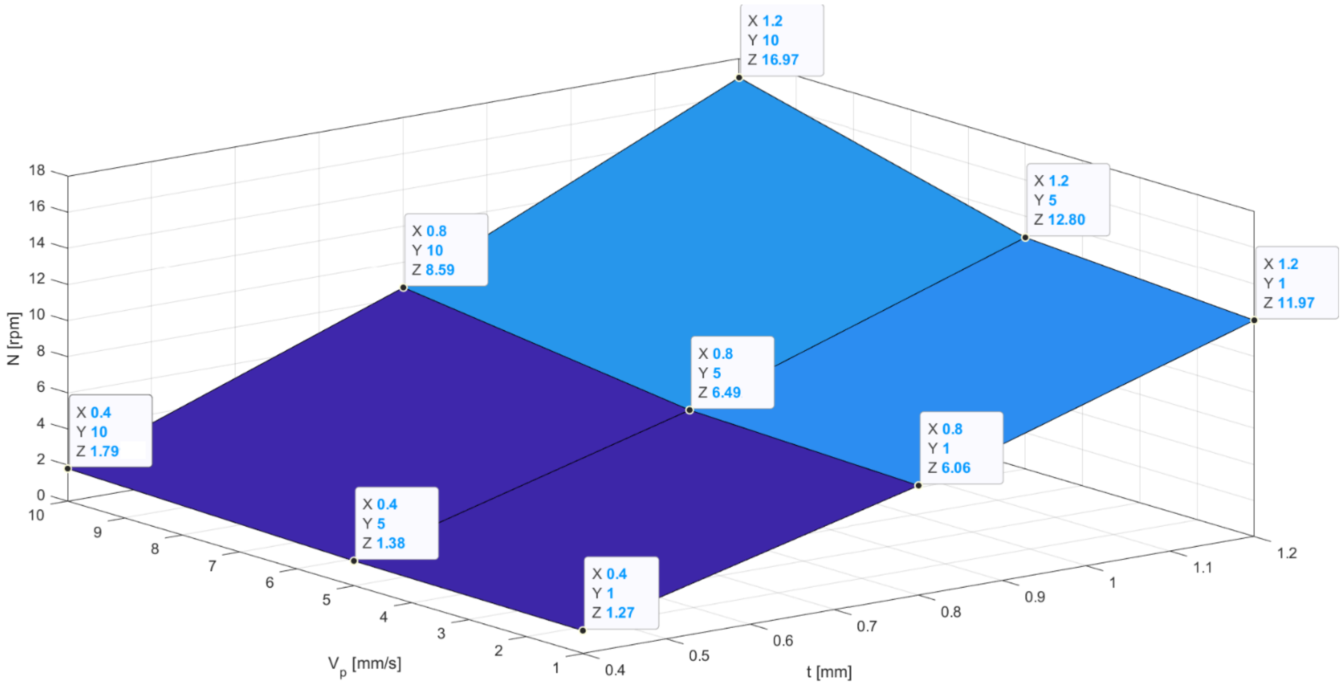

Figure 3.18. Peripheral screw speed as a function of layer height and printing speed.

The peripheral screw speed increases with the layer height and printing speed; this is coherent with the fact that mass flow rate increases with both parameters (Table 3.7): to extrude a higher mass flow rate, it is mandatory to increase the peripheral screw speed.

The same trend can be observed through the analysis of the PAM extrusion pressure profiles for different parameter configurations. The variation with respect to the layer height is clearly visible in Figure 3.19.

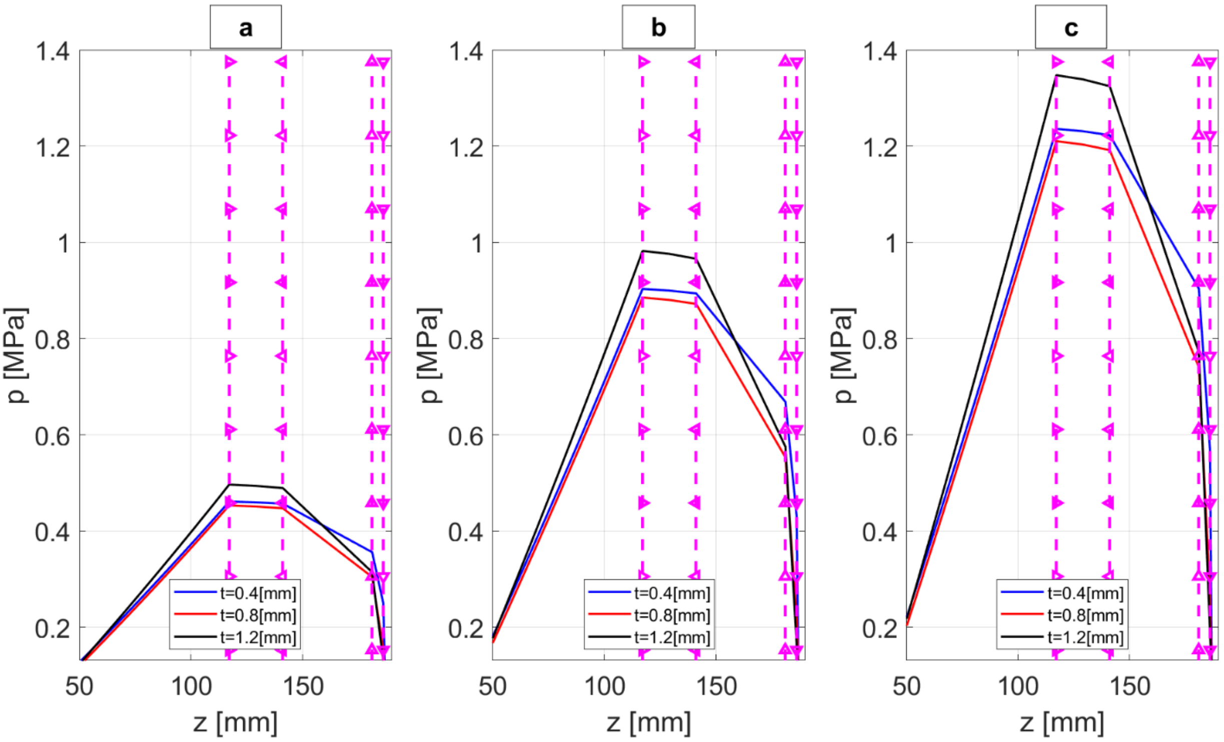

Figure 3.19. Pressure profiles at different layer heights for a.) V_p = 1 [mm/s], b.) V_p = 5 [mm/s], and c.) V_p = 10 [mm/s]. Right-pointing triangle markers: screw end; Left-pointing triangle markers: coupling element end; Upward-pointing triangle markers: nozzle tapered section end; Downward-pointing triangle markers: nozzle capillary section end.

In previous figure, it can be observed that higher pressures develop along the screw extruder, when dealing with higher layer height (fixed printing speed); this is due to the higher mass flow rate being requested (Table 3.7).

The pressure profile dependence upon the printing speed is better illustrated in Figure 3.20.

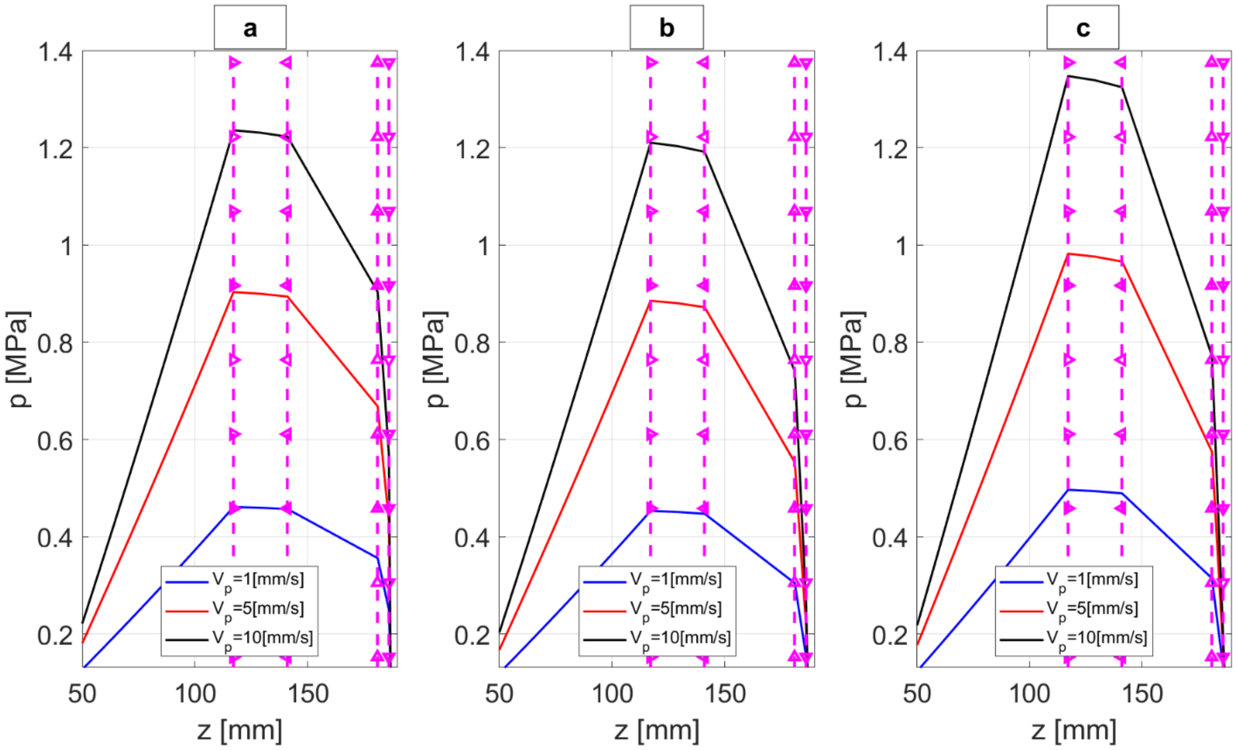

Figure 3.20. Pressure profiles at different printing speeds for a.) t = 0.4 [mm], b.) t = 0.8 [mm], and c.) t = 1.2 [mm]. Right-pointing triangle markers: screw end; Left-pointing triangle markers: coupling element end; Upward-pointing triangle markers: nozzle tapered section end; Downward-pointing triangle markers: nozzle capillary section end.

In Figure 3.20, a similar pattern is found, when higher printing speeds are considered (for fixed layer height), for the same reason.

About the counterpressure that develops in the deposited strand, the following figure shows how it varies with operating parameters:

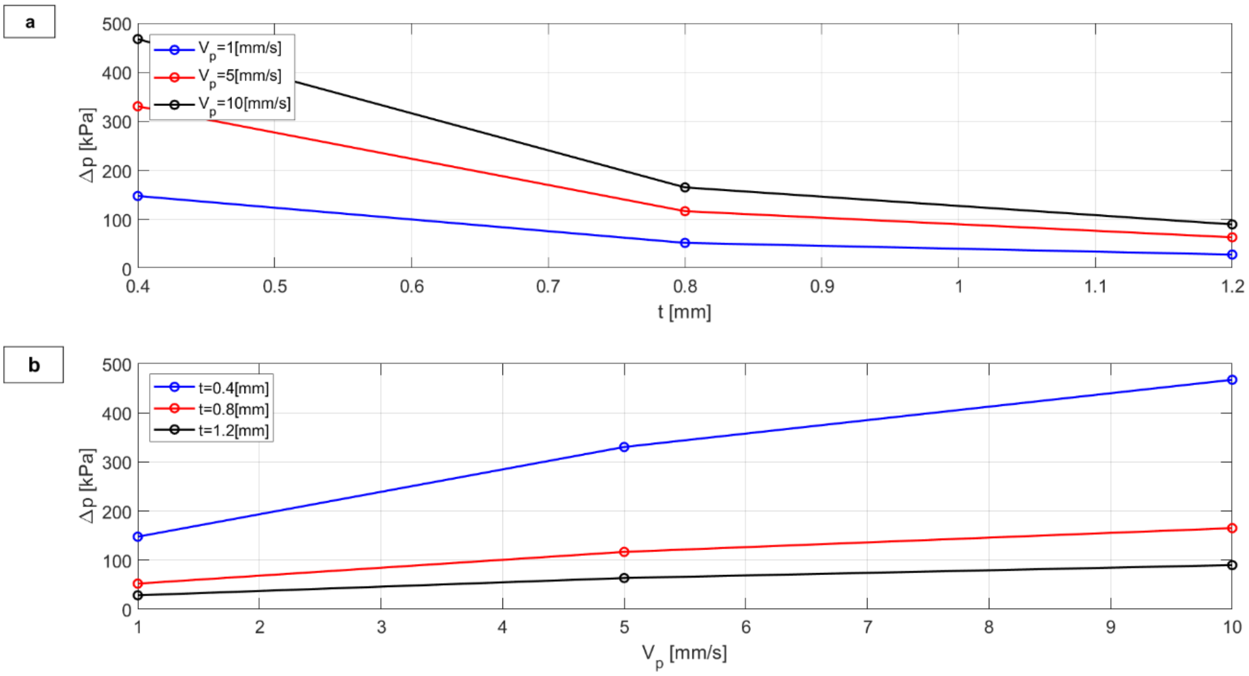

Figure 3.21. Pressure profiles at different printing speeds for a.) t = 0.4 [mm], b.) t = 0.8 [mm], and c.) t = 1.2 [mm].

The counterpressure increases with printing speed, while decreasing with layer height. Both trends were first described for FFF in [85]; they remain unchanged when it comes to PAM extrusion modeling, when dealing with the m-control.

Finally, the melting profile is considerably affected by the lower layer height at all printing speeds, as shown in Figure 3.22.

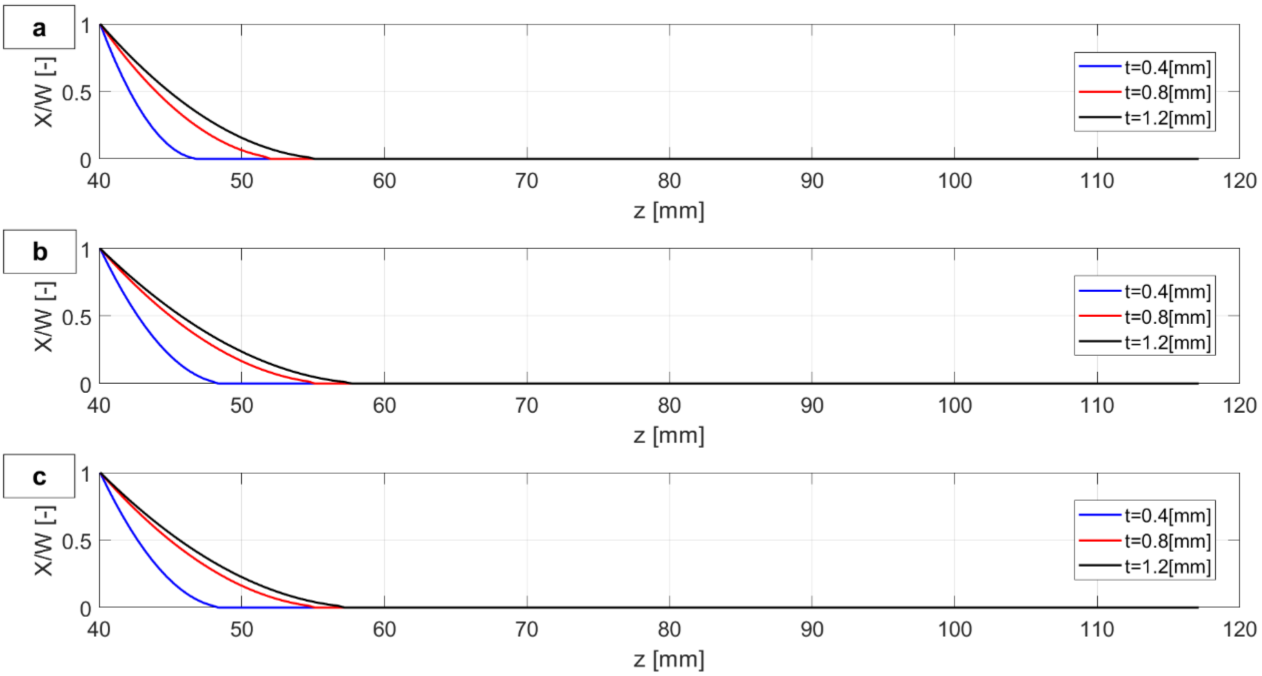

Figure 3.22. Solid bed profile as a function of the down-channel position along the compression zone when a.) $V_p = 1$ [mm/s], b.) $V_p = 5$ [mm/s], and c.) $V_p = 10$ [mm/s].

The results, as a function of printing speed, are better illustrated in Figure 3.23.

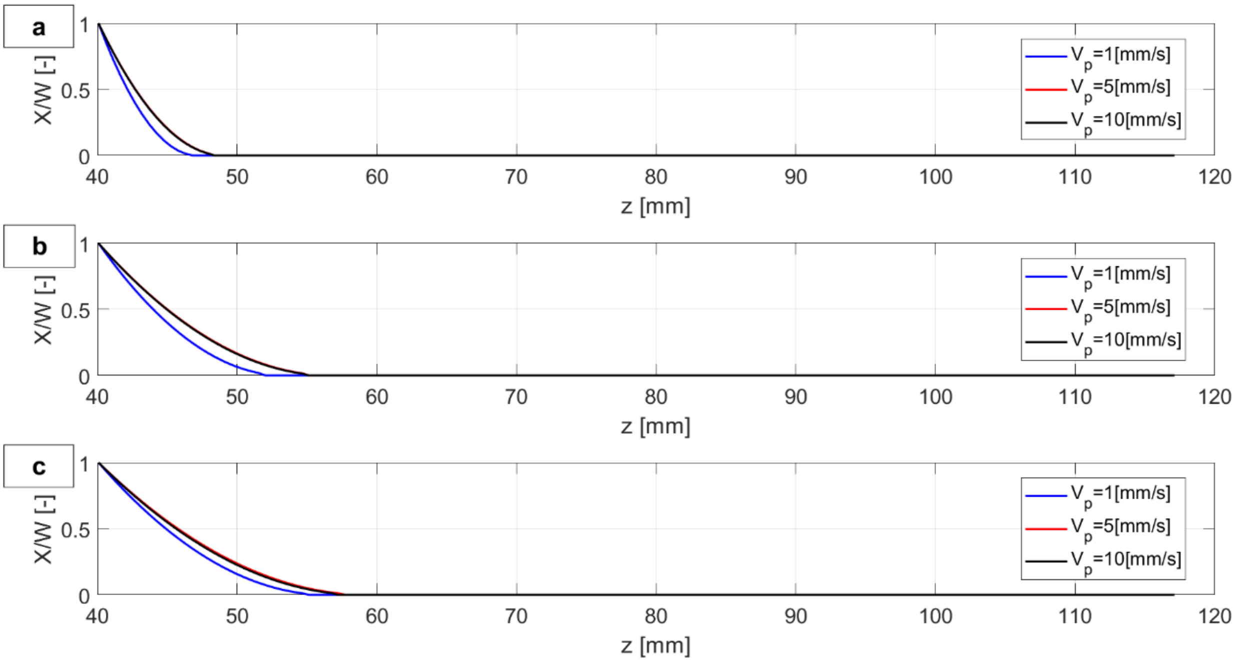

Figure 3.23. Solid bed profile as a function of the down-channel position along the compression zone when a.) t = 0.4 [mm], b.) t = 0.8 [mm], and c.) t = 1.2 [mm].

From Figure 3.23, there is a lower dependence of the melting profile on the printing speed.

An increase in the melting length is observed when larger layer heights and printing speeds are considered. The melting spatial delay can be explained as follows. Increasing the layer height for a given printing speed allows the extrusion of higher flow rates; as a consequence, the peripheral screw speed has to increase too. Therefore, the mean flow speed is higher and melting occurs further downstream. A similar trend can be found in [95,96], where it is shown that increasing the peripheral screw speed increases the mass flow rate and give a spatial melting delay; this is fully coherent with the findings of the PAM m-control logic.

Similarly, increasing the printing speed for fixed operating parameters, produces a rise in mass flow rate. Screw-speed grows in a way which allows to extrude that given amount of mass flow rate. For that reason, the behavior at higher printing speed is very similar to that of layer height; the underlying physical reason for the spatial melting delay is the same.

3.6. Conclusions

In this Chapter, the mathematical formulation usually followed when dealing with SSE process has been extended to one of the most promising MEX techniques, that is the PAM.

Because of the hybrid nature of the PAM, combining both aspects of SSE (the screw-barrel system) and the widespread FFF (the deposited strand), the control logic must be changed. While in SSE it is possible to prescribe the peripheral speed and to find the mass flow rate (N-control) the opposite applies to PAM (m-control). Latter logic allows to print strands with prescribed geometrical characteristics, at a given printing speed.

At first, a model aimed at describing the classical SSE process (N-control), together with a simple procedure for its experimental and numerical validation, is presented. The main outcomes of the N-control iterative calculation model are:

- melting profile,
- mass flow rate, and
- pressure profile.

The latter two were evaluated after each iteration and were found to be strongly related. In fact, the iteration process stops when the final pressure, evaluated at the nozzle exit (SSE modeling), approximately reaches the atmospheric value. The corresponding mass flow rate is the convergence value. Moreover, both experimental and numerical validations were conducted for SSE, starting from the mass flow rate predicted by the analytical model for the ABS MFI-22 material. The deviation of the analytical value with respect to the experimental value is approximately 9.34[%]. This is mainly because of the assumptions implemented in the mathematical formulation. Among them, it must be recognized that the extrusion temperature can locally deviate from the value set through the proportional–integral–derivative controller. Therefore, both the rheological and thermodynamic material parameters are subject to gradual variations in the operating temperature range. This aspect was disregarded, and the thermodynamic properties were evaluated only in the solid and molten phases.

The analytical formulation was then extended to PAM extrusion (m-control). A model aimed at describing the influence of two of the main operating parameters that differ between PAM and SSE, namely, printing speed and layer height, was formulated.

The main outcomes of the m-control iterative calculation model are:

- melting profile,
- mass flow rate, and

- pressure profile.

It was shown that the peripheral screw speed increases with both layer height and printing speed, because of the higher mass flow rate being requested.

A reduction in overall pressure profile is a natural consequence of the lower layer heights, because of the lower mass flow rate being extruded.

About the counterpressure, it has been found that it increases with printing speed, while decreasing with layer height; these trends are fully coherent with the ones being documented in [85].

Moreover, the melting profile exhibit a distinct dependence on the two printing parameters; when higher values are considered, a spatial melting delay occurs, because of the increase in mass flow rate (following from mass conservation, (3.46)).

Further work will be dedicated to a more extensive validation of the mathematical model. The goal is to apply the code to other PAM screw models and to test other materials and rheological models (in particular, the Cross-WLF, which is one of the most widely used for thermoplastic materials). To be said, a more advance mathematical model for the description of the fluid flow of a Cross-WLF fluid in a nozzle has been recently introduced in [98] and further details will be given in Chapter 5.

Furthermore, the local variation of material properties will be accounted for.

4. A non-Newtonian, non-isothermal and three-dimensional CFD model of strand deposition in PAM

4.1. Chapter organization

In this Chapter, CFD has been applied to study the effect of process parameters on the geometrical characteristics and thermal distribution of the first layer deposited in PAM; the influence of non-dimensional layer height, printing speed and nozzle temperature has been investigated.

This was achieved by means of non-Newtonian, non-isothermal and multiphase three-dimensional simulations. The Volume-Of-Fluid (VOF) surface-tracking algorithm was implemented to track the interface between air and molten polymer.

For the first time both the screw-based extrusion mechanism and thermal effects have been taken in account; in existing literature similar comprehensive studies were done only for FFF.

Validation has been performed by means of a small-scale PAM extruder, manufactured by Direct 3D.

In Section 4.3 the main CFD studies for FFF and PAM have been briefly described. The material properties were introduced in Section 4.4.1. The experimental setup has been detailed in Section 4.4.2, and the values assigned to the process parameters have been explicitly stated. In Section 4.4.3 full details about the multiphase simulations are given. The mesh-independence study has been outlined in Section 4.4.4. The effect of process parameters on extruded mass flow rate is investigated in Section 4.5.1; then, the effect of dimensionless parameters on strand morphology and temperature distribution has been explored in Section 4.5.2 and 4.5.3, respectively. Finally, conclusions have been outlined in Section 4.6.

4.2. Chapter nomenclature

A_1	Second data-fitted coefficient	T_n	Nozzle temperature
A_2	Third data-fitted coefficient	u_m	Mean velocity in the nozzle
A_s	Nozzle outlet cross-sectional area	V^*	Dimensionless speed
c_p	Heat capacity	V_p	Printing speed
D	Nozzle diameter	V_s	Tangential screw speed
D_1	First data-fitted coefficient	W_{max}	Maximum layer width
$fr\%$	Flow rate (percentage)	X^*	Dimensionless X coordinate
h	Layer height	Y^*	Dimensionless Y coordinate
H^*	Dimensionless layer height	Z^*	Dimensionless Z coordinate
$\dot{m}$	Mass flow rate	$\dot{\gamma}$	Shear rate
N	Screw peripheral speed	η	Dynamic viscosity
n	Power-law index	η_0	Zero-shear viscosity
T	Temperature	λ	Thermal conductivity
T^*	Dimensionless temperature	ρ_m	Molten phase density
T_b	Plate temperature	ρ_s	Solid phase density
T_g	Glass transition temperature	τ^*	Fourth data-fitted coefficient

4.3. Introduction

The first CFD studies in the framework of AM were dedicated to FFF; the main works are briefly described, because they are the basis for PAM extrusion modeling. In [89] the strand morphology has been analysed at varying layer height and printing speed; this work was later experimentally validated in [99]. The numerical investigation was extended in [100,101] to study the corner MEX according to different strategies.

Moreover, in [102,103] the interlayer contact between deposited strand has been studied, yet disregarding the filament coalescence; in addition, the influence of temperature has been neglected. A different approach for single strand deposition was proposed in [104], where an improvement of the results of [89] is found by considering the energy equation. The successive layer deposition has been simulated in [105,106], to predict the cooling time and inter-layer contact area. In [107] both single and multi-layer deposition in FFF, together with a study of the solidification process are presented, under the assumption to consider a Newtonian fluid.

Other works [108,109] have investigated the strand deposition through non-conventional nozzles: it resulted that by using a square or a star-shaped cross-section, the deposited strand features a higher inter-layer contact surface (cuboid-like shape) shared with contiguous printed strands, which brings to better bonding and less process-induced voids.

More recently, CFD has proved as a powerful tool to study PAM process. Some of the main perspectives are the prediction of final part properties, manufactured both with net and composite materials, and the individuation of the optimal process parameters [110].

In [111] the strand deposition for different rheological models was simulated: the most important aspect which affects strand morphology in PAM is the inclusion of the shear-thinning behavior in simulations.

In [112] the effect of successive layer deposition has been studied with a remeshing technique performed via the COMSOL-MATLAB LiveLink [113]. Despite the authors propose a 2D simulation, it gives important insights in layer coalescence, through non-isothermal simulations. Moreover, a good agreement with optical micrographs is shown. Thermodynamic aspects related to reheating of the deposited strand caused by the heated nozzle have been addressed in [114]; here, heat transfer has been coupled with fluid flow equations and studied numerically. Infrared thermography provided a very good correspondence with FEM predictions.

In this Chapter the strand deposition in PAM extrusion has been investigated with both experiments and CFD simulations. A Direct 3D pellet extruder has been used to print consistent layers under different values of the most critical printing parameters, that are the non-dimensional printing speed, layer height, and nozzle temperature.

It should be mentioned that in the LFAM the nozzle outlet diameter can be also ten times greater than in FFF; the present study focuses on the mesoscale between the dimensions typical of FFF and LFAM (nozzle diameter: 1.2 [mm]).

4.4. Materials and Methods

In this section, the relevant material's properties have been introduced. Then, full details on experimental and CFD investigations were given.

4.4.1. Material

In this study, a particular grade of Polylactic acid (PLA) manufactured by NatureWorks (NatureWorks Ingeo 3251D) has been used to investigate the first layer deposition on a heated built plate with a PAM extruder. The material is initially given in the form of almost spherical pellet of around 3 [mm] diameter.

The parameters involved in CFD simulations are:

- Rheological properties:
  - Dynamic viscosity, which is a function of both temperature and shear rate, $\eta(T;\ \dot{\gamma})$, and
  - Glass transition temperature, T_g.
- Thermophysical properties:
  - Density at solid (ρ_s) and molten (ρ_m) states,
  - thermal conductivity, $\lambda(T)$, and
  - heat capacity $c_p(T)$,

The Moldflow software (Moldflow Plastics Labs. Ithaca, NY 14850, USA) was used to collect the rheological and thermophysical material properties needed in simulations.
The dynamic viscosity $\eta(T;\ \dot{\gamma})$ follows the Cross-WLF model:

$$\eta = \frac{\eta_0}{1+\left(\frac{\eta_0\dot{\gamma}}{\tau^*}\right)^{1-n}} \tag{4.1}$$

Here η_0 is the zero-shear viscosity:

$$\eta_0 = D_1 e^{-\frac{A1(T-T_g)}{A2+(T-T_g)}} \tag{4.2}$$

Former parameters are detailed in Table 4.1:

Table 4.1. Rheological parameters for Ingeo 3251D.

Symbol	**Parameter name**	**Value**
D_1	First data-fitted coefficient	2.045E+07
A_1	Second data-fitted coefficient	16.71
A_2	Third data-fitted coefficient	51.60 [K]
T_g	Glass transition temperature	373.15 [K]
n	Power-law index	0.3846
τ^*	Fourth data-fitted coefficient	1.29E+05

Thermal conductivity and heat capacity have been represented in Figure 4.1, together with the indication of the test standards:

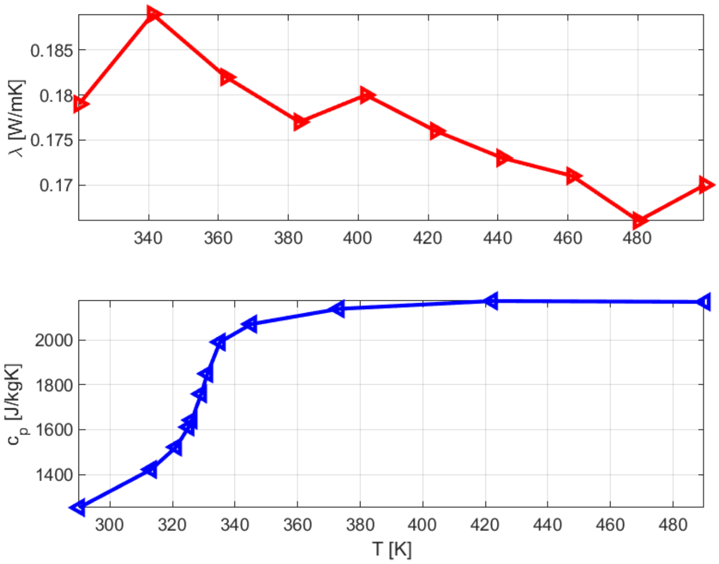

Figure 4.1. Thermal conductivity (ASTM D5930) and heat capacity (ASTM E1269).

About density, it has been assumed a linear transition between the solid (ρ_s=1195.5 [kg/m^3]) and molten (ρ_m= 1050.1 [kg/m^3]) values, in CFD computations.

4.4.2. Experimental investigations

A Direct 3D PAM extruder (Direct 3D s.r.l.) has been employed to study the first layer deposition under a wide set of process parameters.

The extruder consists of a constant pitch screw placed inside a heated barrel. At first, the pelletized material is conveyed in a hopper. Then, it is gradually heated above T_g. Finally, the molten polymer is extruded through a nozzle, to be deposited layer-by-layer, as in conventional FFF.

The mechanical torque is provided by a Nema17 HS4401 stepper motor, to be delivered to the vertical screw by means of a timing belt (gear ratio 4:1).

The pressure starts to rise in the conveying zone, up to the last screw vanes. Then, pressure drops in the nozzle and deposited layer, up to the atmospheric value [115].

The most important extrusion parameters which impact layer deposition in PAM were nozzle outlet diameter (D), layer height (h), printing speed (V_p), flow rate ($fr\%$) and both nozzle (T_n) and built plate (T_b) temperatures.

To be said, for a given flow rate, the peripheral speed (V_s) is set; for that reason, it will be referred directly to the screw peripheral speed.

On this basis, the minimal set of non-dimensional parameters are:

- $H^* = h/D$,
- $T^* = T_n/T_b$, and
- $V^* = V_s/V_p$.

In all investigations, the printing speed and built plate temperature were fixed to 20 [mm/s] and 60 [°C], respectively. Moreover, the nozzle outlet diameter was 1.2 [mm].

Two nozzle temperatures (190 and 210 [°C]), two flow rate values (500 and 1000[%], that result in 30 and 60 [rpm], respectively) and three layer heights (0.3, 0.6 and 0.9 [mm]) have been examined.
A total of 12 investigations were carried out (Table 4.2):

Table 4.2. Full set of experimental dimensionless printing conditions.

Index	T^*	D^*	V^*	Index	T^*	D^*	V^*
1	3.15	0.25	0.95	7	3.5	0.25	0.95
2	3.15	0.25	1.89	8	3.5	0.25	1.89
3	3.15	0.5	0.95	9	3.5	0.5	0.95
4	3.15	0.5	1.89	10	3.5	0.5	1.89
5	3.15	0.75	0.95	11	3.5	0.75	0.95
6	3.15	0.75	1.89	12	3.5	0.75	1.89

The experimental workflow for a generic printing condition has been reported in Figure 4.2:

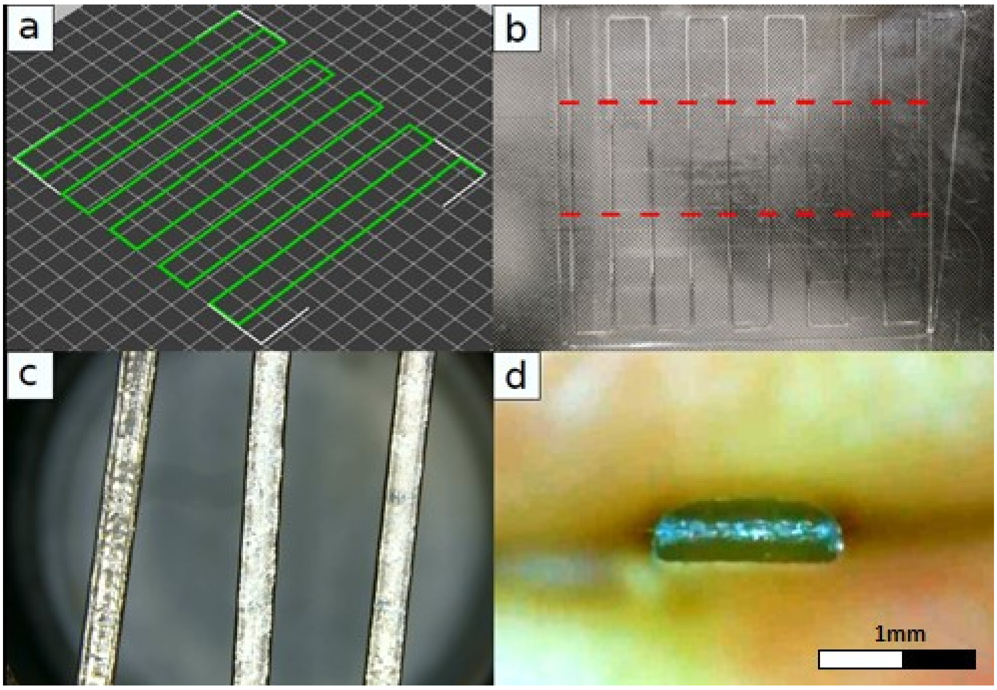

Figure 4.2. a.) GCode of the serpentine geometry; b.) Printed samples with indication of trim start and stop; c) trimmed samples at microscope; d.) Best sample cross-section.

At first, a serpentine geometry was printed in each experimental condition (Figure 4.2 – a): a total of 10 straight layers were cut (Figure 4.2 – b) and their widths were analyzed to provide replications (Figure 4.2 – c); a Tomlov DM11 7’’ optical microscope was used for investigating strands’ geometries.
For a given printing condition, the mean and standard deviation of strand width were estimated, together with the coefficient of variation (COV): a low COV (<10) was found in all printing conditions, which confirmed the consistency of first strand deposition.
Then, the relative deviation of each strand width from mean value was calculated, to find the best one; its cross-section (Figure 4.2 – d) was observed through the Tomlov microscope.

The cross-sectional area (A_s) was calculated with a MATLAB subroutine and the mean velocity in the nozzle calibration zone was evaluated by mass flow rate conservation from nozzle outlet to the deposited strand:

$$u_m = 4\frac{A_s}{\pi D^2}V_p\frac{\rho_s}{\rho_m} \tag{4.3}$$

The mean velocity values were the input boundary conditions for the computational studies.

4.4.3. Numerical investigations

The CFD analyses were performed with the commercial FVM software Ansys Fluent.

The computational domain consists of the nozzle calibration zone, the air gap between the nozzle outlet and built plate. The nozzle tip geometry was taken out from the original rectangular domain (Figure 4.3).

The screw tip was not included in the computational domain because it was proved that swirling motion does not influence the flow field, at least for net polymers [116].

A structured mesh with hexahedral elements was adopted; their number was gradually inflated near the nozzle outlet and built plate, to fully capture the local boundary layer regions.

For instance, the CFD modeling of the $D^* = 0.25$ case has been reported in Figure 4.3:

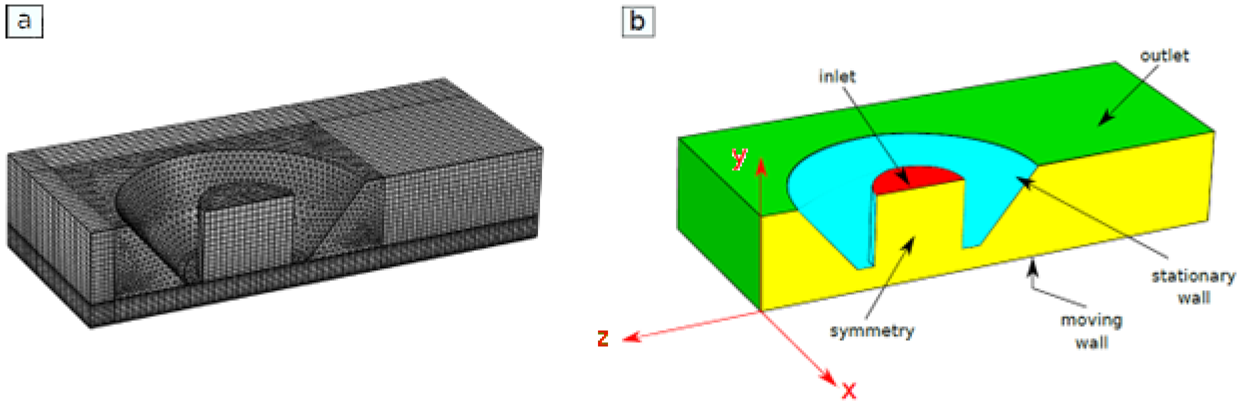

Figure 4.3. a.) Meshed domain with near-wall elements inflation and b.) boundary conditions and reference system.

Because of the symmetry boundary condition (plane yz), only half of the geometry was considered for CFD simulations, leading to a drastic reduction in computation time.

The modeling of flow deposition is three-dimensional, non-isothermal and aimed at capturing the non-Newtonian flow behavior. In fact, it has been shown that the most important factor which affects the shape of the deposited strand is the inclusion of the non-Newtonian behavior, instead of the actual rheological model [111].

The boundary conditions have been highlighted in Figure 4.3 – b. The printing speed (V_p) is assigned to the build plate instead of the nozzle, to avoid domain remeshing.

An implicit numerical scheme with interfacial anti-diffusion and implicit body force was adopted; the interface between the molten polymer and surrounding air was captured by means of the VOF method, because of its robustness in free-surface tracking. The VOF is based on the definition and pointwise evaluation of a non-dimensional scalar fraction function, whose value goes from zero to one, for air and PLA respectively.

The 3D interface is easily determined by the geometrical reconstruction of the mesh nodes where the fraction function is 0.5.

A second order upwind scheme was adopted to discretize momentum and energy equations, to lower numerical diffusion, while the compressive method was used for the continuity equation of the volume fraction of the VOF method.

Only the volume fraction threshold residual was lowered to 1E-06 (default value was 1E-05), to achieve a better approximation of the interface.

The time-stepping was automatically set to guarantee a Courant number of 0.25, so to enhance numerical stability. The overall study stops after finding the steady state extrudate profile.

After a mesh-independence study (Section 4.4.4), the experimental and numerical strand shapes were compared in all operating conditions.

4.4.4. Mesh-independence study

Before carrying out all CFD simulations, a first numerical study, aiming at finding the better mesh resolution was undertaken. To do this, two different resolutions (i.e., 50 and 60 [um]) were selected. Their numerical meaning is that of characteristic lengths of the hexahedral elements used in CFD meshes.

The simulations were performed on an Intel-Xeon E5-4620 CPU, with 8 physical cores.

In Figure 4.4 the comparison between the numerical and experimental strands is given:

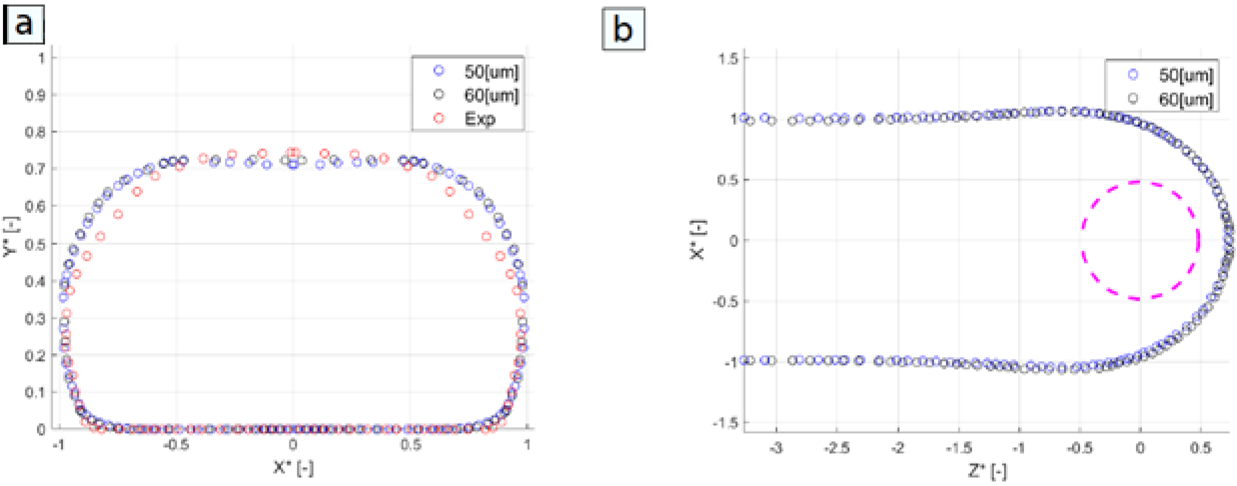

Figure 4.4. Mesh-independence study of a.) cross-sectional strand profile at the control volume outlet and b.) extrudate profile along printing direction (staggered magenta line indicates the nozzle exit shape, for comparison); Case study: Index 6 in Table 4.1.

For the sake of clarity, the cartesian coordinates have been reported in non-dimensional form, with respect to nozzle outlet diameter.

The strand cross-sectional profiles are very close to experiments, and there is no valuable difference between 50 and 60 [um] (Figure 4.4 – a). The same can be said with respect to the full three-dimensional extrudate shape (top view: Figure 4.4 – b); for that reason, the 60 [um] mesh resolution was selected for further analyses.

4.5. Results and discussion

In this section, the comparison between experiments and CFD in all extrusion conditions has been made.

Fluent has been widely used for this purpose, when dealing with sub millimetric nozzle diameters and conventional FFF [89,99].

In other works, a 2D approach has been detailed [116–119], to deal with screw-based MEX of reinformed thermoplastics. In [111] a 3D model has been proposed, but the study does not account for the effect of temperature, and it is limited to a single printing condition.
Instead, the interaction of the minimum set of non-dimensional parameters is here considered (Table 4.1): a full-factorial experimental and numerical design of experiment has been adopted for this purpose.

4.5.1. Mass flow rate

After finding the optimal mesh resolution (60 [um]), the CFD simulations were done with respect to all 12 experimental conditions reported in Table 4.2. The discrepancy between the experimental and numerically computed extrudate cross-sectional profiles was evaluated. Then, the effect of the abovementioned dimensionless processing parameters on the extrudate shape and temperature distribution has been explored.
The analysis starts with the mean inlet speed evaluation (4.3), calculated through the experimental measurement of cross-sectional areas. Then, the mean flow velocity in the nozzle calibration zone was used as inlet condition (Figure 4.3 – b) in CFD computations.
A difference with conventional FFF is that the layer width set in the slicing software is different from that found experimentally (Figure 4.6); this is caused by the operating mechanism of the Direct 3D PAM extruder, where the flow rate percentage directly controls the screw rotation, and so the mass flow rate.
For completeness, it should be mentioned that a second control logic consists in setting the right screw speed to print a layer with prescribed height and width (see: Chapter 3).
Instead, in FFF the mass flow rate calculation is straightforward; for prescribed layer height and width, mass flow rate can be evaluated by 1D continuity principle.
Before proceeding with the investigation of CFD results, the effect of nozzle temperature, layer height and screw speed on mass flow rate has been discussed (Figure 4.5).

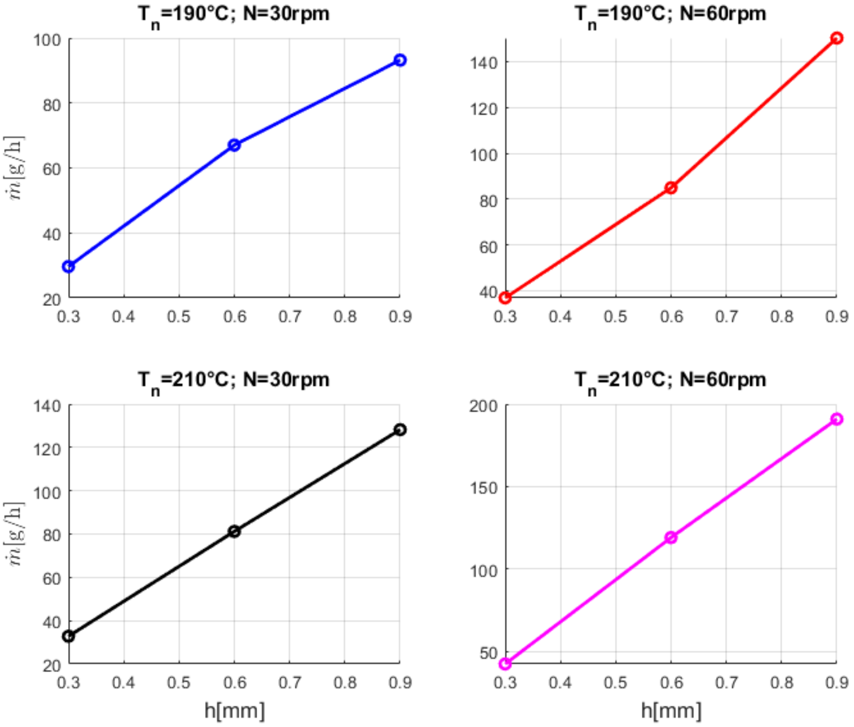

Figure 4.5. Mean extruded mass flow rate ($\dot{m}$) at different values of the operating parameters.

At increasing layer heights, mass flow rate increases because of the lower counterpressure which develops in PAM extrusion.

The same trend applies for the nozzle temperature, but it is due to the lower viscosity in the nozzle calibration zone.

Mass flow rate increases with screw speed, no matter of the nozzle temperature and layer height. These experimental observations are fully coherent with the findings outlined in Chapter 3.

4.5.2. Strand morphology

In Figure 4.6 the comparison between numerical and experimental cross-sectional profiles has been done; X^* and Y^* are the reference system coordinates of Figure 4.3 made dimensionless with respect to nozzle outer diameter.

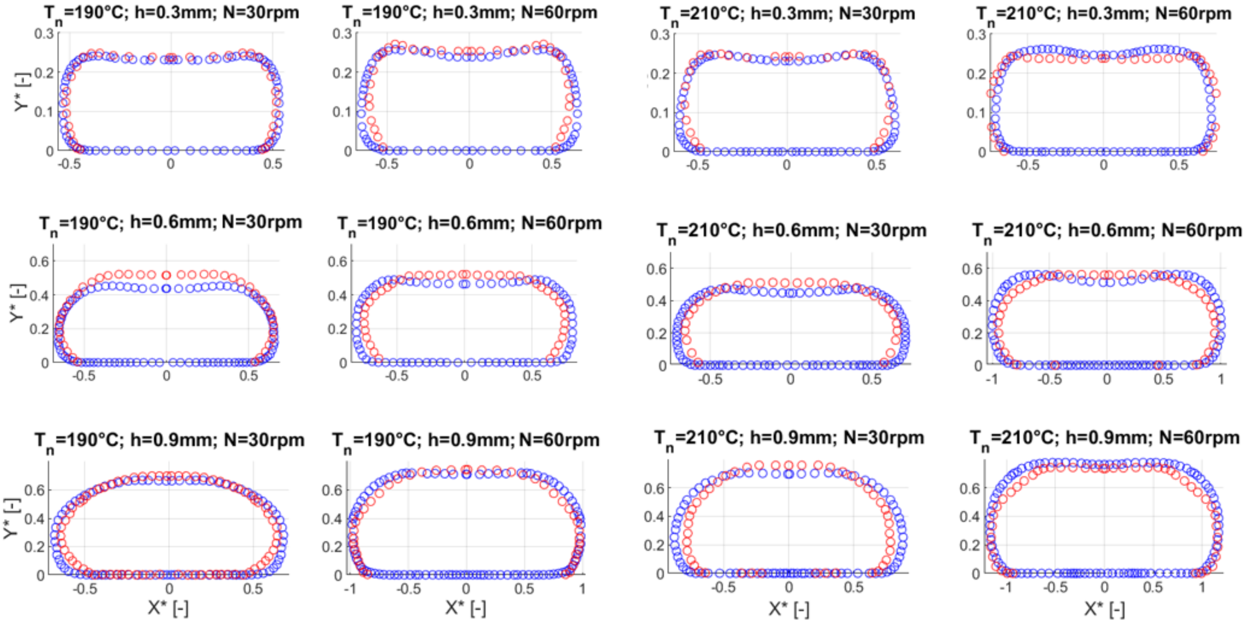

Figure 4.6. Experimental (red) and numerical (blue) cross-section profiles of the deposited strands at different processing conditions (see: Table 4.1).

Overall strand shape is fully captured by the chosen numerical setup. The maximum strand width in CFD is slightly lower than in experiments, especially at $h = 0.6$ [mm]. A possible reason can be related to having disregarded the elastic behavior of the thermoplastic being deposited.

By lowering D^*, a more oblong cross-sectional shape is found, which determines a broader interface for thermal diffusion, which is necessary to create strong inter-layer bonds.

On the other hand, the circular-like shape which arises at high D^* is well captured by FVM.

The non-dimensional temperature T^* impact both layer height and width; an increase of this parameter lead to broader layer widths, together with a central collapse of the upper part of the layer, probably caused by the Newtonian-like behavior of PLA at high temperatures.

The effect of V^* on cross-section shape is the most noticeable; an increase in V^* means a higher mass flow rate; strand width increases consequently; a quantitative analysis has been reported in Table 4.3:

Table 4.3. Increase in maximum layer width (W_{max}) when switching from low to high screw speed, in CFD analyses.

h [mm]	T_n [°C]	Low N [rpm]	W_{max} at low N [um]	High N [rpm]	W_{max} at high N [um]	Increase in W_{max} switching from low to high N (%)
0.3	190	30	1290	60	1552	20.31
0.3	210	30	1460	60	1702	16.57
0.6	190	30	1572	60	1933	22.96
0.6	210	30	1754	60	2400	36.83
0.9	190	30	1612	60	2237	38.77
0.9	210	30	2100	60	2820	34.28

The maximum layer width increases with layer height and temperature. The first trend is related to the higher counterpressure which limits the mass flow rate at low layer heights. The second one is motivated by the more Newtonian-like behavior of the deposited material; it undergoes a larger radial squeezing at higher nozzle temperatures because of the lower viscosity.

4.5.3. Temperature distribution in deposited strands

It is important to study the effect of processing parameters on the overall layer shape and temperature distribution.

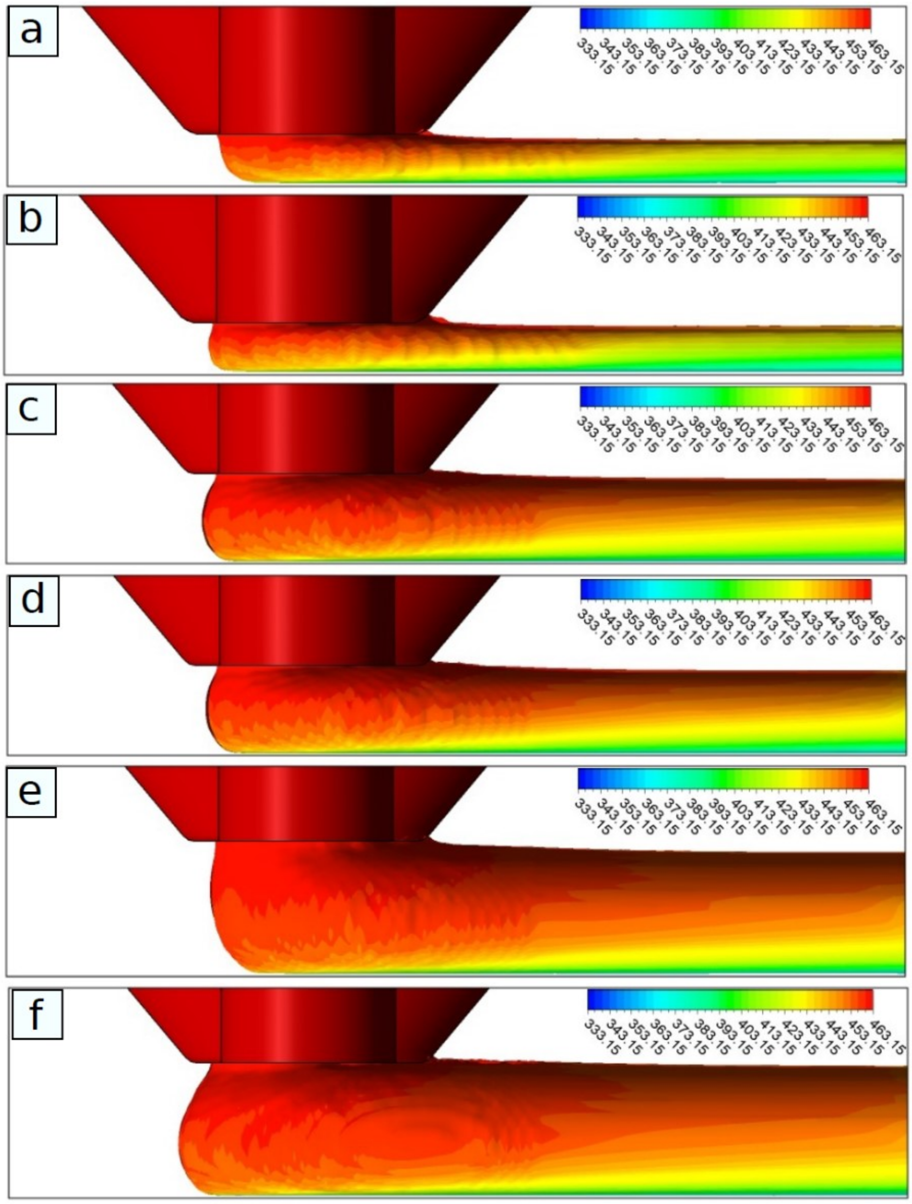

Figure 4.7. Extrudate front shape and temperature distribution at T_n=190 [°C] when a.) h=0.3 [mm] and N=30 [rpm]; b.) h=0.3 [mm] and N=60 [rpm]; c.) h=0.6 [mm] and N=30 [rpm]; d.) h=0.6 [mm] and N=60 [rpm]; e.) h=0.9 [mm] and N=30 [rpm]; f.) h=0.9 [mm] and N=60 [rpm].

In Figure 4.7 it has been given a front view of the deposited layer, at different values of the non-dimensional parameters D^* and V^*, while nozzle temperature was set to 190 [°C].

For a peer comparison, the CFD domains where Navier-Stokes and VOF equations have been solved share the same overall geometrical dimensions.

Because of the heat exchange with both surrounding air and built plate, the deposited strand always shows a temperature decrease along printing direction. However, the cooling rate is affected by process parameters; at lower D^* it can be noted a lower mean temperature, and therefore the layer solidifies quickly. The opposite trend (at high D^*) is motivated by the higher amount of extruded material and low PLA thermal conductivity (see: Figure 4.1), which makes the solidification process slower. In this situation, printing speed must be lowered to avoid depositing the next layer on a partially molten one.

The effect of V^* on temperature profile is negligible, but it affects the shape of the extruded layer; at higher V^*, the melt front which squeezes radially from the nozzle along the opposite of printing direction (backflow, in the following) becomes more pronounced. This is caused by the increase in mass flow rate.

Lastly, the influence of T^* has been evaluated accordingly to Figure 4.8:

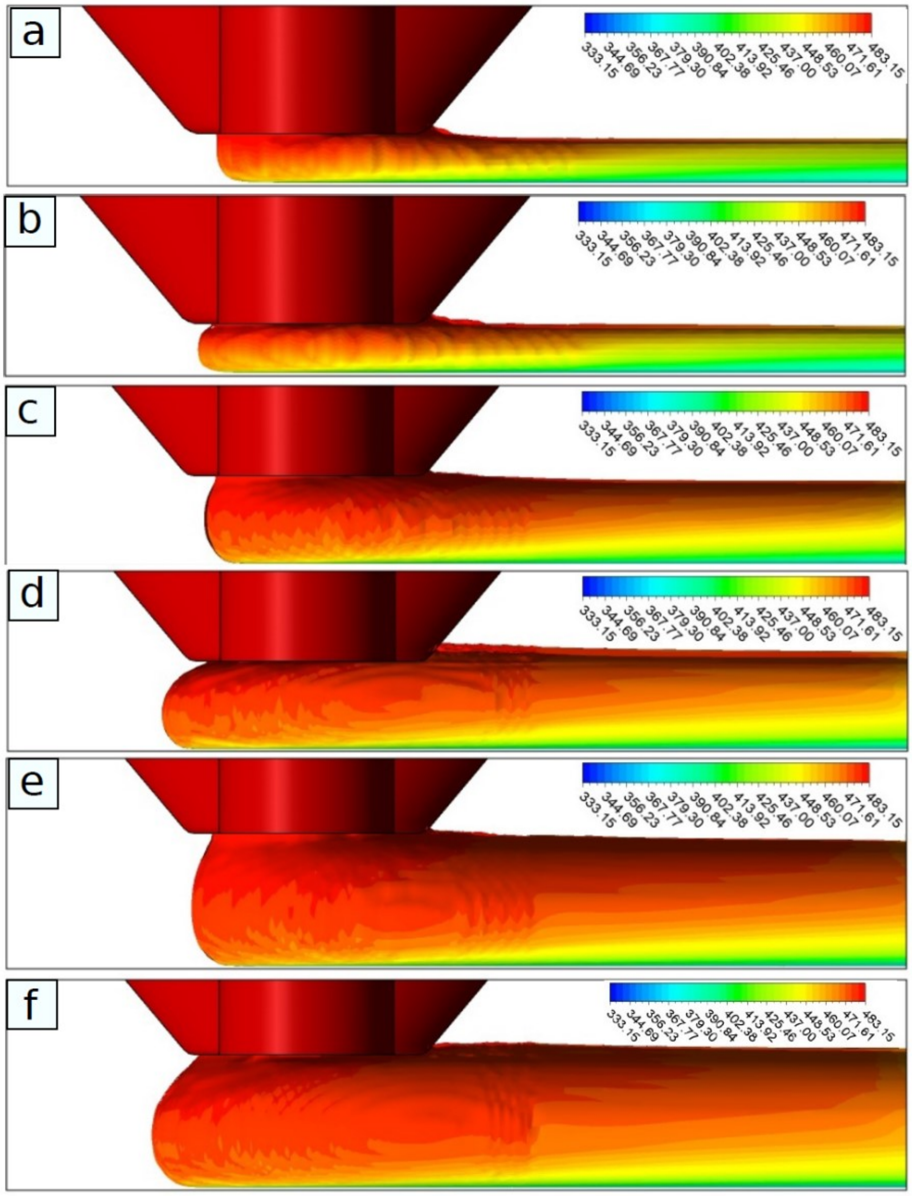

Figure 4.8. Extrudate front shape and temperature distribution at T_n=210 [°C] when a.) h=0.3 [mm] and N=30 [rpm]; b.) h=0.3 [mm] and N=60 [rpm]; c.) h=0.6 [mm] and N=30 [rpm]; d.) h=0.6 [mm] and N=60 [rpm]; e.) h=0.9 [mm] and N=30 [rpm]; f.) h=0.9 [mm] and N=60 [rpm].

The shape of the backflow is significantly affected by a higher nozzle temperature; a temperature increase causes more material to squeeze radially away from the nozzle, mainly because of the lower viscosity.
Previous conclusions on the effect of D^* and V^* on temperature distribution and extrudate shape still hold when considering higher T^*.

4.6. Conclusions

A CFD workflow for PAM extrusion has been presented and experimentally validated with respect to different operating conditions.
A systematic method for the evaluation of the cross-section of the first deposited strand has been proposed. The method differs from the ones conventionally proposed for FFF, where the mass flow rate is already known

because its value is imposed in the slicing software. In PAM extrusion, the flow rate parameter governs the screw peripheral speed, which is the primary factor affecting mass flow rate and layer width. The layer width imposed in PAM slicing software cannot be met, because a variation in screw speed results in a different extruded mass flow rate.

The effect of dimensionless layer height (D^*), temperature (T^*) and speed (V^*) on mass flow rate, strand shape and temperature distribution was investigated.

The D^* parameter has a deep impact on the mechanical properties of the printed part; in fact, by lowering D^*, higher surface finish and both inter- and intra-layer bond can be reached. However, the mass flow rate conveyed by the screw-barrel system is lower because of the higher counterpressure. Strand shape is oblong and thermal contact area increases.

Higher D^* produce more circular-like shaped strands and less backflow. In addition, higher productivity can be achieved.

Dimensionless temperature T^* was varied on two levels in the suggested interval for PLA; increasing T^* lead to higher layer width and lower height (top collapse). This is probably caused by the Newtonian-like flow behavior, which shows up at higher T^*. For the same reason, a slight increase in backflow can be noted.

Finally, higher V^* lead to wider radial squeezing, when layer is deposited on the built plate because of the higher mass flow rate which is delivered by the screw-barrel system.

The analysis of temperature distribution in the deposited strand showed a predominant effect of D^*; for a given observation window along printing direction, lower temperatures develop at decreasing D^*. This is primary related to the lower volume deposition. At high D^*, the low thermal conductivity represents a significant obstacle in achieving a quick solidification process.

In general, it has been shown a good agreement between numerical and experimental results, proving CFD as a milestone in establishing a digital twin for the screw-based MEX.

5. Semi-analytical models aiming at describing the flow of non-Newtonian fluids in tapered and cylindrical ducts, applied to thermoplastics and silicone MEX

5.1. Chapter organization

In this Chapter, mathematical models aiming at describing the fluid flow of non-Newtonian fluids inside ducts with both convergent and cylindrical sections have been formulated.

These geometrical features are typical of the fluid passages of nozzles used practically in all MEX techniques. A generalization of the Jeffery-Hamel theory has been implemented for the description of industrially interesting fluids such as moisture-cured silicones and thermoplastics, which are well described by the Carreau and Cross- Cross-WLF rheological models, respectively.

Results have been compared with CFD simulations and the overall agreement is very good, showing the potential for next experimental applications in predicting some very important and useful quantities, such as the extrusion force, which is critical in MEX.

The novelty relies in the applicability of the generalized Jeffery-Hamel model practically to every viscous flow, no matter what its rheological behavior is.

The Chapter has been organized as follows: in Section 5.4 an iterative method aiming at describing the flow of complex fluids in cylindrical ducts is given, together with the assumptions (5.4.1) and the theoretical formulation (5.4.2). In Section 3 the semi-analytical iterative model for the description of the Jeffery-Hamel flow has been fully explained, together with the assumptions (5.5.1) and the theoretical formulation (5.5.2) as well.

The validation for a thermoplastic material (Cross-WLF model) has been given in Section 5.4.3 (cylindrical die) and 5.5.3 (convergent section). The same has been done for a moisture-cured silicone (Carreau model) in Section 5.4.4 (cylindrical die) and 5.5.4 (convergent section). Finally, Conclusions have been reported in Section 5.6.

5.2. Chapter nomenclature

A_1	First Cross-WLF parameter	T_g	Glass transition temperature
A_2	Second Cross-WLF parameter	$u(r)$	Velocity distribution in cylindrical straight duct (S-F)
D	Straight nozzle diameter (S-F)	$v_r(r;\theta)$	Radial velocity (J-H)
$\overline{\overline{D}}$	Strain rate tensor	v_r^{local}	Local radial velocity profile (J-H)
$f(\theta)$	Polar function (J-H)	$v_{r,max}^{old}$	Old maximum velocity value at given radial position (J-H)
f_{max}	Maximum value for $f(\theta)$ (J-H)	$v_{r,max}^{new}$	New maximum velocity value at given radial position (J-H)
$f_{max,trial}$	Trial maximum value for $f(\theta)$ (J-H)	w_i	i-th interpolation coefficient in the expression of shear rate (S-F)
f_{max}^{new}	New maximum value for $f(\theta)$ (J-H)	z	Axial coordinate (S-F)

k	k-th step index in continuation method (J-H)	$(a;\ b;\ c;\ d;\ d_0;\ d_1)$	Auxiliary coefficients (S-F)
L	Straight nozzle length (S-F)	$(A;\ \ldots;\ R)$	Geometrical features of the SmoothFlow nozzles (J-H)
n	Power-law index	α	Half of the opening angle (J-H)
ΔP	Pressure drop	$\dot{\gamma}$	Shear rate
p_i	i-th interpolation coefficient in the expression of shear stress (S-F)	$\varepsilon_{\Delta p}$	Relative error on pressure drop (S-F)
D_1	Third Cross-WLF parameter	ε_Q	Relative error on volumetric flow rate (S-F)
ΔP_{next}	Pressure difference for the second iteration	ε_{ij}	ij-th component of the strain rate tensor
ΔP_{trial}	Trial value for pressure difference	ξ	Parameter used in third-grade equation solution (S-F)
$\Delta P(j)$	Pressure difference at j-th step	η_0	Zero shear rate viscosity
$\Delta P(j+1)$	Pressure difference (step: j + 1)	η_∞	Infinite shear rate viscosity
Q	Volumetric flow rate	$\eta_{Newtonian}$	Newtonian viscosity value used to start the iterative model (S-F)
Q_{trial}	Trial value for volumetric flow rate (J-H)	η	Dynamic viscosity
$Q_{iteration}$	Volumetric flow rate evaluated at given iteration	θ	Polar coordinate
Q_{real}	Real volumetric flow rate being extruded	λ	Relaxation time in Carreau model
r	Radial coordinate	ρ	Density
s	Sliding parameter for the continuation method (J-H)	τ^*	Fourth Cross-WLF parameter
T	Extrusion temperature	τ_{ij}	ij-th component of the stress tensor
$\bar{\bar{T}}$	Stress tensor	φ	Azimuthal coordinate (J-H)

5.3. Introduction

The fluid flow through both straight circular ducts and smooth convergent tubes characterizes a wide range of physical applications virtually in all branches of engineering.

Practical relapses are in the field of biofabrication [120], bioengineering [121], IM [35,36], compression moulding [122], polymer extrusion through FFF [85,91], PAM [116,123], silicone MEX [124,125], microfluidics [126–129], thermal processing [130–132] and rheological measurements [133].

As a natural consequence, there is a compelling demand for analytical and semi-analytical models which can provide fast and accurate results in terms of fluid dynamics quantities, such as the pressure drop, shear rate and velocity profiles. CFD is very useful to validate new mathematical formulations because of its great accuracy, but it can easily become time consuming with increasing mesh size.

The fluid flow of Newtonian fluids in straight cylindrical ducts allows for a closed-form analytical solution, that is the well-known Poiseuille law: a parabolic velocity profile reaching its maximum on the symmetry axis, which is the centerline of the cylindrical duct.

Newtonian fluids are characterized by the fact that the dynamic viscosity does not depend on shear rate. Most of the materials being implemented in the abovementioned industrial processes show a non-Newtonian behavior. Practical examples are most molten thermoplastic in the higher shear rate regime[35,36], bioinks [120], biofluids [126], nanofluids [134], moisture-cured silicones [124] and gel propellants [135], which follow the power-law model, also known as Ostwald-de-Waele relationship.

Unfortunately, this model cannot be applied for the description of the whole flow field; in absence of inlet swirl motions, the maximum velocity is reached on the nozzle axis, both for straight cylindrical and convergent dies; this means that locally the shear rate is zero. Moving away from axis the shear rate grows, reaching its maximum on the walls.

Most of the materials previously mentioned show a Newtonian plateau at low shear rates. A power-law behavior is observed only at high shear rates, after a transition zone; the rheological Cross-WLF model [136] describes very well this behavior, which characterizes a wide range of thermoplastic materials. Other ones, such as moisture-cured silicones, show a second Newtonian plateau when very high shear rates are reached, as in Carreau model [87].

Different methods have been proposed to deal with these rheological models, aiming at capturing the whole operating shear rate range in the simplified case of the flow in a straight cylindrical channel (i.e., [120,137,138]).

Another problem which deserves particular attention is that of the analytical and numerical solution of the fluid dynamics of complex flows in convergent/divergent sections.

In [139] the plane flow of an incompressible power-law fluid has been studied analytically, finding a solution which agrees well with FEM data only for low convergent angles. A similar approach for power-law fluids has been reported in [140]; here the idea is to solve the Navier-Stokes equations in a cylindrical duct, where the analytical solution of the radial equilibrium is possible if a power-law fluid is considered; then, the same equation, which relates pressure drop and volume flow rate is written in differential form and a law describing the radius as a function of the axial position is introduced; then the integration is performed according to this relation. Latter approach is still valid in principle for more complex fluids when the opening angle is sufficiently small, namely if the flow is almost axial. In [141] the analytical solution of the flow of a power-law fluid in a convergent/divergent section has been discussed, by solving the Navier-Stokes equations written in spherical coordinates; the analytical solution of the reduced third-order ODE is possible only when the 4/3 value is considered for the power-law index. The flow in a convergent/divergent wedge and/or cone can be studied in an approximated way through polar or spherical coordinates, respectively. This flow has been reported in literature as Jeffery-Hamel flow, for which different solutions have been proposed [141,142].

In particular, good results have been found by applying the differential transform method to the solution of the reduced third order ODE for low convergent angles [142]. In [143] the wall friction has been included in the model and an analytical solution is obtained only under a set of simplifying conditions (convergent angle lower than 20[°] and an assumption on the polar function, for linearity). Nonetheless, in the same work semi-analytical solutions are reported, which disregards the two assumptions. Moreover, a very complete work which fully describes the Jeffery-Hamel flow of a power-law fluid has been reported in [135], where a MATLAB code has been developed to solve the fluid dynamics of gel propellants, by means of the bvp4c subroutine (similar applications can be found in [131,132]). A major point is that for a value of the power-law index of 4/3 the results agree with the analytical solution being proposed in [141].

However, molten polymers used in MEX processes are better described by the Cross-WLF rheological behavior. To the present, no model has been reported in literature aiming at describing the flow of a similar class of fluids, especially when dealing with cone/wedge shaped nozzles. Only for straight cylindrical channels an approximate solution has been proposed in [137], based on the Weissenberg-Rabionowitsch-Mooney-Schofield (WRMS) theory.

A goal is that to verify if this previous analytical solution is valid on the whole range of cylindrical ducts diameters and to compare it with a new iterative solution procedure.

Then, the Jeffery-Hamel flow has been thoroughly studied to describe the flow in tapered ducts both for Carreau and Cross-WLF models.

5.4. Mathematical modeling of the flow in cylindrical ducts

In this Section, the model for a viscous flow in a cylindrical duct is presented. Variable names are listed in Section 5.2; all quantities which refer specifically to the problem report the indication (S-F), that stands for 'Straight-Flow'.

The problem domain, together with the 2D axisymmetric model used for CFD computations, have been represented in Figure 5.1:

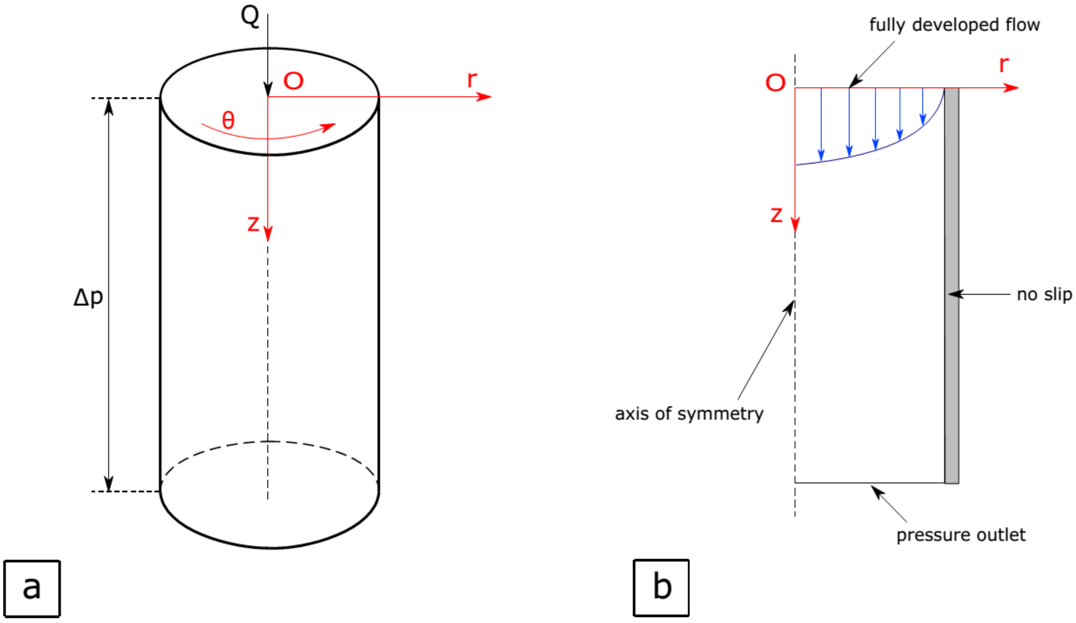

Figure 5.1. a.) Three-dimensional representation of the geometrical domain; b.) Two-dimensional axisymmetric model used for CFD computations, together with the boundary conditions being implemented; Q: volumetric flow rate and Δp: pressure drop.

The numerical validation of the code has been performed in the case of the extrusion of both a thermoplastic material and a moisture-cured silicone, which follow the Cross-WLF and Carreau rheological models, respectively.

Finally, a comparison between the CFD and semi-analytical solution has been conducted.

At the same time, the theory introduced in [137] has been implemented for comparison with the proposed model, in the case of the Cross-WLF model.

5.4.1. Assumptions

The assumptions under which the fluid dynamic problem of the extrusion through a cylindrical die is studied are:

- the flow is assumed stationary, isothermal and incompressible,

- the fluid viscosity law is sufficiently smooth to be well approximated by a third-order polynomial,
- the fluid is a purely viscous one (negligible elongational effects),
- flow field is fully developed along z axis,
- flow field is axisymmetric ($\partial(\cdot)/\partial\theta = 0$), and
- body forces and inertial effects are negligible.

With respect to the assumption on the smoothness of the rheological models, R-squared (R^2) has been calculated, when applying the model to thermoplastics and silicones (see: Sections 5.4.3 and 5.4.4); its high value (over 0.99 in all computations) justifies the assumption to deal with a third-order polynomial.
Moreover, by means of the last three abovementioned assumptions, the stress tensor $\bar{\bar{\tau}}$ reduces to a single nonzero component, τ_{rz}.
As an example, the shear stress for most thermoplastic materials can be expressed according to Cross-WLF model as:

$$\tau_{rz} = \eta\,\dot{\gamma}_{rz} = \frac{\eta_0}{1+\left(\frac{\eta_0\dot{\gamma}_{rz}}{\tau^*}\right)^{1-n}}\,\dot{\gamma}_{rz} \tag{5.4}$$

The shear stress is interpolated over a relevant range of shear rates; at first iteration, this range is chosen to be simply of one decade, and the expression of the polynomial interpolation is:

$$\tau_{rz} \approx \sum_{i=0}^{3} p_i\;\dot{\gamma}_{rz}^{i} \tag{5.5}$$

Where p_i is the i-th coefficient used in the cubic interpolation.

5.4.2. Iterative model

The equations of motion are written according to the cylindrical coordinates used in Figure 5.1; under the abovementioned assumptions, the equation to be solved is the momentum conservation along the axial direction (z in Figure 5.1 – a):

$$-\frac{\partial p}{\partial z} = \frac{1}{r}\frac{\partial}{\partial r}(r\tau_{rz}) \tag{5.6}$$

Integrating at first with respect to z:

$$-\frac{\Delta P}{L} = \frac{1}{r}\frac{\partial}{\partial r}(r\tau_{rz}) \tag{5.7}$$

Then, it can be integrated along the radial direction, after performing a separation of variables:

$$-\frac{\Delta P}{L}\frac{r}{2} = \tau_{rz} \tag{5.8}$$

The integration constant is zero because shear stress is zero on the symmetry axis.
By inserting (5.5) in (5.8), it follows a cubic equation:

$$p_3\dot{\gamma}_{rz}^3 + p_2\dot{\gamma}_{rz}^2 + p_1\dot{\gamma}_{rz} + p_0 + \frac{\Delta P}{L}\frac{r}{2} = 0 \tag{5.9}$$

Whose solution can be found by the following positions [144]:

$$a = p_3 \tag{5.10}$$

$$b = p_2 \tag{5.11}$$

$$-c = p_1 \tag{5.12}$$

$$d = p_0 + \frac{\Delta P}{L}\frac{r}{2} \tag{5.13}$$

And:

$$d_0 = b^2 - 3ac \tag{5.14}$$

$$d_1 = 2b^3 - 9abc + 27a^2d \tag{5.15}$$

$$C = \sqrt[3]{\frac{d_1 + \sqrt{d_1^2 - 4d_0^3}}{2}} \tag{5.16}$$

The shear rate can be evaluated by means of (5.9) with the general formula:

$$\dot{\gamma}_{rz} = -\frac{1}{3a}\left[b + C\xi^t + \left(\frac{d_0}{C\xi^t}\right)\right] \tag{5.17}$$

Where ξ is:

$$\xi = \frac{-1 + \sqrt{-3}}{2} \tag{5.18}$$

Variable t can assume only the discrete values $\{0; 1; 2\}$, giving the three possible mathematical solutions. The only physically admissible one can be found by imposing $t = 0$ in (5.17), which gives:

$$\dot{\gamma}_{rz} = -\frac{1}{3a}\left(b + C + \frac{d_0}{C}\right) \tag{5.19}$$

Iterations are needed since the shear rate $\dot{\gamma}_{rz}$ is a function of both the radial position r and the pressure drop ΔP. The iterative process starts assigning a trial value for the pressure difference, Δp_{trial}.
By the definition of shear rate, the velocity profile is determined:

$$u(r) = -\int \dot{\gamma}_{rz} dr \tag{5.20}$$

It is possible to expand as a polynomial series the expression: $\dot{\gamma}_{rz} = \dot{\gamma}_{rz}(r)$; in the MATLAB implementation, a fifth-order polynomial has proved to be a very good approximation:

$$\dot{\gamma}_{rz} \approx \sum_{i=0}^{5} w_i\, r^i \tag{5.21}$$

Former integral equation (5.20) becomes:

$$u(r) = -\sum_{i=0}^{5} w_i \frac{r^{i+1}}{i+1} + c \tag{5.22}$$

The integration constant, c, is found by imposing the no-slip boundary condition at nozzle wall:

$$u(r = D/2) = 0 \tag{5.23}$$

The velocity profile is given by substitution:

$$u(r) = -\sum_{i=0}^{5} w_i \frac{r^{i+1}}{i+1} + \sum_{i=0}^{5} w_i \frac{(D/2)^{i+1}}{i+1} \tag{5.24}$$

Considering an axisymmetric flow, the iteration value of the volumetric flow rate is evaluated as:

$$Q_{\text{iteration}} = 2\pi \int_0^{D/2} u(r) r\, dr \tag{5.25}$$

By considering the polynomial interpolation (5.21), this last integral is straightforward. Finally, the relative error on volumetric flow rate is calculated:

$$\varepsilon_Q = 100\, \frac{Q_{\text{real}} - Q_{\text{iteration}}}{Q_{\text{real}}} \tag{5.26}$$

By considering two subsequent iterations, namely j and j + 1, the pressure difference is modified as follows:

$$\Delta P(j+1) = \Delta P(j) - \Delta P(j)\varepsilon_Q(j) \tag{5.27}$$

If the real pressure drop ΔP_{real} is known experimentally or numerically, the relative error in pressure drop prediction can be evaluated:

$$\varepsilon_{\Delta P} = 100\, \frac{\Delta P_{\text{real}} - \Delta P_{\text{iteration}}}{\Delta P_{\text{real}}} \tag{5.28}$$

The iterative process, which is based on the evaluation of both the volumetric flow rate and pressure drop, stops when the relative error goes below the tolerance ε. Moreover, the iterative process needs a trial pressure drop value, ΔP_{trial}, to start. All these quantities are user defined.

In the case of Δp_{trial}, a first value can be imposed by mean of the well-known Poiseuille equation; by considering a low viscosity (i.e., $\eta_{\text{Newtonian}} = 10$ [Pa s] in all next calculations) its value is:

$$\Delta P_{\text{trial}} = -128\, \frac{\eta_{\text{Newtonian}}\, L\, Q_{\text{real}}}{\pi D^4} \tag{5.29}$$

The use of the Poiseuille equation allows to reach convergence without any problem.

5.4.3. Application – Extrusion of thermoplastics

The model is applied for simulating the flow of a Cross-WLF fluid inside E3Dv6 nozzles. They have been chosen primarily because their internal geometry is entirely known [145]. In Figure 5.2, all dimensions have been reported for completeness:

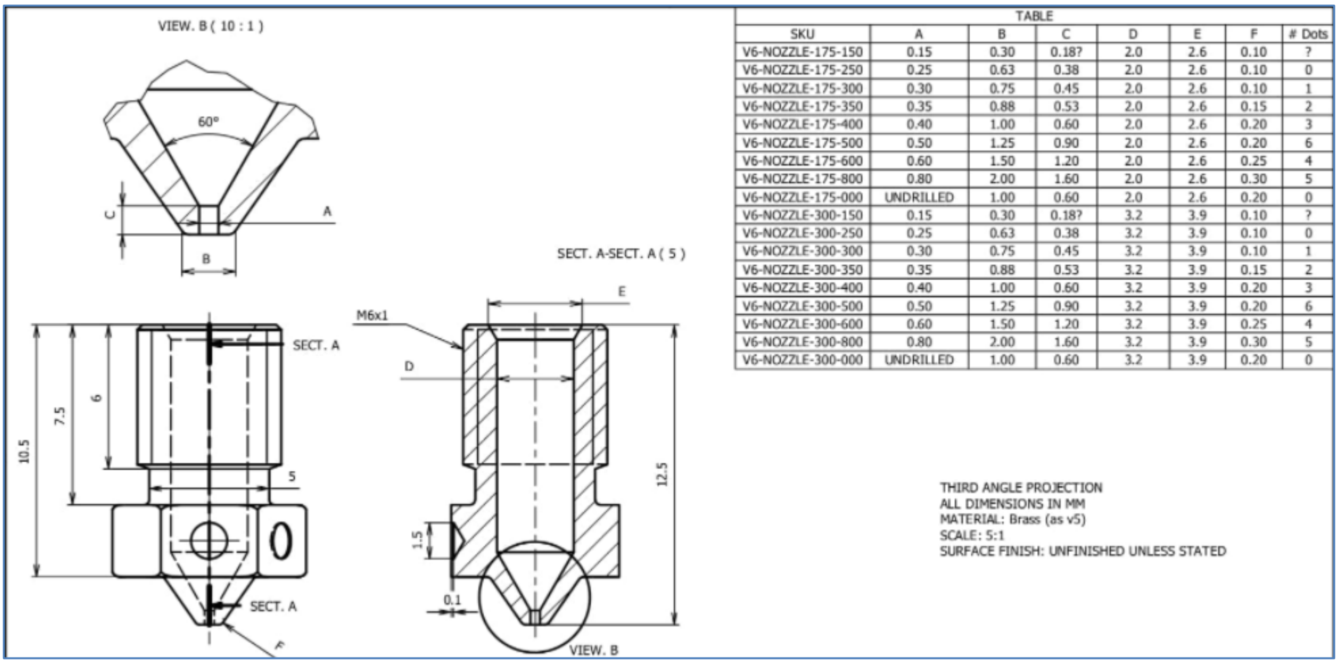

TABLE							
SKU	A	B	C	D	E	F	# Dots
V6-NOZZLE-175-150	0.15	0.30	0.18?	2.0	2.6	0.10	?
V6-NOZZLE-175-250	0.25	0.63	0.38	2.0	2.6	0.10	0
V6-NOZZLE-175-300	0.30	0.75	0.45	2.0	2.6	0.10	1
V6-NOZZLE-175-350	0.35	0.88	0.53	2.0	2.6	0.15	2
V6-NOZZLE-175-400	0.40	1.00	0.60	2.0	2.6	0.20	3
V6-NOZZLE-175-500	0.50	1.25	0.90	2.0	2.6	0.20	6
V6-NOZZLE-175-600	0.60	1.50	1.20	2.0	2.6	0.25	4
V6-NOZZLE-175-800	0.80	2.00	1.60	2.0	2.6	0.30	5
V6-NOZZLE-175-000	UNDRILLED	1.00	0.60	2.0	2.6	0.20	0
V6-NOZZLE-300-150	0.15	0.30	0.18?	3.2	3.9	0.10	?
V6-NOZZLE-300-250	0.25	0.63	0.38	3.2	3.9	0.10	0
V6-NOZZLE-300-300	0.30	0.75	0.45	3.2	3.9	0.10	1
V6-NOZZLE-300-350	0.35	0.88	0.53	3.2	3.9	0.15	2
V6-NOZZLE-300-400	0.40	1.00	0.60	3.2	3.9	0.20	3
V6-NOZZLE-300-500	0.50	1.25	0.90	3.2	3.9	0.20	6
V6-NOZZLE-300-600	0.60	1.50	1.20	3.2	3.9	0.25	4
V6-NOZZLE-300-800	0.80	2.00	1.60	3.2	3.9	0.30	5
V6-NOZZLE-300-000	UNDRILLED	1.00	0.60	3.2	3.9	0.20	0

THIRD ANGLE PROJECTION
ALL DIMENSIONS IN MM
MATERIAL: Brass (as v5)
SCALE: 5:1
SURFACE FINISH: UNFINISHED UNLESS STATED

Figure 5.2. E3Dv6 nozzle drawings (from [145]).

In this application, the critical zone where previous analytical modeling techniques [137] fail is the last calibration length with diameter A, and length C (Figure 5.2 – View B). In fact, it will be shown that the relative error is very big for lower diameters.

Nonetheless, these solutions can be still applied in modeling IM and SSE processes, where nozzle dimensions are higher than in FFF.

In all calculations the threshold value for relative tolerance, whose expression was given in (5.28), was set to $\pm 1[\%]$.

The material being studied is the LATILON 24D AM NT:0038R polymer, manufactured by Lati s.r.l.. The main parameters used in the computations are listed in the following Table 5.1:

Table 5.1. LATILON parameters being used in CFD and semi-analytical computations.

Symbol	Parameter name	Value
n	Power-law exponent	0.1863
A_1	First Cross-WLF temperature fit constant	32.659
A_2	Second Cross-WLF temperature fit constant	51.6
D_1	Third Cross-WLF temperature fit constant	9.4e+12
τ^*	Critical shear stress level	629065
T_g	Glass transition temperature	426.30 [°C]
T	Extrusion temperature	280 [°C]

Q_{real}	Volumetric flow rate	1E-09 [m^3/s]

The dynamic viscosity has been represented at the specified extrusion temperature in the following Figure 5.3:

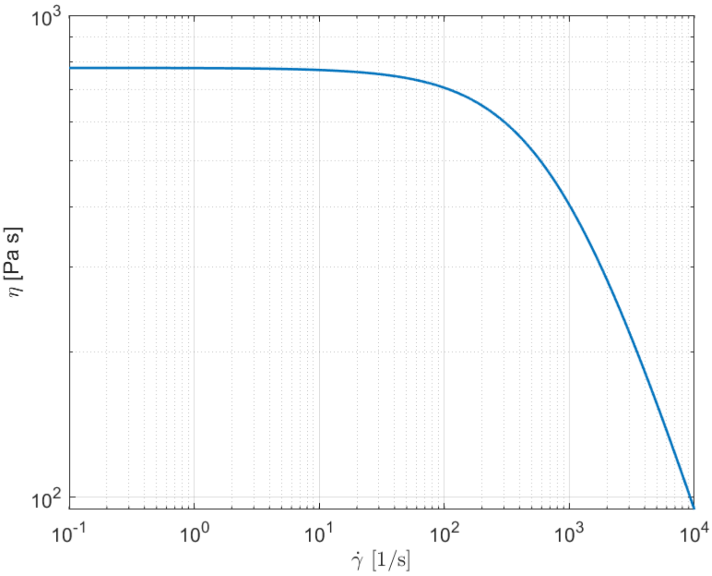

Figure 5.3. LATILON dynamic viscosity (T=280 [°C]); $\dot{\gamma}$: shear rate; η: dynamic viscosity.

The results in terms of relative error for different nozzle diameters are shown in Figure 5.4:

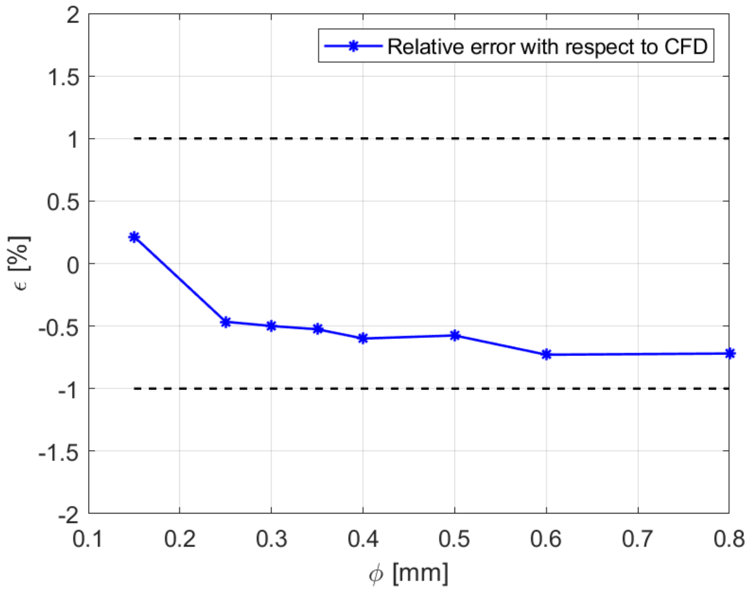

Figure 5.4. Relative error at different diameters; ϕ: nozzle diameter; ϵ: relative error on pressure drop.

Figure 5.4 shows the relative error on pressure drop with respect to reference values evaluated by means of CFD analyses in COMSOL Multiphysics v. 5.5 (Fluid Flow module). The proposed model results fall in the established tolerance of $\pm 1[\%]$ for all considered nozzle sizes.

Finally, another parameter which is critical for calculations is the velocity profile. Latter quantity has been investigated, and the results of the comparison between semi-analytical and CFD computations is shown in Figure 5.5:

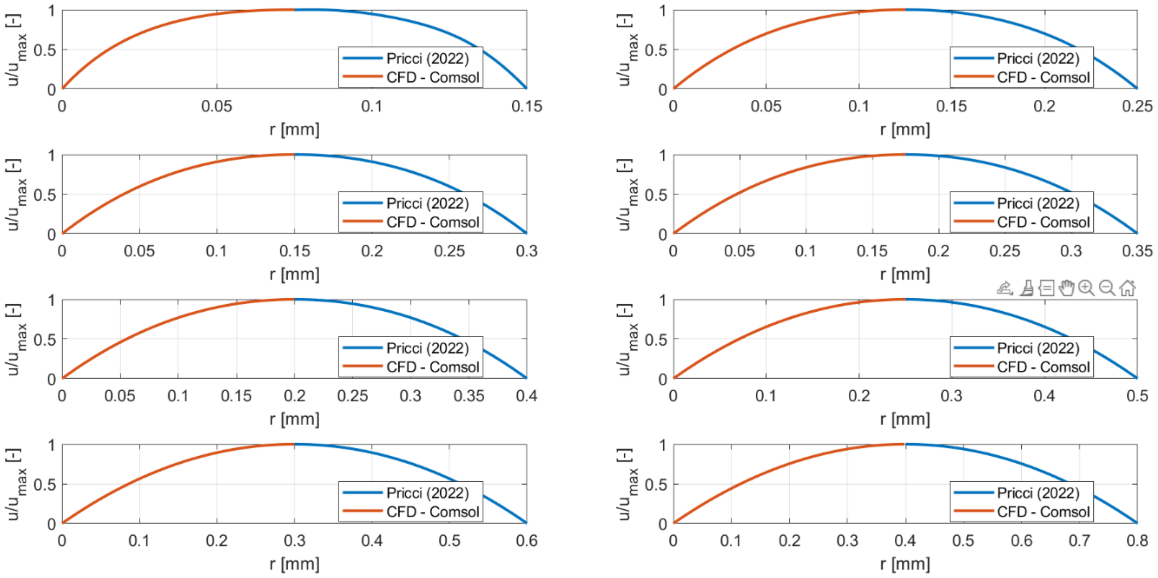

Figure 5.5. Non-dimensional velocity profiles for the E3Dv6 nozzles; r: radial coordinate; u_{max} : maximum velocity; u: local velocity.

Similarly, obtained by applying the analytical formulation proposed in [137] has been reported in the following Figure 5.6, together with present results; for the theory being exposed in the model proposed by Sochi large errors can be observed at lower nozzle diameters, as also indicated in Figure 5.7:

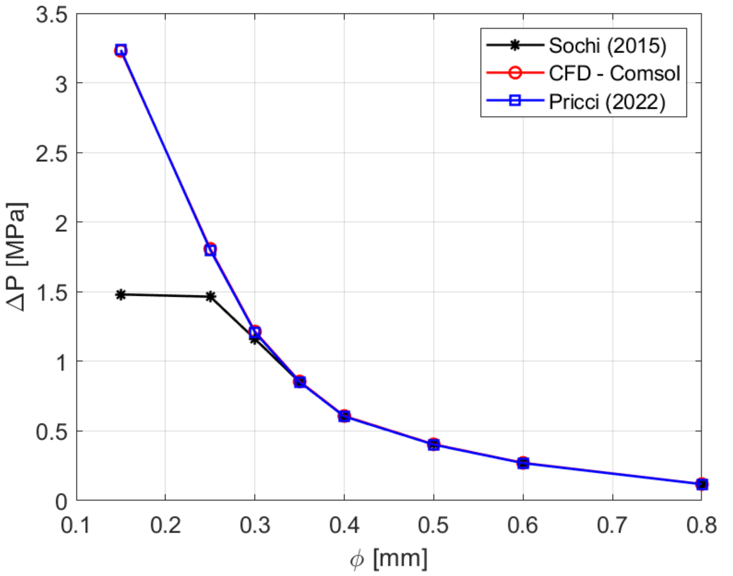

Figure 5.6. Pressure drop behaviour in E3Dv6 nozzles predicted in [137] (Sochi 2015) against the iterative procedure being presented (Pricci 2022), together with CFD results (CFD – Comsol); ϕ: nozzle diameter; ΔP: pressure drop.

Analytical, numerical and iterative methods states the decrease in pressure drop with increasing nozzle diameter. Intutively, the mean velocity reduces with increasing diameter, leading to a lower pressure drop across the straight duct. This can also be noted for Newtonian fluids (5.29).

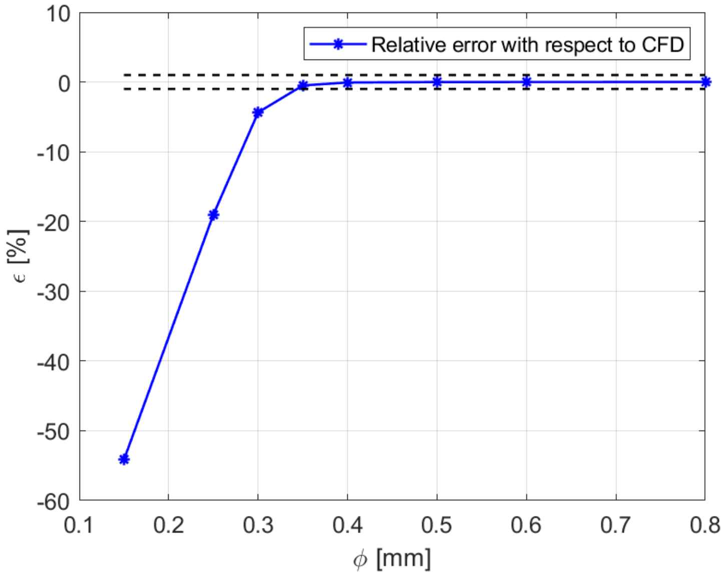

Figure 5.7. Relative error behaviour with respect to CFD computations [137]; ϕ: nozzle diameter; ϵ: relative error on pressure drop. The error bars refer to a user-defined absolute relative tolerance of 1[%].

5.4.4. Application – Extrusion of moisture-cured silicone

A commercially available silicone (DOWSIL ® 737, DOWSIL, Michigan, USA) has been used for modeling (present Chapter) and experimental (Chapter 6) purposes. DOWSIL ® 737 cures upon exposure to atmospheric moisture, in accordance with the datasheet [39].

The Carreau rheological model is used to perform the CFD COMSOL computations:

$$\eta = \eta_\infty + (\eta_0 - \eta_\infty)[1 + (\lambda\dot{\gamma})^2]^{\frac{n-1}{2}} \quad (5.30)$$

The meaning of the different parameters has been reported the following Table 5.2:

Table 5.2. Rheological parameters for the moisture-cured silicone [124].

Symbol	**Parameter name**	**Value**
n	Power-law exponent	0.5
η_∞	Infinite shear rate viscosity	0 [Pa s]
η_0	Zero shear rate viscosity	62.5 [Pa s]
λ	Relaxation time	0.0173 [s]

The dynamic viscosity has been represented for the extrusion temperature in Figure 5.8:

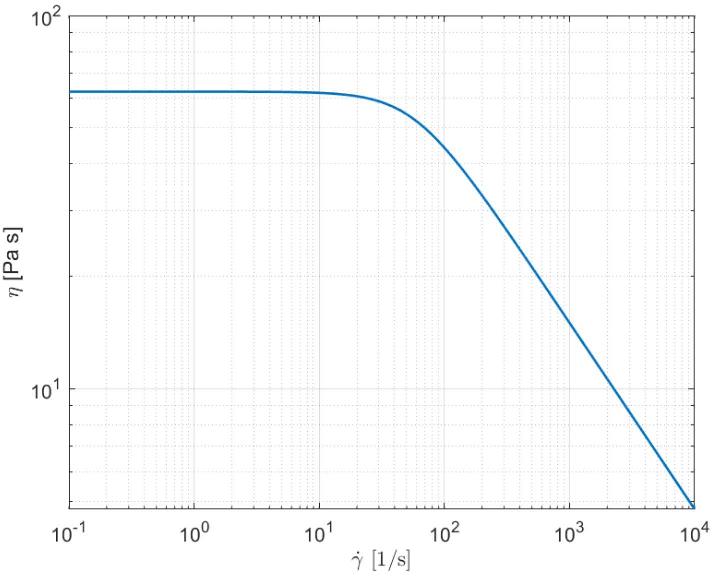

Figure 5.8. Silicone viscosity according to the Carreau model; $\dot{\gamma}$: shear rate; η: dynamic viscosity.

The same cylindrical dies of the previous case are investigated, with a diameter up to 0.5 [mm]. The results in terms of relative error for different nozzle diameters are shown in the Figure 5.9:

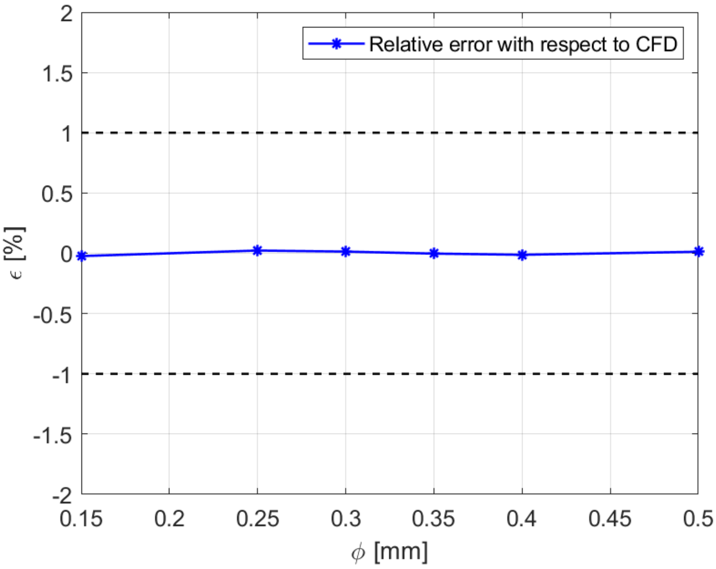

Figure 5.9. Relative error at different diameters; ϕ: nozzle diameter; ϵ: relative error on pressure drop.

In Figure 5.10 the prediction in terms of velocity profile show a good agreement also in simulating the silicone extrusion.

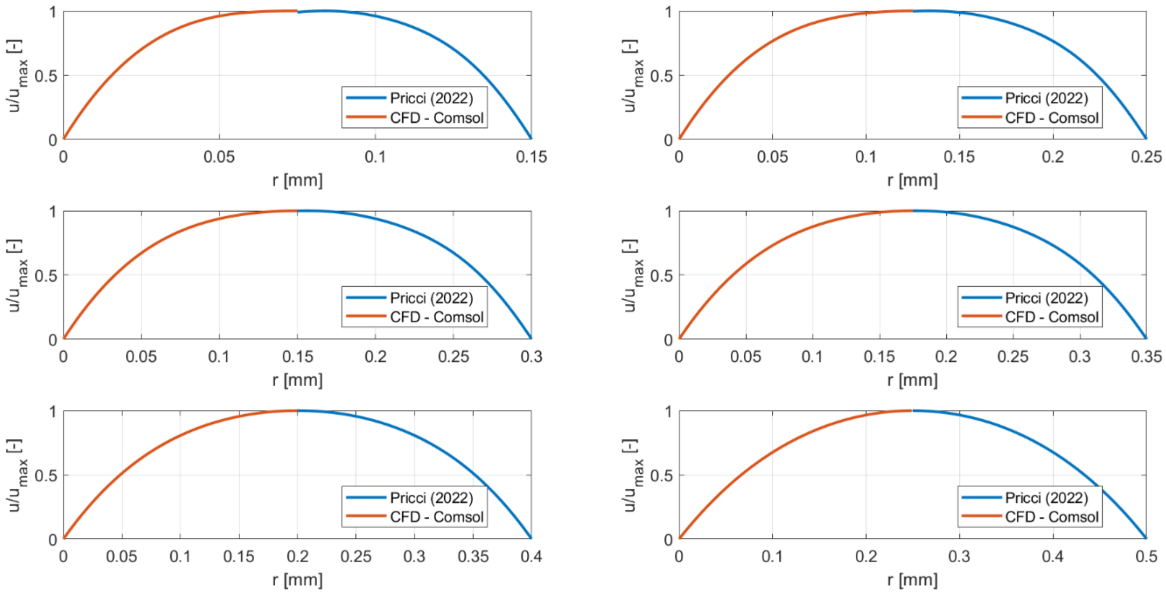

Figure 5.10. Non-dimensional velocity profiles for silicone extrusion; r: radial coordinate; u_{max} : maximum velocity; u: local velocity.

It can be noted a very good correspondence of the proposed iterative formulation with CFD results.
The error analysis has been given, for all nozzle diameters in Table A.1-A.6 (see: Appendix A).
As highlighted in the error analysis, results have been validated also against a different numerical method, other than the FEM-based COMSOL package; a FVM solver has implemented to solve the non-linear transport equations in the case of the Carreau rheological model.
The FVM solver has been employed to compute the maximum flow velocity on a structured grid, by means of the SIMPLE scheme, second order discretization for pressure and QUICK scheme for velocity variables; the iterative process ends when all residuals goes below 1E-07.
The results collected in Table A.1-A.6 show a very good agreement of all three proposed methods; to be said, the proposed iterative model requires a hundredth of the iterations required by the FVM solver (with default under-relaxation factors, to provide numerical stability).
Moreover, the iterative method has been compared with existing literature. In [146] it has been measured the fully developed flow in a cylindrical duct under different Reynolds numbers and fluid rheologies.
Denoted as u_m the mean velocity, evaluated as the ratio between the volumetric flow rate and cylinder cross-sectional area a benchmark analysis of the velocity field has been conducted in Figure 5.11:

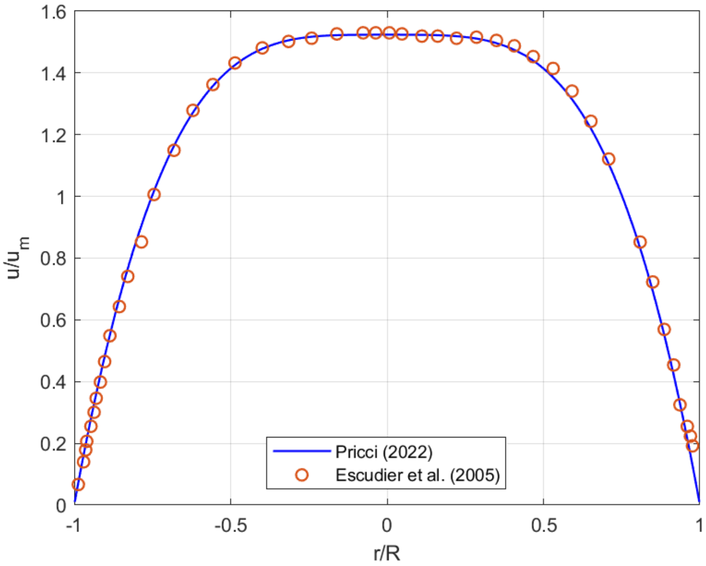

Figure 5.11. Non-dimensional velocity profiles estimated by means of the iterative code and measured by a laser Doppler anemometry for 0.2[%] polyacrylamide aqueous solution; r: radial coordinate; R: cylinder radius; u: local velocity; u_m: mean fully developed velocity; other conditions: u_m=0.564 [m/s] ; R=0.05 [m], ρ=1000 [kg/m^3]; λ=11.1 [s]; n=0.33; μ_0=2.94 [Pa s]; μ_∞=3.55E-03 [Pa s].

The overall correspondence with the experimental measurements is very good, paving the way for the application of the iterative method in the extrusion of different biofluids whose rheology follows the Carreau model.

These applications show the feasibility of applying the iterative method to the solution of the viscous flow in a cylindrical die.

5.5. Mathematical modeling of the flow in tapered ducts

Here, the theory for the solution of Jefferey-Hamel flow in a cone will be introduced. It extends the works presented in [135], were the power-law fluid constitutive relation (that is, Ostwald model) was considered.

The variables used in the model are listed in Section 5.2. All quantities which refer specifically to the problem being presented in this paragraph report the indication (J-H), that stands for 'Jeffery-Hamel'.

The fluid flow in a cone can be studied by choosing spherical coordinates (r; θ; φ); the radial coordinate is taken as positive if it points from the center of an ideal sphere outwards. The other two coordinates are the polar and azimuthal ones, respectively (see: Figure 5.12 – c):

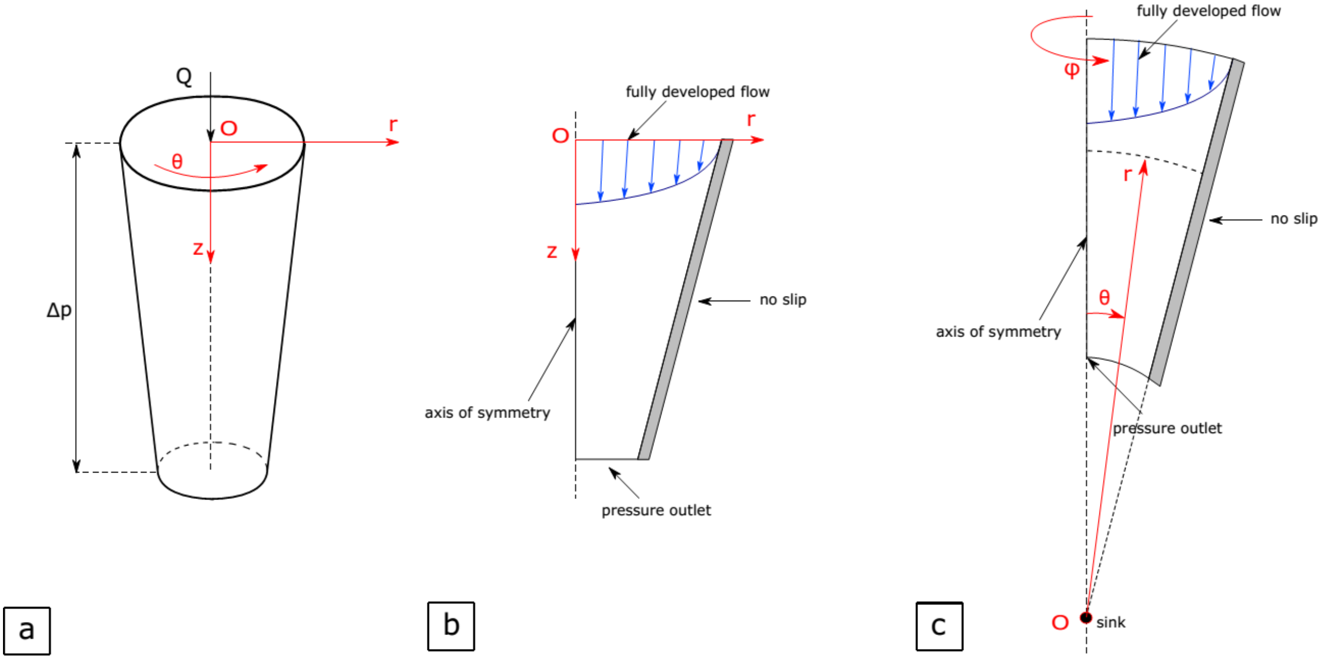

Figure 5.12. a.) Real Geometry; b.) 2D model used in CFD calculations; c.) 2D model used for the Jeffery-Hamel modeling.

5.5.1. Assumptions

The assumptions underlying the mathematical formulation of the Jeffery-Hamel flow are the following:

- The flow is assumed as incompressible, stationary and isothermal,
- Negligible inertial effects and body forces,
- No-slip condition at walls,
- Flow field is characterized by azimuthal symmetry ($\partial(\cdot)/\,\partial\varphi = 0$), and
- The flow is directed only radially (namely, the only non-zero velocity component in spherical coordinates is $v_r = v_r(r;\,\theta)$).

5.5.2. Theoretical formulation

The mass conservation in spherical coordinates can be written as:

$$\frac{\partial}{\partial r}(\rho r^2 v_r) = 0 \tag{5.31}$$

Integrating (5.31) with respect to the radial direction, an expression for the radial velocity is found:

$$v_r = -\frac{f(\theta)}{\rho r^2} \tag{5.32}$$

Where $f(\theta)$ is a function which depends only on polar coordinate. Here the minus sign is due to the fact that the flow is directed inwards, while the positive radial direction is outwards, as pointed in Figure 5.12 – c.

It is now possible to introduce the strain rate tensor in spherical coordinates [147]; all the assumptions have been implemented to simplify the final expression of all nonzero components:

$$\varepsilon_{rr} = \frac{\partial v_r}{\partial r} \tag{5.33}$$

$$\varepsilon_{\theta\theta} = \frac{v_r}{r} \tag{5.34}$$

$$\varepsilon_{\varphi\varphi} = \frac{v_r}{r} \tag{5.35}$$

$$\varepsilon_{r\theta} = \frac{1}{2}\left(\frac{1}{r}\frac{\partial v_r}{\partial \theta}\right) \tag{5.36}$$

$$\varepsilon_{r\varphi} = \frac{1}{2}\left(\frac{1}{r\sin\theta}\frac{\partial v_r}{\partial \varphi}\right) \tag{5.37}$$

Named $\overline{\overline{D}}$ the strain rate tensor, it is possible to define the shear rate as [148]:

$$\dot{\gamma} = \sqrt{2\,\mathrm{tr}\left(\overline{\overline{D}}^2\right)} \tag{5.38}$$

The shear stress tensor $\overline{\overline{T}}$ is:

$$\overline{\overline{T}} = 2\eta(\dot{\gamma})\,\overline{\overline{D}} \tag{5.39}$$

Here the dynamic viscosity $\eta(\dot{\gamma})$ is defined according to the rheology of the fluid being extruded (e.g., (4.1) if the fluid is a molten thermoplastic following the Cross-WLF model).
Now, the radial and polar momentum equilibrium equations in spherical coordinates can be written according to previous assumptions as:

$$\frac{\partial P}{\partial r} = \frac{1}{r^2}\frac{\partial}{\partial r}(r^2\tau_{rr}) + \frac{1}{r\sin\theta}\frac{\partial}{\partial \theta}(\tau_{r\theta}\sin\theta) + \frac{1}{r\sin\theta}\frac{\partial \tau_{r\varphi}}{\partial \varphi} - \frac{\tau_{\theta\theta} + \tau_{\varphi\varphi}}{r} \tag{5.40}$$

$$\frac{1}{r}\frac{\partial P}{\partial \theta} = \frac{1}{r^2}\frac{\partial}{\partial r}(r^2\tau_{r\theta}) + \frac{1}{r\sin\theta}\frac{\partial}{\partial \theta}(\tau_{\theta\theta}\sin\theta) + \frac{1}{r\sin\theta}\frac{\partial \tau_{\theta\varphi}}{\partial \varphi} + \frac{\tau_{r\theta}}{r} - \frac{\cot\theta}{r}\tau_{\varphi\varphi} \tag{5.41}$$

By deriving (5.40) with respect to θ, and by first multiplying both members of (5.41) for r and then deriving it with respect to r itself, it is possible to combine the equations to obtain a single momentum equilibrium equation of the form:

$$\frac{\partial}{\partial \theta}\left\{\frac{1}{r^2}\frac{\partial}{\partial r}(r^2\tau_{rr}) + \frac{1}{r\sin\theta}\frac{\partial}{\partial \theta}(\tau_{r\theta}\sin\theta) + \frac{1}{r\sin\theta}\frac{\partial \tau_{r\varphi}}{\partial \varphi} - \frac{\tau_{\theta\theta}+\tau_{\varphi\varphi}}{r}\right\} = \frac{\partial}{\partial r}\left\{r\left[\frac{1}{r^2}\frac{\partial}{\partial r}(r^2\tau_{r\theta}) + \frac{1}{r\sin\theta}\frac{\partial}{\partial \theta}(\tau_{\theta\theta}\sin\theta) + \frac{1}{r\sin\theta}\frac{\partial \tau_{\theta\varphi}}{\partial \varphi} + \frac{\tau_{r\theta}}{r} - \frac{\cot\theta}{r}\tau_{\varphi\varphi}\right]\right\} \quad \textbf{(5.42)}$$

After developing the partial derivatives, a third-order ordinary differential equation (ODE) is derived. The goal is to solve this equation, together with the proper boundary conditions:

$$f(\theta = 0) = f_{max} \quad \textbf{(5.43)}$$

$$f(\theta = \alpha) = 0 \quad \textbf{(5.44)}$$

$$f'(\theta = 0) = 0 \quad \textbf{(5.45)}$$

Here f_{max} is the maximum velocity, which is reached on the axis because of the assumption to consider azimuthal symmetry. Moreover, the boundary condition introduced in (5.45) is coherent with the fact that the maximum velocity is reached on the symmetry axis.

All derivatives are performed symbolically in MATLAB, by means of the MATLAB Symbolic Toolkit. For that reason, the final equations valid for Cross-WLF and Carreau fluids have not been reported here.

It is important to note that the unknown function which appears in the third-order ODE is $f(\theta)$ and that the variables which appears after developing partial derivatives together with all possible simplifications are both r and θ. The equation is solved incrementally, by fixing a value for the radial position, namely $\bar{r}$, and then solving the third-order ODE, where the only variable is the polar coordinate θ. After finding the polar flow field at the given radial coordinate, the original equation is solved by substituting the next radial position and finding the new polar flow field; this incremental process is applied from inlet up to outlet of the fluid domain. The complication in the solution process is that the value of f_{max} is not known a priori; a solution is that to assume a trial value for the maximum velocity in the flow domain (1 [mm/s] in all computations) and to set:

$$f_{max} = f_{max,trial} \quad \textbf{(5.46)}$$

This is an initial trial value for f_{max}, which allows to calculate a trial value for the volume flow rate, according to the following equality in spherical coordinates, under the azimuthal flow assumption:

$$Q_{trial} = 2\pi \int_0^{\alpha} r^2\, v_r(r;\theta)_{trial} \sin\theta \, d\theta \quad \textbf{(5.47)}$$

Then the relative error with respect to the known volume flow rate Q is calculated:

$$\varepsilon_Q = 100\frac{Q_{trial} - Q}{Q} \quad \textbf{(5.48)}$$

And the maximum velocity value is modified accordingly:

$$v_{r,max}^{new} = v_{r,max}^{old} - v_{r,max}^{old}\,\varepsilon_Q \quad \textbf{(5.49)}$$

Then, the boundary condition (5.43) at next iteration can be found by applying (5.32):

$$f_{max}^{new} = -\rho r^2 v_{r,max}^{new} \quad \textbf{(5.50)}$$

The iterative solution process continues until the relative error on the volumetric flow rate (5.48) goes below the user defined threshold. Then, the iterative process is performed for the next radial position, up to the outlet. The MATLAB subroutine bvp5c has been implemented [149]; the solution of the boundary value problem (BVP) is returned with a fifth order accuracy. For some computations an error was returned, that means that the bvp5c function cannot solve such a complex equilibrium equation directly. In fact, it has been documented in [141] that the possibility to obtain a solution for the BVP is strictly affected by the initial condition, which is the trial function $f_{trial}(\theta)$. To give a smother solution process the continuation method is implemented.
Let's take the equations $g(x) = 0$, for which the solution is difficult to find and $h(x) = 0$, for which a simpler solution is possible. A linear combination of the two equations is:

$$z(x) = s\, g(x) + (1 - s)\, h(x) = 0; \quad 0 < s < 1 \tag{5.51}$$

Where s is a sliding parameter; if it is zero, the equality $z(x) = 0$ reduces to the equation for which solution can be easily found, namely $h(x) = 0$. If the parameter's value is unit, the equation whose solution is difficult to find, namely $g(x) = 0$, is returned. Now, the solution procedure can be divided in a series of N steps, where the equation that will be solved at k-th step of the continuation method will have the form:

$$z_k(x) = s_k\, g(x) + (1 - s_k)\, h(x) = 0 \tag{5.52}$$

The sliding factor characterizing this step is:

$$s_k = \frac{k}{N}; \quad k = \{0; 1; 2; \dots\} \tag{5.53}$$

If the number of steps is sufficient, this method allows to pass from the simple to the difficult solution, almost independently from the choice of the trial value.
The continuation method can be further generalized to solve differential equations. Let's now contextualize to a third-order ODE such as that being derived previously. Let's introduce the following BVP:

$$\begin{cases} s\left[\sum_{i=0}^{3} a_i f^{(i)}(\theta)\right] + (1 - s)\left[\sum_{i=0}^{3} b_i f^{(i)}(\theta)\right] = 0 \\ f(\theta = 0) = f_{max} \\ f(\theta = \alpha) = 0 \\ f'(\theta = 0) = 0 \end{cases} \tag{5.54}$$

It is possible to note that the boundary conditions are the same as (5.43)-(5.45). These conditions are shared by both the simple and the difficult to solve ODEs. The ODE in (5.54) is written as a sum of linear terms, but this is done only for illustrative purposes. The third-order ODE is a linear combination of the original one, whose coefficients are a_i and of a new one, whose coefficients are b_i, which is assumed as much simpler to be solved.
As a simpler model ODE, it has been chosen a functional form of $f(\theta)$ which gives a parabolic velocity profile, whose maximum is achieved for $\theta = 0$, where the function itself is f_{max}. This value is imposed as a new one at each iteration, according to previous description. The simple ODE is constructed starting from the known solutions, and it has the final form:

$$f'''(\theta) + \frac{1}{2}\theta f''(\theta) + f'(\theta) - f(\theta) + \frac{2 f_{max}\theta}{\alpha^2} = 0 \tag{5.55}$$

Where α is the semi-cone angle. The initial choice for the function f(θ) has proven to be very good; in fact, in all simulations the number of steps used to perform the continuation method has bene posed as $N = 3$, providing fast iterations. However, the choice for the initial function is not casual; in fact, it is known that for Newtonian fluids in a circular duct the velocity profile follows a parabolic pattern. Coming to non-Newtonian fluids this is no longer true, but it is straightforward to use the Newtonian case as the initial trial profile for the computation of the true velocity field.

Another factor which can affect the results is the number of mesh nodes used as input for the bvp5c function, together with the problem (5.54). A mesh of 30 nodes has been resulted in a good compromise between mesh-independent results and a reasonable computational time.

In the Results section it will be discussed extensively how the flow field develops according both to CFD and semi-analytical computations.

5.5.3. Code validation - Extrusion of thermoplastics

In this section, the comparison in terms of velocity profile between the CFD and semi-analytical BVP solutions for a Jeffery-Hamel flow will be presented. The thermoplastic material being extruded is the LATILON, for which the rheological and thermodynamical data have been reported earlier (Table 5.1).

The nozzle inlet and outlet dimensions are chosen as equivalent to that of the real extrusion nozzles. Similarly, the half of the cone opening angle is the same (30[°] – see: Figure 5.13). The flow rates being investigated ranges from 5.31 to 63.72 [mm^3/s]; for clearness, they have been normalized with respect to the lowest value.

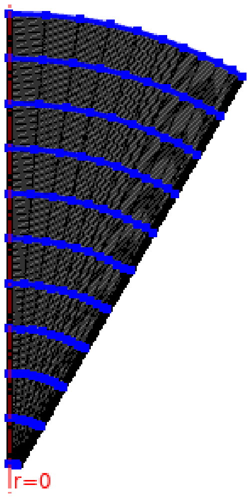

Figure 5.13. 2D axisymmetric Jeffery-Hamel problem modelled in COMSOL – only half of the plane geometry is modelled because of symmetry.

The Jeffery-Hamel flow has been modelled in COMSOL and the computational mesh has been reported in Figure 5.13. The grid is structured with a total of 11 radial cut sections (highlighted in blue in Figure 5.13) to investigate the local flow field. The number of nodes between contiguous cuts is 20. On each of the intermediate radial positions, velocity magnitude is computed.

The number of elements placed on each of the circumferential positions is gradually varied to perform the mesh independence test, according to the following Figure 5.14:

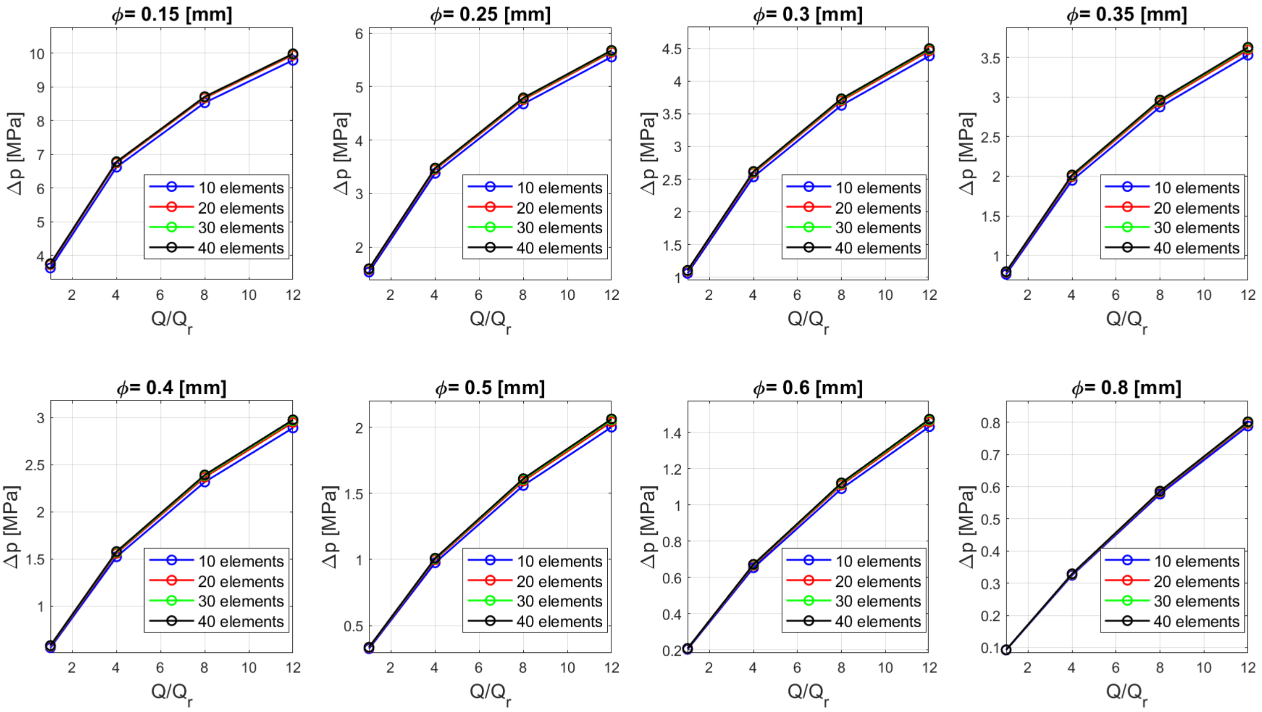

Figure 5.14. Flow characteristics for the spherically equivalent E3Dv6 nozzles' last convergent section (Jeffery-Hamel flow), at different mesh resolutions and nozzle sizes; ϕ: Nozzle exit diameter; ΔP: Pressure drop; Q: Volumetric flow rate; Q_r: reference flow rate ($5.31[\mathrm{mm}^3/\mathrm{s}]$).

To be said, flow characteristics (that is, pressure drop as a function of flow rate) follow an almost linear pattern, especially at higher nozzle diameters. In this case the shear rates are much lower, and fluid behaves as a Newtonian one. The opposite happens when lower nozzle diameters are considered, leading to increasingly non-linear flow characteristics. This has been highlighted already for the power-law model [38], especially at lower power-law index, where non-Newtonian behavior increases; moreover, the overall pressure drop is higher in latter case, because of the higher mean velocity.

Other simulations, where more than 40 elements were involved did not give different results and provided higher computational times; for that reason, 40 elements have been chosen for further computations.

The local velocity field has been computed at all the 11 radial positions; it is only a function of the polar coordinate, namely: $\mathrm{v}_\mathrm{r}^{\mathrm{local}} = \mathrm{v}_\mathrm{r}^{\mathrm{local}}(\theta)$. The same information has been extracted through CFD simulations performed in COMSOL and, by applying a proper scaling process for the polar coordinate θ, it becomes possible to compare the velocity profiles.

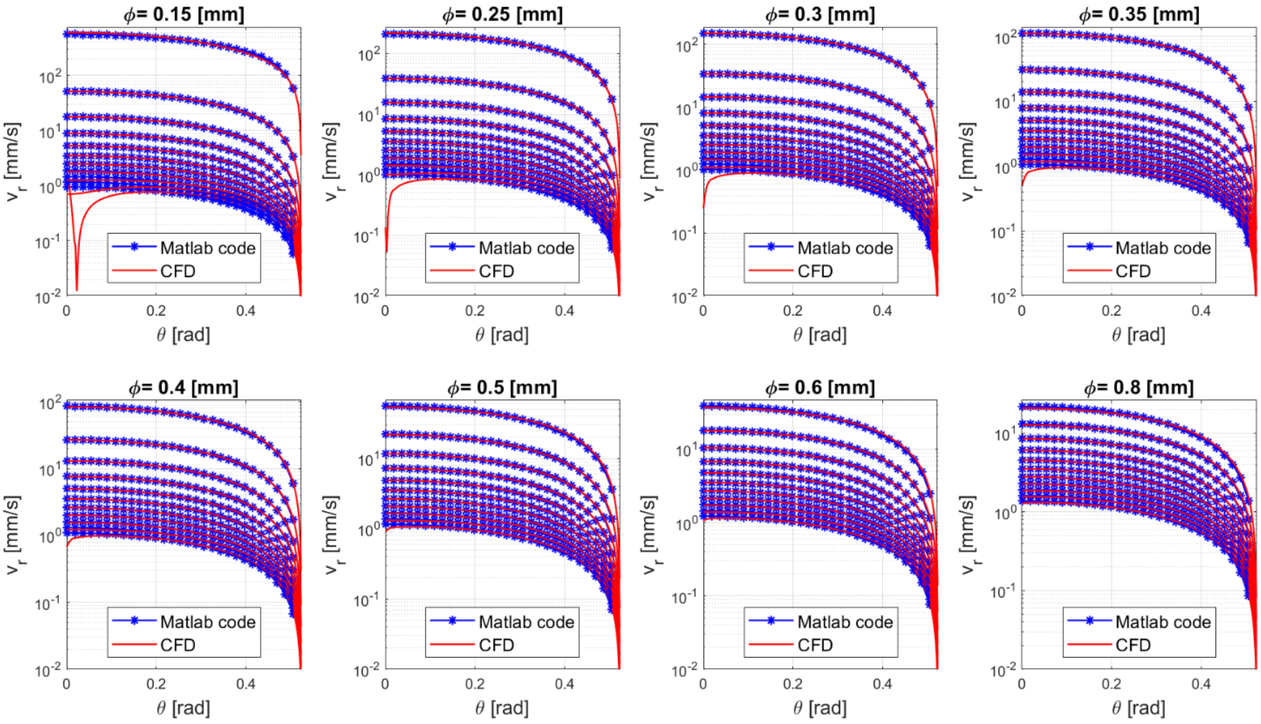

Figure 5.15. Velocity profiles for all the commercial E3Dv6 nozzles in the last converging section; ϕ: Nozzle exit diameter; θ: Polar coordinate; flow rate: $Q = 5.31[mm^3/s]$; thermoplastic material: LATILON.

Figure 5.15 shows how the MATLAB code can predict accurately the velocity profile at all radial positions; this is true for all the commercial E3Dv6 nozzles being investigated. The only exception is for the inlet section to the nozzles characterized by a lower exit diameter, because of numerical singularities; the boundary condition being imposed at inlet is that of a fully developed flow. Because of this assumption one expects to find a parabolic-like profile at inlet section, which is still well represented by the MATLAB results.

The error on the inlet velocity profile is not critical for the evaluation of derived quantities (e.g., the extrusion force in FFF), because it is a region of the computational domain characterized by lower pressure drops, and so it can be considered as a minor contribution.

Moreover, the radial velocity has been represented logarithmically, so to enhance the possible discrepancies between numerical and semi-analytical profiles. The results, however, are still very close. It is also important to remind that in CFD modeling the inertial effects are still considered, but their effect on the final velocity profile is negligible.

Because the flow field does not differ much between the CFD and semi-analytical analysis of a Jeffery-Hamel flow, the final step is that to make a comparison with the pressure field deriving from studying the fluid dynamics inside the real geometry.

Moreover, an extension of both the theory presented for axial flows in [137] and in Section 5.4.2 has been implemented, so to evaluate the error in all three cases.

As previously done for the Jeffery-Hamel flow geometrical approximation, the real nozzle geometries (see: Figure 5.2) have been investigated by means of a mesh-independence study; an unstructured mesh has been implemented, with an inflation near wall so to capture the boundary layer fluid dynamics.

All simulations have been performed on 2D axis symmetrical models, through COMSOL.

The number of finite elements is gradually increased by means of the default meshing techniques implemented in the FEM solver.

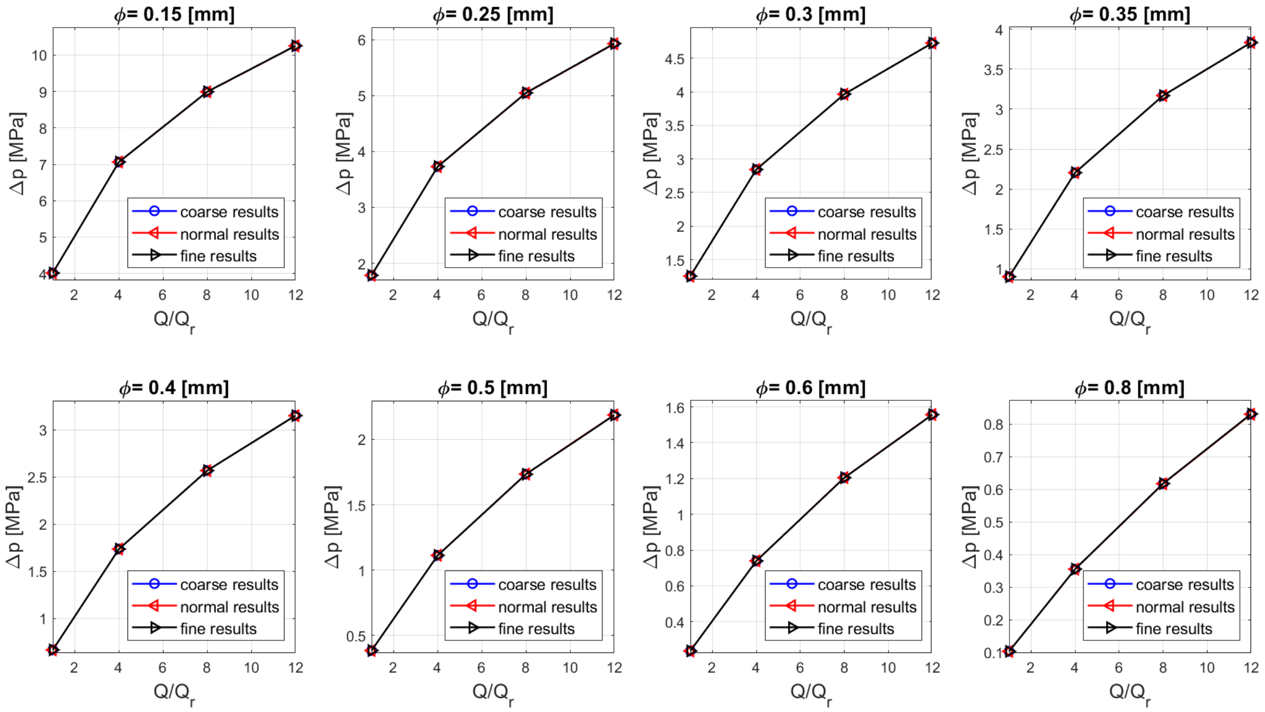

Figure 5.16. Flow characteristics for the last convergent in E3Dv6 nozzles, at different mesh resolutions and nozzle sizes; ϕ: Nozzle exit diameter; ΔP: Pressure drop; Q: Volumetric flow rate; Q_r: reference flow rate $(5.31[\mathrm{mm}^3/\mathrm{s}])$.

In Figure 5.16 the nozzle flow characteristics have been represented for all the commercial E3Dv6 nozzles, at different mesh resolutions. The results do not differ too much using finer meshes, and this is true for all nozzle geometries. In the following analysis, the default normal mesh will be implemented.

Finally, a direct comparison with an extension of the method being proposed in [137] has been implemented, taking the results of Figure 5.16 as reference for relative error computations:

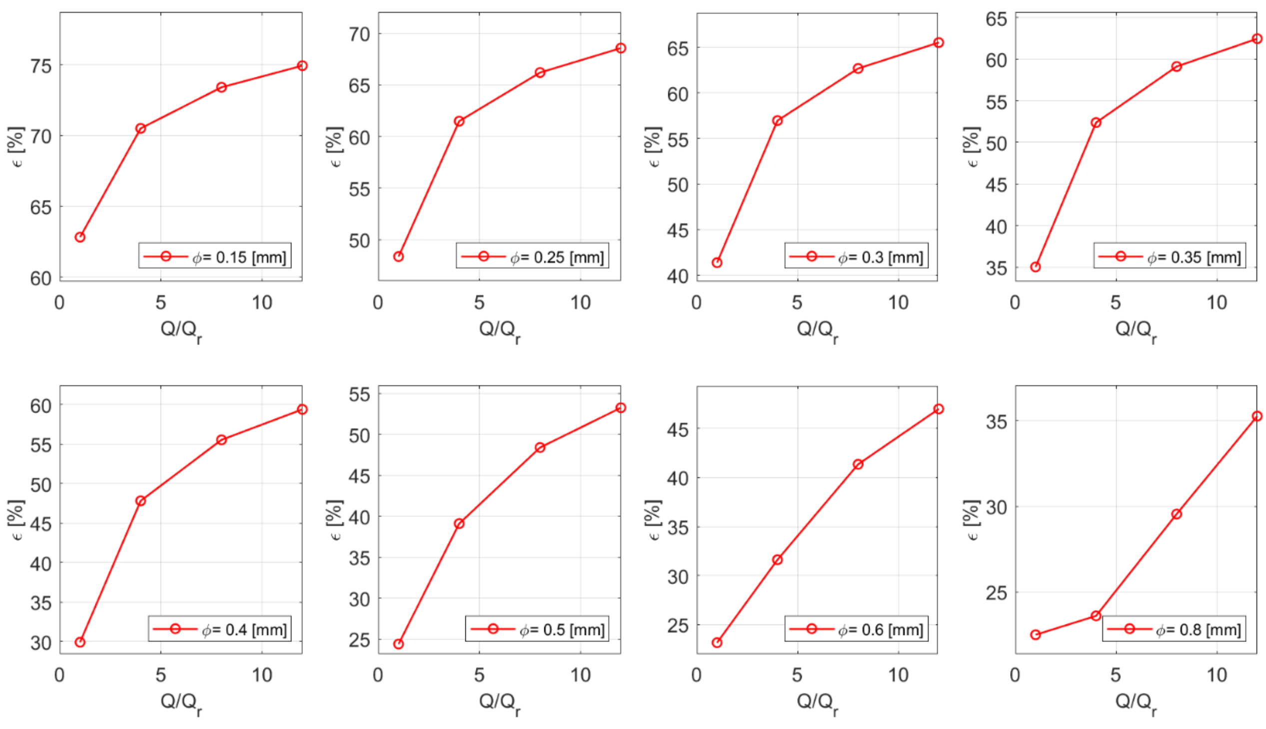

Figure 5.17. Relative error deriving from the application of the extension of the theory based on WRMS model [137]; ϕ: Nozzle exit diameter; Q: volumetric flow rate; Q_r: reference flow rate ($5.31[mm^3/s]$); ϵ: relative error on pressure drop.

In Figure 5.17 it can be easily seen that the trend is that of an increase in relative error with respect to the flow rate. Moreover, the error is greater for lower nozzle dimensions; this is easily explained by the fact that it has been proven in the previous section concerning the cylindrical die that at lower diameters the theory presented in [137] the highest errors.

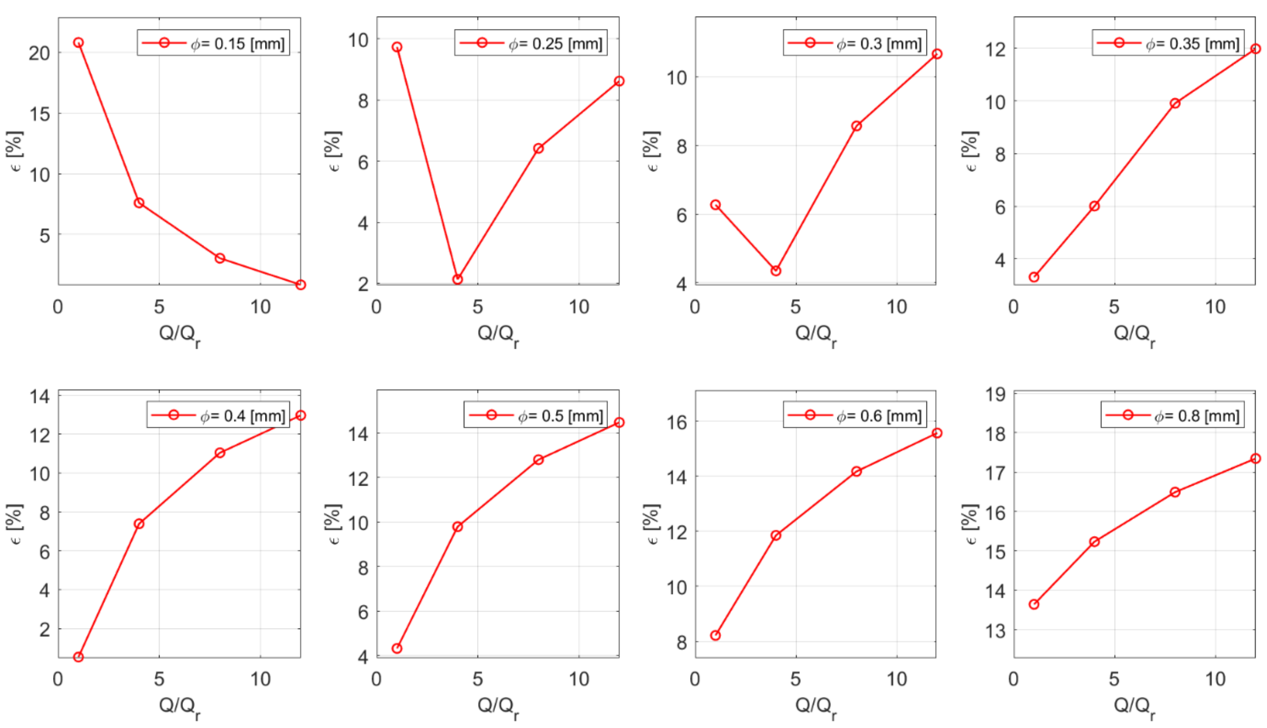

Figure 5.18. Relative error deriving from the application of the extension of the theory presented for the straight channel; ϕ: Nozzle exit diameter; Q: volumetric flow rate; Q_r: reference flow rate ($5.31[mm^3/s]$); ϵ: relative error on pressure drop.

In Figure 5.18 the relative error seems to follow a pattern like in Figure 5.17, especially for the highest nozzle dimensions. Nevertheless, its value is much lower for all nozzles and flow rates being considered; this appears as a natural consequence of the fact that the pressure drop in all the intermediate straight cylindrical nozzles used for the axial discretization of the convergent is predicted iteratively with an error of 0.1[%]. This is still true at lower diameters, so the relative errors are evidently comparable for all the nozzles. The maximum relative error still reaches 20[%], probably because dividing the convergent in a series of axial steps enforces the flow to be considered as purely axial, while it has both radial and polar components in a cylindrical reference frame.

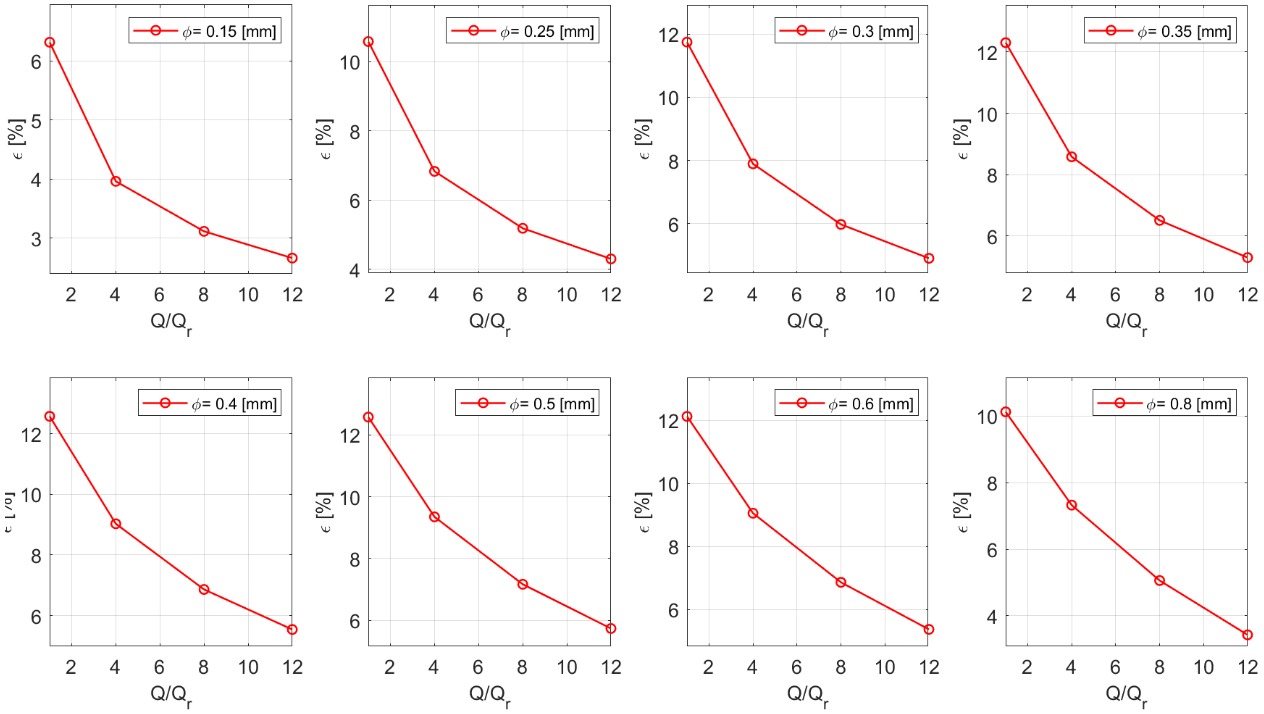

Figure 5.19. Relative error deriving from the application of the Jeffery-Hamel model applied to Cross-WLF fluids; ϕ: Nozzle exit diameter; Q: volumetric flow rate; Q_r: reference flow rate ($5.31[mm^3/s]$); ϵ: relative error on pressure drop.

In Figure 5.19 the relative error which arises from considering the flow in a convergent nozzle as the equivalent of a Jeffery-Hamel flow field has been represented. It can be noted that the trend is decreasing independently from the nozzle being chosen, and that the maximum value is reached at lower flow rates.

It must be underlined that at the higher nozzle dimensions the relative errors deriving from the application of the theory presented for straight ducts and that presented for the Jeffery-Hamel flow have opposed trends. This suggests the possibility to define an operation window where a method or the other can be used to lower as much as possible the relative error in pressure drop prediction.

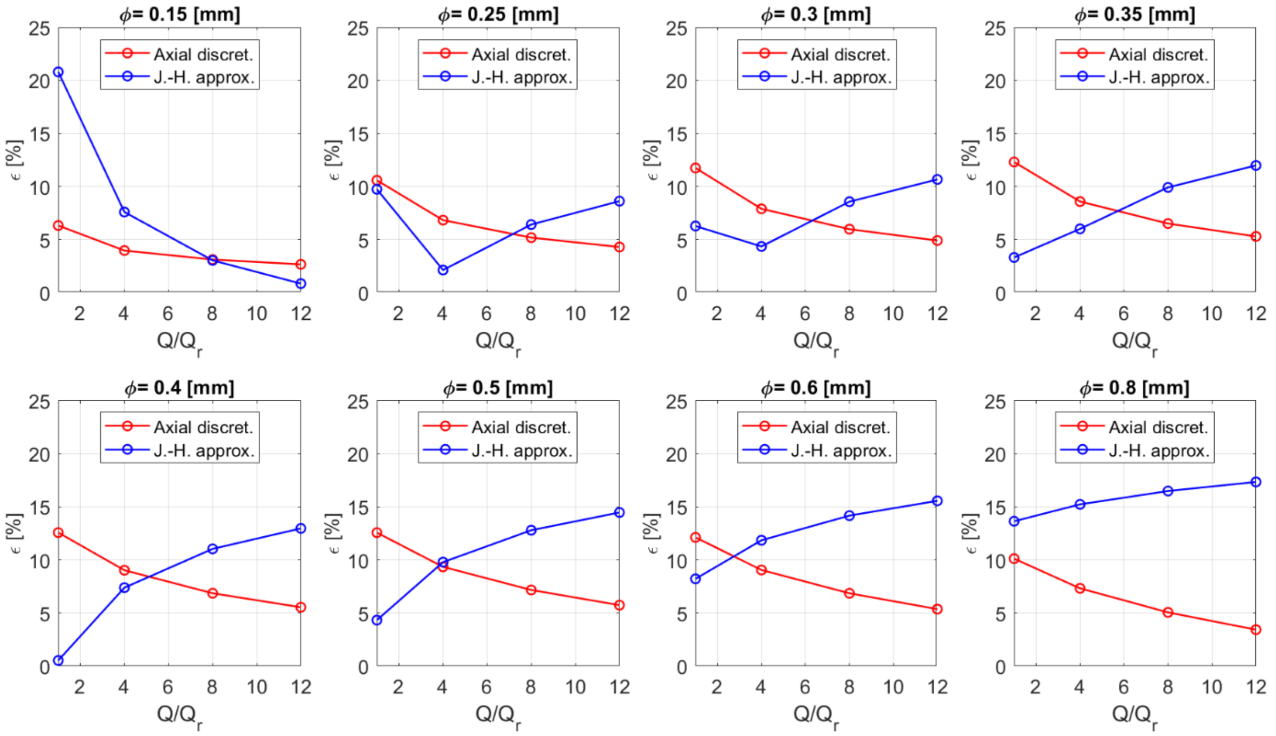

Figure 5.20. Comparison of the two proposed methods - Determination of the operating window; ϕ: Nozzle exit diameter; Q: volumetric flow rate; Q_r: reference flow rate ($5.31[mm^3/s]$); ϵ: relative error on pressure drop.

The individuation of the operating window can be done according to Figure 5.20, where both the curves of Figure 5.18 and Figure 5.19 have been overlapped; it can be concluded that by choosing the proper method the relative error in the last convergent section of an extruding nozzle for FFF is always lower than 10[%]. Finally, it must be considered that the main contribution to the overall extrusion force is represented by the last cylindrical section, where the diameter is minimum for a given nozzle. According to the theory presented earlier, pressure drop and consequently the contribution to the extrusion force can be predicted with a prescribed accuracy. It means that this contribution will lower the overall error in extruding force computation, because of the lower relative weight of the convergent section to the results.

5.5.4. Code validation – Extrusion of moisture-cured silicone

According to the following Figure 5.21, the goal is that to verify if the assumption to implement a Jeffery-Hamel flow for describing the fluid dynamics behavior in the last convergent section is reasonable; the criterion is the evaluation of the pressure drop for a range of real flow rates that can be extruded through these tapered dies.

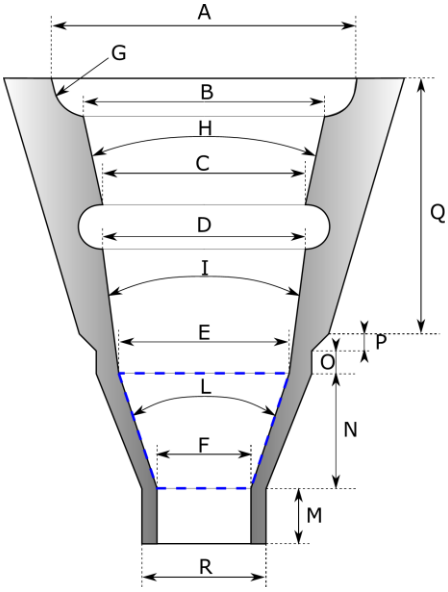

Figure 5.21. SmoothFlow nozzles internal shape; the target modeling region has been highlighted in blue dashes.

The investigation is limited to the last convergent because the opening angle is the highest for prescribed nozzle, which means that the errors deriving from approximating the real geometry with the Jeffery-Hamel one will be maximum. All dimensions are summarized in the following Table 5.3:

Table 5.3. SmoothFlow nozzles dimensions; all linear dimensions in [mm] and angular ones in [°].

Std. code	**A**	**B**	**C**	**D**	**E**	**F**	**G**	**H**	**I**	**L**	**M**	**N**	**O**	**P**	**Q**	**R**
7018052	5.28	4.19	4.055	4.01	3.45	1.6002	R3.5	3.41	3.41	6.10	0	17.4	0.69	0.46	12.86	2.00
7018099	5.28	4.19	4.055	4.01	3.45	1.1938	R3.5	3.41	3.41	7.49	0	17.27	0.69	0.46	12.95	1.63
7018157	5.28	4.19	4.055	4.01	3.45	0.8382	R3.5	3.41	3.41	8.66	0	17.27	0.69	0.46	12.86	1.24
7018216	5.28	4.19	4.055	4.01	3.45	0.5842	R3.5	3.41	3.41	9.50	0	17.27	0.69	0.46	12.95	1.02
7018297	5.28	4.19	4.055	4.01	3.45	0.4064	R3.5	3.41	3.41	10.08	0	17.27	0.69	0.46	12.95	0.81
7018390	5.28	4.19	4.055	4.01	3.45	0.2540	R3.5	3.41	3.41	10.59	0	17.27	0.69	0.46	12.95	0.79
7018416	5.28	4.19	4.055	4.01	3.45	0.2032	R3.5	3.41	3.41	10.83	0.76	17.14	0.69	0.46	12.95	0.41

The results in terms of both pressure drop and relative error with respect to CFD computations have been represented in Figure 5.22:

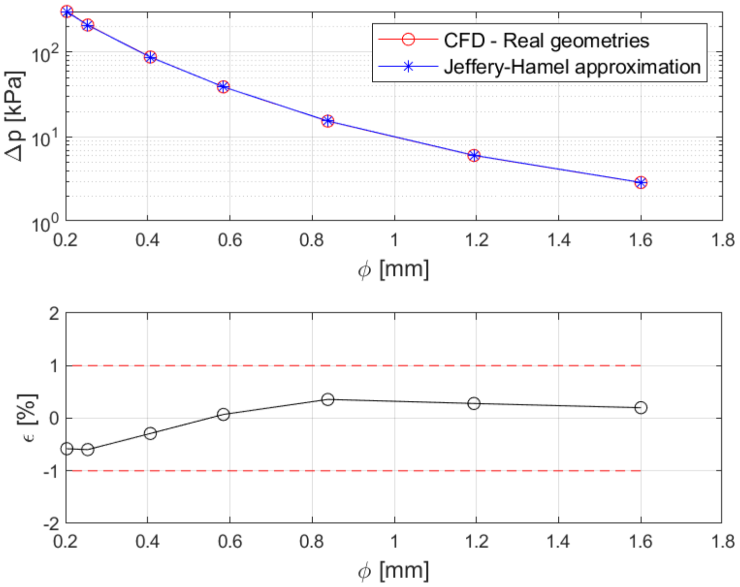

Figure 5.22. Pressure drop predictions through the real convergent geometries and Jeffery-Hamel approximation (top), together with the relative error of the latter with respect to the former (bottom); Δp: pressure drop; ϕ: nozzle exit diameter; ϵ: relative error on pressure drop; the red dotted lines delimit the $\pm 1[\%]$ relative error range ($Q = 1[mm^3/s]$).

Pressure drop decreases with increasing nozzle diameters for the same reasons being introduced for the fluid flow in straight ducts. The assumption to use the Jeffery-Hamel flow model gives pressure drops in good agreement at all convergent geometries being investigated. This is mainly due to the opening angles, which are lower by far if compared to that used for the E3Dv6 nozzles; this means that the equivalent and real tapered 2D axis symmetrical geometries are practically equivalents.

Finally, an error analysis has been done for the moisture-cured silicone extrusion; the FVM code has been implemented to perform a comparison with both CFD and semi-analytical data (at different mesh resolutions, governed by the parameter N in the bvp5c subroutine). Discretization schemes and threshold values for the residuals are the same as for the study of the straight duct. In Table A.7 (see: Appendix A), the complete error analysis has been reported, at all nozzle diameters, showing a very good agreement of the semi-analytical model with both FEM and FVM formulations. It has also been demonstrated that a mesh resolution with $N = 30$ gives a relative error which is always under $1[\%]$, with respect to both numerical methods.

5.6. Conclusions

In the present paper the description of the fluid flow in both axisymmetric straight cylindrical ducts and tapered dies has been investigated.

For the straight cylindrical ducts an iterative method based on the polynomial interpolation in the relevant shear rate range has been proposed; here the novelty with respect to previous is that the wall shear rate has not to be specified as input to the model. The interpolation range for dynamic viscosity is continuously evaluated, giving high fidelity polynomial descriptions.

The results are overall in very good agreement with CFD solutions both for Cross-WLF and Carreau rheological models, especially if compared to previous literature; this is particularly true at low nozzle diameters, which are more typical of some AM processes as FFF, silicone extrusion and bioprinting.

The theory for the straight duct has been also validated against experimental results, with respect to existing literature.

Then, the convergent ducts are described by means of a generalization on the study of the Jeffery-Hamel flow; the pressure drop prediction is still dependent on the opening angle, because the real geometry can be very different from that deriving from assuming the flow in spherical coordinates.

A further application is considered with respect to the extrusion of a moisture-cured silicone through commercial nozzles for which all internal features are known. The results in the last convergent section agree very well with CFD, opening the possibility to use the Jeffery-Hamel model for modeling the overall silicone-based extrusion process.

A first limitation of this work relies in the clear difficulty to apply the Jeffery-Hamel assumption to flows characterized by too high taper angles; in this case the inlet flow has both radial and axial components, which cannot be disregarded.

A second limitation is in the volumetric inlet flow rate; if its value is too high, the contribution of the convective term of the Navier-Stokes equation produces a discrepancy between numerical and semi-analytical velocity profiles [135]. Consequently, errors occurs in pressure profile, too.

In next Chapter, the proposed theory has been applied to moisture-cured silicone MEX. More emphasis has been given to the complete MEX process modeling.

6. Application of the generalized MEX model to the silicone based additive manufacturing

6.1. Chapter organization

MEX has become a highly desirable AM technology for creating silicone-based structures in the biomedical and soft robotics fields due to its ease of fabrication of complex structures without molding or casting. However, the lack of mathematical models for silicone MEX has limited its application.

The present Chapter seeks to bridge this gap by introducing semi-analytical and numerical models of the MEX process that can predict the extrusion force in practical scenarios, accounting the counterpressure force from the deposited silicone beads on a substrate.

The development of a tool capable of predicting the printing force arising in silicone MEX, such as the one proposed in this Chapter, can expand the role of MEX in the fabrication of silicone structures beyond the current limitations by improving the manufacturing process control, enabling the creation of thin-walled structures, and enhancing accuracy.

The Chapter has been organized as follows: in Section 6.4.1 the properties of the moisture-cured silicone and custom-made MEX setup have been introduced. The semi-analytical formulation has been briefly recalled in Section 6.4.2. A model for the counterpressure arising in bead extrusion has been outlined in Section 6.4.3. Details on CFD computations have been given in Section 6.4.4. The investigation on free-air extrusion and real MEX process has been performed in Section 6.5.1 and 6.5.2, respectively. A comparison with CFD results for both extrusion conditions has been given in Section 6.5.3. Finally, conclusions have been reported in Section 6.6.

6.2. Chapter nomenclature

A_s	Syringe front area	W_{bead}	Layer width
D_s	Syringe diameter	y	Vertical coordinate (layer deposition)
D_{ext}	Nozzle internal exit diameter	y_z	Integration constant (layer deposition)
$D_{ext}^{(n)}$	Nozzle outer exit diameter	z	Streamwise coordinate (layer deposition)
$f(\theta)$	Polar function (Jeffery-Hamel flow in a cone)	α	Half of the opening angle (Jeffery-Hamel flow in a cone)
f_{max}	Maximum value for $f(\theta)$ (Jeffery-Hamel flow in a cone)	$\dot{\gamma}$	Shear rate
F_C	Force due to counterpressure	Δp_N	Pressure drop in the nozzle

F_N	Nozzle contribution to extrusion force	Δp_C	Counterpressure
F_T	Overall extrusion force	η_0	Zero shear rate viscosity
n	Power-law index	η_∞	Infinite shear rate viscosity
p	Pressure	η	Dynamic viscosity
Q	Volumetric flow rate	θ	Polar coordinate (Jeffery-Hamel flow in a cone)
r	Radial coordinate (Jeffery-Hamel flow in a cone)	λ	Relaxation time in Carreau model
t	Layer thickness	ρ	Density
$u_z(y)$	Nonzero velocity component (layer deposition)	τ_{ij}	ij-th component of the stress tensor
$v_r(r;\theta)$	Radial velocity (Jeffery-Hamel flow in a cone)	φ	Azimuthal coordinate (Jeffery-Hamel flow in a cone)
V_p	Printing speed	ϕ	Nozzle outlet diameter

6.3. Introduction

Silicone has been used for a variety of applications, including medical [150–156], electronics [157], and aerospace fields [158]. More recently, this class of materials, which has both organic and inorganic features [159], has become common for actuators in soft robotics [160–162] and wearable devices [163,164]. The increasing usage of silicone is due to its high elongation to failure (up to 1260[%]) [165], low elastic modulus (0.5-30 [MPa]) [125], thermal and electrical insulation, softness, compliance, high fatigue life [166,167], resistance to ultraviolet radiation[168], chemical stability, and biocompatibility with specific architectural materials as nickel-titanium composites [169,170].

The utilization of a flexible manufacturing method is needed to take full advantage of silicone; MEX appears to offer many benefits for the fabrication of complex silicone geometries. Several studies have shown the suitability of MEX for the fabrication of meniscus implants [171], soft robots [172–174], soft structures with embedded actuators [175], sensors [176], open-cell foams [177], grippers and rehabilitation devices [178].

MEX processes are negatively affected by poor repeatability, accuracy, and control [179]; a way to improve these aspects consists of the mitigation of the forces occurring during the extrusion process. When these forces are too high, deformation and skewing of the final 3D printed part might occur resulting in manufacturing waste. Several process parameters have been studied and held accountable for the reduction of printing forces, such as flow rate, nozzle diameter, layer thickness and printing speed [85,115,125]. An excellent method to study the printing forces consists in developing analytical and numerical models: in this way process parameters can be set (during the slicing phase) to reduce the overall manufacturing force [180]. The silicone MEX characteristics in free-air conditions were evaluated in [181], finding a good correlation between the computed flow rate and FEM results at different pressure inputs. In [182] the effect of pressure and time of application was investigated via FEM for the extrusion of silicone in a MEX system: the authors pointed out that the viscosity variation affects mainly the layer width. In [124] the force generated in silicone MEX was computed via FVM, showing a discrepancy with the force values experimentally obtained, especially at higher flow rate values.

In this Chapter, silicone MEX has been modeled through the computational and semi-analytical methodologies introduced in Chapter 5 with the following goal: to predict the overall printing force in real 3D printing scenarios.

These models have been experimentally validated by using a custom-made MEX machine capable of extruding silicone: in particular, the effect of three process parameters (i.e., flow rate, layer thickness and nozzle diameter) has been explored. It has been shown that the counterpressure force resulting from the interaction between the extruded bead and the build plate needs to be mitigated, to reduce the overall printing force.

The custom-made silicone MEX setup was developed in the HBS Laboratory (University of Texas at Dallas, Richardson, TX).

Models show a very high accuracy in predicting the printing force, considering the counterpressure force, as a function of the process parameters (nozzle size, flow rate and layer thickness). The semi-analytical model accuracy ranges between 89.7[%] and 99.7[%], while the numerical accuracy ranges between 95.4[%] and 99.3[%].

The novelty is twofold: i) the modeling of the counterpressure force, and ii) the correlation of printing forces to process parameters (i.e., nozzle size, layer thickness, flow, and printing speed), making the proposed model suitable for the prediction of every force contribution (force into the nozzle and counterpressure force) in practical silicone 3D printing scenarios.

6.4. Materials and methods

The goal is to provide models capable of predicting the force occurring during silicone MEX, as a function of the process parameters set in the slicing software (i.e., nozzle dimension, flow rate, and layer thickness).

First, the rheological model needed to simulate the silicone extrusion through a nozzle has been recalled, as are the last advances aimed at solving the Jeffery-Hamel problem for a Carreau fluid [98]. The present study extends the findings of [98], where a general theory for the extrusion of a generic non-Newtonian fluid through a tapered duct is introduced; in this Chapter, that model has been implemented (considering several process parameters) along with experimental validation. Subsequentially, an original semi-analytical MATLAB model to correlate the force occurring during the 3D printing process with the abovementioned process parameters (counterpressure modeling) has been developed and validated by using a custom-made MEX silicone 3D printer alongside CFD tests.
All variables are listed in Section 6.2.

6.4.1. Material data and silicone MEX setup

The moisture-cured silicone introduced in the mathematical model for the flow of complex fluids in cylindrical ducts (see: Section 5.4.4) has been chosen for practical extrusion tests; particular attention has been paid to avoid its curation during the experiments by setting a very low extrusion time (1 to 5 [min]).
The present material has been successfully utilized in [98,166,167,181] to create soft structures via the MEX method.
The dynamic viscosity $\eta(\dot{\gamma})$ is defined according to the Carreau model:

$$\eta = \eta_\infty + (\eta_0 - \eta_\infty)[1 + (\lambda\dot{\gamma})^2]^{\frac{n-1}{2}} \tag{6.1}$$

The main properties have been listed in previous Chapter and are briefly recalled:

Table 6.1. Parameters for the moisture-cured silicone.

Symbol	Parameter name	Value
ρ	Density	1040 [kg/m^3]
n	Power-law exponent	0.5
η_∞	Infinite-shear-rate viscosity	0 [Pa s]
η_0	Zero-shear-rate viscosity	62.5 [Pa s]
λ	Relaxation time	0.0173 [s]

A custom-made inexpensive MEX 3D printer has been used to validate the proposed models, by performing several experiments. The working mechanism is here described: a syringe (acting as silicone reservoir) is pushed by a pushing plate connected to a stepper motor: in this way, the silicone flows out from a calibrated nozzle, as shown in Figure 6.1 – a.
The custom-made 3D printing machine [175] has been equipped with a measurement setup to evaluate the printing force during the extrusion process.
The main elements used to evaluate the force are here described:

- A very thin piezoresistive force sensor (Flex Force A 301) has been placed between the pushing part and the syringe piston. The sensor can measure forces between 4.4 [N] and 4448 [N].

- The force sensor is connected to the Arduino Uno microcontroller board through a voltage divider circuit.

- Force was recorded using the “CoolTerm” software.

Two different nozzle sizes (ϕ1.6 [mm] and ϕ0.84 [mm]), three flow rate values (in [ml/h]) and two layer thickness values (in [mm]) have been investigated.

It is worth mentioning that layer thickness is hereinafter defined as the process parameter (nominal layer thickness) that can be set in the slicing software and not as the actual thickness measured on extruded silicone beads.

As described in Section 6.5, two sets of experiments were carried out: the first one to evaluate the force during free-air extrusion and the second one to evaluate the counterpressure contribution while extruding beads over the build plate.

The forces occurring during the extrusion of silicone over a substrate (build plate) are described in Sections 2.2 and 2.3 and can be summarized in two main aspects: i) the force generated inside the nozzle $\mathrm{F_N}$, and ii) the counterpressure force $\mathrm{F_C}$ occurring in real case of 3D printing scenario due to the interaction between the extruded layer and the substrate (build plate). As a matter of fact, the overall total printing force $\mathrm{F_T}$ result is the sum of $\mathrm{F_N}$ and $\mathrm{F_C}$. Both the force contributions, shown in a schematic representation in Figure 6.1 – b, have been modeled and experimentally verified.

As a first step, the extrusion force values in free-air extrusion have been measured: namely the force generated into the nozzle $\mathrm{F_N}$. In the second part of this study, a new set of experiments was carried out to 3D print silicone beads on the built plate (the same process parameters used to calculate $\mathrm{F_C}$ have been set): the overall extrusion force $\mathrm{F_T}$ was directly measured with the proposed setup and by deducting $\mathrm{F_N}$ to $\mathrm{F_T}$, the counterpressure contribution $\mathrm{F_C}$ has been calculated:

$$\mathrm{F_C} = \mathrm{F_T} - \mathrm{F_N} \tag{6.2}$$

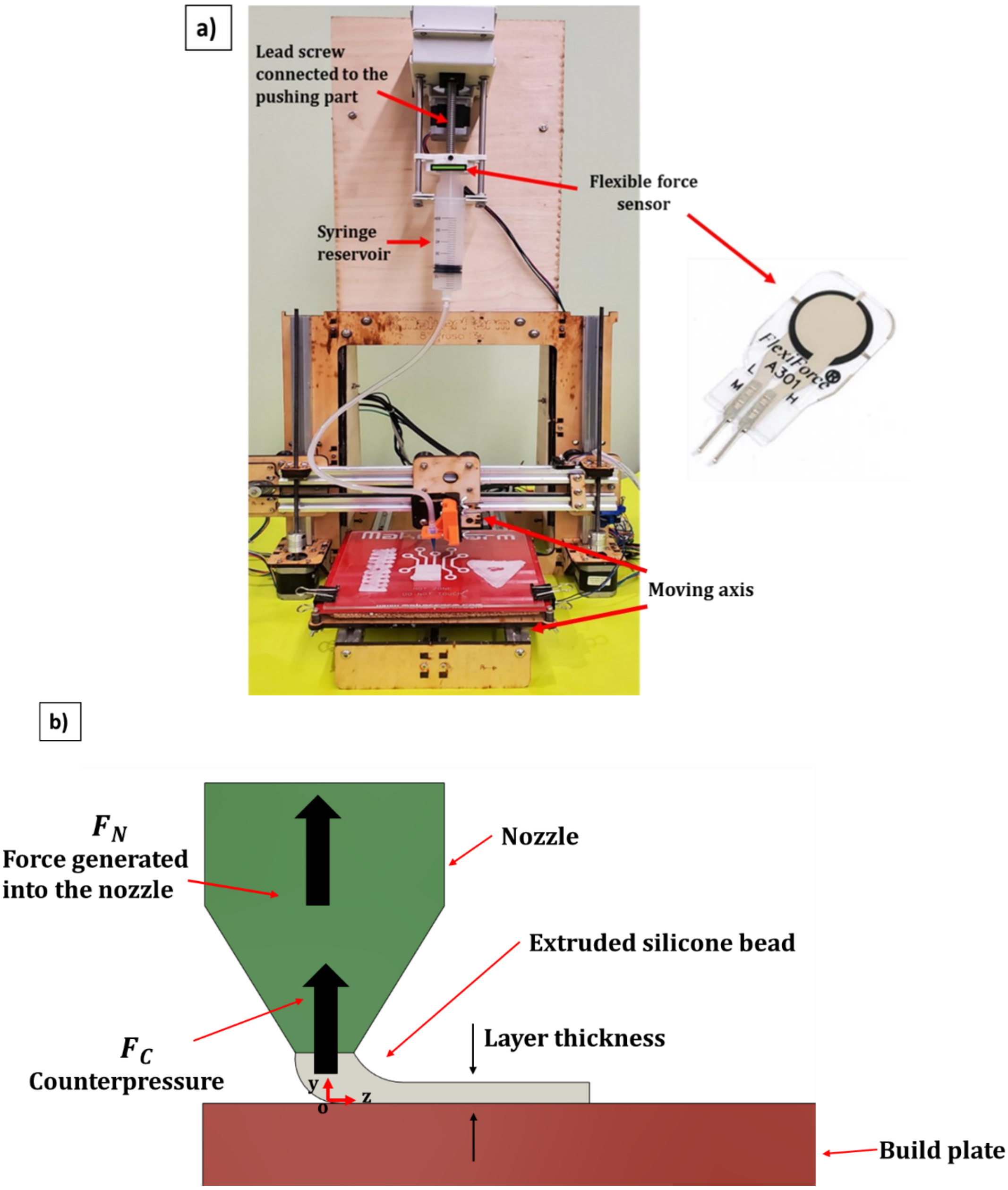

Figure 6.1. a.) Custom-made MEX 3D Printer for the silicone extrusion with force sensor to detect the extruding force, and b.) schematic representation of forces in silicone MEX.

6.4.2. Semi-analytical model of the fluid flow in the nozzle – a brief recall

According to previous Chapter, the fluid flow in a nozzle can be studied by choosing spherical coordinates (r; θ; φ); the radial coordinate is taken as positive if it points from the center of an ideal sphere outwards. The other two coordinates are the polar and azimuthal ones, respectively (see: Figure 6.2 – c):

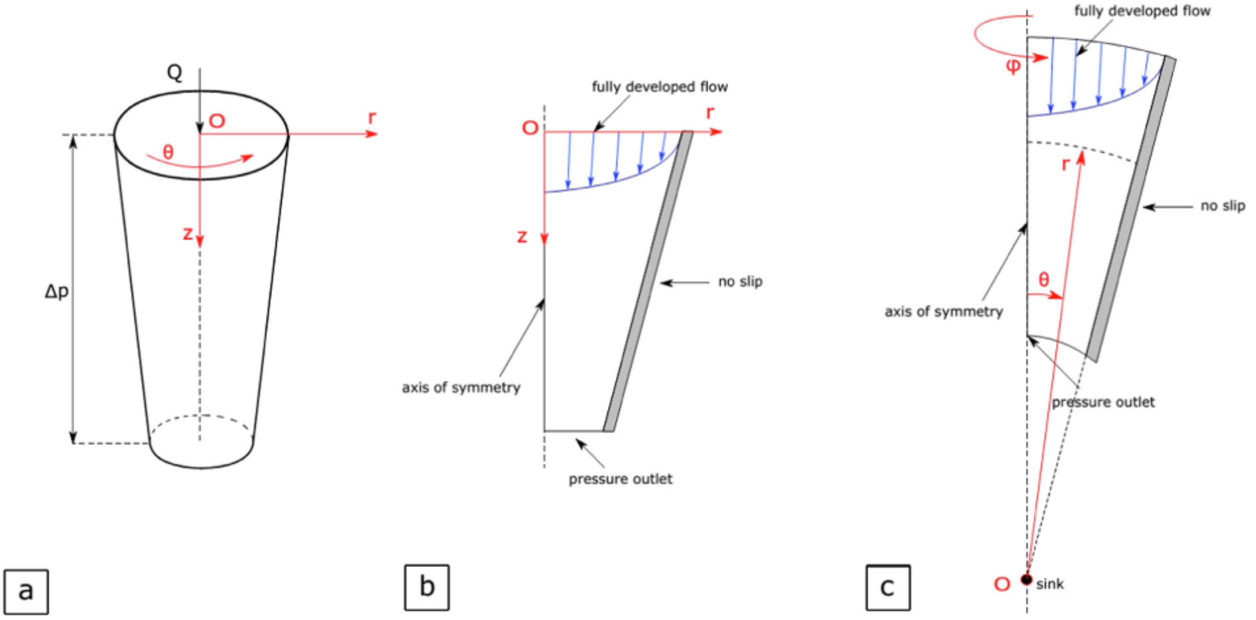

Figure 6.2. Modeling of flow through a nozzle, a.) Real nozzle geometry; b.) 2D axisymmetric model; c.) 2D axisymmetric model used for the Jeffery-Hamel modeling.

The assumptions underlying the mathematical formulation of the Jeffery-Hamel flow in a cone are as follows:

- The flow is assumed to be incompressible, stationary and isothermal,
- Negligible inertial effects and body forces,
- No-slip condition at walls,
- Azimuthal symmetry ($\partial(\cdot)/\,\partial\varphi = 0$), and
- Purely radial flow (namely, the only nonzero velocity component in spherical coordinates is $v_r = v_r(r;\,\theta)$).

The main purpose is to solve the mass and momentum equations in spherical coordinates. Because of the assumption of dealing with purely radial flow, the mass conservation gives:

$$v_r = -\frac{f(\theta)}{\rho r^2} \tag{6.3}$$

Here ρ is the fluid density, $f(\theta)$ a polar coordinate-dependent function and r the radial coordinate where the flow field is calculated (see: Figure 6.2 – c). The flow is directed inwards, while the positive radial direction is outwards, and this motivates the minus sign.
The momentum conservation along radial and azimuthal coordinates gives:

$$\frac{\partial P}{\partial r} = \frac{1}{r^2}\frac{\partial}{\partial r}(r^2\tau_{rr}) + \frac{1}{r\sin\theta}\frac{\partial}{\partial\theta}(\tau_{r\theta}\sin\theta) + \frac{1}{r\sin\theta}\frac{\partial\tau_{r\varphi}}{\partial\varphi} - \frac{\tau_{\theta\theta}+\tau_{\varphi\varphi}}{r} \tag{6.4}$$

$$\frac{1}{r}\frac{\partial P}{\partial \theta} = \frac{1}{r^2}\frac{\partial}{\partial r}(r^2\tau_{r\theta}) + \frac{1}{r\sin\theta}\frac{\partial}{\partial\theta}(\tau_{\theta\theta}\sin\theta) + \frac{1}{r\sin\theta}\frac{\partial\tau_{\theta\varphi}}{\partial\varphi} + \frac{\tau_{r\theta}}{r} - \frac{\cot\theta}{r}\tau_{\varphi\varphi} \tag{6.5}$$

Equations (6.4) and (6.5) can be combined to erase the derivative of pressure with respect to the azimuthal coordinate. By deriving (6.4) with respect to θ, and by first multiplying both members of (6.5) for r and then deriving it with respect to r itself, it is possible to combine them to obtain a single momentum equation:

$$\begin{aligned}\frac{\partial}{\partial\theta}\left\{\frac{1}{r^2}\frac{\partial}{\partial r}(r^2\tau_{rr}) + \frac{1}{r\sin\theta}\frac{\partial}{\partial\theta}(\tau_{r\theta}\sin\theta) + \frac{1}{r\sin\theta}\frac{\partial\tau_{r\varphi}}{\partial\varphi} - \frac{\tau_{\theta\theta}+\tau_{\varphi\varphi}}{r}\right\} \\ = \frac{\partial}{\partial r}\left\{r\left[\frac{1}{r^2}\frac{\partial}{\partial r}(r^2\tau_{r\theta}) + \frac{1}{r\sin\theta}\frac{\partial}{\partial\theta}(\tau_{\theta\theta}\sin\theta) + \frac{1}{r\sin\theta}\frac{\partial\tau_{\theta\varphi}}{\partial\varphi} + \frac{\tau_{r\theta}}{r} - \frac{\cot\theta}{r}\tau_{\varphi\varphi}\right]\right\}\end{aligned} \tag{6.6}$$

The shear stress components are expressed coherently in spherical coordinates and the dependence of dynamic viscosity from shear rate is specified accordingly to (4.1).

After developing the partial derivatives, a third-order ODE is derived. All derivatives are performed by using MATAB Symbolic Toolkit. After some developments, the ODE presents both r and θ variables. The value of r is imposed by discretizing the cone in a series of axial steps; a representation of a generic calculation step was presented in Figure 6.2 – c.

The variable which appears in the final ODE is f(θ), and the problem is BVP with the following boundary conditions:

$$f(\theta = 0) = f_{max} \tag{6.7}$$

$$f(\theta = \alpha) = 0 \tag{6.8}$$

$$f'(\theta = 0) = 0 \tag{6.9}$$

Here f_{max} is the maximum value of f(θ), which is reached on the axis because of the assumption of azimuthal symmetry.

The BVP is solved iteratively by means of the MATLAB function bvp5c, together with a continuation method to provide numerical stiffness (see: Chapter 5). The iterative process continues until the actual flow rate is found. In Section 6.5, it will be discussed how the flow field develops according both to CFD and semi-analytical computations.

6.4.3. Modeling the bead deposition

A key aspect characterizing MEX processes is the counterpressure contribution: this is the force generated during the bead deposition due to the interaction between the material flowing out from the nozzle and the substrate (build plate or previous extruded layer).

Here only the first layer deposition has been modeled; it has been schematically represented in Figure 6.3.

The 2D domain where the mass and momentum equations have been numerically discretized and solved, is shown in Figure 6.3 – d, alongside with boundary conditions.

The cross-section of the extruded bead is assumed to be rectangular in all the calculations.

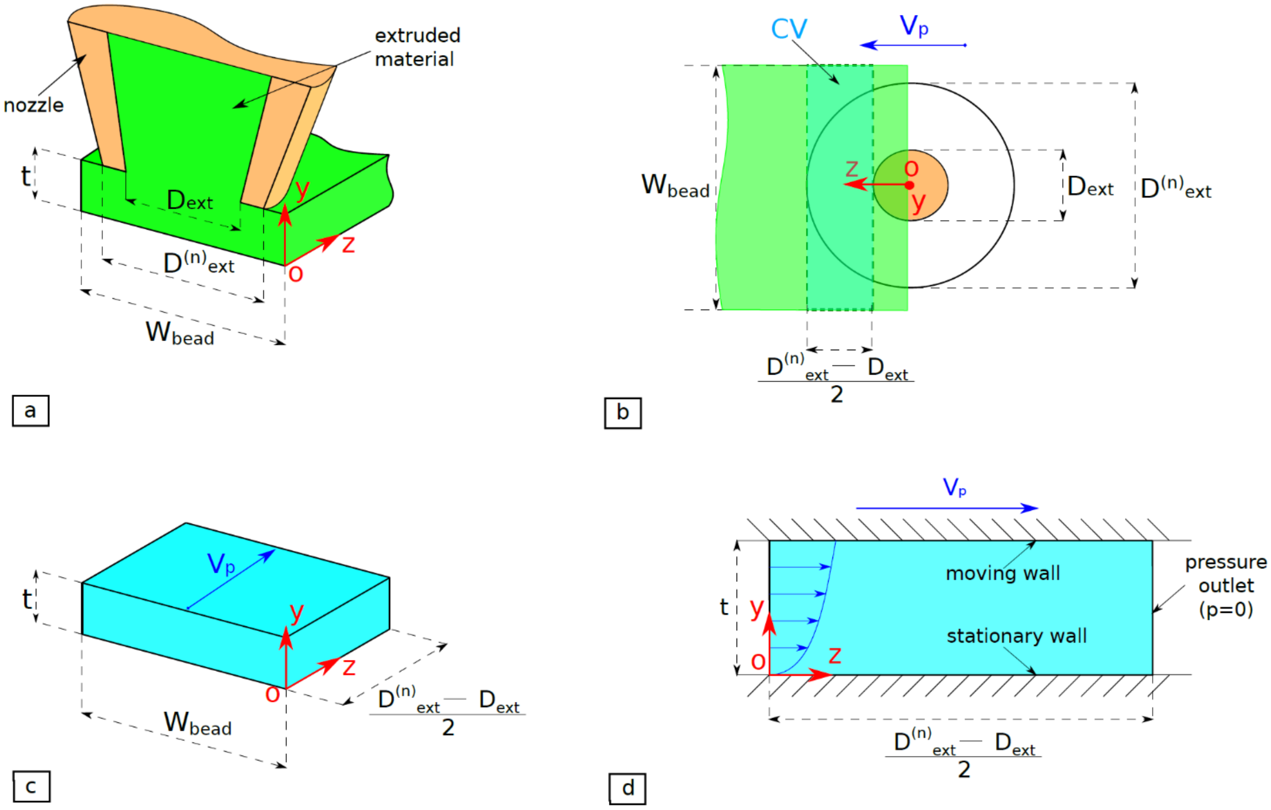

Figure 6.3. a.) Internal nozzle and layer geometries; b.) Bottom view of the deposition process, with indication of the control volume (CV); c.) 3D model of the computational CV; d.) Boundary conditions.

The following assumptions have been made:

- The flow is incompressible, stationary and isothermal,
- Negligible inertial and body forces,
- No-slip condition at walls (Figure 6.3 – d),
- The nozzle printing speed is given to the upper wall of the control volume (V_p, in the following), and
- The only nonzero velocity component is $u_z(y)$.

From the last assumption it appears clear that the only nonzero shear rate is $\dot{\gamma}_{zy}$, renamed as $\dot{\gamma}$, for brevity. Since the goal is solving the momentum equation and finding velocity and pressure profiles by means of the boundary conditions of Figure 6.3, the rheological model (4.1) has been interpolated:

$$\eta = p_4 + p_3\dot{\gamma} + p_2\dot{\gamma}^2 + p_1\dot{\gamma}^3 \tag{6.10}$$

The momentum equation along printing direction is:

$$\frac{\partial \tau}{\partial y} = \frac{\partial p}{\partial z} \tag{6.11}$$

Where τ is the shear stress:

$$\tau = \eta \dot{\gamma} \tag{6.12}$$

By integrating (6.11) with respect to y, and by using the shear stress definition (6.12) together with the interpolation for the dynamic viscosity (6.10), (6.11) can be rewritten as follows:

$$p_4 + p_3\dot{\gamma} + p_2\dot{\gamma}^2 + p_1\dot{\gamma}^3 = \frac{\partial p}{\partial z}(y - y_z) \tag{6.13}$$

Here y_z is an integration constant, to be determined through the proper boundary conditions on u_z.
The only physical solution of (6.13) is:

$$\dot{\gamma} = -\frac{1}{3p_1}\left[p_2 + \left(\frac{d_1 + \sqrt{d_1^2 - 4d_0^3}}{2}\right)^{1/3} + d_0\left(\frac{d_1 + \sqrt{d_1^2 - 4d_0^3}}{2}\right)^{3}\right] \tag{6.14}$$

Where the following positions have been made:

$$d_0 = p_2^2 - 3p_1p_3 \tag{6.15}$$

And:

$$d_1 = 2p_2^3 - 9p_1p_2p_3 + 27p_1^2\left[p_4 - \frac{\partial p}{\partial z}(y - y_z)\right] \tag{6.16}$$

As shown in Figure 6.3 – d, the kinematics boundary conditions are:

$$\begin{cases} u_z(y = 0) = 0 \\ u_z(y = t) = V_p \end{cases} \tag{6.17}$$

By applying the shear rate definition, (6.17) can be rewritten in an integral form:

$$\int_0^t \dot{\gamma}(y)\, dy = V_P \tag{6.18}$$

Where $\dot{\gamma}(y)$ has been expressed in (6.14).
Then, mass conservations along printing direction gives:

$$Q = W_{bead}\int_0^t y\, \dot{\gamma}(y)\, dy + t\, W_{bead}\, V_p \tag{6.19}$$

Here Q is the volumetric flow rate, t the specified layer thickness and W_{bead} the layer width:

$$W_{bead} = \frac{Q}{t\, V_p} \tag{6.20}$$

The system (6.18)-(6.19) is solved in a MATLAB subroutine, after discretizing the integrals with Gauss-Legendre quadrature. The outcomes are the integration constant y_z and the pressure gradient $\partial p/\partial z$. The, counterpressure Δp_C is calculated by integration along z-direction, as in Figure 6.3 – d:

$$\Delta p_C = \int_0^{\frac{D_{ext}^{(n)} - D_{ext}}{2}} \frac{\partial p}{\partial z} dz \tag{6.21}$$

The syringe pushing area is (see: Section 6.4.1):

$$A_s = \frac{\pi D_s^2}{4} \tag{6.22}$$

Here D_s in the syringe diameter. The counterpressure force is:

$$F_C = A_s \, \Delta p_C \tag{6.23}$$

6.4.4. Numerical model

6.4.4.1. Force generated into the nozzle – no counterpressure contribution

The semi-analytical method aiming at modeling the silicone fluid dynamics in the nozzle has been validated against both CFD and experimental data. The isothermal single-phase flow of a Carreau fluid has been modeled through COMSOL. The main goal is to check the discrepancy between:

- Velocity fields at different axial positions.
- Overall pressure drops.

The outcomes of the CFD flow simulations in the nozzle geometry and from the solution of the BVP problem proposed in Section 6.4.2 have been compared.

To lower the number of degrees of freedom, a 2D axisymmetric domain has been modeled.

The description of the computational domain, together with the boundary conditions being implemented, has been reported in 2 – b.

The boundary conditions are:

- Velocity inlet: a fully developed flow has been imposed; under a prescribed value of the volumetric flow rate, COMSOL evaluates a parabolic-like inlet velocity profile. This condition is more representative of the experimental setup since the force measurement is performed in stationary extrusion conditions,
- No slip: there is no relative motion between the silicone particles and the nozzle walls,
- Symmetry axis: it allows to study the 3D problem via a 2D axisymmetric model, and
- Pressure outlet: a zero average pressure is imposed at the nozzle outlet and fluid flow is assumed to be fully developed.

To make a comparison between velocity fields calculated at different axial positions by means of the semi-analytical and CFD codes, 22 sections have been placed between the inlet and the outlet of each nozzle (11 in the first tapered control volume and 11 in the second one). At each axial position the velocity field was extracted and compared.

6.4.4.2. Counterpressure contribution

The semi-analytical formulation for the bead deposition (Section 6.4.3) has been compared with numerical results, found by means of 2D fluid flow analyses in COMSOL.

The boundary conditions are:

- Velocity inlet: a fully developed flow has been imposed; under a prescribed value of the volumetric flow rate, COMSOL evaluates a parabolic-like inlet velocity profile,

- Pressure outlet: fully developed flow with zero average pressure, and

- No slip: no relative motion between the silicone particles and the nozzle wall.
    - Upper wall: its velocity corresponds to V_p.
    - Lower wall: the built plate is assumed to be stationary.

Gravity, inertia, and surface tension effects were not included because of the higher magnitude of viscous effects.

The fluid flow has been solved on a high-fidelity structured mesh, with inflation near the walls, where higher velocity gradients are expected.

A mesh-independence study has been performed to find the optimum number of elements for both the fluid flow in the nozzle and in the deposited layer (see: Appendix B – Section B.2).

6.5. Results and discussion

In the present Section, the results obtained from the semi-analytical, numerical and experimental phases are described and compared. Two set of data have been collected: i) extrusion in free-air (only F_N) and ii) bead deposition over the build plate (both F_N and F_C).

6.5.1. Free-air extrusion – force into the nozzle, no counterpressure

Two nozzle dimensions have been investigated: a big nozzle (outlet diameter of 1.6 [mm]) and a small nozzle (outlet diameter of 0.84 [mm]). The velocity and pressure fields inside the nozzles have been evaluated to find the pumping characteristics in free-air extrusion.

After evaluating the pressure drop through the nozzle, the corresponding extrusion force component is given by the equation:

$$F_N = A_s \Delta p_N \tag{6.24}$$

Here A_s is the syringe front area (6.22) and Δp_N is the pressure drop which develops along the nozzle.

Two flow rate values (in [ml/h]) have been studied for every nozzle: a low value and a high value.

Recalling the extrusion mechanism of the custom-made 3D printer is needed to explain the different flow rates values.

A stepper motor is connected to the pushing part which in turn pushes the syringe piston: the amount of material per time unit flowing out from the nozzle depends on how fast the motor spins. Two values of rotation per minute (RPM) have been set for both the nozzles: a low value (identical for both the nozzles) and a high value (identical for both the nozzles). This explains why the low and high value of flow rate for the two nozzles is not the same: it is a direct consequence of the RPM of the motor. The value changed in the slicing software was not the flow value but the RPM of the motor. The flow rates values are listed in Table 6.2.

Table 6.2. Experimental nozzle forces at varying flow rates and nozzle sizes.

Nozzle [mm]	RPM set for the motor	Flow rate [ml/h]	Flow rate value	Nozzle force (F_N), measured experimentally [N]
Small (ϕ0.84)	Low	4.88	Low	11.49
Small (ϕ0.84)	High	21.55	High	37.43
Big (ϕ1.6)	Low	7.31	Low	2.70
Big (ϕ1.6)	High	24.35	High	13.12

Before making a comparison with the semi-analytical and experimental data, the minimum number of finite elements with no significant variation in terms of nozzle extrusion force has been evaluated: the mesh-independence study for the free-air extrusion has been performed, and the ‘Coarse’ mesh has been adopted for all computations (see: Appendix B – Section B.2).

6.5.2. Bead deposition over the build plate – counterpressure

The effect of the counterpressure needs to be added to the force generated into the nozzle to correlate the overall extrusion force to the layer thickness (t) process parameter. The same flow rate values used in 3.1 have been used here too.

In Table 6.3 the layer thickness values for every combination of nozzle and flow rate values are listed as well as the counterpressure forces experimentally measured using (6.2).

Table 6.3. Experimental counterpressure forces at varying flow rates, layer thicknesses and nozzle sizes.

Nozzle [mm]	Flow value	Layer thickness (t) [mm]	Percentage of nozzle outlet diameter/ value	Counterpressure force (F_c), measured experimentally [N]
Small (ϕ0.84)	Low	0.336	40[%]/ Low	30.49
Small (ϕ0.84)	Low	0.672	80[%]/ High	10.35
Small (ϕ0.84)	High	0.336	40[%]/ Low	30.52
Small (ϕ0.84)	High	0.672	80[%]/ High	10.36
Big (ϕ1.6)	Low	0.64	40[%]/ Low	17.95
Big (ϕ1.6)	Low	1.28	80[%]/ High	5.54
Big (ϕ1.6)	High	0.64	40[%]/ Low	17.98

Big (ϕ1.6)	High	1.28	80[%]/ High	5.58

Two values of layer thickness (t) have been studied: they have been arbitrarily selected as percentage of the nozzle outlet diameter: the low value of t for both the nozzles corresponds to the 40[%] of the outlet diameter, while the high value to the 80[%].

In this case, the goal is the validation of the counterpressure contribution and the correlation with the layer thickness parameter by means of FEM analyses.

Thus, equation (6.23) has been used to compute the bead contribution to extrusion force. The influence of flow rate and layer thickness on the extrusion force has been modeled in COMSOL, by means of a set of structured meshes.

6.5.3. Results comparison

A semi-analytical model based on the Jeffery-Hamel approximation has been developed under the same boundary conditions of Figure 6.2 – c to calculate the nozzle extrusion force F_N.

The overall nozzle geometry is made up of two tapered sections (see: Figure B.1 – a). The Jeffery-Hamel approximation can be applied to each of them: in this way the overall nozzle pressure drop is calculated as the sum of two separated contributions.

Velocity profiles have been evaluated at different axial positions (see: Figure B.1 – b) for all the nozzle dimensions and flow rate values highlighted in Table 6.2.

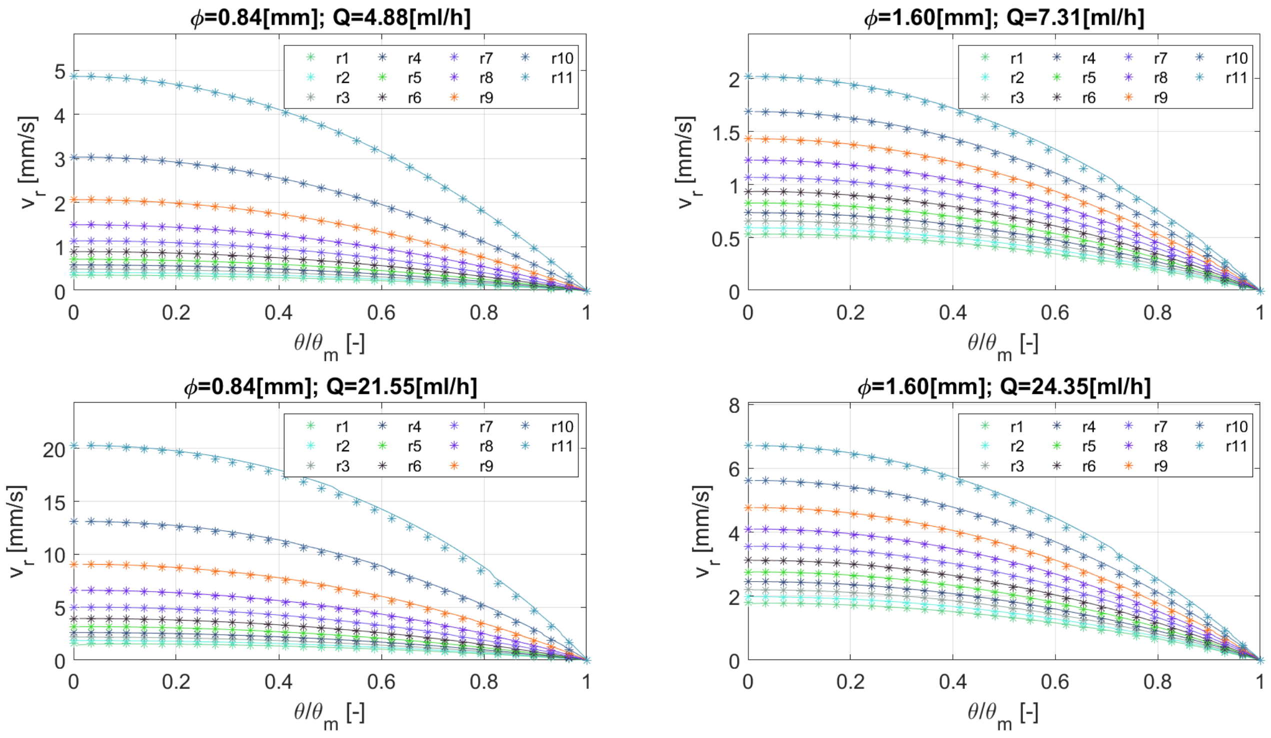

Figure 6.4. Velocity profiles in the second tapered control volume of the nozzles: comparison between CFD and Jeffery-Hamel semi-analytical approximation (points: MATLAB results; lines: CFD results); θ: Polar coordinate; Q: flow rate; ϕ: nozzle outlet diameter; v_r: radial velocity; θ_m: maximum azimuthal position; rk: k-th cut section along the control volume, according to Figure B.1 – b.

Figure 6.4 shows a very high correlation between velocity profiles computed analytically and numerically, for every nozzle diameter and flow rate value. As a matter of fact, the Jeffery-Hamel approximation can be considered valid: in [135] it has been shown that the deviation of Jeffery-Hamel flow assumption from real operating conditions increases at higher Reynolds numbers and taper angles.

For the sake of completeness, the same comparison has been made for the first tapered section, as shown in Figure 6.5.

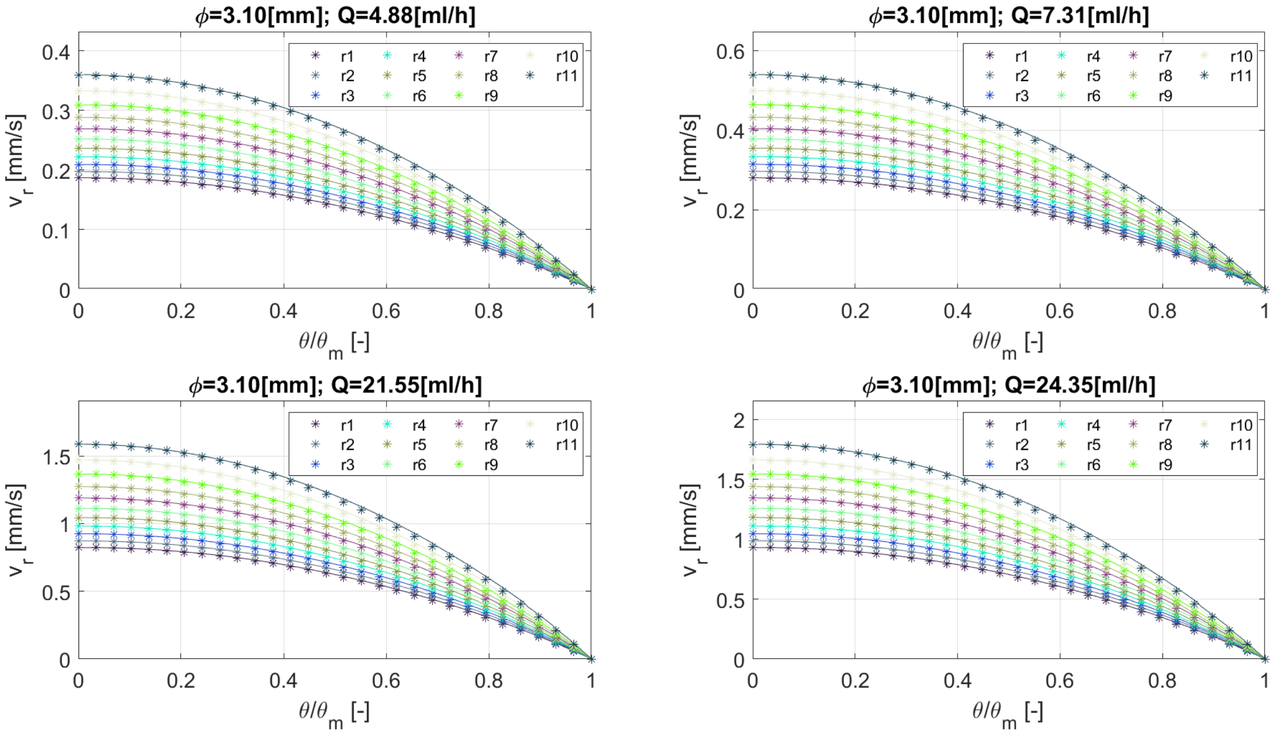

Figure 6.5. Velocity profiles in the first tapered control volume of the nozzles: comparison between CFD and Jeffery-Hamel semi-analytical approximation (points: MATLAB results; lines: CFD results); θ: Polar coordinate; Q: flow rate; ϕ: first tapered zone outlet diameter; v_r: radial velocity; θ_m: maximum azimuthal position; r_k: k-th cut section along the control volume, according to Figure B.1 – b.

Jeffery-Hamel approximation compares very well with CFD and the velocity values in Figure 6.5 are lower than the ones in Figure 6.4 because of the higher diameters considered.

Afterwards, F_N values obtained both from the simulation (CFD and semi-analytical models) and experimental phases have been evaluated. Moreover, the nozzle extrusion force (F_N) obtained when the silicone was considered a Newtonian fluid (with a dynamic viscosity of 62.5 [Pa s], namely the zero-shear viscosity of the Carreau model) has been calculated. The overall F_N comparison among the results obtained (MATLAB, Newtonian fluid, CFD and experimental) as a function of flow rate, for every nozzle, is shown in Figure 6.6.

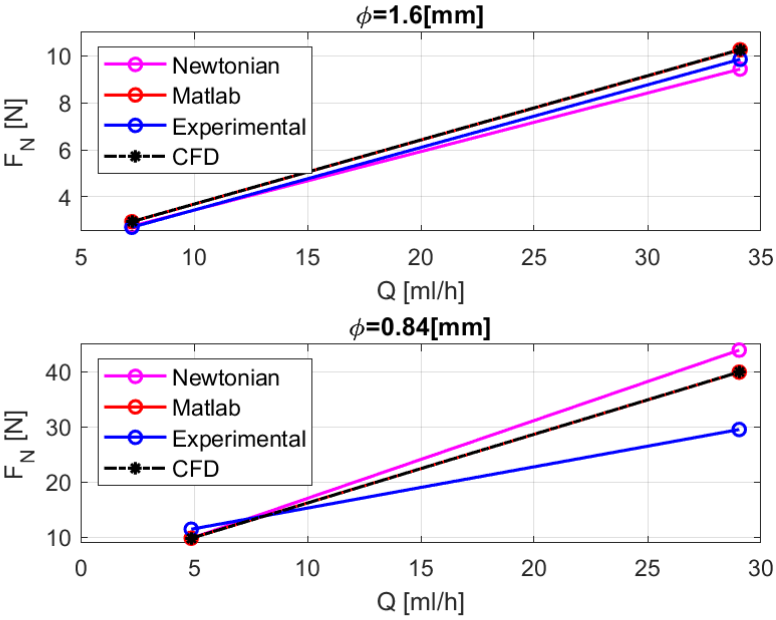

Figure 6.6. Measured and predicted nozzle extrusion force as a function of the volumetric flow rate; F_N: nozzle extrusion force; Q: flow rate; Ø: nozzle outlet diameter.

The results obtained by considering the silicone as a Newtonian and non-Newtonian fluid are very close for the highest nozzle diameter (ϕ1.6 [mm]). This is due to the low shear rates occurring when high diameters and low flow rates are considered; the investigation of the shear rates is provided in Appendix B (Section B.3). On the other hand, there is a discrepancy when considering the smallest nozzle diameter (ϕ0.84 [mm]), especially for high flow rates. This might be due to the high shear rates, in which the fluid is characterized by a shear thinning behavior.

From the comparative analysis of the F_N it stood out a reasonable agreement between the experimental and the non-Newtonian simulation results for the ϕ1.6 [mm] nozzle, while there is a moderate deviation for the ϕ0.84 [mm], at high flow rates.

Different reasons can lead to the discrepancy between the non-Newtonian model and experiments:

i) The assumption of neglectable elongational effects; the rheological model considers only viscous effects, modeling the silicone as a Carreau fluid.

ii) The Carreau parameters come from the scientific literature, but a deviation from this model at intermediate shear rates (where shear-thinning behavior occurs (see: Appendix B – Section B.3)) could occur.

iii) The material of the nozzles is thermoplastic, with a low stiffness if compared to steel. The pressure at the outlet can generate non-neglectable radial deformations of the nozzles, practically enlarging the nozzle and leading to a lower measured force.

Regarding the deposited bead, the validation is done directly with respect to the counterpressure F_C.

The calculations, based on the theory introduced in Section 6.4.3, were implemented in both MATLAB and COMSOL codes, to compare them with the experimental results (Figure 6.7).

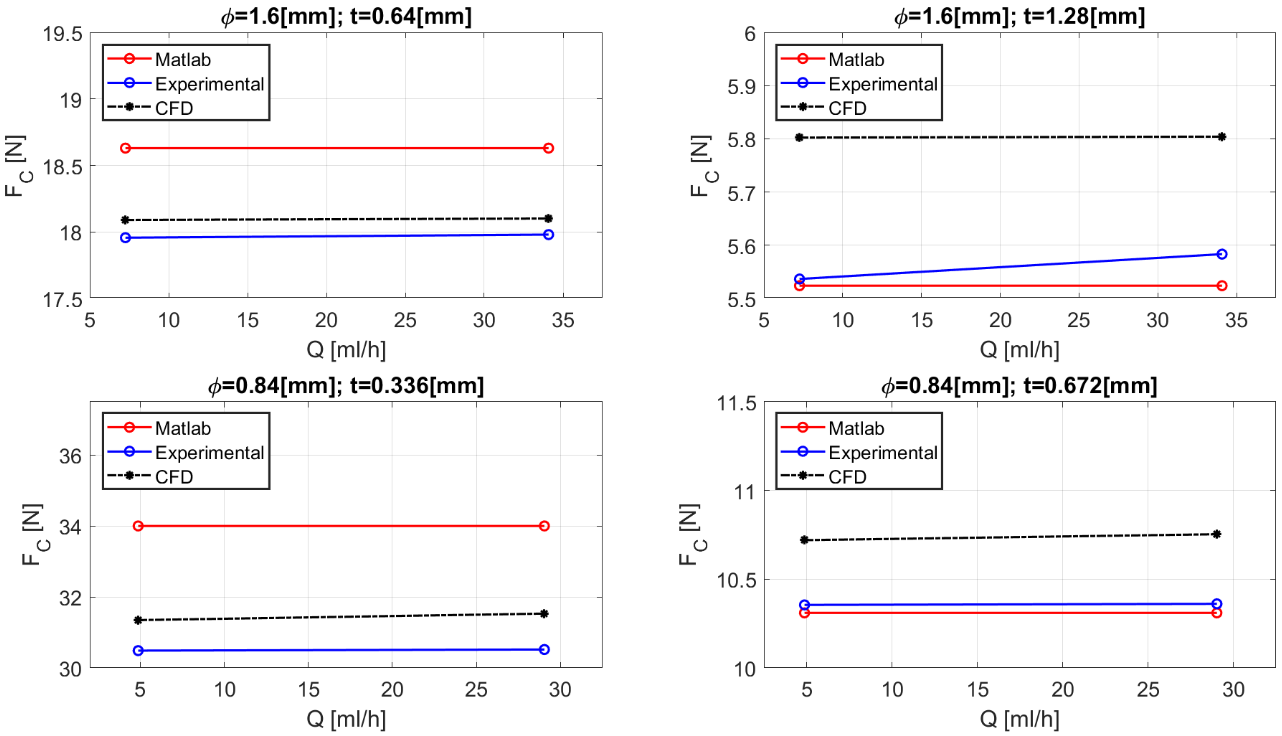

Figure 6.7. Measured and predicted counterpressure force as a function of the volumetric flow rate and layer thickness; F_C: counterpressure force; Q: flow rate; ∅: nozzle outlet diameter; t: layer thickness.

The counterpressure contribution F_C to the overall force F_T is found to be almost independent from the flow rate, for all the tested nozzle dimensions and layer thickness values. Moreover, both semi-analytical and numerical data are very close to the experimental one, giving confidence in applying the theory introduced in Section 6.4.3 to predict this last force contribution.

Finally, the overall extrusion force F_T, calculated as the sum of F_N and F_C, has been computed.

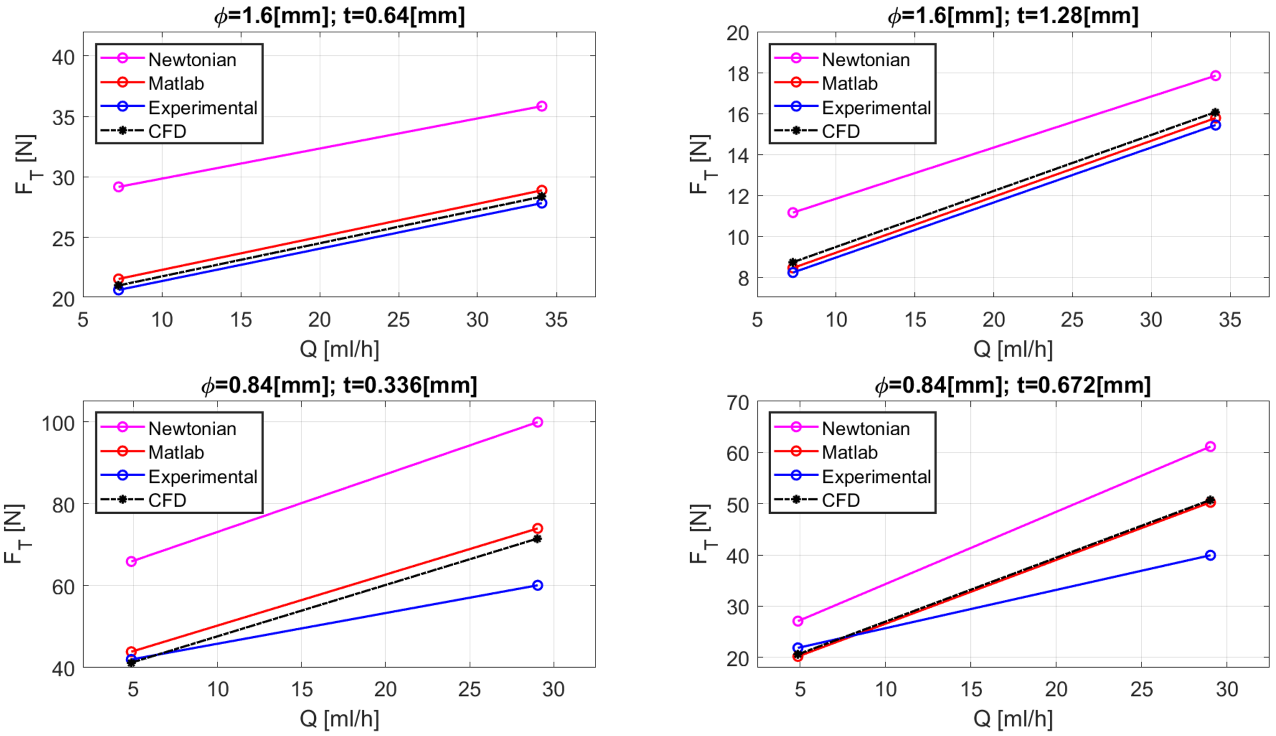

Figure 6.8. Measured and predicted overall extrusion force as a function of the volumetric flow rate and layer thickness; F_T: overall extrusion force; Q: flow rate; Ø: nozzle outlet diameter; t: layer thickness.

The discrepancy between CFD and semi-analytical data is mainly due to F_C (see: Figure 6.7); in fact, from Figure 6.6 there is no difference between the computational results.

The deviation of the predicted overall extrusion force from experimental data in Figure 6.8 is more related to the nozzle contribution. Overall, if the flow field in both the nozzle and deposited layer is considered as Newtonian, F_T deviates a lot from experimental data in all extrusion conditions.

By analyzing the obtained results (simulations and experiments) the relationship between the layer thickness (t) and the counterpressure force (F_C) appears clear. The layer thickness negatively affects the counterpressure F_C: when low value of t are set, high values of F_C (and consequently of the overall printing force F_T) are reached, on the other hand at high value of t, very low value of F_C are obtained.

At low values of the layer thickness parameter, the pressure increases, resulting in increase of F_C, and F_T: this happens because the available free section for a given volumetric flow rate to pass through becomes smaller.

This Chapter provides a tool to predict the overall force as a function of the layer thickness: to reduce the overall printing force via silicone MEX, high values of layer thickness need to be set.

In Table 6.4 the contribution of the layer thickness on the counterpressure F_C and overall force F_T is reported, showing a maximum decrease of the overall printing force of 60.76[%] when the layer thickness was changed from 0.64 [mm] to 1.28 [mm].

The proposed models have also been characterized in terms of accuracy with respect to the experimental data obtained printing silicone beads on the build plate, as shown in Table 6.5. In particular very high accuracy values for both the models have been obtained: an accuracy spanning from 89.7[%] and 99.8[%] was found for the semi-analytical model as well as an accuracy ranging from 95.4[%] and 99.3[%] for CFD.

The following models represent a very powerful tool to obtain 3D printed silicone structures with improved properties: by setting the right combination of process parameters (i.e., nozzle size, flow, and printing speed), the counterpressure force F_C can be lowered even while printing at low values of layer thickness. In this way, the amount and size of voids between consecutive layers will be abruptly reduced, improving both the mechanical properties and the accuracy [183,184]. The force prediction through the proposed model is very appealing, especially for the fabrication of 3D printed silicone-based biomedical devices, requiring high accuracy and good mechanical performance, such as meniscus implants [185–188].

Table 6.4. Reduction in total force when switching from low to high layer thickness value.

Method	**Nozzle [mm]**	**Flow rate [ml/h]**	**Low layer thickness value [mm]**	**Total force at low layer thickness, F_T [N]**	**High layer thickness value [mm]**	**Total force at high layer thickness, F_T [N]**	**Reduction in F_T switching from low to high t (%)**
CFD	0.84	4.87	0.336	41.20	0.672	20.57	50.06
Experimental				41.98		21.84	47.96
MATLAB				43.86		20.17	54.00
CFD	0.84	29.04	0.336	71.51	0.672	50.73	29.05
Experimental				60.08		39.93	33.55
MATLAB				73.97		50.27	32.03
CFD	1.6	7.26	0.64	21.03	1.28	8.74	58.43
Experimental				20.66		8.24	60.12
MATLAB				21.57		8.46	60.76
CFD	1.6	34.08	0.64	28.37	1.28	16.07	43.34
Experimental				27.83		15.44	44.53
MATLAB				28.89		15.78	45.36

Table 6.5. Accuracy of CFD and semi-analytical MATLAB models in all experimental conditions.

Nozzle [mm]	**Flow rate value**	**Layer thickness (t) [mm]**	**Accuracy of the CFD model (%)**	**Accuracy of the MATLAB model (%)**
Small (ϕ0.84)	Low	0.336	97.26	89.67
Small (ϕ0.84)	Low	0.672	96.59	99.56
Small (ϕ0.84)	High	0.336	96.79	89.76
Small (ϕ0.84)	High	0.672	96.35	99.50
Big (ϕ1.6)	Low	0.64	99.26	96.38
Big (ϕ1.6)	Low	1.28	95.42	99.77

Big (ϕ1.6)	High	0.64	99.33	96.51
Big (ϕ1.6)	High	1.28	96.19	98.93

6.6. Conclusions

This paper describes a tool for predicting the extrusion force in the MEX technology for silicone, based on three process parameters: layer thickness, flow rate, and nozzle diameter.

The impact of the counterpressure due to the silicone beads deposition has been analyzed and found to play a key role in reducing the overall printing force.

The models introduced in Chapter 5 have been thoroughly validated through experiments using a custom-made silicone 3D printer, developed at HBS Laboratory.

The models showed very high accuracy (up to 99.7[%] for the semi-analytical and 99.3[%] for CFD) in predicting overall printing force, indicating their applicability to real 3D printing scenarios and the potential for improving manufacturing process control.

Additional studies have focused on novel methods to lower the printing force, by means of a completely different actuation method, that is the Lorentz force. The abovementioned work, whose content is not part of the present dissertation, has shown the potential of the proposed mathematical and CFD methods for further application in silicone MEX.

7. Conclusions and research perspectives

Additive Manufacturing (AM) plays a vital role in Fourth Industrial Revolution (4IR) because it allows to produce functional parts with lower waste and higher cost savings, if compared to traditional manufacturing processes. However, AM processes are very complex because they involve different thermophysical phenomena; in fact, it is quite common to find the best processing parameters empirically.

Because of the abovementioned advantages, a better understanding of these underlying phenomena is mandatory; an excellent method to analyze manufacturing processes is mathematical modeling.

The main aim of the present Ph.D. thesis was to develop semi-analytical and numerical algorithms for MEX AM.

Thanks to the work done at the Interdisciplinary Additive Manufacturing (IAM) Lab, Polytechnic University of Bari, Italy and Humanoid Bio-Robotic and Smart materials (HBS) Lab, University of Texas at Dallas, USA, new fully predictive algorithms were formulated and experimentally validated.

At first, a mathematical model describing the influence of some of the most critical process parameters (printing speed and layer height) on PAM process has been formulated. The effect of counterpressure arising when printing with a layer height less than nozzle outlet diameter on the extruded mass flow rate has been shown.

This model is semi-analytical and iterative; it can be used to predict the extruded mass flow rate for a given screw peripheral speed (N-control algorithm) or to find the peripheral speed which allows to extrude a layer with prescribed geometrical features (m-control algorithm).

The proposed formulation applies to generalized non-Newtonian fluids which obey to the power-law rheology, but further effort should be dedicated to developing a more general model, both for single-screw extrusion and layer deposition of other fluid rheologies. Actually, an iterative model which predicts very well the single-screw extrusion of a generic non-Newtonian melt has been formulated and validated against literature and CFD data, finding a very good agreement.

Then, the capability of CFD to describe layer deposition in PAM extrusion was assessed. Lower layer heights lead to higher surface finishing but reduce mass flow rate in PAM, as already predicted by the mathematical model. In addition, CFD captures very well the shape of the strands being deposited on the build plate, paving the way for further applications in numerical MEX simulation.

Further research should be dedicated to the CFD modeling of multiple layer extrusion in PAM; inter-layer coalescence and intra-layer bonding strength affects the final part strength and must be properly modeled.

Then, a novel semi-analytical formulation to describe the flow in the extrusion nozzles used practically in all MEX techniques was given; the novelty is twofold: i) the semi-analytical method agrees very well with CFD even at low values of nozzle diameter, if compared to existing literature and ii) it applies to all rheological models, paving the way for application in describing the extrusion of thermoplastics, silicones and many other materials behaving as non-Newtonian fluids.

The novel formulation has been experimentally validated with respect to the results obtained with a custom-made silicone MEX setup; a moisture-cured silicone was tested at HBS Lab under different values of layer height and flow rate values: an accuracy spanning from 89.7[%] and 99.8[%] was found.

Further work will be dedicated to testing other silicones, whose curing mechanism differs from moisture-cure; actually, the model has been validated for MEX of Ecoflex 00-10, which is a two-component silicone which cures through the heat. Preliminary results show that the proposed semi-analytical model predicts very well the extrusion force both in free-air and practical manufacturing conditions.

In the author’s opinion, numerical and semi-analytical methods share a great potential in gaining a better understanding of AM, and in particular MEX processes. They can be used to study the effect of process parameters on quantities which are difficult (or impossible) to measure directly.

For that reason, it is expected that mathematical models of AM processes will be used by industrial companies to choose materials and process parameters ever more consciously, in the future.

Appendix A

Table A.1. Error analysis for ϕ0.15 nozzle; it: number of the iteration; u_{max}^{code}: maximum velocity; ε_{rel}^{Q}: relative error on flow rate; u_{max}^{CFD}: maximum velocity, calculated via CFD; ε_{rel}^{CFD}: relative error with respect to CFD; u_{max}^{FVM}: maximum velocity, calculated via FVM; ε_{rel}^{FVM}: relative error with respect to FVM; $Q = 1[mm^3/s]$; all velocities in $[mm/s]$.

it	$\boldsymbol{\varepsilon_{rel}^{Q}}$	$\boldsymbol{u_{max}^{code}}$	**it**	$\boldsymbol{\varepsilon_{rel}^{Q}}$[%]	$\boldsymbol{u_{max}^{code}}$	$\boldsymbol{u_{max}^{CFD}}$	$\boldsymbol{u_{max}^{FVM}}$	$\boldsymbol{\varepsilon_{rel}^{CFD}}$[%]	$\boldsymbol{\varepsilon_{rel}^{FVM}}$[%]
1	1.14E+02	-0.020713	27	3.73E+00	0.097210	0.0945	0.0946	0.794625525	0.6667
2	7.23E+01	0.036270	28	3.20E+00	0.096728				
3	1.13E+01	0.125177	29	2.76E+00	0.096315				
4	1.36E+02	0.324042	30	2.37E+00	0.095961				
5	4.31E+02	0.689821	31	2.04E+00	0.095658				
6	7.86E+02	1.017053	32	1.76E+00	0.095398				
7	4.14E+02	0.476526	33	1.51E+00	0.095174				
8	1.66E+02	0.244973	34	1.31E+00	0.094982				
9	1.13E+02	0.197735	35	1.13E+00	0.094816				
10	8.23E+01	0.169493	36	9.70E-01	0.094674				
11	6.30E+01	0.151736	37	8.37E-01	0.094552				
12	4.97E+01	0.139434	38	7.22E-01	0.094446				
13	3.99E+01	0.130459	39	6.23E-01	0.094355				
14	3.25E+01	0.123673	40	5.38E-01	0.094277				
15	2.68E+01	0.118407	41	4.64E-01	0.094209				
16	2.23E+01	0.114240	42	4.01E-01	0.094151				
17	1.86E+01	0.110890	43	3.46E-01	0.094100				
18	1.57E+01	0.108165	44	2.99E-01	0.094057				
19	1.32E+01	0.105926	45	2.58E-01	0.094019				
20	1.12E+01	0.104073	46	2.23E-01	0.093987				
21	9.52E+00	0.102527	47	1.92E-01	0.093959				
22	8.11E+00	0.101233	48	1.66E-01	0.093935				
23	6.92E+00	0.100142	49	1.43E-01	0.093914				
24	5.92E+00	0.099221	50	1.24E-01	0.093896				

25	5.07E+00	0.098440	51	1.07E-01	0.093881				
26	4.35E+00	0.097776	52	9.24E-02	0.093867				

Table A.2. Error analysis for ϕ0.25 nozzle; it: number of the iteration; $\mathrm{u}_{\mathrm{max}}^{\mathrm{code}}$: maximum velocity; $\varepsilon_{\mathrm{rel}}^{\mathrm{Q}}$: relative error on flow rate; $\mathrm{u}_{\mathrm{max}}^{\mathrm{CFD}}$: maximum velocity, calculated via CFD; $\varepsilon_{\mathrm{rel}}^{\mathrm{CFD}}$: relative error with respect to CFD; $\mathrm{u}_{\mathrm{max}}^{\mathrm{FVM}}$: maximum velocity, calculated via FVM; $\varepsilon_{\mathrm{rel}}^{\mathrm{FVM}}$: relative error with respect to FVM; $\mathrm{Q} = 1[\mathrm{mm}^3/\mathrm{s}]$; all velocities in $[\mathrm{mm/s}]$.

it	ε_{rel}^{Q}	u_{max}^{code}	it	ε_{rel}^{Q}[%]	u_{max}^{code}	u_{max}^{CFD}	u_{max}^{FVM}	ε_{rel}^{CFD}[%]	ε_{rel}^{FVM}[%]
1	1.43E+02	-0.023153	27	3.64E+00	0.035819	0.03468	0.0346	0.104385	0.127
2	5.38E+01	0.020847	28	3.13E+00	0.035651				
3	2.20E+01	0.057838	29	2.70E+00	0.035507				
4	1.31E+02	0.103878	30	2.32E+00	0.035383				
5	2.72E+02	0.154281	31	2.00E+00	0.035277				
6	3.70E+02	0.173304	32	1.73E+00	0.035186				
7	2.58E+02	0.120732	33	1.49E+00	0.035108				
8	1.43E+02	0.082165	34	1.29E+00	0.035040				
9	1.01E+02	0.068034	35	1.11E+00	0.034982				
10	7.52E+01	0.059542	36	9.61E-01	0.034932				
11	5.83E+01	0.053942	37	8.30E-01	0.034888				
12	4.64E+01	0.049977	38	7.18E-01	0.034851				
13	3.75E+01	0.047040	39	6.20E-01	0.034818				
14	3.07E+01	0.044795	40	5.36E-01	0.034791				
15	2.54E+01	0.043038	41	4.64E-01	0.034767				
16	2.12E+01	0.041637	42	4.01E-01	0.034746				
17	1.78E+01	0.040506	43	3.47E-01	0.034728				
18	1.50E+01	0.039581	44	3.00E-01	0.034712				
19	1.27E+01	0.038818	45	2.59E-01	0.034699				
20	1.08E+01	0.038184	46	2.24E-01	0.034687				
21	9.17E+00	0.037655	47	1.94E-01	0.034677				
22	7.83E+00	0.037210	48	1.68E-01	0.034668				
23	6.70E+00	0.036834	49	1.45E-01	0.034661				

24	5.74E+00	0.036516	50	1.26E-01	0.034654				
25	4.92E+00	0.036246	51	1.09E-01	0.034649				
26	4.23E+00	0.036016	52	9.41E-02	0.034644				

Table A.3. Error analysis for ϕ0.30 nozzle; it: number of the iteration; u_{max}^{code}: maximum velocity; ε_{rel}^{Q}: relative error on flow rate; u_{max}^{CFD}: maximum velocity, calculated via CFD; ε_{rel}^{CFD}: relative error with respect to CFD; u_{max}^{FVM}: maximum velocity, calculated via FVM; ε_{rel}^{FVM}: relative error with respect to FVM; $Q = 1[mm^3/s]$; all velocities in $[mm/s]$.

it	ε_{rel}^{Q}	u_{max}^{code}	it	ε_{rel}^{Q}[%]	u_{max}^{code}	u_{max}^{CFD}	u_{max}^{FVM}	ε_{rel}^{CFD}[%]	ε_{rel}^{FVM}[%]
1	1.65E+02	-2.47E-02	28	3.00E+00	2.52E-02	0.024517	0.02452	-5.67E-02	-8.18E-02
2	4.49E+01	1.70E-02	29	2.60E+00	2.51E-02				
3	4.40E+01	4.49E-02	30	2.25E+00	2.50E-02				
4	1.41E+02	7.05E-02	31	1.95E+00	2.50E-02				
5	2.33E+02	8.92E-02	32	1.69E+00	2.49E-02				
6	2.47E+02	8.46E-02	33	1.47E+00	2.49E-02				
7	1.64E+02	6.26E-02	34	1.27E+00	2.48E-02				
8	1.09E+02	4.98E-02	35	1.11E+00	2.48E-02				
9	8.07E+01	4.32E-02	36	9.61E-01	2.47E-02				
10	6.23E+01	3.89E-02	37	8.34E-01	2.47E-02				
11	4.94E+01	3.59E-02	38	7.25E-01	2.47E-02				
12	3.99E+01	3.37E-02	39	6.30E-01	2.47E-02				
13	3.27E+01	3.21E-02	40	5.47E-01	2.46E-02				
14	2.70E+01	3.08E-02	41	4.76E-01	2.46E-02				
15	2.26E+01	2.97E-02	42	4.13E-01	2.46E-02				
16	1.90E+01	2.89E-02	43	3.59E-01	2.46E-02				
17	1.60E+01	2.82E-02	44	3.12E-01	2.46E-02				
18	1.36E+01	2.77E-02	45	2.72E-01	2.46E-02				
19	1.16E+01	2.72E-02	46	2.36E-01	2.46E-02				
20	9.89E+00	2.68E-02	47	2.05E-01	2.46E-02				
21	8.47E+00	2.65E-02	48	1.79E-01	2.46E-02				
22	7.27E+00	2.62E-02	49	1.55E-01	2.45E-02				

23	6.26E+00	2.60E-02	50	1.35E-01	2.45E-02				
24	5.39E+00	2.58E-02	51	1.17E-01	2.45E-02				
25	4.65E+00	2.56E-02	52	1.02E-01	2.45E-02				
26	4.01E+00	2.54E-02	53	8.89E-02	2.45E-02				
27	3.47E+00	2.53E-02							

Table A.4. Error analysis for ϕ 0.35 nozzle; it: number of the iteration; u_{max}^{code}: maximum velocity; ε_{rel}^{Q}: relative error on flow rate; u_{max}^{CFD}: maximum velocity, calculated via CFD; ε_{rel}^{CFD}: relative error with respect to CFD; u_{max}^{FVM}: maximum velocity, calculated via FVM; ε_{rel}^{FVM}: relative error with respect to FVM; $Q = 1[mm^3/s]$; all velocities in $[mm/s]$.

it	ε_{rel}^{Q}	u_{max}^{code}	*it*	ε_{rel}^{Q}[%]	u_{max}^{code}	u_{max}^{CFD}	u_{max}^{FVM}	ε_{rel}^{CFD}[%]	ε_{rel}^{FVM}[%]
1	1.93E+02	-2.65E-02	28	2.90E+00	1.89E-02	0.018428	0.01841	-9.68E-02	-5.43E-02
2	3.64E+01	1.41E-02	29	2.54E+00	1.89E-02				
3	7.18E+01	3.70E-02	30	2.22E+00	1.88E-02				
4	1.51E+02	4.99E-02	31	1.94E+00	1.88E-02				
5	1.84E+02	5.23E-02	32	1.69E+00	1.87E-02				
6	1.49E+02	4.42E-02	33	1.48E+00	1.87E-02				
7	1.05E+02	3.64E-02	34	1.30E+00	1.87E-02				
8	7.78E+01	3.18E-02	35	1.13E+00	1.86E-02				
9	6.06E+01	2.88E-02	36	9.93E-01	1.86E-02				
10	4.84E+01	2.67E-02	37	8.70E-01	1.86E-02				
11	3.94E+01	2.52E-02	38	7.62E-01	1.86E-02				
12	3.25E+01	2.40E-02	39	6.67E-01	1.85E-02				
13	2.71E+01	2.31E-02	40	5.85E-01	1.85E-02				
14	2.28E+01	2.24E-02	41	5.12E-01	1.85E-02				
15	1.93E+01	2.18E-02	42	4.49E-01	1.85E-02				
16	1.64E+01	2.13E-02	43	3.94E-01	1.85E-02				
17	1.40E+01	2.08E-02	44	3.45E-01	1.85E-02				
18	1.20E+01	2.05E-02	45	3.02E-01	1.85E-02				
19	1.03E+01	2.02E-02	46	2.65E-01	1.85E-02				
20	8.92E+00	2.00E-02	47	2.32E-01	1.85E-02				

21	7.71E+00	1.98E-02	48	2.04E-01	1.85E-02				
22	6.68E+00	1.96E-02	49	1.79E-01	1.85E-02				
23	5.80E+00	1.94E-02	50	1.57E-01	1.85E-02				
24	5.04E+00	1.93E-02	51	1.37E-01	1.85E-02				
25	4.38E+00	1.92E-02	52	1.20E-01	1.85E-02				
26	3.82E+00	1.91E-02	53	1.06E-01	1.84E-02				
27	3.33E+00	1.90E-02	54	9.26E-02	1.84E-02				

Table A.5. Error analysis for ϕ 0.40 nozzle; it: number of the iteration; $\mathrm{u}_{\mathrm{max}}^{\mathrm{code}}$: maximum velocity; $\varepsilon_{\mathrm{rel}}^{\mathrm{Q}}$: relative error on flow rate; $\mathrm{u}_{\mathrm{max}}^{\mathrm{CFD}}$: maximum velocity, calculated via CFD; $\varepsilon_{\mathrm{rel}}^{\mathrm{CFD}}$: relative error with respect to CFD; $\mathrm{u}_{\mathrm{max}}^{\mathrm{FVM}}$: maximum velocity, calculated via FVM; $\varepsilon_{\mathrm{rel}}^{\mathrm{FVM}}$: relative error with respect to FVM; $\mathrm{Q} = 1[\mathrm{mm}^3/\mathrm{s}]$; all velocities in $[\mathrm{mm}/\mathrm{s}]$.

it	ε_{rel}^{Q}	u_{max}^{code}	it	$\varepsilon_{rel}^{Q}[\%]$	u_{max}^{code}	u_{max}^{CFD}	u_{max}^{FVM}	$\varepsilon_{rel}^{CFD}[\%]$	$\varepsilon_{rel}^{FVM}[\%]$
1	2.29E+02	-2.85E-02	29	2.52E+00	1.48E-02	0.01447	0.014505	-8.99E-02	-3.45E-02
2	2.84E+01	1.20E-02	30	2.22E+00	1.48E-02				
3	1.16E+02	3.28E-02	31	1.96E+00	1.47E-02				
4	1.42E+02	3.42E-02	32	1.74E+00	1.47E-02				
5	1.17E+02	3.01E-02	33	1.53E+00	1.47E-02				
6	8.73E+01	2.61E-02	34	1.36E+00	1.47E-02				
7	6.74E+01	2.34E-02	35	1.20E+00	1.46E-02				
8	5.38E+01	2.16E-02	36	1.06E+00	1.46E-02				
9	4.38E+01	2.03E-02	37	9.40E-01	1.46E-02				
10	3.63E+01	1.93E-02	38	8.32E-01	1.46E-02				
11	3.04E+01	1.85E-02	39	7.36E-01	1.46E-02				
12	2.57E+01	1.79E-02	40	6.52E-01	1.46E-02				
13	2.18E+01	1.74E-02	41	5.77E-01	1.45E-02				
14	1.87E+01	1.70E-02	42	5.11E-01	1.45E-02				
15	1.61E+01	1.66E-02	43	4.53E-01	1.45E-02				
16	1.39E+01	1.63E-02	44	4.01E-01	1.45E-02				
17	1.21E+01	1.61E-02	45	3.55E-01	1.45E-02				
18	1.05E+01	1.59E-02	46	3.15E-01	1.45E-02				

19	9.15E+00	1.57E-02	47	2.79E-01	1.45E-02				
20	8.00E+00	1.55E-02	48	2.47E-01	1.45E-02				
21	7.00E+00	1.54E-02	49	2.19E-01	1.45E-02				
22	6.14E+00	1.53E-02	50	1.94E-01	1.45E-02				
23	5.39E+00	1.52E-02	51	1.72E-01	1.45E-02				
24	4.74E+00	1.51E-02	52	1.52E-01	1.45E-02				
25	4.17E+00	1.50E-02	53	1.35E-01	1.45E-02				
26	3.67E+00	1.50E-02	54	1.20E-01	1.45E-02				
27	3.24E+00	1.49E-02	55	1.06E-01	1.45E-02				
28	2.85E+00	1.49E-02	56	9.40E-02	1.45E-02				

Table A.6. Error analysis for ϕ 0.50 nozzle; it: number of the iteration; u_{max}^{code}: maximum velocity; ε_{rel}^{Q}: relative error on flow rate; u_{max}^{CFD}: maximum velocity, calculated via CFD; ε_{rel}^{CFD}: relative error with respect to CFD; u_{max}^{FVM}: maximum velocity, calculated via FVM; ε_{rel}^{FVM}: relative error with respect to FVM; $Q = 1[mm^3/s]$; all velocities in $[mm/s]$.

it	ε_{rel}^{Q}	u_{max}^{code}	it	ε_{rel}^{Q}[%]	u_{max}^{code}	u_{max}^{CFD}	u_{max}^{FVM}	ε_{rel}^{CFD}[%]	ε_{rel}^{FVM}[%]
1	3.27E+02	-3.29E-02	36	2.61E+00	9.93E-03	0.009619	0.00968	-8.26E-01	2.07E-01
2	1.39E+01	9.08E-03	37	2.36E+00	9.91E-03				
3	1.51E+03	-2.14E-01	38	2.13E+00	9.88E-03				
4	2.60E+02	4.00E-02	39	1.93E+00	9.87E-03				
5	3.25E+02	3.90E-02	40	1.75E+00	9.85E-03				
6	2.03E+02	2.72E-02	41	1.58E+00	9.83E-03				
7	1.32E+02	2.13E-02	42	1.43E+00	9.82E-03				
8	9.84E+01	1.84E-02	43	1.29E+00	9.81E-03				
9	7.71E+01	1.65E-02	44	1.17E+00	9.80E-03				
10	6.23E+01	1.52E-02	45	1.06E+00	9.79E-03				
11	5.16E+01	1.43E-02	46	9.60E-01	9.78E-03				
12	4.34E+01	1.36E-02	47	8.70E-01	9.77E-03				
13	3.70E+01	1.30E-02	48	7.88E-01	9.76E-03				
14	3.18E+01	1.25E-02	49	7.14E-01	9.76E-03				
15	2.76E+01	1.22E-02	50	6.47E-01	9.75E-03				

16	2.41E+01	1.19E-02	51	5.86E-01	9.74E-03				
17	2.11E+01	1.16E-02	52	5.31E-01	9.74E-03				
18	1.86E+01	1.14E-02	53	4.81E-01	9.73E-03				
19	1.64E+01	1.12E-02	54	4.36E-01	9.73E-03				
20	1.46E+01	1.10E-02	55	3.96E-01	9.73E-03				
21	1.30E+01	1.09E-02	56	3.59E-01	9.72E-03				
22	1.15E+01	1.07E-02	57	3.25E-01	9.72E-03				
23	1.03E+01	1.06E-02	58	2.95E-01	9.72E-03				
24	9.21E+00	1.05E-02	59	2.67E-01	9.72E-03				
25	8.25E+00	1.04E-02	60	2.42E-01	9.71E-03				
26	7.40E+00	1.04E-02	61	2.20E-01	9.71E-03				
27	6.64E+00	1.03E-02	62	1.99E-01	9.71E-03				
28	5.97E+00	1.02E-02	63	1.81E-01	9.71E-03				
29	5.37E+00	1.02E-02	64	1.64E-01	9.71E-03				
30	4.84E+00	1.01E-02	65	1.48E-01	9.70E-03				
31	4.36E+00	1.01E-02	66	1.35E-01	9.70E-03				
32	3.93E+00	1.00E-02	67	1.22E-01	9.70E-03				
33	3.55E+00	1.00E-02	68	1.11E-01	9.70E-03				
34	3.20E+00	9.98E-03	69	1.00E-01	9.70E-03				
35	2.89E+00	9.95E-03	70	9.10E-02	9.70E-03				

Table A.7. Error analysis for silicone extrusion at all nozzle sizes; N: number of elements used for the MATLAB bvp5c subroutine; $\mathrm{u}_{\mathrm{max}}^{\mathrm{code}}$: maximum velocity at nozzle outlet; $\varepsilon_{\mathrm{rel}}^{\mathrm{N=45}}$: relative error with respect to N=45; $\mathrm{u}_{\mathrm{max}}^{\mathrm{CFD}}$: maximum velocity at nozzle outlet, calculated via CFD; $\varepsilon_{\mathrm{rel}}^{\mathrm{CFD}}$: relative error with respect to CFD; $\mathrm{u}_{\mathrm{max}}^{\mathrm{FVM}}$: maximum velocity, calculated via FVM; $\varepsilon_{\mathrm{rel}}^{\mathrm{FVM}}$: relative error with respect to FVM; $\mathrm{Q} = 1[\mathrm{mm}^3/\mathrm{s}]$; all velocities in $[\mathrm{mm/s}]$.

ϕ $[mm]$	N	u_{max}^{code}	$\varepsilon_{rel}^{N=45}$[%]	u_{max}^{CFD}	u_{max}^{FVM}	ε_{rel}^{CFD}[%]	ε_{rel}^{FVM}[%]
0.2032	5	0.053476	-0.4175	0.0531	0.0529	-7.03E-03	1.09E+00
	15	0.053267	-0.0248			-3.13E-03	6.94E-01
	30	0.053255	-0.0035			-2.92E-03	6.71E-01
	45	0.053254	0.0000			-2.89E-03	6.69E-01

0.254	5	0.034422	-0.4171	0.0342	0.034	-6.46E-03	1.24E+00
	15	0.034288	-0.0259			-2.57E-03	8.47E-01
	30	0.034280	-0.0036			-2.35E-03	8.24E-01
	45	0.034279	0.0000			-2.31E-03	8.21E-01
0.4064	5	0.014240	-0.4995	0.0141	0.0141	-9.82E-03	9.93E-01
	15	0.014174	-0.0349			-5.23E-03	5.25E-01
	30	0.014170	-0.0050			-4.93E-03	4.96E-01
	45	0.014169	0.0000			-4.88E-03	4.89E-01
0.5842	5	0.007336	-0.5919	0.0072804	0.00725	-7.62E-03	1.19E+00
	15	0.007296	-0.0430			-2.18E-03	6.34E-01
	30	0.007294	-0.0063			-1.81E-03	6.07E-01
	45	0.007293	0.0000			-1.75E-03	5.93E-01
0.8302	5	0.003637	-0.6152	0.003611	0.00359	-7.06E-03	1.31E+00
	15	0.003616	-0.0455			-1.40E-03	7.24E-01
	30	0.003615	-0.0067			-1.02E-03	6.96E-01
	45	0.003614	0.0000			-9.49E-04	6.69E-01
1.1938	5	0.001798	-0.6184	0.0017856	0.00177	-6.73E-03	1.58E+00
	15	0.001787	-0.0458			-1.04E-03	9.60E-01
	30	0.001787	-0.0067			-6.52E-04	9.60E-01
	45	0.001787	0.0000			-5.85E-04	9.60E-01
1.60	5	0.001000	-0.6164	9.94E-04	9.92E-04	-5.97E-03	8.06E-01
	15	0.000994	-0.0457			-2.98E-04	2.02E-01
	30	0.000994	-0.0067			9.15E-05	2.02E-01
	45	0.000994	0.0000			1.59E-04	2.02E-01

Appendix B

B.1. Nozzle internal geometries

A schematic representation of the internal features of a general-purpose nozzle used for silicone extrusion has been given in the following Figure B.1:

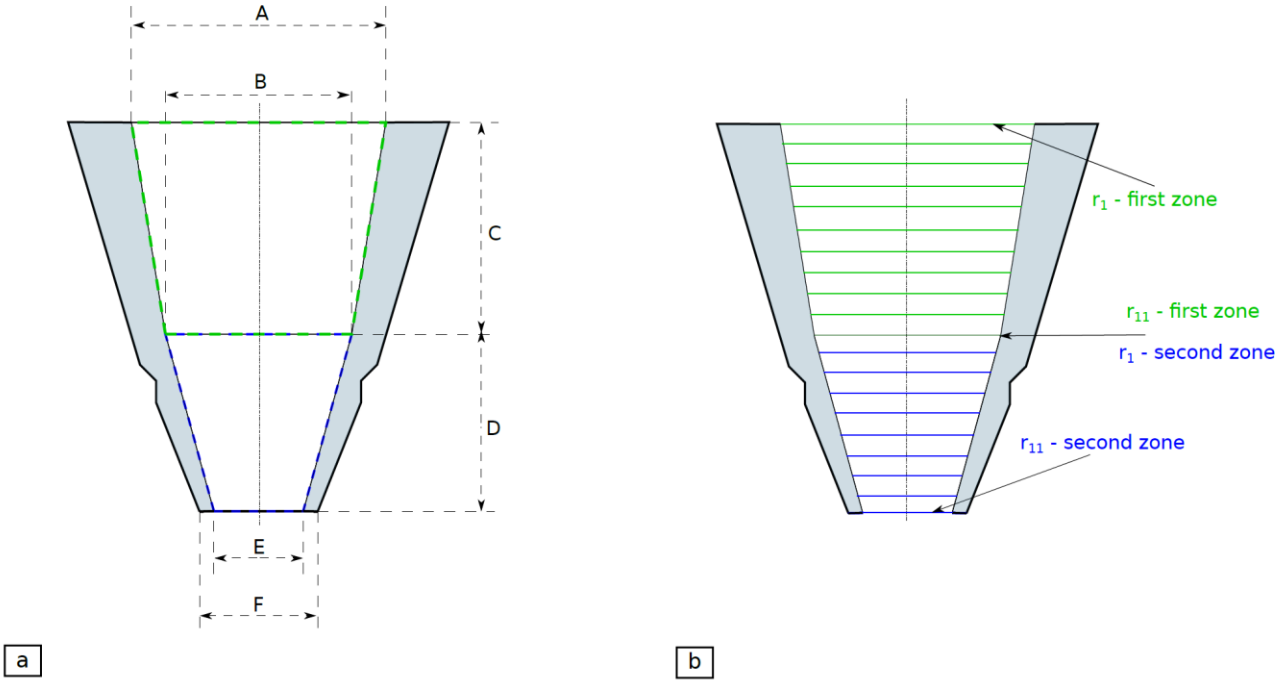

Figure B.1. a.) Fingerinspire dispenser's internal features; dashed yellow line: first tapered control volume; dashed blue line: second tapered control volume; b.) intermediate axial positions used in CFD and semi-analytical computations; green lines: first tapered control volume; blue lines: second tapered control volume.

The relevant dimensions for the two nozzles employed in the investigations have been detailed in Table B.1:

Table B.1. Investigated nozzles dimensions; all dimensions in [mm].

Name	**A**	**B**	**C**	**D**	**E**	**F**
Small	4.35	3.10	14.35	17.65	0.84	1.44
Big	4.35	3.10	14.35	17.65	1.60	2.20

B.2. Mesh-independence studies

An unstructured mesh has been chosen to study the flow in the nozzle. COMSOL gives the possibility to automatically build an unstructured mesh, based on the physics that is modeled; in present case, the Fluid Flow module automatically refines the mesh near the flow boundaries, because of the higher local velocity gradients. More details on the finite elements' parameters being used in discretizing the nozzle internal geometry are provided in Table B.2:

Table B.2. Mesh statistics for nozzle control volume discretization; maximum and minimum element sizes are in [mm].

Property	Coarse Mesh	Normal Mesh	Fine Mesh
Maximum Element Size	1.44E-01	9.67E-02	7.53E-02
Minimum Element Size	6.45E-03	4.30E-03	2.15E-03
Maximum Element Growth Rate	1.20	1.15	1.13
Total number of elements	5519	7077	11274
Average Element Quality	0.8913	0.9119	0.9248

Velocity variables are discretized with second-order shape functions, while first order ones were sufficient for pressure.

The comparison between extrusion forces at different mesh resolutions is summarized in the following figure:

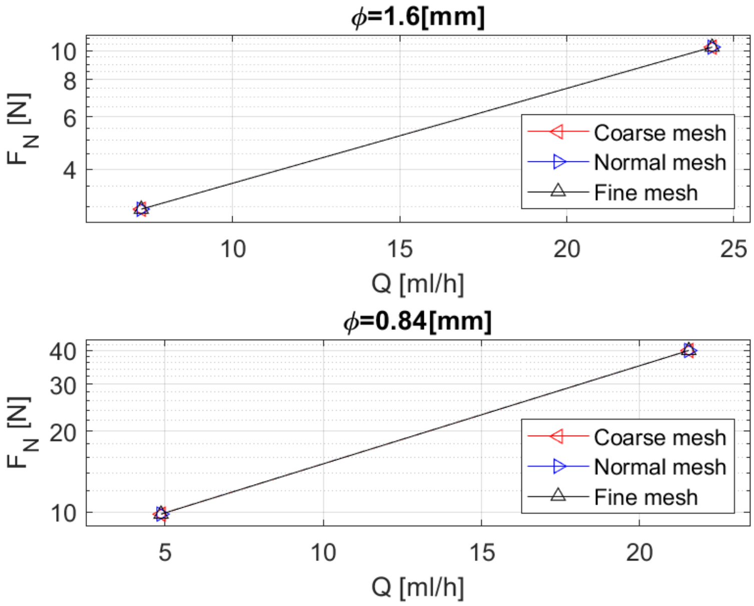

Figure B.2. Mesh-independence study on nozzle extrusion force; F_N: extrusion force; ϕ: nozzle outlet diameter; Q: volumetric flow rate.

It can be easily seen that there is no significant variation between nozzle force computations, in each operating condition. The coarse mesh has been shown to be sufficient for flow field computation, and it has been implemented to make the comparison with semi-analytical and experimental data.

A second mesh-independence study concerns the bead deposition, which is of interest for modeling the real manufacturing process.

In this case, a set of fully structured meshes has been implemented. The shape function orders were the same as in modeling the free-air extrusion.

The number of finite elements along the layer thickness and printing direction was varied. The following table summarizes the number of elements being used in the finite element discretization:

Table B.3. Mesh statistics for layer control volume discretization; the number of elements is the same for each layer thickness being investigated.

Property	Mesh 1	Mesh 2	Mesh 3
Elements along thickness	30	50	70
Elements along width	80	140	190

Total number of elements	2400	7000	13300

The results of the mesh-independence study for the bead have been reported in the following Figure B.3:

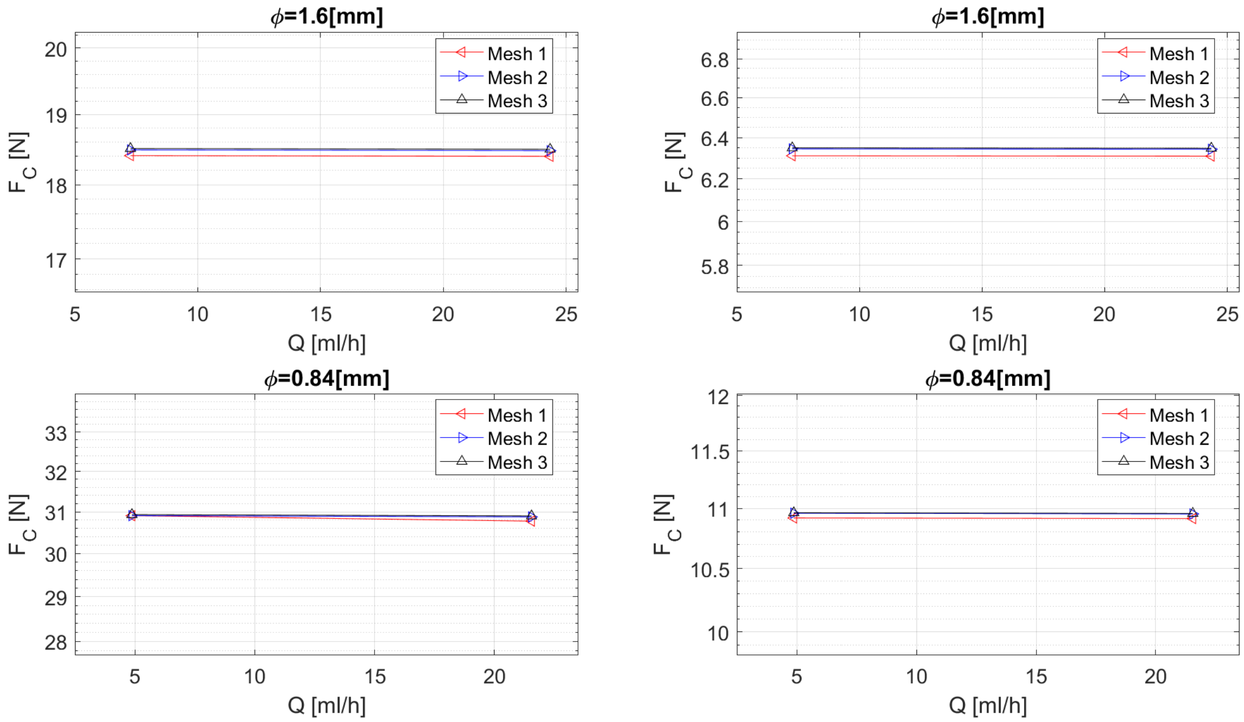

Figure B.3. Mesh-independence study on nozzle extrusion force; F_C: extrusion force; ϕ: nozzle outlet diameter; Q: volumetric flow rate.

The discrepancy is very low, and it is almost imperceptible when comparing ‘Mesh 2’ with ‘Mesh 3’; for that reason, Mesh 2 parameters have been implemented in all calculations.

B.3. Discrepancy between Newtonian and non-Newtonian curves

To give a better insight into the discrepancy between numerical and experimental results at higher flow rates and lower diameters (that is, at higher mean shear rates), the shear rate is evaluated numerically for all the 22 sections taken along nozzle axis.

From Table B.2, it is known that the first tapered section is equal for all nozzles; for that reason, the only parameter which is gradually changed according to the experimental setup is flow rate:

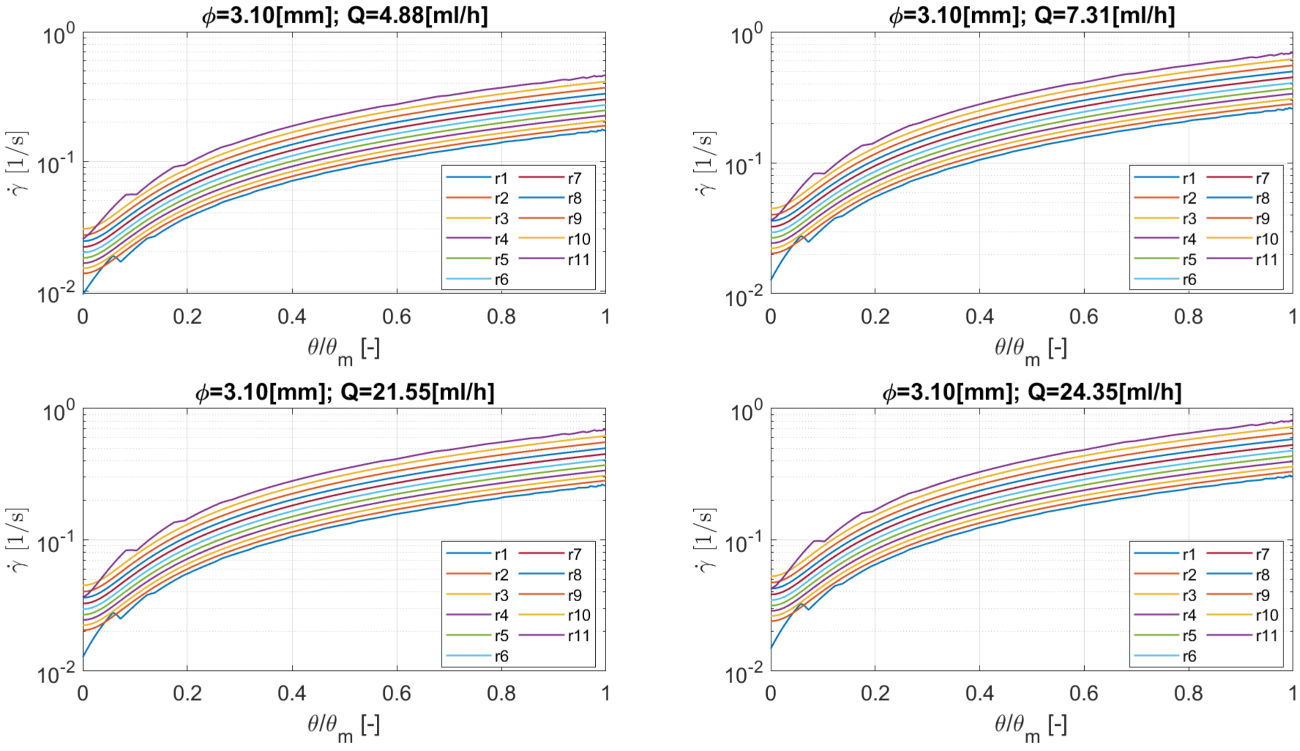

Figure B.4. Shear rate profiles in the first tapered control volume of the nozzles, found by means of CFD simulations; θ: Polar coordinate; r_k: k-th cut section along the control volume, according to Figure B.1 - b; ϕ: nozzle outlet diameter; Q: flow rate; $\dot{\gamma}$: shear rate; θ_m: maximum azimuthal position.

For the last tapered zone, both the internal features and flow rates are different:

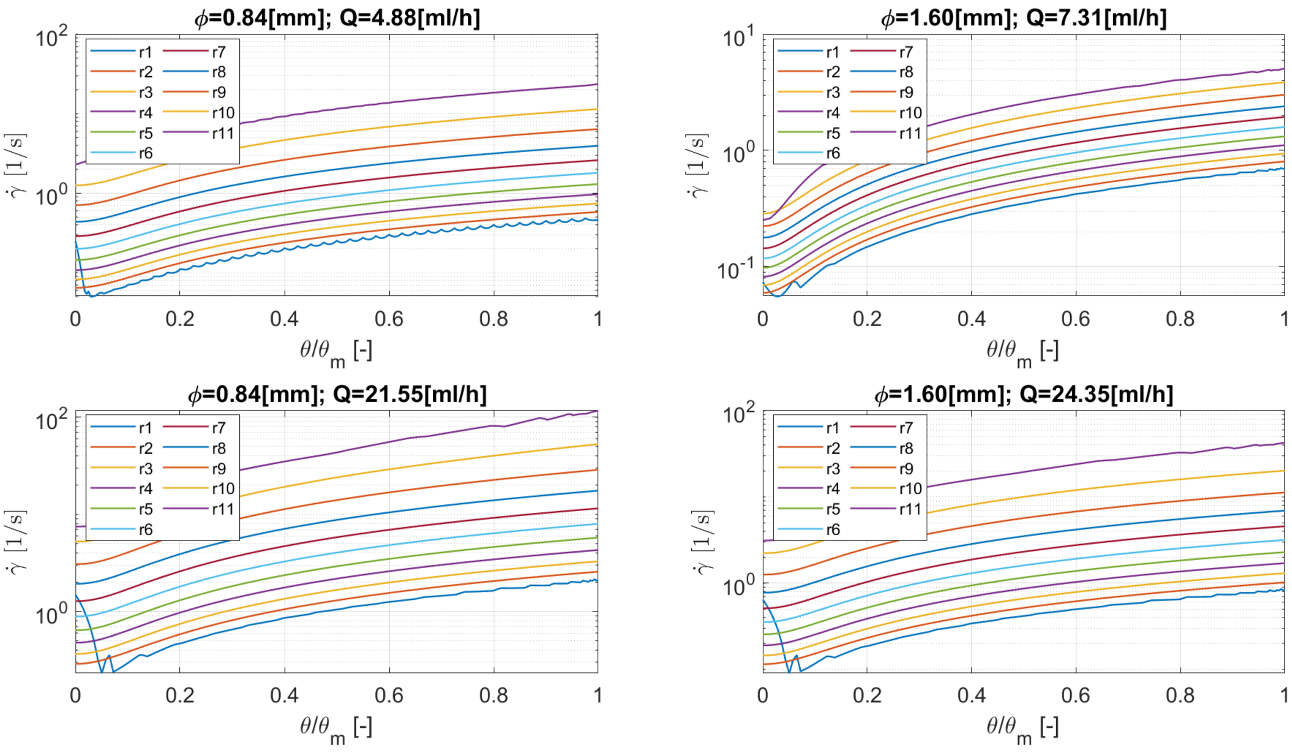

Figure B.5. Shear rate profiles in the second tapered control volume of the nozzles, found by means of CFD simulations; θ: Polar coordinate; r_k: k-th cut section along the control volume, according to Figure B.1 - b; ϕ: nozzle outlet diameter; Q: flow rate; $\dot{\gamma}$: shear rate; θ_m: maximum azimuthal position.

It can be observed that the fluid always behaves as a Newtonian fluid in the first tapered section (Figure B.4), but this zone contributes less to the final force prediction, because most of the pressure drop develops in the second tapered zone. Here the shear rate is significantly higher (Figure B.5), especially at lower nozzle diameter and higher flow rates.

According to the declared silicone rheology, the first Newtonian plateau ends at about 15 [1/s]; then, there is a transition zone, up to 25 [1/s] and, finally, the power-law regime. The results are in reasonable agreement when the maximum shear rate falls in the Newtonian regime, and this aspect explains also the very good agreement between the proposed semi-analytical code and the Newtonian model.

Bibliography

[1] A. Haleem, M. Javaid, Additive Manufacturing Applications in Industry 4.0: A Review, Journal of Industrial Integration and Management. 04 (2019) 1930001. https://doi.org/10.1142/S2424862219300011.

[2] S. Whyman, K.M. Arif, J. Potgieter, Design and development of an extrusion system for 3D printing biopolymer pellets, The International Journal of Advanced Manufacturing Technology. 96 (2018). https://doi.org/10.1007/s00170-018-1843-y.

[3] A. Bellini, L. Shor, S.I. Guceri, New developments in fused deposition modeling of ceramics, Rapid Prototyp J. 11 (2005). https://doi.org/10.1108/13552540510612901.

[4] C.E. Duty, V. Kunc, B. Compton, B. Post, D. Erdman, R. Smith, R. Lind, P. Lloyd, L. Love, Structure and mechanical behavior of Big Area Additive Manufacturing (BAAM) materials, Rapid Prototyp J. 23 (2017) 181–189. https://doi.org/10.1108/RPJ-12-2015-0183.

[5] B. K. Post, R. F. Lind, P. D. Lloyd, V. Kunc, J. M. Linhal, L. J. Love, The Economics of Big Area Additive Manufacturing, in: Solid Freeform Fabrication Symposium – An Additive Manufacturing Conference, 2016.

[6] P. Chesser, B. Post, A. Roschli, C. Carnal, R. Lind, M. Borish, L. Love, Extrusion control for high quality printing on Big Area Additive Manufacturing (BAAM) systems, Addit Manuf. 28 (2019). https://doi.org/10.1016/j.addma.2019.05.020.

[7] A. La Gala, R. Fiorio, M. Erkoç, L. Cardon, D.R. D'hooge, Theoretical Evaluation of the Melting Efficiency for the Single-Screw Micro-Extrusion Process: The Case of 3D Printing of ABS, Processes. 8 (2020). https://doi.org/10.3390/pr8111522.

[8] A. Altinkaynak, M. Gupta, M. A. Spalding, S. L. Crabtree, Investigation of melting in a single-screw extruder, in: Annual Technical Conference - ANTEC, Conference Proceedings, 2006.

[9] A. Altinkaynak, M. Gupta, M. A. Spalding, S. L. Crabtree, Numerical investigation of the effect of screw temperature on the melting profile in a single-screw extruder, in: SPE ANTEC, 2007.

[10] A. Altınkaynak, M. Gupta, M.A. Spalding, S.L. Crabtree, Melting in a Single Screw Extruder: Experiments and 3D Finite Element Simulations, International Polymer Processing. 26 (2011). https://doi.org/10.3139/217.2419.

[11] W. H. Darnell, E. A. J. Mol, Solids Conveying in Extruders, Society Plastics Engineers. 12 (1956) 20–29.

[12] C. I. Chung, New ideas about solids conveying in screw extruders, SPE Journal. (1970).

[13] C.I. Chung, Plasticating single-screw extrusion theory, Polym Eng Sci. 11 (1971). https://doi.org/10.1002/pen.760110204.

[14] K. Schnieder, Technical report on plastics processes in the feeding zone of an extruder, Aachen: Institute of Plastics Processing. (1969).

[15] E. Broyer, Z. Tadmor, Solids conveying in screw extruders part I: A modified isothermal model, Polym Eng Sci. 12 (1972). https://doi.org/10.1002/pen.760120103.

[16] Z. Tadmor, E. Broyer, Solids conveying in screw extruders part II: Non isothermal model, Polym Eng Sci. 12 (1972). https://doi.org/10.1002/pen.760120510.

[17] G.A. Campbell, N. Dontula, Solids Transport in Extruders, International Polymer Processing. 10 (1995). https://doi.org/10.3139/217.950030.

[18] J.G.A. Lovegrove, J.G. Williams, Pressure generation mechanisms in the feed section of screw extruders, Polym Eng Sci. 14 (1974). https://doi.org/10.1002/pen.760140809.

[19]. Zhang and V. Sernas, Incompressible Model of Solids, Journal of Reifnroced Plastics and Composites. 22 (2002).

[20] A. Karandikar, Numerical Analysis of Melting and Melt Flow Behaviour in Extrusion Deposition Process, 2016. http://raiith.iith.ac.in/2679/1/ME14MTECH11017.pdf (accessed August 11, 2021).

[21] J. Trippe, V. Schöppner, Investigation of the influence of material and pellet shape on the dissipation in the solids conveying zone of single-screw extruders based on the discrete element method (DEM), in: 2017. https://doi.org/10.1063/1.5016742.

[22] O. Celik, C. Bonten, Three-dimensional simulation of a single-screw extruder's grooved feed section, in: 2016. https://doi.org/10.1063/1.4965509.

[23] J.-S. Leßmann, R. Weddige, V. Schöppner, A. Porsch, Modelling the Solids Throughput of Single Screw Smooth Barrel Extruders as a Function of the Feed Section Parameters, International Polymer Processing. 27 (2012) 469–477. https://doi.org/10.3139/217.2588.

[24] P.A. Moysey, M.R. Thompson, Discrete particle simulations of solids compaction and conveying in a single-screw extruder, Polym Eng Sci. 48 (2008) 62–73. https://doi.org/10.1002/pen.20845.

[25] P.A. Moysey, M.R. Thompson, Modelling the solids inflow and solids conveying of single-screw extruders using the discrete element method, Powder Technol. 153 (2005). https://doi.org/10.1016/j.powtec.2005.03.001.

[26] P.A. Moysey, M.R. Thompson, Investigation of solids transport in a single-screw extruder using a 3-D discrete particle simulation, Polym Eng Sci. 44 (2004). https://doi.org/10.1002/pen.20248.

[27] O.P. Michelangelli, M. Yamanoi, A. Gaspar-Cunha, J.A. Covas, Modelling pellet flow in single extrusion with DEM, Proceedings of the Institution of Mechanical Engineers, Part E: Journal of Process Mechanical Engineering. 225 (2011). https://doi.org/10.1177/0954408911418159.

[28] Z. Tadmor, Fundamentals of plasticating extrusion. I. A theoretical model for melting, Polym Eng Sci. 6 (1966). https://doi.org/10.1002/pen.760060303.

[29] B. H. Maddock, A Visual Analysis of Flow and Mixing in Extruder Screws, SPE Journal. 15 (1959) 383–389.

[30] C. Rauwendaal, An improved analytical melting theory, 9 (1989) 331–336.

[31] J.T. Lindt, A dynamic melting model for a single-screw extruder, Polym Eng Sci. 16 (1976). https://doi.org/10.1002/pen.760160411.

[32] Z. Tadmor, C. G. Gogos, Principles of polymer processing, 2006.

[33] G. Menges, K. P. Klenk, Melting and plasticating of unplasticized PVC powder in the screw extruder, Kunststoffe. (1967).

[34] D.E. McClelland, C.I. Chung, Shear stress at polymer/metal interface during melting in extrusion, Polym Eng Sci. 23 (1983). https://doi.org/10.1002/pen.760230209.

[35] R. Steller, J. Iwko, Polymer Plastication during Injection Molding Part I: Mathematical Model, International Polymer Processing. 23 (2008). https://doi.org/10.3139/217.2041.

[36] J. Iwko, R. Steller, Polymer Plastication during Injection Molding Part II: Simulations and Experiments, International Polymer Processing. 23 (2008). https://doi.org/10.3139/217.2042.

[37] H. Potente, M. Bornemann, M. Kurte-Jardin, Analytical Model for the Throughput and Drive Power Calculation in the Melting Section of Single Screw Plasticizing Units considering Wall-Slippage, International Polymer Processing. 24 (2009). https://doi.org/10.3139/217.2163.

[38] K. Wilczyński, A. Nastaj, A. Lewandowski, K.J. Wilczyński, K. Buziak, Fundamentals of Global Modeling for Polymer Extrusion, Polymers (Basel). 11 (2019) 2106. https://doi.org/10.3390/polym11122106.

[39] K. Wilczyński, K. Buziak, K. Wilczyński, A. Lewandowski, A. Nastaj, Computer Modeling for Single-Screw Extrusion of Wood–Plastic Composites, Polymers (Basel). 10 (2018). https://doi.org/10.3390/polym10030295.

[40] A. Lewandowski, K. Wilczyński, Global Modeling of Single Screw Extrusion with Slip Effects, International Polymer Processing. 34 (2019). https://doi.org/10.3139/217.3653.

[41] H. S. Rowell and D. Finlayson, Screw Viscosity Pumps, 126 (1928) 249–287.

[42] J.F. Carley, R.S. Mallouk, J.M. McKelvey, Simplified Flow Theory for Screw Extruders, Ind Eng Chem. 45 (1953). https://doi.org/10.1021/ie50521a032.

[43] J.F. Carley, R.A. Strub, Basic Concepts of Extrusion, Ind Eng Chem. 45 (1953). https://doi.org/10.1021/ie50521a031.

[44] R.S. Mallouk, J.M. McKelvey, Power Requirements of Melt Extruders, Ind Eng Chem. 45 (1953). https://doi.org/10.1021/ie50521a035.

[45] O. Demiryürek, E. Koç, Design basis and hydrodynamic performance analysis of single-screw extruders. II – viscous power loss, Industrial Lubrication and Tribology. 61 (2009). https://doi.org/10.1108/00368790910960020.

[46] C. Rawuendaal, J. F. Ingen Housz, Leakage flow of an isothermal power law fluid, Advances in Polymer Technology. 8 (1988) 289–316.

[47] M. Reiner, A Mathematical Theory of Dilatancy, American Journal of Mathematics. 67 (1945). https://doi.org/10.2307/2371950.

[48] R. Rivlin, Solution of Some Problems in the Exact Theory of Visco-Elasticity, Indiana University Mathematics Journal. 5 (1956). https://doi.org/10.1512/iumj.1956.5.55004.

[49] Z. Rotem, R. Shinnar, Non-newtonian flow-between parallel boundaries in linear movement, Chem Eng Sci. 15 (1961). https://doi.org/10.1016/0009-2509(61)85006-9.

[50] H. Kaiser, C.W. Smith, Prediction of Flow of a Melted Plastic Through a Screw Extruder, Journal of Basic Engineering. 91 (1969). https://doi.org/10.1115/1.3571160.

[51] Z.S. Safar, G.S.A. Shawki, Performance of thrust bearings operating with non-Newtonian lubricating films, Tribol Int. 12 (1979). https://doi.org/10.1016/0301-679X(79)90160-9.

[52] T. Liu, K. Chen, Generalized Couette flow in channels of irregular cross-section, Journal of the Chinese Institute of Engineers. 10 (1987). https://doi.org/10.1080/02533839.1987.9676980.

[53] P.M. Coelho, R.J. Poole, Heat Transfer of Power-Law Fluids in Plane Couette–Poiseuille Flows with Viscous Dissipation, Heat Transfer Engineering. 41 (2020). https://doi.org/10.1080/01457632.2019.1611139.

[54] S. Middleman, Flow of Power Law Fluids in Rectangular Ducts, Transactions of the Society of Rheology. 9 (1965). https://doi.org/10.1122/1.549009.

[55] Y. Li, F. Hsieh, Modeling of flow in a single screw extruder, J Food Eng. 27 (1996). https://doi.org/10.1016/0260-8774(95)00016-X.

[56] Y. Li, F. Hsieh, New Melt Conveying Models for a Single Screw Extruder, J Food Process Eng. 17 (1994). https://doi.org/10.1111/j.1745-4530.1994.tb00341.x.

[57] R.T. Steller, J. Iwko, Generalized Flow of Ellis Fluid in the Screw Channel, International Polymer Processing. 16 (2001). https://doi.org/10.3139/217.1649.

[58] R.T. Steller, Theoretical model for flow of polymer melts in the screw channel, Polym Eng Sci. 30 (1990). https://doi.org/10.1002/pen.760300704.

[59] N. G. Gaylord, H. M. Hulburt, Processing of Thermoplastic Materials, (1959).

[60] H. P. Squires, Screw extruder pumping efficiency, S.P.E.J. 58 (1958).

[61] J. M. McKelvey, Polymer Processing, John Wiley & Sons, 1962.

[62] M.L. Booy, Influence of channel curvature on flow, pressure distribution, and power requirements of screw pumps and melt extruders, Polym Eng Sci. 3 (1963). https://doi.org/10.1002/pen.760030305.

[63] J.I. Orisaleye, O.A. Adefuye, A.A. Ogundare, O.L. Fadipe, Parametric analysis and design of a screw extruder for slightly non-Newtonian (pseudoplastic) materials, Engineering Science and Technology, an International Journal. 21 (2018). https://doi.org/10.1016/j.jestch.2018.03.001.

[64] R.M. Griffith, Fully Developed Flow in Screw Extruders. Theoretical and Experimental Study, Industrial & Engineering Chemistry Fundamentals. 1 (1962). https://doi.org/10.1021/i160003a004.

[65] C.M.B.L.-B. and J.M. W. Roland, The Effect of Channel Curvature on the Flow Rate and Viscous Dissipation of Power-Law Fluids, in: SPE ANTEC, 2018.

[66] M.L. Hami, J.F.T. Pittman, Finite element solutions for flow in a single-screw extruder, including curvature effects, Polym Eng Sci. 20 (1980). https://doi.org/10.1002/pen.760200505.

[67] K.P. Choo, M.L. Hami, J.F.T. Pittman, Deep channel operating characteristics of a single screw extruder: Finite element predictions and experimental results for isothermal non-Newtonian flow, Polym Eng Sci. 21 (1981). https://doi.org/10.1002/pen.760210208.

[68] J. Nebrensky, J.F.T. Pittman, J.M. Smith, Flow and heat transfer in screw extruders: I. A variational analysis applied in helical co-ordinates, Polym Eng Sci. 13 (1973). https://doi.org/10.1002/pen.760130307.

[69] Q. Yu, G.-H. Hu, Development of a helical coordinate system and its application to analysis of polymer flow in screw extruders Part I. The balance equations in a helical coordinate system, J Nonnewton Fluid Mech. 69 (1997). https://doi.org/10.1016/S0377-0257(96)01534-0.

[70] Q. Yu, G.-H. Hu, Development of a helical coordinate system and its applications to analysis of polymer flow in screw extruders. Part II: A helical channel model for single screw extruders, Polym Eng Sci. 38 (1998). https://doi.org/10.1002/pen.10247.

[71] J.-W. Wang, J.R.G. Andrews, Numerical simulation of flow in helical ducts, AIChE Journal. 41 (1995). https://doi.org/10.1002/aic.690410504.

[72] H. Potente, H. Ridder, R.V. Cunha, Global Concept for Describing and Investigation of Wall Slip Effects in the Extrusion Process, Macromol Mater Eng. 287 (2002). https://doi.org/10.1002/mame.200290013.

[73] H. Potente, H. Ridder, Pressure/Throughput Behavior of a Single-screw Plasticising Unit in Consideration of Wall Slippage, International Polymer Processing. 17 (2002). https://doi.org/10.3139/217.1679.

[74] H. Potente, M. Kurte, H. Ridder, Influence of Non-Newtonian Behaviour on the Processing Characteristics of Wall-slipping Materials, International Polymer Processing. 18 (2003). https://doi.org/10.3139/217.1730.

[75] G. Ferretti, R. Montanari, A finite-difference method for the prediction of velocity field in extrusion process, J Food Eng. 83 (2007). https://doi.org/10.1016/j.jfoodeng.2007.01.002.

[76] H. Horiguchi, K. Takahashi, T. Yokota, Numerical Simulation of the Flow Field in the Mixing Section of a Screw Extruder by the Lattice Gas Automata Method., Journal of Chemical Engineering. 36 (2003). https://doi.org/10.1252/jcej.36.110.

[77] J.M. Buick, J.A. Cosgrove, Numerical simulation of the flow field in the mixing section of a screw extruder by the lattice Boltzmann model, Chem Eng Sci. 61 (2006). https://doi.org/10.1016/j.ces.2005.11.070.

[78] N.D. Polychronopoulos, J. Vlachopoulos, Computer Flow Simulation of Moffatt Eddies in Single Screw Extrusion, International Polymer Processing. 33 (2018). https://doi.org/10.3139/217.3574.

[79] M.A. Spalding, E.I. Garcia-Meitin, S.L. Kodjie, G.A. Campbell, T.W. Womer, Troubleshooting and mitigating gels in polyethylene film products, Journal of Plastic Film & Sheeting. 34 (2018). https://doi.org/10.1177/8756087917722586.

[80] K.P. Choo, N.R. Neelakantan, J.F.T. Pittman, Experimental deep-channel velocity profiles and operating characteristics for a single-screw extruder, Polym Eng Sci. 20 (1980). https://doi.org/10.1002/pen.760200506.

[81] C. Rauwendaal, T.A. Osswald, G. Tellez, P.J. Gramann, Flow Analysis in Screw Extruders-Effect of Kinematic Conditions, International Polymer Processing. 13 (1998). https://doi.org/10.3139/217.980327.

[82] H. Potente, M. Bornemann, D. Heinrich, J. Pape, Investigations into Kinematic Reversal in Non-isothermal Flows in Single-screw Machines, International Polymer Processing. 21 (2006). https://doi.org/10.3139/217.0126.

[83] F. Habla, S. Obermeier, L. Dietsche, O. Kintzel, O. Hinrichsen, CFD Analysis of the Frame Invariance of the Melt Temperature Rise in a Single-screw Extruder, International Polymer Processing. 28 (2013). https://doi.org/10.3139/217.2753.

[84] M. Kurte-Jardin, H. Potente, K. Sigge, M. Bornemann, Modeling the Temperature Development of Wall-slipping Polymers in Single-screw Channels, International Polymer Processing. 24 (2009). https://doi.org/10.3139/217.2125.

[85] G. Percoco, L. Arleo, G. Stano, F. Bottiglione, Analytical model to predict the extrusion force as a function of the layer height, in extrusion based 3D printing, Addit Manuf. 38 (2021) 101791. https://doi.org/10.1016/J.ADDMA.2020.101791.

[86] Z. Tadmor, I. Klein, Engineering Principles of plasticating Extrusion, 1970.

[87] R. Bird, Armostrong R. C., Hassager O., Dynamics of polymeric liquids Vol 1 Fluid dynamics, 1987.

[88] A. Dey, N. Yodo, A Systematic Survey of FDM Process Parameter Optimization and Their Influence on Part Characteristics, Journal of Manufacturing and Materials Processing. 3 (2019) 64. https://doi.org/10.3390/jmmp3030064.

[89] R. Comminal, M.P. Serdeczny, D.B. Pedersen, J. Spangenberg, Numerical modeling of the strand deposition flow in extrusion-based additive manufacturing, Addit Manuf. 20 (2018) 68–76. https://doi.org/10.1016/j.addma.2017.12.013.

[90] V. Ngamaramvaranggul, N. Thongjub, Simulation of Die-swell Flow for Wet Powder Mass Extrusion in Pharmaceutical Process, Applied Science and Engineering Progress. 13 (2020). https://doi.org/10.14416/j.asep.2020.03.004.

[91] M.P. Serdeczny, R. Comminal, D.B. Pedersen, J. Spangenberg, Experimental and analytical study of the polymer melt flow through the hot-end in material extrusion additive manufacturing, Addit Manuf. 32 (2020) 100997. https://doi.org/10.1016/J.ADDMA.2019.100997.

[92] N. Shadvar, E. Foroozmehr, M. Badrossamay, I. Amouhadi, A.S. Dindarloo, Computational analysis of the extrusion process of fused deposition modeling of acrylonitrile-butadiene-styrene, International Journal of Material Forming. 14 (2021) 121–131. https://doi.org/10.1007/s12289-019-01523-1.

[93] D. Tang, F.H. Marchesini, L. Cardon, D.R. D’hooge, State of the-Art for Extrudate Swell of Molten Polymers: From Fundamental Understanding at Molecular Scale toward Optimal Die Design at Final Product Scale, Macromol Mater Eng. 305 (2020) 2000340. https://doi.org/10.1002/mame.202000340.

[94] Albis, Albis - Properties of Terluran GP-22, (n.d.). https://www.albis.com/en/products/download/doc/en/SI/styrolution/TerluranGP-22.pdf (accessed March 31, 2022).

[95] E.E. Acur, J. Vlachopoulos, Numerical simulation of a single-screw plasticating extruder, Polym Eng Sci. 22 (1982) 1084–1094. https://doi.org/10.1002/pen.760221706.

[96] K. Wilczyński, A Computer Model for Single-Screw Plasticating Extrusion, Polym Plast Technol Eng. 35 (1996) 449–477. https://doi.org/10.1080/03602559608000931.

[97] M. Holzinger, J. Blase, A. Reinhardt, L. Kroll, New additive manufacturing technology for fibre-reinforced plastics in skeleton structure, Journal of Reinforced Plastics and Composites. 37 (2018) 1246–1254. https://doi.org/10.1177/0731684418763988.

[98] A. Pricci, M.D. de Tullio, G. Percoco, Semi-analytical models for non-Newtonian fluids in tapered and cylindrical ducts, applied to the extrusion-based additive manufacturing, Mater Des. 223 (2022) 111168. https://doi.org/10.1016/j.matdes.2022.111168.

[99] M.P. Serdeczny, R. Comminal, D.B. Pedersen, J. Spangenberg, Experimental validation of a numerical model for the strand shape in material extrusion additive manufacturing, Addit Manuf. 24 (2018) 145–153. https://doi.org/10.1016/j.addma.2018.09.022.

[100] R. Comminal, M.P. Serdeczny, D.B. Pedersen, J. Spangenberg, Numerical modling of the material deposition and contouring in fused deposition modeling, in: Solid Freeform Fabrication 2018:

Proceedings of the 29th Annual International (Ed.), Solid Freeform Fabrication 2018: Proceedings of the 29th Annual International, 2018.

[101] R. Comminal, M.P. Serdeczny, D.B. Pedersen, J. Spangenberg, Motion planning and numerical simulation of material deposition at corners in extrusion additive manufacturing, Addit Manuf. 29 (2019) 100753. https://doi.org/10.1016/j.addma.2019.06.005.

[102] M.P. Serdeczny, R. Comminal, D.B. Pedersen, J. Spangenberg, Numerical simulations of the mesostructure formation in material extrusion additive manufacturing, Addit Manuf. 28 (2019) 419–429. https://doi.org/10.1016/j.addma.2019.05.024.

[103] R. Comminal, S. Jafarzadeh, M. Serdeczny, J. Spangenberg, Estimations of Interlayer Contacts in Extrusion Additive Manufacturing Using a CFD Model, in: Industrializing Additive Manufacturing, Springer International Publishing, Cham, 2021: pp. 241–250. https://doi.org/10.1007/978-3-030-54334-1_17.

[104] B. Behdani, M. Senter, L. Mason, M. Leu, J. Park, Numerical Study on the Temperature-Dependent Viscosity Effect on the Strand Shape in Extrusion-Based Additive Manufacturing, Journal of Manufacturing and Materials Processing. 4 (2020) 46. https://doi.org/10.3390/jmmp4020046.

[105] J. Du, Z. Wei, X. Wang, J. Wang, Z. Chen, An improved fused deposition modeling process for forming large-size thin-walled parts, J Mater Process Technol. 234 (2016) 332–341. https://doi.org/10.1016/j.jmatprotec.2016.04.005.

[106] H. Xia, J. Lu, G. Tryggvason, Fully resolved numerical simulations of fused deposition modeling. Part II – solidification, residual stresses and modeling of the nozzle, Rapid Prototyp J. 24 (2018) 973–987. https://doi.org/10.1108/RPJ-11-2017-0233.

[107] E.P. Furlani, V. Sukhotskiy, A. Verma, V. Vishnoi, P. Amiri Roodan, Numerical Simulation of Extrusion Additive Manufacturing: Fused Deposition Modeling, TechConnect Briefs. 4 (2018) 118–121.

[108] M.E.A. PAPON, A. HAQUE, M.A.R. SHARIF, Effect of Nozzle Geometry on Melt Flow Simulation and Structural Property of Thermoplastic Nanocomposites in Fused Deposition Modeling, in: American Society for Composites 2017, DEStech Publications, Inc., Lancaster, PA, 2017. https://doi.org/10.12783/asc2017/15339.

[109] E.A. Papon, A. Haque, M.A.R. Sharif, Numerical study for the improvement of bead spreading architecture with modified nozzle geometries in additive manufacturing of polymers, Rapid Prototyp J. 27 (2021) 518–529. https://doi.org/10.1108/RPJ-05-2019-0142.

[110] T.G. Crisp, Weaver Jason M., Review of Current Problems and Developments in Large Area Additive Manufacturing (LAAM), in: Solid Freeform Fabrication 2021: Proceedings of the 32nd Annual International Solid Freeform Fabrication Symposium – An Additive Manufacturing Conference, 2021.

[111] R. Comminal, M.P. Serdeczny, N. Ranjbar, M. Mehrali, D.B. Pedersen, H. Stang, J. Spangenberg, Modelling of material deposition in big area additive manufacturing and 3D concrete printing, in: Joint Special Interest Group Meeting between Euspen and ASPE, 2019. www.euspen.eu.

[112] A.-D. Le, B. Cosson, A.C.A. Asséko, Simulation of large-scale additive manufacturing process with a single-phase level set method: a process parameters study, The International Journal of Advanced Manufacturing Technology. 113 (2021) 3343–3360. https://doi.org/10.1007/s00170-021-06703-5.

[113] Comsol Multiphysics, LiveLink ™ for MATLAB ® User's Guide, 2009. www.comsol.com/blogs.

[114] B. Cosson, A.C. Akué Asséko, L. Pelzer, C. Hopmann, Radiative Thermal Effects in Large Scale Additive Manufacturing of Polymers: Numerical and Experimental Investigations, Materials. 15 (2022) 1052. https://doi.org/10.3390/ma15031052.

[115] A. Pricci, M.D. de Tullio, G. Percoco, Modeling of extrusion-based additive manufacturing for pelletized thermoplastics: Analytical relationships between process parameters and extrusion outcomes, CIRP J Manuf Sci Technol. 41 (2023) 239–258. https://doi.org/10.1016/j.cirpj.2022.11.020.

[116] Z. Wang, D.E. Smith, Numerical analysis of screw swirling effects on fiber orientation in large area additive manufacturing polymer composite deposition, Compos B Eng. 177 (2019) 107284. https://doi.org/10.1016/J.COMPOSITESB.2019.107284.

[117] Z. Wang, Z. Fang, D.E. Smith, Effects of local fiber orientation state on thermal-mechanical behaviors of composite parts made by large area polymer deposition additive manufacturing, in: Solid Freeform Fabrication 2021: Proceedings of the 32nd Annual International, 2021.

[118] Z. Wang, D.E. Smith, A Fully Coupled Simulation of Planar Deposition Flow and Fiber Orientation in Polymer Composites Additive Manufacturing, Materials. 14 (2021) 2596. https://doi.org/10.3390/ma14102596.

[119] Z. Wang, D.E. Smith, Finite element modelling of fully-coupled flow/fiber-orientation effects in polymer composite deposition additive manufacturing nozzle-extrudate flow, Compos B Eng. 219 (2021) 108811. https://doi.org/10.1016/j.compositesb.2021.108811.

[120] S.J. Müller, E. Mirzahossein, E.N. Iftekhar, C. Bächer, S. Schrüfer, D.W. Schubert, B. Fabry, S. Gekle, Flow and hydrodynamic shear stress inside a printing needle during biofabrication, PLoS One. 15 (2020). https://doi.org/10.1371/JOURNAL.PONE.0236371.

[121] A.R. Haghighi, S. Asadi Chalak, Mathematical modeling of blood flow through a stenosed artery under body acceleration, Journal of the Brazilian Society of Mechanical Sciences and Engineering. 39 (2017) 2487–2494. https://doi.org/10.1007/S40430-017-0716-X/FIGURES/11.

[122] P. Kaushik, P.K. Mondal, S. Chakraborty, Flow dynamics of a viscoelastic fluid squeezed and extruded between two parallel plates, J Nonnewton Fluid Mech. 227 (2016) 56–64. https://doi.org/10.1016/j.jnnfm.2015.11.007.

[123] A. Pricci, M.D. de Tullio, G. Percoco, Analytical and Numerical Models of Thermoplastics: A Review Aimed to Pellet Extrusion-Based Additive Manufacturing, Polymers, Vol. 13, Page 3160. 13 (2021) 3160. https://doi.org/10.3390/POLYM13183160.

[124] Jeffrey S. Plott, Extrusion-based Additive Manufacturing of Silicone Elastomer Parts, The University of Michigan, 2017.

[125] J. Plott, X. Tian, A. Shih, Measurement and Modeling of Forces in Extrusion-Based Additive Manufacturing of Flexible Silicone Elastomer With Thin Wall Structures, J Manuf Sci Eng. 140 (2018). https://doi.org/10.1115/1.4040350.

[126] H.S. Gaikwad, P.K. Mondal, S. Wongwises, Softness Induced Enhancement in Net Throughput of Non-Linear Bio-Fluids in Nanofluidic Channel under EDL Phenomenon, Sci Rep. 8 (2018) 7893. https://doi.org/10.1038/s41598-018-26056-6.

[127] R. Sarma, N. Deka, K. Sarma, P.K. Mondal, Electroosmotic flow of Phan-Thien–Tanner fluids at high zeta potentials: An exact analytical solution, Physics of Fluids. 30 (2018) 062001. https://doi.org/10.1063/1.5033974.

[128] S. Balasubramanian, P. Kaushik, P.K. Mondal, Dynamics of viscoelastic fluid in a rotating soft microchannel, Physics of Fluids. 32 (2020) 112003. https://doi.org/10.1063/5.0025157.

[129] T. Siva, B. Kumbhakar, S. Jangili, P.K. Mondal, Unsteady electro-osmotic flow of couple stress fluid in a rotating microchannel: An analytical solution, Physics of Fluids. 32 (2020) 102013. https://doi.org/10.1063/5.0023747.

[130] M. Kumar, P.K. Mondal, Buoyancy driven flow of a couple stress fluid from an isothermal vertical plate: the role of spatially periodic magnetic field, Phys Scr. 96 (2021) 125014. https://doi.org/10.1088/1402-4896/ac2af3.

[131] L. Zhang, M.M. Bhatti, O.A. Bég, H.J. Leonard, S. Kuharat, Numerical study of natural convection dissipative electro-magnetic non-Newtonian flow through a non-Darcy channel, ZAMM - Journal of Applied Mathematics and Mechanics / Zeitschrift Für Angewandte Mathematik Und Mechanik. (2022). https://doi.org/10.1002/zamm.202100608.

[132] L. Zhang, N. Tariq, M.M. Bhatti, E.E. Michaelides, Mixed Convection Flow over an Elastic, Porous Surface with Viscous Dissipation: A Robust Spectral Computational Approach, Fractal and Fractional. 6 (2022) 263. https://doi.org/10.3390/fractalfract6050263.

[133] C.W. Macosko, Rheology: Principles, Measurements, and Applications, 1996.

[134] M.M. Bhatti, R. Ellahi, M. Hossein Doranehgard, Numerical study on the hybrid nanofluid (Co3O4-Go/H2O) flow over a circular elastic surface with non-Darcy medium: Application in solar energy, J Mol Liq. 361 (2022) 119655. https://doi.org/10.1016/j.molliq.2022.119655.

[135] S. Rahimi, D. Durban, S. Khosid, Wall friction effects and viscosity reduction of gel propellants in conical extrusion, J Nonnewton Fluid Mech. 165 (2010) 782–792. https://doi.org/10.1016/j.jnnfm.2010.04.003.

[136] M.M. Cross, Relation between viscoelasticity and shear-thinning behaviour in liquids, Rheol. Acta. 18 (1979) 609–614.

[137] T. Sochi, Analytical solutions for the flow of Carreau and Cross fluids in circular pipes and thin slits, Rheol Acta. 54 (2015) 745–756. https://doi.org/10.1007/s00397-015-0863-x.

[138] S.K. Kim, Flow-rate based method for velocity of fully developed laminar flow in tubes, J Rheol (N Y N Y). 62 (2018) 1397–1407. https://doi.org/10.1122/1.5041958.

[139] G. deVries, D.B. Craig, J.B. Haddow, Pseudo-plastic converging flow, Int J Mech Sci. 13 (1971) 763–772. https://doi.org/10.1016/0020-7403(71)90045-2.

[140] J. Vlachopoulos, P.S. Scott, Pressure Drop for Molten Polymer Flow Through Tapered Dies, 1985.

[141] S.I. Voropayev, S.A. Smirnov, F.Y. Testik, On the case when steady converging/diverging flow of a non-Newtonian fluid in a round cone permits an exact solution, Mech Res Commun. 31 (2004) 477–482. https://doi.org/10.1016/j.mechrescom.2003.11.014.

[142] H.S. Patel, R. Meher, Analytical Investigation of Jeffery–Hamel Flow by Modified Adomian Decomposition Method, Ain Shams Engineering Journal. 9 (2018) 599–606. https://doi.org/10.1016/j.asej.2016.02.007.

[143] J. Nagler, Jeffery-Hamel flow of non-Newtonian fluid with nonlinear viscosity and wall friction, Appl Math Mech. 38 (2017) 815–830. https://doi.org/10.1007/s10483-017-2206-8.

[144] Cubic equation - Wikipedia, (n.d.). https://en.wikipedia.org/wiki/Cubic_equation (accessed February 14, 2022).

[145] E3D v6 Stainless Steel Nozzle - Ooznest | Kits, Parts & Supplies, (n.d.). https://ooznest.co.uk/product/e3d-v6-stainless-steel-nozzle/ (accessed February 13, 2022).

[146] M.P. Escudier, R.J. Poole, F. Presti, C. Dales, C. Nouar, C. Desaubry, L. Graham, L. Pullum, Observations of asymmetrical flow behaviour in transitional pipe flow of yield-stress and other shear-thinning liquids, J Nonnewton Fluid Mech. 127 (2005) 143–155. https://doi.org/10.1016/j.jnnfm.2005.02.006.

[147] Brennen C. E., An Internet Book on Fluid Dynamics Kinematics of Deformation and Motion, n.d. http://brennen.caltech.edu/fluidbook/basicfluiddynamics/kinematics/kinematics.pdf (accessed February 12, 2022).

[148] A. Farina, L. Fusi, A. Mikelić, G. Saccomandi, A. Sequeira, E.F. Toro, Non-Newtonian Fluid Mechanics and Complex Flows, Springer International Publishing, Cham, 2018. https://doi.org/10.1007/978-3-319-74796-5.

[149] L.F. Shampine, Singular boundary value problems for ODEs, Appl Math Comput. 138 (2003) 99–112. https://doi.org/10.1016/S0096-3003(02)00111-X.

[150] T. Rey, J.-B. Le Cam, G. Chagnon, D. Favier, M. Rebouah, F. Razan, E. Robin, P. Didier, L. Heller, S. Faure, K. Janouchova, An original architectured NiTi silicone rubber structure for biomedical applications, Materials Science and Engineering: C. 45 (2014) 184–190. https://doi.org/10.1016/j.msec.2014.08.062.

[151] M. Carrabba, C. De Maria, A. Oikawa, C. Reni, I. Rodriguez-Arabaolaza, H. Spencer, S. Slater, E. Avolio, Z. Dang, G. Spinetti, P. Madeddu, G. Vozzi, Design, fabrication and perivascular implantation of bioactive scaffolds engineered with human adventitial progenitor cells for stimulation of arteriogenesis in peripheral ischemia, Biofabrication. 8 (2016) 015020. https://doi.org/10.1088/1758-5090/8/1/015020.

[152] C. De Maria, G. Vozzi, L. Moroni, Multimaterial, heterogeneous, and multicellular three-dimensional bioprinting, MRS Bull. 42 (2017) 578–584. https://doi.org/10.1557/mrs.2017.165.

[153] N. Paxton, W. Smolan, T. Böck, F. Melchels, J. Groll, T. Jungst, Proposal to assess printability of bioinks for extrusion-based bioprinting and evaluation of rheological properties governing bioprintability, Biofabrication. 9 (2017) 044107. https://doi.org/10.1088/1758-5090/aa8dd8.

[154] V.H.M. Mouser, F.P.W. Melchels, J. Visser, W.J.A. Dhert, D. Gawlitta, J. Malda, Yield stress determines bioprintability of hydrogels based on gelatin-methacryloyl and gellan gum for cartilage bioprinting, Biofabrication. 8 (2016) 035003. https://doi.org/10.1088/1758-5090/8/3/035003.

[155] M. Razavi, R. Primavera, A. Vykunta, A.S. Thakor, Silicone-based bioscaffolds for cellular therapies, Materials Science and Engineering: C. 119 (2021) 111615. https://doi.org/10.1016/j.msec.2020.111615.

[156] M. Zare, E.R. Ghomi, P.D. Venkatraman, S. Ramakrishna, Silicone-based biomaterials for biomedical applications: Antimicrobial strategies and 3D printing technologies, J Appl Polym Sci. 138 (2021) 50969. https://doi.org/10.1002/app.50969.

[157] K. Tian, J. Bae, S.E. Bakarich, C. Yang, R.D. Gately, G.M. Spinks, M. in het Panhuis, Z. Suo, J.J. Vlassak, 3D Printing of Transparent and Conductive Heterogeneous Hydrogel–Elastomer Systems, Advanced Materials. 29 (2017) 1604827. https://doi.org/10.1002/adma.201604827.

[158] M. Bont, C. Barry, S. Johnston, A review of liquid silicone rubber injection molding: Process variables and process modeling, Polym Eng Sci. 61 (2021) 331–347. https://doi.org/10.1002/pen.25618.

[159] H. Ou, M. Sahli, T. Barrière, J.C. Gelin, Multiphysics modelling and experimental investigations of the filling and curing phases of bi-injection moulding of thermoplastic polymer/liquid silicone rubbers, The International Journal of Advanced Manufacturing Technology. 92 (2017) 3871–3882. https://doi.org/10.1007/s00170-017-0425-8.

[160] D. Rus, M.T. Tolley, Design, fabrication and control of soft robots, Nature. 521 (2015) 467–475. https://doi.org/10.1038/nature14543.

[161] K.-J. Cho, J.-S. Koh, S. Kim, W.-S. Chu, Y. Hong, S.-H. Ahn, Review of manufacturing processes for soft biomimetic robots, International Journal of Precision Engineering and Manufacturing. 10 (2009) 171–181. https://doi.org/10.1007/s12541-009-0064-6.

[162] G. Stano, G. Percoco, Additive manufacturing aimed to soft robots fabrication: A review, Extreme Mech Lett. 42 (2021) 101079. https://doi.org/10.1016/j.eml.2020.101079.

[163] Ig Mo Koo, Kwangmok Jung, Ja Choon Koo, Jae-Do Nam, Young Kwan Lee, Hyouk Ryeol Choi, Development of Soft-Actuator-Based Wearable Tactile Display, IEEE Transactions on Robotics. 24 (2008) 549–558. https://doi.org/10.1109/TRO.2008.921561.

[164] Y. Menguc, Y.-L. Park, E. Martinez-Villalpando, P. Aubin, M. Zisook, L. Stirling, R.J. Wood, C.J. Walsh, Soft wearable motion sensing suit for lower limb biomechanics measurements, in: 2013 IEEE International Conference on Robotics and Automation, IEEE, 2013: pp. 5309–5316. https://doi.org/10.1109/ICRA.2013.6631337.

[165] A. Hamidi, Y. Tadesse, 3D printing of very soft elastomer and sacrificial carbohydrate glass/elastomer structures for robotic applications, Mater Des. 187 (2020) 108324. https://doi.org/10.1016/j.matdes.2019.108324.

[166] J. Plott, A. Shih, The extrusion-based additive manufacturing of moisture-cured silicone elastomer with minimal void for pneumatic actuators, Addit Manuf. 17 (2017) 1–14. https://doi.org/10.1016/j.addma.2017.06.009.

[167] J. Plott, X. Tian, A.J. Shih, Voids and tensile properties in extrusion-based additive manufacturing of moisture-cured silicone elastomer, Addit Manuf. 22 (2018) 606–617. https://doi.org/10.1016/j.addma.2018.06.010.

[168] H.-H. Moretto, M. Schulze, G. Wagner, Silicones, in: Ullmann's Encyclopedia of Industrial Chemistry, Wiley-VCH Verlag GmbH & Co. KGaA, Weinheim, Germany, 2000. https://doi.org/10.1002/14356007.a24_057.

[169] S. Shang, L. Gan, M.C. Yuen, S. Jiang, N. Mei Luo, Carbon nanotubes based high temperature vulcanized silicone rubber nanocomposite with excellent elasticity and electrical properties, Compos Part A Appl Sci Manuf. 66 (2014) 135–141. https://doi.org/10.1016/j.compositesa.2014.07.014.

[170] F. Yan, X. Zhang, F. Liu, X. Li, Z. Zhang, Adjusting the properties of silicone rubber filled with nanosilica by changing the surface organic groups of nanosilica, Compos B Eng. 75 (2015) 47–52. https://doi.org/10.1016/j.compositesb.2015.01.030.

[171] E. Luis, H.M. Pan, S.L. Sing, A.K. Bastola, G.D. Goh, G.L. Goh, H.K.J. Tan, R. Bajpai, J. Song, W.Y. Yeong, Silicone 3D Printing: Process Optimization, Product Biocompatibility, and Reliability of Silicone Meniscus Implants, 3D Print Addit Manuf. 6 (2019) 319–332. https://doi.org/10.1089/3dp.2018.0226.

[172] O.D. Yirmibesoglu, J. Morrow, S. Walker, W. Gosrich, R. Canizares, H. Kim, U. Daalkhaijav, C. Fleming, C. Branyan, Y. Menguc, Direct 3D printing of silicone elastomer soft robots and their performance comparison with molded counterparts, in: 2018 IEEE International Conference on Soft Robotics (RoboSoft), IEEE, 2018: pp. 295–302. https://doi.org/10.1109/ROBOSOFT.2018.8404935.

[173] S. Walker, U. Daalkhaijav, D. Thrush, C. Branyan, O.D. Yirmibesoglu, G. Olson, Y. Menguc, Zero-Support 3D Printing of Thermoset Silicone Via Simultaneous Control of Both Reaction Kinetics and Transient Rheology, 3D Print Addit Manuf. 6 (2019) 139–147. https://doi.org/10.1089/3dp.2018.0117.

[174] A. Miriyev, B. Xia, J.C. Joseph, H. Lipson, Additive Manufacturing of Silicone Composites for Soft Actuation, 3D Print Addit Manuf. 6 (2019) 309–318. https://doi.org/10.1089/3dp.2019.0116.

[175] S.M.A.I. Ovy, G. Stano, G. Percoco, M. Cianchetti, Y. Tadesse, Inexpensive monolithic additive manufacturing of silicone structures for bio-inspired soft robotic systems, Engineering Research Express. 5 (2023) 015016. https://doi.org/10.1088/2631-8695/acb587.

[176] K.B. Putra, X. Tian, A.J. Shih, Soft Shear and Compressive Contact Stresses Sensor With Conductive Microfluidic Channels Fabricated by Additive Manufacturing, IEEE Sens J. 22 (2022) 7674–7683. https://doi.org/10.1109/JSEN.2022.3159452.

[177] D. Ma, X. Tian, J. Han, L. Xia, Modeling for silicone foam material extrusion with liquid rope coiling, Int J Mech Sci. 249 (2023) 108234. https://doi.org/10.1016/j.ijmecsci.2023.108234.

[178] M. Schaffner, J.A. Faber, L. Pianegonda, P.A. Rühs, F. Coulter, A.R. Studart, 3D printing of robotic soft actuators with programmable bioinspired architectures, Nat Commun. 9 (2018) 878. https://doi.org/10.1038/s41467-018-03216-w.

[179] W. van den Bogert, J. Lorenz, X. Yi, N. Fazeli, A.J. Shih, Lumped-Parameter Modeling and Control for Robotic High-Viscosity Fluid Dispensing in Additive Manufacturing, ArXiv. (2022).

[180] A. Colpani, A. Fiorentino, E. Ceretti, Feasibility analysis and characterization of an extrusion-based AM process for a two-component and biocompatible silicone, J Manuf Process. 49 (2020) 116–125. https://doi.org/10.1016/j.jmapro.2019.11.017.

[181] Y. Jin, J. Plott, A.J. Shih, Extrusion-Based Additive Manufacturing of the Moisture-Cured Silicone Elastomer, in: International Solid Freeform Fabrication Symposium, 2015.

[182] F. Liravi, R. Darleux, E. Toyserkani, Additive manufacturing of 3D structures with non-Newtonian highly viscous fluids: Finite element modeling and experimental validation, Addit Manuf. 13 (2017) 113–123. https://doi.org/10.1016/j.addma.2016.10.008.

[183] T.J. Coogan, D.O. Kazmer, Healing simulation for bond strength prediction of FDM, Rapid Prototyp J. 23 (2017) 551–561. https://doi.org/10.1108/RPJ-03-2016-0051.

[184] T.J. Coogan, D.O. Kazmer, Prediction of interlayer strength in material extrusion additive manufacturing, Addit Manuf. 35 (2020) 101368. https://doi.org/10.1016/j.addma.2020.101368.

[185] F. Liravi, E. Toyserkani, A hybrid additive manufacturing method for the fabrication of silicone bio-structures: 3D printing optimization and surface characterization, Mater Des. 138 (2018) 46–61. https://doi.org/10.1016/j.matdes.2017.10.051.

[186] D.A. Porter, N. Davis, P.S. Krueger, A.L. Cohen, D. Son, Additive manufacturing by material extrusion with medical grade silicone elastomers and IR laser curing, Rapid Prototyp J. 26 (2020) 145–155. https://doi.org/10.1108/RPJ-10-2018-0279.

[187] E. Luis, H.M. Pan, A.K. Bastola, R. Bajpai, S.L. Sing, J. Song, W.Y. Yeong, 3D Printed Silicone Meniscus Implants: Influence of the 3D Printing Process on Properties of Silicone Implants, Polymers (Basel). 12 (2020) 2136. https://doi.org/10.3390/polym12092136.

[188] E. Luis, H.M. Pan, S.L. Sing, R. Bajpai, J. Song, W.Y. Yeong, 3D Direct Printing of Silicone Meniscus Implant Using a Novel Heat-Cured Extrusion-Based Printer, Polymers (Basel). 12 (2020) 1031. https://doi.org/10.3390/polym12051031.